

University of Ljubljana

Faculty of Electrical Engineering

Rok Šmerc

**Mechanisms of electroporation
and physicochemical factors of
importance to
electroporation-based therapies**

DOCTORAL DISSERTATION

Ljubljana, 2025

University of Ljubljana

Faculty of Electrical Engineering

Rok Šmerc

**Mechanisms of electroporation
and physicochemical factors of
importance to
electroporation-based therapies**

DOCTORAL DISSERTATION

Mentor: Assist. Prof. Samo Mahnič-Kalamiza, PhD

Ljubljana, 2025

Univerza v Ljubljani

Fakulteta za elektrotehniko

Rok Šmerc

**Mehanizmi elektroporacije in
fizikalno-kemijski dejavniki
pomembni pri terapijah z
elektroporacijo**

DOKTORSKA DISERTACIJA

Mentor: doc. dr. Samo Mahnič-Kalamiza

Ljubljana, 2025

Senat Fakultete za elektrotehniko Univerze v Ljubljani je na seji dne, 10.06.2021 odobril kandidatu:

ROK ŠMERC

temo za doktorsko disertacijo z naslovom:

Mehanizmi elektroporacije in fizikalno-kemijski dejavniki pomembni pri terapijah z elektroporacijo

Mechanisms of electroporation and physicochemical factors of importance to electroporation-based therapies

Komisija za doktorski študij Univerze v Ljubljani je po pooblastilu Senata Univerze v Ljubljani temo potrdila na seji dne: 06.07.2021.

Senat Fakultete za elektrotehniko Univerze v Ljubljani je kandidatu na seji dne, 19.06.2025 priznal naslednje izvirne prispevke k znanosti:

- 1 Večnivojsko numerično modeliranje in eksperimentalna potrditev anizotropije skeletne mišice.
- 2 Eksperimentalno potrjen numerični model pH sprememb, povzročenih z elektroporacijskimi pulzi.
- 3 Eksperimentalna karakterizacija elektroosmotskega toka v tkivih pri PEF in DC pogojih.

Komisija za zagovor doktorske disertacije:

prof. dr. Marko Topič, predsednik
izr. prof. dr. Bor Kos, član
izr. prof. dr. Selma Čorović, članica
Prof. Antoni Ivorra, PhD, član
doc. dr. Samo Mahnič Kalamiza, mentor



Dekan:

prof. dr. Marko Topič



I, the undersigned student, ROK ŠMERC, registration number 64190362, the author of the written final work of studies, entitled: Mechanisms of electroporation and physicochemical factors of importance to electroporation-based therapies,

DECLARE,

1. ¹ **a)** The written final work of studies is a result of my independent work and that I have used the AI tools responsibly (in particular by checking primary sources, by not entering copyrighted works into the AI tools, by critically evaluating the results, which may be incomplete, incorrect or untrue) and am solely responsible for the content of the copyright work I have created.
b) The written final work of studies is a result of own work of more candidates and fulfils the conditions determined by the Statute of UL for joint final works of studies and is a result of my independent work in the required share and that I have used the AI tools responsibly (in particular by checking primary sources, by not entering copyrighted works into the AI tools, by critically evaluating the results, which may be incomplete, incorrect or untrue) and am solely responsible for the content of the copyright work I have created.
2. I have acquired all the necessary permissions for the use of data and copyrighted works in the written final work of studies and have clearly marked them in the written final work of studies.
3. I have acted in accordance with ethical principles during the preparation of the written final work of studies and have, where necessary, obtained agreement of the ethics commission.
4. I give my consent to use of the electronic form of the written final work of studies for the detection of content similarity with other works, using similarity detection software that is connected with the study information system of the university member.
5. I transfer to the UL – free of charge, non-exclusively, geographically and time-wise unlimited – the right of saving the work in the electronic form, the right of reproduction, as well as the right of making the written final work of studies available to the public on the world wide web via the Repository of UL.
6. I have acquired from publishers, to which I have previously exclusively transferred material copyright for articles, all the necessary permissions for the inclusion of articles in the electronic form of the dissertation. The permissions enable the UL – free of charge, non-exclusively, geographically and time-wise unlimited – to save the work in the electronic form and its reproduction as well as to make the dissertation available to the public on the world wide web via the Repository of UL.
7. I give my consent to publication of my personal data that are included in the written final work of studies and in this declaration, together with the publication of the written final work of studies.
8. I give my consent to use of my birth date in COBISS record.

In: Ljubljana
Date: 24. 6. 2025

Student's signature:

¹ Choose a) or b).

PREFACE

The present doctoral dissertation is the result of numerical modelling, experimental investigations, data analysis, research and development related to mechanisms of electroporation in tissues. The work was carried out during the doctoral studies at the Laboratory of Biocybernetics, Faculty of Electrical Engineering, University of Ljubljana. The results of the research work are presented in the following five papers, which have been published in or submitted to international scientific journals.

- **Paper 1:** R. Šmerc, D. A. Ramirez, S. Mahnič-Kalamiza, J. Dermol-Černe, D. C. Sigg, L. M. Mattison, P. A. Iaizzo, and D. Miklavčič. A multiscale computational model of skeletal muscle electroporation validated using *in situ* porcine experiments, *IEEE Transactions on Biomedical Engineering*, vol. 60, no. 6, pp. 1826-1837, June 2023.
- **Paper 2:** R. Šmerc, M. Stručić, M. Kranjc, I. Serša, D. Miklavčič, and S. Mahnič-Kalamiza. Electrical pathways through the intricate network of skeletal muscle fibres: Insights from MRI-validated numerical modelling, *IEEE Transactions on Biomedical Engineering*, in press, 2025.
- **Paper 3:** R. Šmerc, D. Miklavčič, and S. Mahnič-Kalamiza. Skeletal muscle death from the perspective of electrical impedance as evidenced by experiment and numerical modelling, *Computers in Biology and Medicine*, under review.
- **Paper 4:** R. Šmerc, D. Miklavčič, and S. Mahnič-Kalamiza. An experimentally validated numerical model of pH changes in surrogate tissue induced by electroporation pulses, *Electrochimica Acta*, vol. 511: 145363, January 2025.

- **Paper 5: R. Šmerc** and S. Mahnič-Kalamiza. On the importance of electroosmosis in pulsed electric field treatment of food matrices, *Results in Engineering*, under review.

Acknowledgements

First and foremost, I am deeply grateful to my supervisor Samo. Your knowledge, guidance, and support have been invaluable throughout my doctoral studies. Thank you for your patience and for always being there when I needed help. It has truly been a pleasure working with you.

I also wish to thank Damijan for providing me with the opportunity to enter the world of science and electroporation. His insightful comments and thorough feedback on the manuscripts have greatly improved the quality of this work.

Next, I would like to thank the members of my doctoral studies committee, Selma, Toni, and Bor, for generously dedicating their time and expertise to the careful evaluation of this dissertation.

I also wish to thank all the colleagues at the Laboratory of Biocybernetics for the friendly working environment, discussions, and help whenever needed.

Last but not least, I would like to thank my parents, my brother Žiga, and my love Sara, who have always supported me and believed in me, offering encouragement and understanding throughout this journey.

Table of contents

Abstract	1
Razširjen povzetek v slovenščini	3
I Uvod	7
I.1. Pojav elektroporacije	7
I.2. Uporaba elektroporacije	8
I.3. Električne lastnosti tkiv	9
I.3.1. Anizotropija skeletnih mišic	10
I.4. Dodatni pojavi, ki spremljajo elektroporacijo	11
I.4.1. Elektrokemični učinki pulznih električnih polj	11
I.4.2. Gibanje tekočine pod vplivom električnega polja	13
I.5. Namen doktorske disertacije	14
II Znanstveni članki	17
III Razprava	21
III.1. Raziskava anizotropije skeletne mišice z večnivojskim modeliranjem	21
III.2. Modeliranje tokovnih poti v skeletni mišici	25
III.3. <i>Post-mortem</i> spremembe anizotropije skeletne mišice	28
III.4. Modeliranje pH sprememb, povzročenih z elektroporacijo	32
III.5. Eksperimentalna raziskava elektroosmoze	36

IV	Zaključek	43
V	Izvirni prispevki k znanosti	47
	Mechanisms of electroporation and physicochemical factors of importance to electroporation-based therapies	49
1	Introduction	51
1.1.	The phenomenon of electroporation	51
1.2.	Applications of electroporation	52
1.3.	Electrical properties of tissues	53
1.3.1.	Skeletal muscle anisotropy	54
1.4.	Additional phenomena accompanying electroporation	55
1.4.1.	Electrochemical effects of pulsed fields	55
1.4.2.	Electric field-induced fluid motion	56
1.5.	Aims of the dissertation.	58
2	Research papers	61
2.1.	Paper 1	65
2.2.	Paper 2	81
2.3.	Paper 3	97
2.4.	Paper 4	121
2.5.	Paper 5	135
3	Discussion	155
3.1.	Investigating skeletal muscle anisotropy through multiscale modelling	155
3.2.	Modelling of current pathways in skeletal muscle	157
3.3.	<i>Post-mortem</i> changes in skeletal muscle anisotropy	160
3.4.	Modelling of electroporation-induced pH-dynamics	163
3.5.	Experimental investigation of electroosmosis.	166
4	Conclusions	171

5	Original scientific contributions	175
	References	177

Abstract

Electroporation is a biophysical phenomenon induced by the application of short electrical high-voltage pulses to biological tissue. These pulses temporarily increase the permeability of the cell membrane, allowing ions and molecules to which the membrane is otherwise impermeable to pass through, thus entering or leaving the cells. Depending on the pulse parameters, electroporation can either be reversible, allowing the cells to recover, or irreversible, leading to cell death. Thanks to its precise control over membrane permeability, electroporation is widely used in biomedicine, biotechnology, and food processing. Its applications range from tumour ablation, gene therapy, electrochemotherapy, treatment of cardiac arrhythmias to various applications in the food industry.

Despite the widespread use of electroporation, several important factors influencing its efficacy remain poorly understood. This doctoral dissertation investigates three such factors: skeletal muscle anisotropy, electrochemically induced pH changes, and electroosmotic flow, and explores their implications for electroporation-based treatments.

Firstly, the anisotropic electrical behaviour of skeletal muscle tissue was investigated in detail. Multiscale numerical models were developed to represent skeletal muscle from the level of individual cells up to the tissue level, capturing how the microscale structure influences the macroscopic electrical properties. The models and findings were validated by *in vivo* ablation experiments as well as *ex vivo* MRI-based current density imaging and impedance spectroscopy. Together, these approaches have demonstrated that the anisotropy of skeletal muscle significantly influences the electric field distribution, lesion geometry, and current pathways. Experimental and numerical results have shown that the anisotropic

electrical properties originate primarily from the cell plasma membrane.

Secondly, a mechanistic numerical model was constructed to predict the electrochemically induced pH dynamics associated with electroporation pulses, particularly relevant for gene electrotransfer protocols. This model accounted for the electrochemical reactions at the electrodes and was experimentally validated using agarose gels with embedded pH indicators. A calibrated imaging system was developed to enable real-time tracking of pH fronts. The developed model reliably captured the spatial and temporal evolution of acidic and alkaline zones, providing quantitative insights into the extent and implications of pH variations during electroporation treatments.

Thirdly, electroosmotic flow, a relatively understudied phenomenon of electrically induced fluid transport, was experimentally characterised in plant tissue (potato), animal skeletal muscle, and agarose phantoms under pulsed electric field (PEF) and direct current (DC) conditions. The experimental results demonstrated a significant electroosmotically driven contribution to tissue deformation and fluid movement, revealing synergistic effects between electroporation-induced membrane permeabilisation and subsequent electroosmotic fluid transport, especially at lower current amplitudes. This systematic characterisation highlights the potential role of electroosmotic flow in influencing fluid motion during electroporation and supports its consideration in the development of future electroporation-based applications.

The dissertation comprises five original scientific papers, each presenting experimental and theoretical advances. Collectively, the work advances our understanding of the mechanisms and physicochemical factors shaping electroporation-based treatments, offering new insights and practical contributions for future applications. Together, the findings and models provide a solid foundation for improving the design and optimisation of electroporation-based protocols across biomedical, biotechnological, and food-related applications.

Keywords: electroporation; electroporation-based treatments; pulsed electric field (PEF) treatment; pulsed field ablation (PFA); numerical modelling; skeletal muscle anisotropy; electrochemistry; pH changes; electroosmosis.

Razširjen povzetek v slovenščini

Povzetek

Elektroporacija je biofizikalni pojav, ki ga povzroči dovajanje kratkih visokonapetostnih električnih pulzov biološkemu tkivu. Dovajanje pulzov povzroči začasno povečanje prepustnosti celične membrane, kar omogoči prehod ionov in molekul, ki sicer ne bi mogli skozi membrano, v celico ali iz nje. Odvisno od parametrov pulzov je elektroporacija lahko reverzibilna, pri kateri si celice po določenem času opomorejo, ali ireverzibilna, ki vodi v celično smrt. Zaradi možnosti selektivnega spreminjanja prepustnosti celične membrane se elektroporacija široko uporablja v biomedicini, biotehnologiji in živilski industriji. Njene aplikacije segajo od ablacije tumorjev, genskega zdravljenja, elektrokemoterapije in zdravljenja srčnih aritmij do različnih postopkov v živilski industriji.

Kljub razširjeni uporabi elektroporacije ostaja več pomembnih dejavnikov, ki vplivajo na njeno učinkovitost, slabo raziskanih. Ta doktorska disertacija obravnava tri takšne dejavnike: anizotropijo skeletne mišice, elektrokemično povzročene spremembe pH, in elektroosmozni tok, ter raziskuje njihov pomen za terapije, temelječe na elektroporaciji.

Najprej smo podrobno raziskali anizotropno električno obnašanje skeletne mišice. Razvili smo večnivojske numerične modele, ki predstavljajo skeletno mišico od ravni posameznih celic do ravni celotnega tkiva, pri čemer zajamejo vpliv mikroskopske strukture na makroskopske električne lastnosti. Modele in izsledke smo potrdili z ablacijskimi poskusi *in vivo*, in z MRI-slikanjem gostote toka ter impedančno spektroskopijo *ex vivo*. Skupaj so ti pristopi pokazali, da anizotropija skeletne mišice pomembno vpliva na porazdelitev električnega polja, geometrijo lezij, in poti električnega toka v tkivu. Eksperimentalni in numerični rezultati so pokazali, da anizotropne električne lastnosti mišice izvirajo predvsem

iz neprepustnosti plazemske membrane celice.

V drugem delu smo razvili mehanistični numerični model za napovedovanje elektrokemično povzročenih sprememb pH, povezanih z dovajanjem elektroporacijskih pulzov, zlasti pri protokolih, kot se uporabljajo pri genski elektrotransfekciji. V modelu smo upoštevali elektrokemične reakcije na elektrodah in ga eksperimentalno potrdili z uporabo agaroznih gelov, ki smo jim dodali pH indikatorje. Razvili smo kalibriran sistem slikanja, ki omogoča sledenje pH frontam v realnem času. Razviti model je zanesljivo zajel prostorsko in časovno evolucijo kislih in bazičnih območij ter podal vpogled v obseg in posledice pH sprememb med in po postopku elektroporacije.

V tretjem delu raziskav smo obravnavali elektroosmozni tok, ki je sorazmerno slabo raziskan pojav električno inducirane gibanja tekočin. Eksperimentalno smo ga ovrednotili v rastlinskem tkivu (krompir), skeletni mišici živalskega izvora, in agaroznih fantomih pri obdelavi s pulzirajočim električnim poljem (PEF) ter enosmernim tokom (DC). Rezultati so pokazali pomemben prispevek elektroosmozno inducirane toka k deformaciji tkiva in gibanju tekočin. Zlasti pri nižjih jakostih toka je sinergijsko delovanje med povečanjem prepustnosti membran zaradi elektroporacije in kasnejšim elektroosmoznim tokom še posebej izrazito. Ta sistematična karakterizacija poudarja pomen elektroosmoze na vpliv gibanja tekočin med elektroporacijo ter podpira njeno vključitev v prihodnji razvoj aplikacij, temelječih na elektroporaciji.

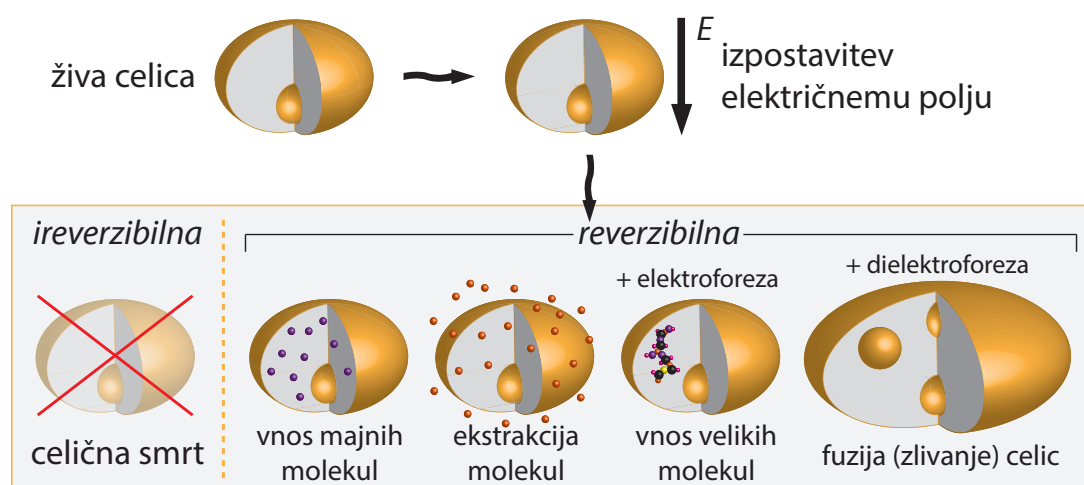
Disertacija vključuje pet izvirnih znanstvenih člankov, ki vsak zase predstavljajo nova eksperimentalna in teoretična dognanja. Skupaj prispevajo k boljšemu razumevanju mehanizmov in fizikalno-kemijskih dejavnikov, ki oblikujejo potek terapij, temelječih na elektroporaciji, ter ponujajo nova spoznanja in rešitve za prihodnjo rabo. Ugotovitve in razviti modeli skupaj predstavljajo osnovo za izboljšanje načrtovanja in optimizacije elektroporacijskih postopkov v biomedicini, biotehnologiji, in živilski industriji.

Ključne besede: elektroporacija; elektroporacijske terapije; pulzirajoča električna polja (PEF); ablacija s pulzirajočim poljem (PFA); numerično modeliranje; anizotropija skeletne mišice; elektrokemija; pH spremembe; elektroosmoza.

I Uvod

I.1 Pojav elektroporacije

Elektroporacija je biofizikalni pojav, pri katerem kratki visokonapetostni električni pulzi začasno spremenijo celovitost celičnih membran. Ti pulzi povzročijo nastanek prehodnih hidrofilnih por, kar bistveno poveča prepustnost membrane. Takšne spremembe v prepustnosti omogočajo vstop ali izstop molekul oziroma ionov, kot so zdravila, nukleinske kisline in proteini, ki sicer ne morejo prehajati skozi membrano. Ali elektroporacija povzroči reverzibilno permeabilizacijo membrane ali trajno poškodbo celic, je v prvi vrsti odvisno od amplitude, trajanja, in frekvence uporabljenih električnih pulzov. Če je intenziteta pulzov razmeroma nizka, si celične membrane po dovajanju pulzov opomorejo, kar pomeni reverzibilno elektroporacijo. Nasprotno pa pulzi višje intenzitete povzročijo trajno poškodbo membran in posledično celično smrt – pojav, ki ga imenujemo ireverzibilna elektroporacija [1], [2], [3], [4]. Shematski prikaz pojava elektroporacije je podan na Sliki I.1.



Slika I.1: Shematski prikaz pojava elektroporacije, ki ponazarja možne izide glede na parametre pulzov (amplituda, oblika, trajanje) [5].

I.2 Uporaba elektroporacije

Tako reverzibilna kot tudi ireverzibilna elektroporacija sta našli široko uporabo na različnih področjih, zlasti v biomedicini [6], biotehnologiji [7], okoljskih vedah [8], in predelavi hrane [9]. V biomedicini se reverzibilna elektroporacija uporablja v terapijah, kot je npr. genska elektrotransfekcija. Ker omogoča učinkovit vnos genskega materiala v celice, ima ključno vlogo pri genskih terapijah in protokolih cepljenja [10], [11], [12]. Poleg tega se reverzibilna elektroporacija uporablja v elektrokemoterapiji za izboljšanje vnosa kemoterapevtskih učinkovin v celice. S povečanjem vnosa zdravila v tumorske celice elektrokemoterapija omogoča učinkovitejše lokalno zdravljenje in hkrati zmanjšuje potrebo po visokih sistemskih odmerkih kemoterapevtika [13], [14], [15].

Ireverzibilna elektroporacija se je izkazala kot učinkovita metoda za ablacijo tumorjev, saj zaradi svojega netermičnega delovanja omogoča selektivno uničenje rakavih celic ob ohranjanju strukture okoliškega zdravega tkiva [16], [17], [18], [19], [20]. Ireverzibilna elektroporacija postaja vse pomembnejša tudi na področju kardiologije za zdravljenje srčnih aritmij, zlasti atrijske fibrilacije. Z njo se izvaja ablacija za izolacijo pljučnih ven in učinkovito prekinitev aritmičnih prevodnih poti. V tem kontekstu se tehnologija imenuje ablacija s pulzirajočim poljem

(angl. *pulsed field ablation*, PFA) [21], [22], [23], [24], [25].

Poleg medicine se je elektroporacija uveljavila tudi v živilski industriji, kjer je ponavadi poimenovana kot obdelava s pulzirajočim električnim poljem (angl. *pulsed electric field treatment*, PEF). V tem kontekstu se PEF najpogosteje uporablja kot predobdelava za izboljšanje procesov masnega transporta. Tako denimo povečuje izplen soka [9], omogoča učinkovitejše sušenje z izboljšanim izločanjem vode [26], povečuje biološko dostopnost dragocenih bioaktivnih spojin [27], [28], in prispeva k zmanjšanju koncentracije nezaželenih oziroma škodljivih snovi [29], [30]. Poleg tega se PEF raziskuje tudi kot orodje v postopkih konzerviranja, kot je krioprezervacija, kjer omogoča boljšo penetracijo krioprotektivnih snovi v celične strukture, s čimer ohranja teksturo in okus živil ter preprečuje nastanek ledenih kristalov [31].

I.3 Električne lastnosti tkiv

Učinkovitost uporabe elektroporacijskih postopkov ni odvisna le od parametrov pulzov, temveč tudi od električnih lastnosti tkiva. Biološka tkiva izkazujejo kompleksen električni odziv, ki ga določa njihova struktura in porazdelitev nabitih delcev znotraj njih. Medsebojno delovanje teh dejavnikov vpliva na razporeditev električnega polja in potek električnega toka po tkivu, kar vodi v izrazite razlike med različnimi tipi tkiv [32], [33], [34], [35], [36], [37]. Na splošno zunajcelični prostori bolje prevajajo električen tok zaradi visoke koncentracije prostih ionov, medtem ko celične membrane zaradi bistveno nižje prevodnosti delujejo kot ovire, ki omejujejo električni tok [38], [39]. Električne lastnosti tkiv se pomembno spreminjajo tudi s frekvenco, kar odraža različne fiziološke mehanizme, ki so aktivni v različnih frekvenčnih območjih [35], [37]. Za optimizacijo elektroporacijskih postopkov je zato ključno dobro razumevanje in poznavanje teh kompleksnih električnih lastnosti tkiva.

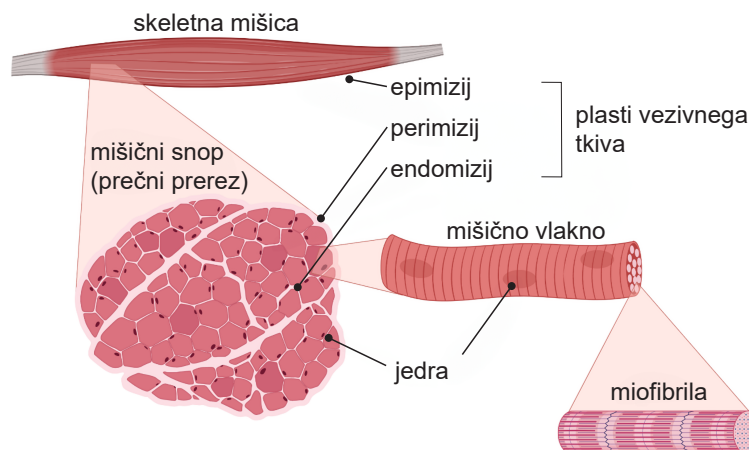
Tehnike, kot je električna impedančna spektroskopija (angl. *electrical impedance spectroscopy*, EIS), imajo ključno vlogo pri podrobni karakterizaciji električnih lastnosti tkiv, saj omogočajo celovit vpogled v njihove uporabne in kapacitivne značilnosti vzdolž širokega frekvenčnega območja [40], [41], [42], [43], [44],

[45]. Dodatne pomembne informacije je moč pridobiti s spremljanjem napetostnih in tokovnih signalov v realnem času med dovajanjem elektroporacijskih pulzov, kar omogoča dinamično sledenje spremembam prevodnosti tkiva med obdelavo [46], [47]. Poleg tega lahko napredne slikovne tehnike, kot je slikanje gostote električnega toka z magnetno resonanco (angl. *current density imaging*, CDI), bistveno prispevajo k razumevanju, kako električni tok teče skozi biološko tkivo med elektroporacijo [48], [49], [50], [51].

I.3.1 Anizotropija skeletnih mišic

Skeletna mišica predstavlja pomembno raziskovalno področje v kontekstu elektroporacije, saj je pogosto izbrana kot tarčno tkivo za gensko elektrotransfekcijo [52], [53], [54]. Ključni dejavnik, ki vpliva na električno obnašanje skeletne mišice, je anizotropija, kar pomeni usmerjenost oziroma smerno odvisnost njenih električnih lastnosti [55], [56], [57]. Anizotropija skeletne mišice izhaja predvsem iz urejene orientacije mišičnih vlaken v zapleteni mreži vezivnih tkiv, kot so endomizij, perimizij in epimizij [58], [59]. Vsako mišično vlakno obdaja plazemska membrana – sarkolema – ki skupaj z okoliškim vezivnim tkivom deluje kot izolacijska pregrada, ki omejuje gibanje ionov (Slika I.2). Te izolacijske plasti učinkovito ovirajo tok električnega toka v smeri pravokotno na orientacijo mišičnih vlaken [60]. Posledično skeletna mišica izkazuje izrazite smerne razlike v električni prevodnosti: prevodnost vzdolž vlaken je višja kot prečno na vlakna, kar je še posebej izrazito pri nizkih frekvencah [35], [37].

Smerne razlike v prevodnosti pomembno vplivajo na prostorsko porazdelitev električnega polja v skeletni mišici, s tem pa neposredno določajo izid elektroporacijskih terapij. Celovito razumevanje anizotropnega električnega obnašanja je zato ključnega pomena za natančno napovedovanje interakcij med električnim poljem in mišičnim tkivom, za optimizacijo postopkov, ki temeljijo na elektroporaciji, ter za izboljšanje učinkovitosti terapij v biomedicini.



Slika I.2: Zgradba skeletne mišice. Skeletna mišica je razdeljena na različne podstrukture, ki so med seboj ločene s plastmi vezivnega tkiva. Celotna mišica je obdana s plastjo vezivnega tkiva, imenovano epimizij. Znotraj mišice se nahajajo snopi (prikazani v prečnem prerezu), od katerih je vsak ovit s perimizijem. Posamezen snop sestavlja mišična vlakna, obdana z endomizijem. Mišična vlakna so večjedrna in vsebujejo miofibrile [61].

I.4 Dodatni pojavi, ki spremljajo elektroporacijo

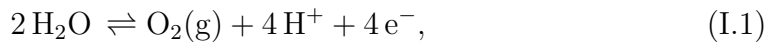
Elektroporacijo spremljajo tudi sekundarni pojavi, ki lahko vplivajo na odziv tkiva in potek masnega transporta. Nekateri med njimi, kot je segrevanje tkiva zaradi Joulovih izgub, so že dobro raziskani [62], [63], [64], [65], [66], [67], medtem ko nekateri drugi še niso. Med manj raziskane, a vse bolj prepoznane kot ključne, sodijo poškodbe tkiva zaradi sprememb pH, ki nastanejo kot posledica elektrokemičnih reakcij [68], [69], ter vloga elektroosmoze pri masnem transportu med elektroporacijo [70], [71], [72]. Ti pojavi zato zahtevajo nadaljnje raziskave.

I.4.1 Elektrokemični učinki pulznih električnih polj

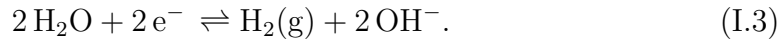
Elektrokemični učinki pulznih električnih polj predstavljajo pomemben pojav, ki spremlja elektroporacijo in močno vpliva na tkivo na lokalnem nivoju. Ti učinki izvirajo predvsem iz reakcij elektrolize vode, do katerih pride na stiku med elektrodo in tkivom ob dovajanju električnih pulzov v biološko tkivo. Reakcije

elektrolize vode pri elektrodah povzročijo nastanek izrazitih lokalnih pH gradientov: v bližini anode nastane kislo okolje, medtem ko se v bližini katode razvije bazično okolje [68], [69], [73], [74], [75].

Glavne elektrokemične reakcije, ki povzročajo spremembe pH med dovajanjem električnih pulzov, so oksidacijske reakcije (izguba elektronov) na anodi in redukcijske reakcije (pridobivanje elektronov) na katodi. Na anodi se oksidirajo molekule vode in kloridni ioni, pri čemer nastanejo vodikovi ioni ter plina kisik in klor [76], [77], [78]:



Opisani reakciji povzročita nastanek kislinskih pH front v okolici anode. Nasprotno pa se na katodi reducirajo molekule vode, pri čemer nastanejo hidroksidni ioni in vodik v plinastem stanju, kar vodi do nastanka bazičnih pH front [79]:



Elektrokemično povzročene spremembe pH imajo pomembne posledice za terapije, ki temeljijo na elektroporaciji [80], [81], [82], [83]. Na primer, pri genski elektrotransfekciji je ohranjanje fiziološko ustreznih pH pogojev ključno za ohranitev integritete plazmidne DNA in s tem za učinkovito transfekcijo. Znatna sprememba pH lahko poškoduje genetski material in zmanjša preživetje celic, kar poslabša terapevtsko učinkovitost [84], [85], [86].

Nasprotno pa so pri nekaterih tumorskih terapijah pH gradienti namenoma povzročeni za izboljšanje terapevtskih izidov. V okviru elektrokemične terapije tumorjev se uporablja nadzorovani enosmerni tok nizke jakosti za ustvarjanje lokaliziranega kislega in bazičnega okolja, ki povzroči tarčno smrt tumorskih celic [76], [77], [87], [88], [89]. Novejši pristop, ki združuje elektroporacijo in elektrolizo – znan kot metoda E2 – izkorišča te lokalne spremembe pH za izboljšano ablacijo tkiva, saj spodbuja vnos elektrolitskih produktov v celice preko permeabiliziranih membran [90], [91], [92], [93]. Raziskave kažejo, da je mogoče z večjim številom nizkonapetostnih pulzov doseči primerljive volumne ablacije, kot pri običajni ireverzibilni elektroporaciji z visokimi napetostmi, kar dodatno poudarja vlogo elektrokemično induciranih sprememb pH pri poškodbah tkiva in

terapevtskih rezultatih [94]. Razumevanje elektrokemičnih učinkov elektroporacije je zato ključno za optimizacijo elektroporacijskih protokolov in zmanjšanje neželenih poškodb tkiva v kliničnih in eksperimentalnih okoljih.

I.4.2 Gibanje tekočine pod vplivom električnega polja

Drugi pojav, ki je v raziskavah elektroporacije pogosto spregledan, kljub njegovemu potencialu, da pomembno vpliva na transport tekočin in raztopljenih snovi v biološkem tkivu, izpostavljenemu električnemu polju, je elektroosmoza. Elektroosmoza označuje gibanje tekočine, običajno vode, skozi porozno strukturo kot posledica električnega polja. To gibanje je posledica elektrokinetičnih interakcij na nabitih kontaktnih območjih med trdnino in tekočino, kjer tvorba električnega dvosloja povzroči premik ionov v zunanjem električnem polju. Med migracijo ionov pod vplivom električnega polja ti delujejo z vlečno silo na okoliško tekočino, kar povzroči pretok tekočine [72]. Navidezna elektroosmozna hitrost u_{EOS} je v poroznih medijih podana z enačbo:

$$u_{\text{EOS}} = \frac{\varepsilon_w \zeta \varepsilon}{\eta \lambda^2} \nabla \phi, \quad (\text{I.4})$$

kjer je ε_w permitivnost vode (F/m), ζ zeta potencial (V) na nabitih površinah, ε poroznost medija, η dinamična viskoznost tekočine (Pa·s), λ tortuoznost (brez enote), ki opisuje kompleksnost poti gibanja tekočine, in $\nabla \phi$ gradient električnega potenciala (V/m) [95]. Zeta potencial je še posebej pomemben, saj določa smer in velikost elektroosmoznega toka glede na naboj na meji med trdnino in tekočino [96].

Večina bioloških tkiv ima negativen zeta potencial, kar pomeni, da se tekočina običajno pomika od anode proti katodi [97], [98], [99]. V živilskih aplikacijah na osnovi rastlinskih tkiv lahko obdelava s PEF izboljša elektroosmozno dehidracijo s povečanjem prepustnosti membran in s spodbujanjem izločanja vode. S tem se izboljša energetska učinkovitost in zmanjša potreba po konvencionalnem toplotnem sušenju, kar ugodno vpliva tako na kakovost izdelka, kot na okoljski odtis [71], [100].

Tudi v biomedicini lahko elektroosmozni tok pomembno vpliva na izid terapije. Pri zdravljenju tumorjev elektroosmoza spodbuja gibanje tekočine od anode

proti katodi, kar povečuje lokalno dehidracijo in ojača destruktivne učinke lokaliziranih pH sprememb [101], [102], [103]. Elektroosmozni učinki ponujajo obetavne možnosti tudi pri ciljanem transportu zdravil, zlasti v okviru elektrokinetičnega, konvekcijsko okrepljenega transporta. Ta tehnika uporablja električna polja za usmerjanje terapevtskih učinkovin v globlja in sicer nedostopna tkiva, vključno z možgani. Omogoča natančnejše in manj invazivno apliciranje zdravil pri nižjih infuzijskih tlakih kot konvencionalne metode [104], [105]. Elektroosmoza tako odpira možnosti za boljši nadzor nad masnim transportom med elektroporacijo. Za izboljšanje natančnosti in učinkovitosti zdravljenja v živilskih in biomedicinskih aplikacijah je nadaljnje raziskovanje njenih mehanizmov in učinkov zelo pomembno.

I.5 Namen doktorske disertacije

Temeljni cilj te disertacije je prispevati k razvoju terapij, ki temeljijo na elektroporaciji, z izboljšanjem razumevanja temeljnih mehanizmov njenega delovanja, podprtim z eksperimentalno potrjenimi numeričnimi modeli izbranih fizikalno-kemijskih in anatomskih dejavnikov, ki vplivajo na izid terapij. V raziskavah so obravnavane tri glavne smeri: anizotropija skeletnih mišic, elektrokemično povzročene spremembe pH, ter z električnim poljem pogojen transport tekočine (tj., elektroosmoza). Vsak od teh pojavov pomembno vpliva na učinkovitost, varnost, in prenosljivost elektroporacijskih terapij v klinično prakso.

Prvi cilj je bil raziskati vlogo električne anizotropije skeletne mišice ter njen vpliv na izid elektroporacije. Čeprav je dobro znano, da se prevodnost mišičnega tkiva spreminja glede na usmerjenost mišičnih vlaken, specifični vplivi na porazdelitev električnega polja in toka ter s tem povezani biološki odzivi doslej še niso bili celovito raziskani. V ta namen je bila uporabljena večnivojska metoda modeliranja, ki se je začela na ravni posameznih mišičnih vlaken in razširila na kompleksne, anatomsko navdihnjene geometrije mišičnega tkiva. Razvite modele smo ovrednotili z analizo vzorcev poškodb, opaženih *in vivo*, ter z MRI-slikanjem gostote električnega toka. Poleg tega smo z impedančno spektroskopijo spremljali anizotropne električne lastnosti mišice v času po smrti, numerične simulacije pa so služile kot orodje za interpretacijo in potrditev eksperimentalno opaženih spre-

memb, povezanih s *post-mortem* razgradnjo tkiva. Eden izmed ključnih ciljev je bil preveriti, ali lahko *post-mortem* izrezana mišica služi kot nadomestek za *in vivo* poskuse in s tem prispeva k zmanjšanju števila poskusov na živalih. Tri študije, ki prispevajo k temu cilju, so ponudile pomemben vpogled v vpliv usmerjenosti mišičnih vlaken na izide zdravljenja, anizotropne poti toka, in časovno odvisne spremembe prevodnosti tkiva po smrti.

Drugi cilj je bil raziskati elektrokemične spremembe pH, ki nastanejo med in po elektroporaciji, s poudarkom na protokolih, pomembnih za gensko elektrottransfekcijo, kjer se običajno uporabljajo daljši monofazni pulzni protokoli. Razvit je bil mehanističen računski model za napovedovanje nastanka in širjenja kislih in bazičnih pH front, ki nastajajo kot posledica elektrolize vode na elektrodah. Model je bil potrjen z eksperimenti v agaroznih gelih, ki so vsebovali pH indikatorje, pri čemer je bilo dinamično spremljanje vrednosti pH omogočeno s kalibriranim slikovnim sistemom. Cilj je bil vzpostaviti zanesljiv eksperimentalni protokol za zajem prostorske in časovne dinamike pH ter oceniti, kako bi te elektrokemične spremembe lahko vplivale na varnost in učinkovitost postopka elektroporacije.

Tretji cilj je obravnaval elektroosmozo kot sočasen pojav pri elektroporaciji in njen pomen v različnih bioloških materialih. Elektroosmozni tok smo eksperimentalno preučili v rastlinskem tkivu (gomolj krompirja), živalski skeletni mišici, in v agaroznih fantomih. V rastlinskem tkivu smo preučili, kako predobdelava s pulzirajočim električnim poljem (PEF) spodbuja elektroosmozno izsuševanje z učinkovitejšim sproščanjem znotrajcelične tekočine. V živalski mišici smo na sveže izrezanem tkivu raziskali vlogo elektroosmoze pri masnem transportu iz vidikov, pomembnih za živilsko predelavo in biomedicinske aplikacije. Agarozne fantome smo uporabili kot nadomestne materiale za raziskovanje elektroosmoze v nadzorovanih eksperimentalnih pogojih.

S spoznanji, pridobljenimi skozi vse tri raziskovalne sklope, ta disertacija prispeva k boljšemu razumevanju ključnih pojavov, ki vplivajo na izid elektroporacijskih terapij. Skupaj tvorijo trdne temelje za izboljšanje načrtovanja, optimizacije, in uporabnosti terapij tako v eksperimentalnih kot tudi v kliničnih okoljih.

II Znanstveni članki

Raziskovalno delo, opravljeno v okviru doktorskega študija, je predstavljeno v petih izvirnih znanstvenih člankih, ki so bili objavljeni ali poslani v objavo v mednarodne recenzirane revije. V sklopu razširjenega povzetka v slovenskem jeziku sta povzeta razprava in zaključek vsakega od člankov.

Prvi članek obravnava vlogo anizotropije skeletne mišice pri elektroporaciji. Študija preučuje, kako usmerjenost električnega polja, ki je dovajano bodisi vzporedno bodisi pravokotno na mišična vlakna, vpliva na obseg ireverzibilne elektroporacije v skeletni mišici. Najprej je bil razvit numerični model, ki simulira elektroporacijo na ravni posameznega mišičnega vlakna in določa, kako se prevodnost spreminja med elektroporacijo. Ti rezultati so bili nato posplošeni na model skeletne mišice, obravnavane kot zvezno tkivo. *In vivo* poskusi so bili izvedeni na skeletni mišici prašiča, kjer smo z elektroporacijo povzročili poškodbe tkiva, ki smo jih nato segmentirali za neposredno primerjavo z numeričnimi napovedmi. Izračunane porazdelitve električnega polja smo primerjali z eksperimentalno dobljenimi *in vivo* poškodbami s pomočjo Sørensen–Diceovega koeficienta podobnosti, da bi določili prag, nad katerim pride do ireverzibilnih poškodb.

Drugi članek nadgrajuje našo prvo študijo z večjo anatomsko natančnostjo modela. Namesto, da bi mišico obravnavali kot homogeno tkivo, smo v tej raziskavi modelirali posamezna mišična vlakna, kar je omogočilo podrobnejši opis zgradbe tkiva. Preučili smo porazdelitev električnega toka znotraj tkiva pri dveh usmeritvah apliciranega električnega polja – vzporedno in pravokotno na mišična vlakna. Eksperimentalne podatke o porazdelitvi toka smo pridobili z uporabo magnetnoresonančne metode slikanja gostote toka (angl. *current density imaging*, CDI), ki omogoča neinvazivno določitev toka znotraj tkiva. Te meritve smo

nato primerjali z numeričnimi simulacijami, da bi preverili, kako natančno model zajema anizotropnost skeletne mišice.

Tretji članek obravnava spremembe anizotropije skeletne mišice v času po smrti. V tej študiji smo združili impedančno spektroskopijo in numerično modeliranje za spremljanje sprememb električnih lastnosti *post-mortem*. Z merjenjem impedance v različnih časovnih obdobjih po smrti smo raziskali, kako se tekom fiziološkega razpada membran spreminja anizotropija mišičnega tkiva. Z numeričnim modelom smo rezultate potrdili in podprli eksperimentalna opažanja, kar nam je omogočilo vpogled v mehanizme, ki povzročajo te spremembe. Poleg tega smo preverili tudi izvedljivost poskusov na *ex vivo* mišičnem tkivu in pokazali, da lahko *ex vivo* študije v določenih primerih služijo kot alternativa poskusom na živih živalih, s čimer prispevamo k zmanjšanju etičnega in ekonomskega bremena.

Četrty članek obravnava elektrokemične procese, ki potekajo med dovajanjem elektroporacijskih pulzov, zlasti v okviru protokolov za gensko elektrotransfekcijo. Razvili smo celovit mehanistični numerični model za napoved sprememb pH v tkivu med in po aplikaciji električnih pulzov. Model se osredotoča na vpliv reakcij elektrolize vode na meji med elektrodami in tkivom, ki povzroči nastanek kislih in bazičnih pH območij. Eksperimentalno smo model potrdili z agaroznimi geli, v katere smo vmešali pH indikatorje. Agarozne gele smo pripravili z različnimi puferskimi sistemi, da bi ocenili, kako kapaciteta pufra vpliva na razvoj pH sprememb. Za sprotno spremljanje teh sprememb smo razvili in kalibrirali slikovni sistem. Cilj tega pristopa je bil vzpostaviti ponovljive eksperimentalne postopke in potrditi, da model zanesljivo napoveduje prostorsko in časovno dinamiko sprememb pH med elektroporacijo.

Peti članek obravnava elektroosmozni tok (EOF) v rastlinskih in živalskih tkivih pri obdelavi s pulzirajočim električnim poljem (PEF) in med dovajanjem enosmernega toka (DC). Za preučevanje elektroosmoznega toka v gomoljih krompirja smo uporabili teksturno analizo, pri čemer smo se osredotočili predvsem na to, ali predobdelava s PEF spodbuja sproščanje znotrajcelične tekočine in predstavlja predpogoj za učinkovito elektroosmozno izsuševanje. Na živalskem tkivu smo izvedli poskuse na sveže izrezani skeletni mišici, da bi ocenili vlogo elektroosmoze pri masnem transportu, ki je pomembna tako za živilsko predelavo kot

za biomedicinske aplikacije. Poleg tega smo kot možne nadomestne materiale za raziskovanje elektroosmotskih pojavov v dobro nadzorovanih eksperimentalnih pogojih preučili agarozne fantome. S temi raziskavami smo pridobili eksperimentalni vpogled v pogosto spregledan prispevek elektroosmoze k prenosu tekočin med elektroporacijskimi obdelavami.

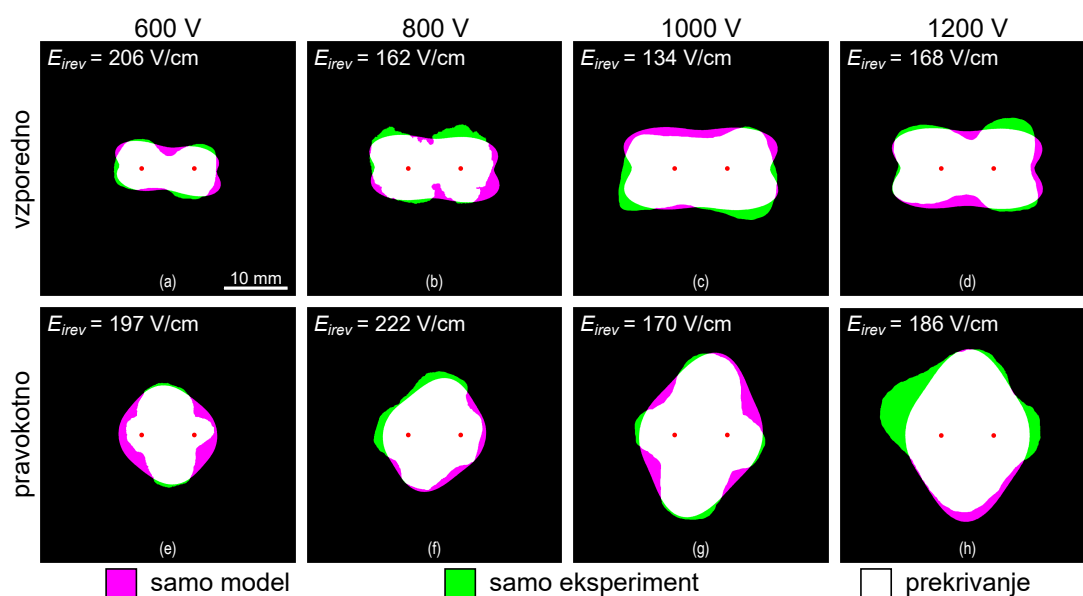
III Razprava

III.1 Raziskava anizotropije skeletne mišice z večnivojskim modeliranjem in eksperimentalno potrditvijo

Smerna odvisnost električne prevodnosti v skeletni mišici ima pomembne posledice za razporeditev električnega polja med elektroporacijo, vendar številni obstoječi modeli tega pojava še vedno ne zajamejo ustrezno. V tem kontekstu smo si v prvi študiji za cilj zadali kvantitativno ovrednotiti vpliv anizotropije skeletne mišice na poškodbe tkiva, povzročene z elektroporacijo, in sicer z združitvijo večnivojskega numeričnega modela in *in vivo* eksperimentalne potrditve. Osrednje vprašanje je bilo, ali razlike v usmerjenosti mišičnih vlaken glede na uporabljeno električno polje – zlasti kadar je to usmerjeno vzporedno ali pravokotno na mišična vlakna – povzročijo značilno različne lezije, ter ali je te učinke mogoče zanesljivo napovedati z mehansitičnim numeričnim modelom.

Za preučitev tega pojava smo uporabili večnivojski modelirni pristop. Najprej smo uporabili model ene mišične celice, da bi določili spremembe prevodnosti na celični ravni med elektroporacijo, podobno kot je bilo že prej izvedeno za kožno tkivo [106], [107], [108]. Te rezultate smo nato posplošili in vključili v večji model tkiva, kjer smo mišico predstavili kot anizotropno prevodno domeno. Modeliranje smo dopolnili z vrsto *in vivo* eksperimentov na skeletni mišici prašičev, pri katerih smo elektroporacijske pulze aplicirali z dvema igelnima elektrodama (medsebojna razdalja 8,0 mm), vstavljenima tako, da je bilo aplicirano električno polje usmerjeno bodisi vzporedno, bodisi pravokotno na smer mišičnih vlaken. Elektroporacijski protokol je vključeval 48 monopolarnih pravokotnih pulzov z dolžino 100 μ s,

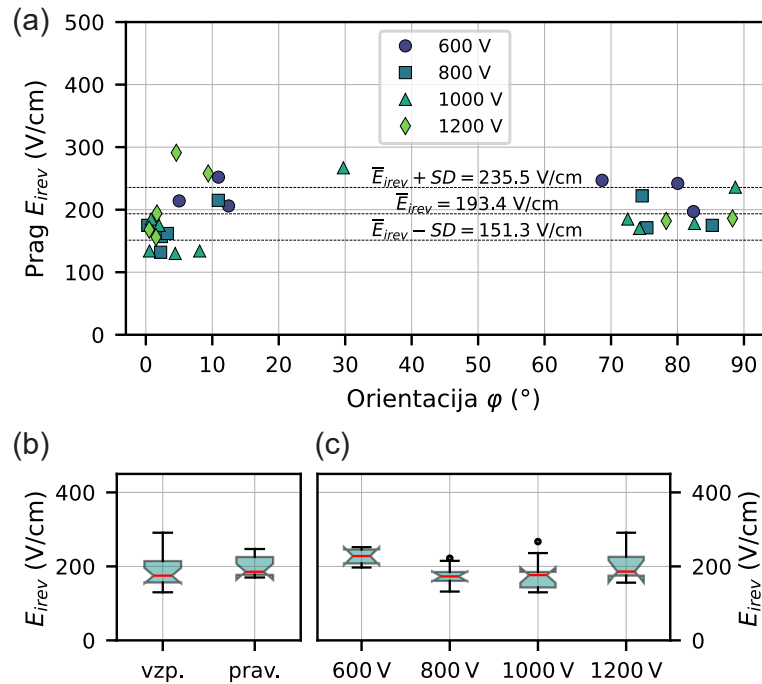
ki smo jih dostavili v šestih vlakih po osem pulzov. V vsakem vlakcu so bili pulzi aplicirani s frekvenco 1000 s^{-1} , z 2-sekundnim premorom med posameznima vlakom. Napetosti pulzov so znašale med 600 V in 1200 V. Po obdelavi smo mišično tkivo izrezali in ga obarvali z indikatorjem 2,3,5-trifenil-2H-tetrazolijevim klorid (TTC), da smo označili območja ireverzibilno elektroporiranega tkiva. Obarvano tkivo smo nato slikali in obdelali za rekonstrukcijo geometrije lezij. Prag električnega polja za ireverzibilno elektroporacijo smo za vsak eksperiment določili z izbiro simulirane konture, ki je dosegla najvišji Sørensen–Diceov koeficient podobnosti [109] s pripadajočo eksperimentalno dobljeno lezijo.



Slika III.1: Primerjava eksperimentalno določenih lezij z rezultati numeričnega modela. Za vsako eksperimentalno skupino je prikazan en vzorec; vzporedna orientacija (tj. električno polje je bilo aplicirano v smeri, vzporedni z usmerjenostjo mišičnih vlaken) je prikazana v (a)–(d), pravokotna orientacija (tj. električno polje je bilo aplicirano v smeri, pravokotni na usmerjenost mišičnih vlaken) pa v (e)–(h). V eksperimentih je bila uporabljena napetost 600 V v (a) in (e), 800 V v (b) in (f), 1000 V v (c) in (g) ter 1200 V v (d) in (h). Za vsak prikazan vzorec je podana vrednost določenega praga za ireverzibilno elektroporacijo.

Ugotovili smo, da usmerjenost uporabljenega električnega polja glede na mišična vlakna pomembno vpliva na morfologijo lezij. Kadar je bilo polje aplicirano vzporedno z vlakni, so bile lezije bolj omejene in so sledile pričakovani obliki

konfiguracije z dvema igelnima elektrodama, kar je podobno rezultatom, ki jih običajno opazimo v električno izotropnem tkivu [110]. Nasprotno pa je pravokotna usmeritev polja povzročila širše lezije, ki so segale daleč od linije, ki povezuje elektrodi, pri čemer se je največje širjenje pojavilo vzdolž ravnine, ki razpolavlja to linijo, kjer je sicer pričakovana najmanjša jakost električnega polja. Te razlike v obliki lezij so bile skladne s predikcijami numeričnega modela in podpirajo sklep, da električna anizotropija mišičnega tkiva močno vpliva na porazdelitev električnega polja in obseg poškodbe, povzročene z elektroporacijo (Slika III.1).



Slika III.2: (a) Določene vrednosti praga za ireverzibilno elektroporacijo (E_{irrev}) za vsak eksperiment, prikazane glede na orientacijo elektrod glede na smer mišičnih vlaken (φ), z označeno povprečno vrednostjo in standardnim odklonom. (b) Rezultat enosmerne analize variance (ANOVA) za podatke iz (a), razdeljene v dve skupini: vzporedno in pravokotno. Rezultat testa ANOVA ne kaže statistično značilne razlike v pragu med skupinama ($p = 0,55$). (c) Rezultat enosmerne ANOVA za podatke iz (a), razdeljene v štiri skupine glede na uporabljeno napetost: 600 V, 800 V, 1000 V in 1200 V. Rezultat testa ne kaže statistično značilne razlike v pragu med skupinami ($p = 0,08$).

Poleg ocene morfologije lezij smo v študiji določili tudi prag električnega po-

lja za ireverzibilno elektroporacijo, specifičen za uporabljen mišično tkivo in protokol pulzov (Slika III.2a). Analiza je pokazala, da je prag ostal enak pri vseh uporabljenih napetostih (600, 800, 1000 in 1200 V), s povprečno vrednostjo 193,4 V/cm in standardnim odklonom 42,1 V/cm (Slika III.2c). Ta ugotovitev je skladna s teorijo elektroporacije, ki napoveduje, da prag ne bi smel biti odvisen od amplitude uporabljenega napetostnega pulza [4]. Pomembno je, da med vzporedno in pravokotno usmeritvijo električnega polja glede na mišična vlakna nismo zaznali statistično značilne razlike v pragu, kar dodatno podpira domnevo, da občutljivost na elektroporacijo ni odvisna od smeri polja, temveč od intrinzičnih celičnih lastnosti (Slika III.2b). Opaženo variabilnost lahko pripišemo biološkim in izvedbenim dejavnikom, ki so značilni za *in vivo* poskuse. Prag, ugotovljen v tej študiji, je bil v primerjavi s predhodnimi (npr. 450 V/cm) [111] razmeroma nizek, kar lahko pojasnimo z večjim številom uporabljenih pulzov ter razlikami v geometriji elektrod in parametrih dovajanja pulzov. Ti rezultati poudarjajo potrebo po interpretaciji vrednosti praga v specifičnem kontekstu uporabljenega terapijskega protokola in eksperimentalnih pogojev [112].

Kljub temu je treba poudariti nekatere omejitve modela. Model je bil razvit in potrjen za eno samo vrsto tkiva, in sicer za prašičjo skeletno mišico, ter za specifičen pulzni protokol. Zato je treba določeni prag in njegovo neodvisnost od smeri električnega polja interpretirati v tem kontekstu. Uporaba modela za druge vrste tkiv ali pri bistveno drugačnih parametrih elektroporacije bi zahtevala ponovno ovrednotenje in eksperimentalno potrditev.

Povzamemo lahko, da ta študija predstavlja večnivojski modelirni pristop, ki združuje dinamiko elektroporacije na ravni posamezne celice z učinki anizotropnega električnega polja na ravni tkiva v skeletni mišici. Model je uspešno poustvaril eksperimentalno opaženo geometrijo lezij in bil nato uporabljen za določitev praga za ireverzibilno elektroporacijo za uporabljeni protokol pulzov. Čeprav model še ne zajema vseh relevantnih pojavov, kot so kompleksni mehanizmi celične smrti, predstavlja osnovo za nadaljnji razvoj modelov, ki upoštevajo anizotropijo tkiva, in s tem izboljšujejo načrtovanje zdravljenj z elektroporacijo.

III.2 Anatonsko natančno modeliranje tokovnih poti v skeletni mišici, potrjeno z MRI-slikanjem

V drugi raziskavi smo nadgradili prejšnje delo in se osredotočili na to, kako notranja struktura skeletne mišice vpliva na porazdelitev električnega toka med apliciranjem električnega polja. Medtem ko je predhodni model [61] anizotropijo upošteval z uporabo anizotropnih funkcij prevodnosti v modelu tkiva kot homogenega volumna, pristop ni vseboval anatomskih podrobnosti. Cilj te študije je bil raziskati, kako vlaknasta struktura mišičnega tkiva vpliva na tokovne poti med izpostavitvijo električnemu polju, ter ali anatomsko navdihnjen model izboljša natančnost napovedi. V ta namen smo razvili numerični model, ki vključuje strukturo posameznih mišičnih vlaken z realističnimi dimenzijami, in ga validirali z uporabo slikanja gostote toka (angl. *current density imaging*, CDI), metode na osnovi magnetne resonance, ki omogoča vizualizacijo toka znotraj tkiva.

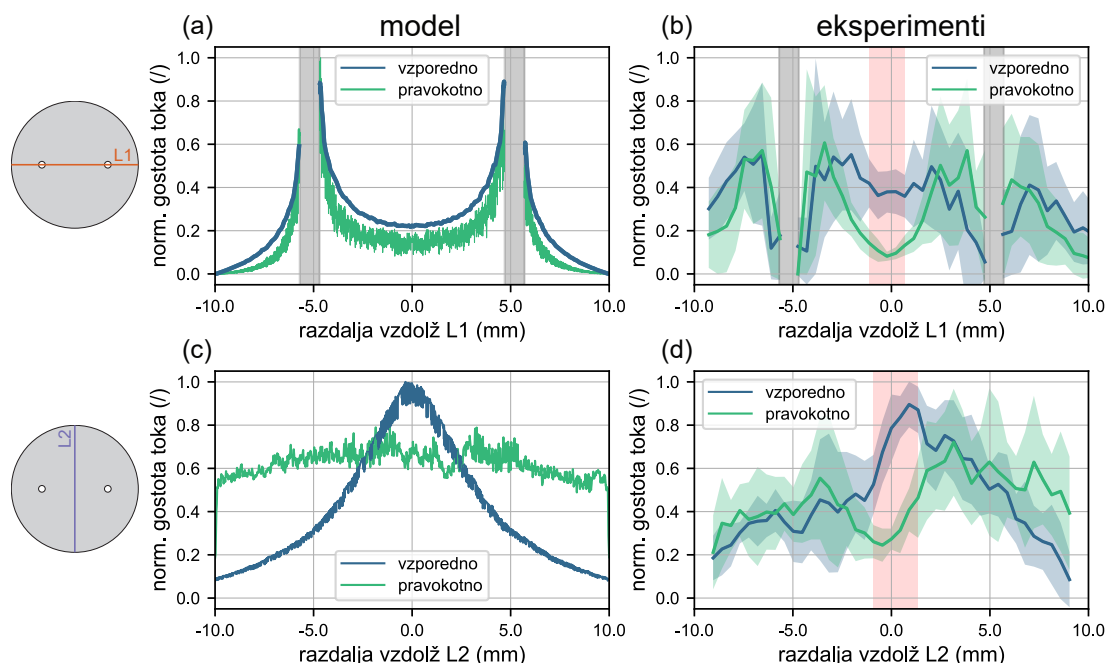
Zgradili smo tridimenzionalni model, ki predstavlja poenostavljeno anatomsko razporeditev vzporednih mišičnih vlaken, vgrajenih v zunajcelični matriks. Dimenzije in medsebojna razdalja vlaken so bile izbrane tako, da ustrezajo tipičnim histološkim značilnostim mišice. V tem modelu je anizotropija izhajala iz eksplisitne geometrijske predstavitve posameznih mišičnih vlaken, vgrajenih v zunajcelični matriks, in ne iz dodeljenih anizotropnih funkcij prevodnosti. Prevodnosti posameznih komponent tkiva smo zato nastavili za konstantne, vrednosti smo pridobili iz literature. Dve igelni elektrodi smo postavili na medsebojno razdaljo 10,4 mm in uporabili dve različni orientaciji glede na smer mišičnih vlaken: v vzporedni orientaciji sta bili elektrodi vstavljeni tako, da je bilo nastalo električno polje poravnano s smerjo mišičnih vlaken, medtem ko je bilo v pravokotni orientaciji električno polje aplicirano pravokotno na vlakna. Za potrditev modela smo izvedli poskuse CDI na prašičji skeletni mišici približno 48 ur *post-mortem*, pri čemer smo uporabili enake postavitev elektrod, kot v modelu. V vsakem poskusu smo aplicirali en sam pravokotni pulz trajanja 800 μ s in amplitude 100 V. Simulirane porazdelitve gostote toka smo nato primerjali z rezultati CDI meritev.

Primerjava med simulacijami in eksperimenti je pokazala, da na tokovne poti močno vpliva orientacija električnega polja glede na mišična vlakna (Slika III.3). V vzporedni orientaciji je bil tok skoncentriran vzdolž najkrajše poti med elektro-

dama, tako v simulaciji, kot tudi v eksperimentih. Nasprotno pa je pravokotna orientacija povzročila bolj razpršene ali preusmerjene tokovne vzorce, ki so sledili smeri mišičnih vlaken. Kvantitativna analiza vzdolž linije, ki povezuje središči elektrod, je pokazala bistveno višje gostote toka v vzporedni orientaciji, medtem ko je bila pri pravokotni aplikaciji polja centralna gostota nižja in je prišlo do prerazporeditve toka nad in pod osjo (Slika III.3a,b). Poleg tega so profili gostote toka vzdolž linije, pravokotne na povezovalno črto med elektrodama, v vzporedni orientaciji pokazali oster centralni vrh, medtem ko je bila v pravokotni orientaciji porazdelitev bolj enakomerna z nižjo centralno vrednostjo, kar odraža preusmerjanje toka vzdolž mišičnih vlaken (Slika III.3c,d). Ti rezultati potrjujejo močan vpliv anizotropije skeletne mišice na porazdelitev toka in podpirajo uporabo geometrijsko natančnih modelov za zanesljivo napovedovanje električne poljske jakosti in tokovne gostote.

Na podlagi teh opažanj potrjujemo anizotropno obnašanje skeletne mišice, kar so pokazale tako simulacije, kot tudi meritve CDI. Posebej je treba izpostaviti opaženo preusmeritev toka v pravokotni orientaciji, ki najverjetneje izhaja iz mikroskopskih gradnikov tkiva, kot so sarkolema in plasti vezivnega tkiva, ki ovirajo tok pravokotno na mišična vlakna. Medtem ko je model zaradi idealizirane geometrije ustvaril simetrične vzorce, so eksperimentalni rezultati pokazali asimetrije, ki jih lahko pripišemo strukturnim heterogenostim v tkivu, na primer variabilnosti gostote vlaken, porazdelitvi vezivnega in maščobnega tkiva, ter prisotnosti žil ali živcev. Poleg tega podatki kažejo, da je anizotropno obnašanje zaznavno tudi 48 ur *post-mortem*. Ti izsledki poudarjajo pomen strukturne anizotropije pri usmerjanju toka, tudi v mrtvem tkivu, in potrjujejo pomembnost uporabe geometrijsko podprtih modelov pri raziskavah elektroporacije.

Kljub naštetim prednostim pa moramo opozoriti tudi na nekatere omejitve. Model skeletne mišice smo zasnovali idealizirano in vanj nismo vključili podrobnih predstavitev heterogenih tkivnih komponent, kar je lahko prispevalo k odstopanjem med simulacijami in eksperimentalnimi rezultati. Poleg tega je med 48-urnim *post-mortem* obdobjem verjetno prišlo vsaj do delne razgradnje celičnih membran, kar pomeni, da je bila anizotropija v eksperimentih v glavnem pogojena s preostalimi strukturnimi komponentami in ne z aktivnimi lastnostmi membran. Čeprav elektroporacije membran v model nismo vključili eksplicitno, verjamemo, da uporabljena jakost apliciranega električnega polja in uporaba zgolj enega pulza



Slika III.3: Podrobna primerjava normalizirane porazdelitve gostote toka vzdolž dveh izbranih opazovalnih linij za skupini z vzporedno (tj. električno polje je bilo aplicirano vzporedno s smerjo mišičnih vlaken) in pravokotno usmeritvijo (tj. električno polje je bilo aplicirano pravokotno na smer mišičnih vlaken). Rezultati vzdolž linije L1 so prikazani v (a) in (b), rezultati vzdolž linije L2 pa v (c) in (d). Simulacijski rezultati so prikazani v (a) in (c), eksperimentalni rezultati pa v (b) in (d). V (a) in (b) siva osenčena območja označujejo položaj elektrod. V (b) in (d) so rezultati prikazani kot povprečne vrednosti \pm standardni odkloni (osenčena območja), pri čemer je $N = 6$. Rdeče osenčena območja v (b) in (d) označujejo segmente, kjer je bila ugotovljena statistično značilna razlika med vzporedno in pravokotno usmeritvijo ($p < 0,05$).

najverjetneje ne bi povzročila elektroporacije, razen neposredno ob elektrodah. Vključitev elektroporacije membran, kot je že bilo izvedeno v preteklih študijah [106], [107], [108], bi povečala kompleksnost modela, vendar ne bi bistveno vplivala na rezultate. Zato je kljub uporabnosti modela pri razumevanju strukturnih dejavnikov anizotropije potrebno biti previden pri razlagi predpostavk modela in vhodnih vrednosti, kot so prevodnost ali lastnosti membrane, zlasti v kontekstu *in vivo* pogojev, kjer se biološki mehanizmi lahko razlikujejo od tistih v *ex vivo* tkivu.

Povzamemo lahko, da smo s to študijo pokazali, da anizotropna prevodnost in struktura mišičnih vlaken pomembno vplivata na porazdelitev toka med apliciranjem zunanjega električnega polja. Ujemanje med simuliranimi in eksperimentalnimi podatki potrjuje uporabnost anatomske navdihnjenih modelov in poudarja pomen vključevanja strukturnih in smernih značilnosti mišičnega tkiva v prihodnje simulacije elektroporacije. Naše ugotovitve tako predstavljajo temelj za natančnejše načrtovanje zdravljenja in bolj zanesljivo napovedovanje učinkov elektroporacije v anizotropnih tkivih.

III.3 *Post-mortem* spremembe anizotropije skeletne mišice, ovrednotene z impedančno spektroskopijo in numeričnim modelom

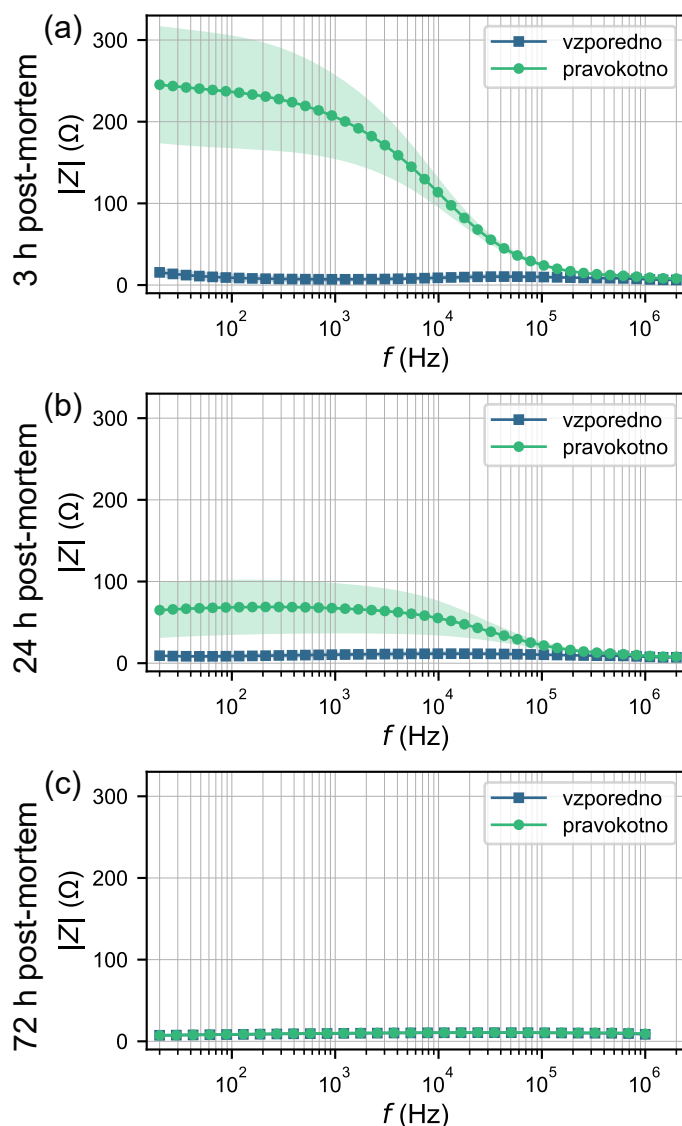
Namen te študije je bil raziskati, kako se anizotropija skeletne mišice spreminja skozi čas po smrti, in v kolikšni meri *post-mortem* tkivo ohranja električne značilnosti žive mišice. Z združitvijo impedančne spektroskopije in numeričnega modeliranja smo želeli pojasniti mehanizme, ki vplivajo na *post-mortem* spremembe električne prevodnosti, ter preveriti, ali je celična membrana res odgovorna za anizotropijo tkiva. Študija je bila osredotočena zlasti na vprašanje, ali lahko strukturne in električne spremembe v *ex vivo* mišičnem tkivu razložimo z zvišano prepustnostjo membran, bodisi kot posledico naravnega razkroja, bodisi kot učinka elektroporacije.

Meritve z impedančno spektroskopijo smo izvedli na vzorcih skeletne mišice prašiča, in sicer 3, 24 in 72 ur *post-mortem*, pri čemer smo impedanco merili v smeri vzporedno in pravokotno na potek mišičnih vlaken (Slika III.4). Tri ure *post-mortem* so meritve pokazale izrazito anizotropijo električne impedance, saj je bila impedanca v pravokotni smeri več kot desetkrat višja pri nizkih frekvencah (Slika III.4a). Tako izrazito razliko lahko pripišemo vlaknasti strukturi mišice in ohranjeni celovitosti celičnih membran kmalu po smrti. Po 24 urah *post-mortem* je bila anizotropija še vedno prisotna, a močno zmanjšana, kar kaže na delno razgradnjo membranskih struktur (Slika III.4b). Po 72 urah anizotropije nismo več zaznali, impedanca pa je bila podobna v obeh smereh, kar nakazuje na popolno razgradnjo celičnih struktur, odgovornih za anizotropijo (Slika III.4c). Ti izsledki

so skladni z rezultati drugih študij na *ex vivo* mišičnem tkivu [34], [35], [37], od katerih so bile nekatere izvedene takoj po smrti živali, in potrjujejo izvedljivost uporabe *post-mortem* mišičnega tkiva kot zanesljivega modela za preučevanje *in vivo* anizotropije.

Da bi ovrednotili vpliv elektroporacije na prepustnost membran, smo impedanco merili neposredno pred in po aplikaciji električnih pulzov. To nam je omogočilo izračun razmerja impedance (po obdelavi glede na pred obdelavo) za kvantifikacijo sprememb prevodnosti tkiva zaradi elektroporacije. Elektroporacijo smo izvedli 3 in 24 ur *post-mortem* z osmimi pulzi dolžine 100 μ s pri napetosti 200 V ali 400 V in ponovitveno frekvenco 1 s⁻¹. Elektrode so bile nameščene 6 mm narazen. Po elektroporaciji smo opazili izrazit padec impedance, zlasti v pravokotni smeri, kjer so membrane poravnane pravokotno na smer uporabljenega električnega polja. Tri ure *post-mortem* in pri napetosti 400 V se je impedanca v pravokotni smeri zmanjšala za do 60 %, v vzporedni smeri pa približno za 20 % (Slika III.5). Po 24 urah se je ta učinek zmanjšal, kar je skladno s postopno izgubo celovitosti membran skozi čas po smrti. Ti rezultati pomembno potrjujejo domnevo, da celična membrana mišičnih vlaken deluje kot glavni impedančni dejavnik, ki prispeva k anizotropiji. Izrazitejši učinki v pravokotni smeri odražajo večjo interakcijo med električnim poljem in membranami, ki ovirajo tok v pravokotni smeri.

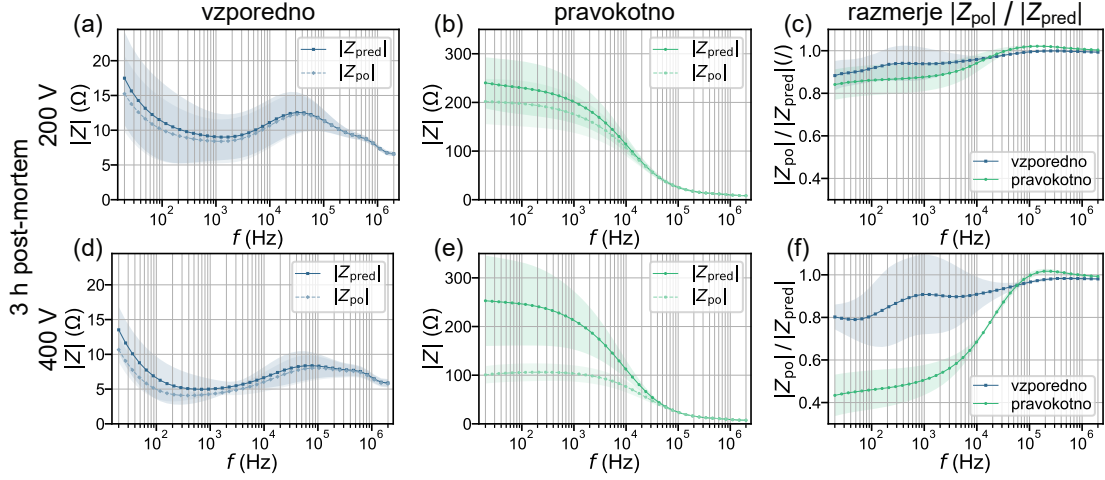
Opažene razlike med obema orientacijama nudijo mehanistično razlago za različne oblike lezij, odvisne od smeri polja, ki so bile opažene tako pri skeletni [61] kot tudi pri srčni mišici [113]. V pravokotni orientaciji večje zmanjšanje impedance kaže na obsežnejši vpliv na membrane, saj električno polje poteka v smeri, ki neposredno seka celične membrane. Nasprotno pa se pri vzporedni usmeritvi električno polje poravna z usmeritvijo mišičnih vlaken, kar omogoča toku, da teče vzdolž njih z manjšo interakcijo prek membran in posledično z manjšim vplivom na membrane. Ti rezultati so pomembni tako za terapije, ki temeljijo na elektroporaciji, kot tudi za numerično modeliranje, saj kažejo, da je povečanje prevodnosti med elektroporacijo odvisno od orientacije. Obstoječi modeli pogosto predpostavljajo enak faktor povečanja prevodnosti v obeh smereh in konstantno razmerje anizotropije pred in po elektroporaciji [111], [113], [114], [115], [116]. Vključitev sprememb prevodnosti, specifičnih glede na orientacijo, bi lahko izboljšala natančnost in napovedno sposobnost teh modelov glede



Slika III.4: Frekvenčno odvisna absolutna impedanca skeletne mišice v vzporedni (tj. impedanca je bila izmerjena v smeri vzporedno z mišičnimi vlakni) in pravokotni (tj. impedanca je bila izmerjena v smeri pravokotno na mišična vlakna) orientaciji pri (a) 3 urah *post mortem*, (b) 24 urah *post mortem* in (c) 72 urah *post mortem*. Rezultati so prikazani kot povprečne vrednosti \pm standardni odkloni (osenčena območja), pri čemer je $N = 12$.

porazdelitve električnega polja in nastanka lezij.

Za potrditev in razlago eksperimentalnih rezultatov smo uporabili numerično



Slika III.5: Frekvenčno odvisna absolutna impedanca skeletne mišice pred elektroporacijo ($|Z_{\text{pred}}|$), po elektroporaciji (tj. v dveh sekundah po elektroporaciji; $|Z_{\text{po}}|$) in njun količnik ($|Z_{\text{po}}|/|Z_{\text{pred}}|$), izmerjene v vzporedni (tj. impedanca je bila izmerjena v smeri vzporedno z mišičnimi vlakni) in pravokotni (tj. impedanca je bila izmerjena v smeri pravokotno na mišična vlakna) orientaciji. Elektroporacijo smo izvedli z osmimi pravokotnimi pulzi, vsak s trajanjem 100 μs , amplitudo 200 V ali 400 V in frekvenco 1 s^{-1} . Uporabljena amplituda pulzov je bila 200 V v (a–c) in 400 V v (d–f). Absolutna impedanca mišice pred in po elektroporaciji, izmerjena v vzporedni orientaciji, je prikazana v (a, d), v pravokotni orientaciji pa v (b, e). Količnik impedanc ($|Z_{\text{po}}|/|Z_{\text{pred}}|$) je prikazan v (c, f). Rezultati so prikazani kot povprečne vrednosti \pm standardni odkloni (osenčena območja), $N = 6$. Opomba: ordinate v grafih (a, d) in (b, e) imajo različne skale.

modeliranje. Razvili smo tridimenzionalni model s poenostavljeno geometrijo, sestavljeno iz valjastih mišičnih vlaken, vgrajenih v kubično domeno. Anizotropija je izhajala iz prostorske razporeditve vlaken in uporabe robnih pogojev kontaktne impedance za modeliranje celičnih membran. Izvedli smo parametrične simulacije, s katerimi smo ocenili, kako spremembe prevodnosti membrane vplivajo na impedanco v obeh orientacijah. Najboljše ujemanje z eksperimentalnimi rezultati smo dosegli pri membranski prevodnosti $5 \times 10^{-7} \text{ S/m}$ pri 3 urah in $1 \times 10^{-4} \text{ S/m}$ pri 24 urah *post-mortem*. V obeh primerih je bila modelirana impedanca v pravokotni orientaciji zelo občutljiva na spremembe prevodnosti membrane, medtem ko je v vzporedni orientaciji ostala večinoma nespremenjena. Ti rezultati potrjujejo hipotezo, da je prepustnost membrane ključen dejavnik pri določanju

anizotropije.

Čeprav so se eksperimentalni in numerični rezultati večinoma ujemali, so bile opažene nekatere razlike, zlasti pri višjih frekvencah in v vzporedni orientaciji. Te razlike so verjetno posledica negotovosti v vrednostih prevodnosti in permisivnosti, povzetimi iz literature, ki so bile uporabljene za znotrajcelični in zunajcelični prostor. Poleg tega je bil model zasnovan s poenostavljeno geometrijo in ni upošteval heterogenosti, kot so maščobno tkivo, krvne žile ali vezivno tkivo, ki lahko prav tako vplivajo na impedanco. Kljub tem omejitvam je model uspešno zajel glavne značilnosti eksperimentalnih podatkov in pokazal občutljivost na parametre, povezane s celovitostjo membrane.

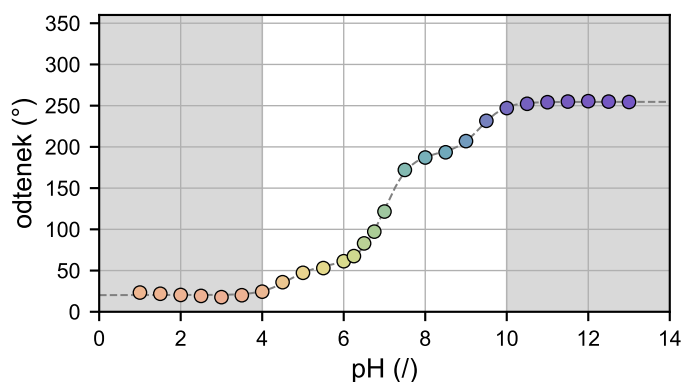
Povzamemo lahko, da je ta študija pokazala, da skeletna mišica ohranja svoje anizotropne impedančne lastnosti do 24 ur *post mortem*, pri čemer ima celična membrana ključno vlogo pri ohranjanju te anizotropije. Ti rezultati podpirajo uporabo *post-mortem* mišičnega tkiva kot zanesljivega modela za razmere *in vivo*, kar ponuja možno alternativo poskusom na živih živalih ter tako prispeva k zmanjševanju etične obremenitve, povezane z uporabo živali v medicinskih raziskavah. Rezultati imajo pomembne implikacije tako za biomedicinske kot tudi za prehrambne aplikacije.

III.4 Modeliranje in sprotna vizualizacija pH sprememb, povzročenih z elektroporacijo

V tej študiji smo si zadali cilj okarakterizirati in napovedati lokalne spremembe pH, ki jih povzroča elektroporacija, in ki nastanejo zaradi elektrokemičnih reakcij na meji med elektrodo in elektrolitom. Za boljše razumevanje in napovedovanje teh učinkov smo razvili mehanističen večfizikalni model, ki temelji na osnovnih načelih elektrokemije, in ga eksperimentalno preverili s skrbno zasnovanimi poskusi na agaroznih gelih. Ti fantomi so služili kot poenostavljeni, vendar nadzorovani nadomestki biološkega tkiva, in so omogočili neposredno vizualizacijo pH sprememb s pomočjo kalibriranega slikovnega sistema in uporabe pH indikatorjev. Z uporabo nepuferiranih in puferiranih medijev smo preučili tudi, kako različna tkivu podobna okolja vplivajo na širjenje pH front.

Poskuse na agaroznih gelih smo izvedli v nepuferirani fiziološki raztopini, bikarbonatnem pufru in HEPES pufru, da bi opazovali razlike v spremembah pH med mediji z različno puferno kapaciteto. Za dovajanje osmih monofaznih pravokotnih pulzov (trajanje 10 ms, ponavljalna frekvenca 1 s^{-1}) pri dveh amplitudah (200 V in 400 V), ki odražajo značilne parametre za gensko elektrotransfekcijo, smo uporabili igelni elektrodi iz platine–iridija z medsebojnim razmikom 14,3 mm. Eksperimentalni sistem smo predstavili z enodimenzionalnim numeričnim modelom, ki je simuliral časovni potek premikanja pH front. Model je temeljil na Nernst–Planckovem sistemu parcialnih diferencialnih enačb in je vključeval ionski transport z mehanizmi migracije in difuzije ter kemijske reakcije na meji med elektrodo in elektrolitom ter znotraj elektrolitskega medija.

Za pretvorbo barvnih informacij iz poskusov na agaroznih gelih v pH vrednosti smo slikovni sistem kalibrirali z uporabo 27 standardnih pufrskih raztopin z vrednostmi pH v razponu od pH 1,0 do 13,0. Vsako raztopino smo zmešali z univerzalnim pH indikatorjem in jo fotografirali v nadzorovanih svetlobnih pogojih. Iz slikovnih podatkov RGB (rdeča, zelena, modra) smo izluščili komponento barvnega odtenka (angl. *hue*) ter jo povezali z znanimi pH vrednostmi posameznih raztopin, da smo lahko določili kalibracijsko krivuljo (Slika III.6). Ta kalibracijska funkcija, sestavljena iz treh sigmoidalnih členov, ki predstavljajo tri komponente indikatorja, je omogočila zanesljivo oceno pH vrednosti na podlagi slikovnih podatkov v uporabnem razponu med pH 4 in 10 ter s tem določanje pH vrednosti za vsako slikovno točko v vseh eksperimentih.



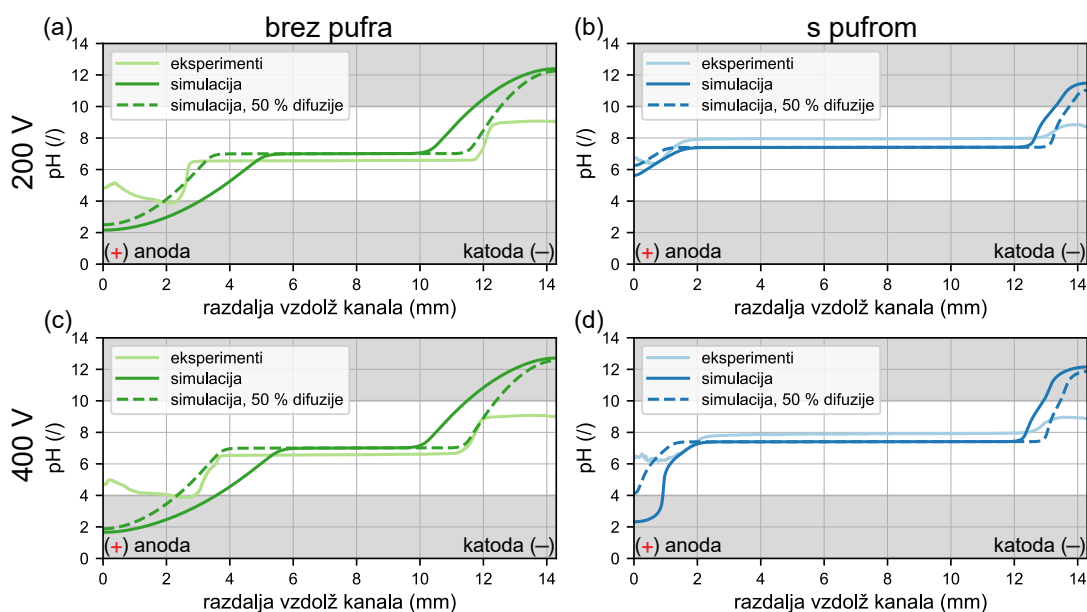
Slika III.6: Kalibracijska krivulja odtenka barve (v stopinjah) kot funkcije pH. Uporabno območje te funkcije je od pH 4 do pH 10, saj so vrednosti odtenka izven tega območja med seboj preveč podobne in zato nezanesljive za razločevanje.

Eksperimentalni rezultati so pokazali jasne razlike v obsegu in ostrini širjenja pH fronte med posameznimi mediji. Kot je bilo pričakovano, je nepuferiran medij izkazoval največje in najizrazitejše spremembe pH, pri čemer se je v bližini anode oblikovalo kislo območje, v bližini katode pa bazično, obe območji pa sta se občutno razširili od elektrod. Bikarbonatni in HEPES pufer sta pokazala bolj omejeno širjenje spremenjenega pH, čeprav so bile zaznane subtilne razlike: HEPES pufer je ustvaril bolj izrazite meje med spremenjenimi in nespremenjenimi območji pH, medtem ko je bikarbonatni pufer nekoliko bolj nevtraliziral kisle spremembe. Opažanja so bila skladna pri vseh ponovitvah, kar potrjuje ponovljivost eksperimentalne metodologije.

Simulacije so se skladale z rezultati poskusov, tako glede trendov kot glede relativne velikosti pH front. Kljub temu je imel model tendenco precenjevanja prostorskega obsega sprememb pH, kar je najverjetneje posledica uporabe difuzijskih koeficientov iz literature za vodne raztopine, ki morda ne odražajo najbolje počasnejše difuzije v agaroznih gelih. Z zmanjšanjem teh koeficientov na 50 % prvotne vrednosti se je ujemanje modela s poskusi bistveno izboljšalo (Slika III.7). To poudarja občutljivost modela na izbiro parametrov in potrebo po dodatni eksperimentalni karakterizaciji za njihovo natančnejšo določitev.

Prednost predstavljenega modela je njegova sposobnost natančnega prikaza dinamičnega obnašanja pH front med in po dovajanju pulzov. Zmožen je bil reproducirati pojave, kot so nadaljnja difuzija sprememb pH po koncu pulza ter, pod določenimi pogoji, tudi umik pH front v puferiranih medijih med pavzami med pulzi. Čeprav tega umika v tej raziskavi nismo opazili, so ga predhodno zaznali v *in vivo* tkivu [69], in bi lahko bil pomemben pri drugih protokolih. Spremembe pH, ki smo jih opazili, pa so z vidika praktičnih aplikacij zelo pomembne. Pri genski elektrotransfekciji lahko že zmerni odmiki od lokalnega pH ogrozijo integriteto DNA ali preživetje celic. V tem kontekstu model predstavlja dragoceno orodje za napovedovanje in morebitno omilitev teh učinkov s pomočjo optimizacije oblike pulzov in konfiguracije elektrod.

Kljub prednostim ima model tudi nekatere omejitve. Trenutno še ne upošteva elektroosmotskih učinkov, ki lahko vplivajo na transport ionov v dejanskem tkivu, prav tako ne vključuje interakcij med pH indikatorji in medijem. Poleg tega pa je potrebno, čeprav je bil trenuten model potrjen v agaroznem mediju, rezul-



Slika III.7: Primerjava med izračunanimi in eksperimentalno določenimi pH porazdelitvami za 8 pravokotnih pulzov z dolžino 10 ms in ponavljalno frekvenco 1 s^{-1} . Amplituda pulzov je bila 200 V v (a) in (b), ter 400 V v (c) in (d). Rezultati za nepuferiran medij so prikazani v (a) in (c), medtem ko so rezultati za puferiran medij prikazani v (b) in (d). Prikazani so rezultati za čas 60 s, da analiza vključuje tudi učinek difuzije. Prekinjene črte predstavljajo rezultate modelov, kjer so bili difuzijski koeficienti zmanjšani na 50 % prvotno uporabljenih vrednosti. Anoda je na levi strani (pri 0 mm), katoda pa na desni (pri 14,3 mm).

tate pri prenosu na dejansko biološko tkivo obravnavati previdno zaradi razlik v strukturi, prekrvavitvi, in kemijski sestavi. Za razširitev modela na bolj zapletene geometrije in njegovo potrditev v *in vivo* pogojih bo potrebnega še več eksperimentalnega in računalniškega dela.

Če povzamemo, predstavili smo mehanistični model, ki je sposoben zajeti pH spremembe, povzročene z elektroporacijo, v poenostavljenem fantomu tkiva. Model, podprt z eksperimentalno potrditvijo s ponovljivimi rezultati, nudi dragocen vpogled v prostorsko-časovno dinamiko pH med elektroporacijo. Čeprav so za izboljšanje napovedne natančnosti potrebne dodatne izboljšave, zlasti glede difuzijskih parametrov, ta pristop postavlja temelje za nadaljnji razvoj modelov, namenjenih optimizaciji protokolov, ki temeljijo na elektroporaciji, in pri katerih

imajo spremljevalni elektrokemični pojavi pomembno vlogo.

Omeniti velja tudi, da se je ta prispevek osredotočil na elektrokemične pH učinke, medtem ko na poškodbe tkiva med elektroporacijo pogosto vplivajo tudi toplotni učinki in ireverzibilna elektroporacija (IRE). Čeprav ti vidiki v tej študiji niso bili eksplicitno modelirani, bi njihova vključitev lahko izboljšala napovedno natančnost načrtovanja terapij. Z vključitvijo modelov, kot sta Pennesova biotoplotna enačba in statističnih modelov preživetja, kot je Peleg–Fermijev model, bi bilo mogoče oceniti poškodbe zaradi povišane temperature oziroma verjetnost celične smrti. Ker bi integracija IRE in/ali toplotnih učinkov v pH model z namenom oblikovanja celovitega modela poškodb tkiva predstavljala preširok izziv za obravnavo v okviru te doktorske disertacije, to nalogo prepuščamo prihodnjim raziskavam, ki si bodo prizadevale razviti bolj popoln simulacijski okvir za terapije, temelječe na elektroporaciji.

III.5 Eksperimentalna raziskava elektroosmoze v rastlinskem in živalskem tkivu pri obdelavi s PEF in enosmernim tokom (DC)

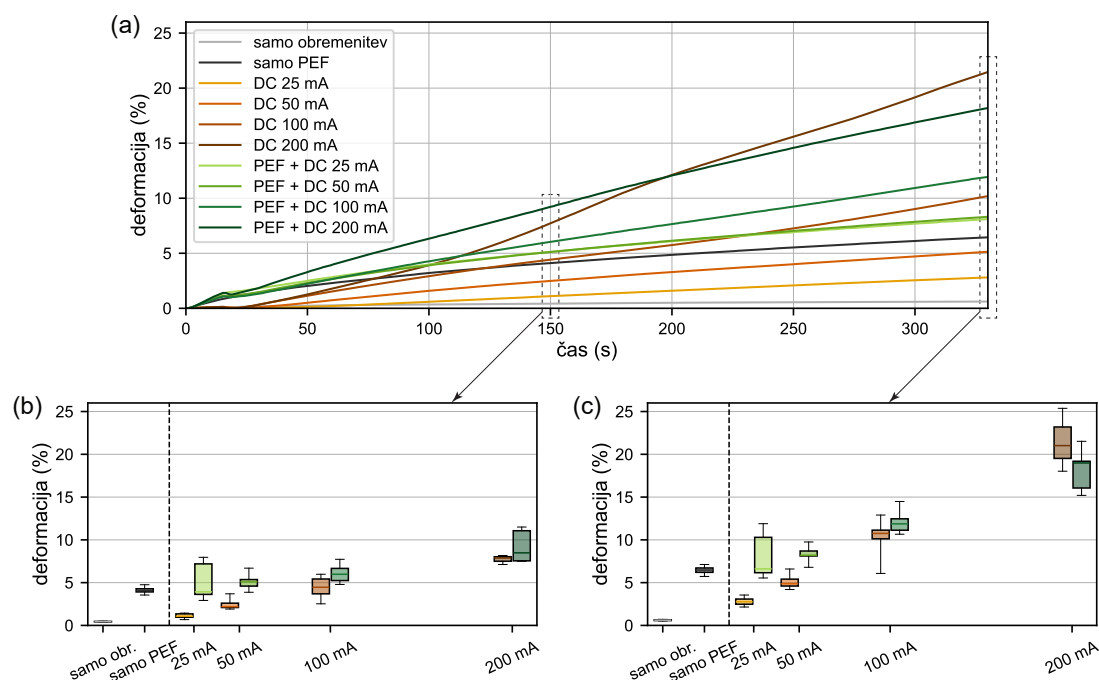
Peta študija je preučevala elektroosmozni tok (EOF) kot spremljajoč pojav med elektroporacijo ter ocenila njegov pomen v različnih bioloških medijih. Elektroosmoza je pojav, pri katerem se tekočina premika skozi porozni medij pod vplivom električnega polja, kar lahko pomembno vpliva na masni transport. V tej raziskavi smo EOF eksperimentalno ovrednotili v treh vrstah medijev: rastlinskem tkivu (gomolji krompirja), skeletni mišici živali in v agaroznih fantomih.

Za oceno elektroosmoze smo uporabili štiri različne eksperimentalne pogoje: zgolj mehansko obremenitev (kontrola), le obdelavo s pulzirajočim električnim poljem (PEF), le enosmerni tok (DC), ter kombinacijo PEF, ki mu je sledil DC. Preizkuse stiskanja smo izvedli s teksturometrom, pri čemer smo vzorce namestili med dve vzporedni elektrodi iz nerjavečega jekla, ki sta služili tako kot stiskalni plošči, kot tudi kot električni kontakti. Na vzorce smo delovali s konstantno tlačno silo 10 N. Vsak vzorec je najprej prestal 30-sekundno fazo predhodnega stiskanja za odstranitev zračnih mehurčkov in zagotovitev dobrega stika z elektrodama.

Premik bata smo nato neprekinjeno beležili 330 sekund. PEF je obsegal osem pravokotnih monofaznih pulzov (trajanje 100 μ s, ponavljalna frekvenca 1 s⁻¹, amplituda 150 V ali 1000 V), ki smo jih dovajali prek elektrod, oddaljenih 6 mm, neposredno po zaključku faze predhodnega stiskanja. V pogojih DC smo 15 sekund po koncu faze predhodnega stiskanja začeli dovajati konstanten tok (25, 50, 100 ali 200 mA), ki je bil prisoten do konca eksperimenta.

Najprej smo raziskali, kako na deformacijo vzorcev krompirja vpliva amplituda enosmerne toka, bodisi samostojno, bodisi po visokonapetostni PEF obdelavi (1000 V). V primerjavi z zgolj mehansko obremenitvijo je PEF sam po sebi povzročil izrazito povečanje deformacije, verjetno zaradi permeabilizacije membran, ki omogoča iztekanje tekočine iz vakuol in celic. Ti rezultati so skladni s predhodnimi ugotovitvami, da elektroporacija poveča mobilnost vode v rastlinskih tkivih, kar dodatno olajša sproščanje turgorskega tlaka [117]. Pri pogojih z zgolj enosmernim tokom se je izoblikoval jasen trend: večje amplitude toka so povzročile vse večjo deformacijo. Vsi DC pogoji so povzročili bistveno večjo deformacijo kot kontrolna obremenitev, kar potrjuje elektroosmozo kot ključni mehanizem. Približno linearen porast deformacije z naraščajočo amplitudo toka odraža teoretično odvisnost elektroosmozne toka od jakosti električnega polja (Slika III.8).

Kombinacija PEF in DC je v splošnem povzročila večjo deformacijo kot zgolj DC, zlasti pri tokovih amplitude 25 in 50 mA, kar nakazuje na sinergistični učinek. Ta učinek najverjetneje izhaja iz strukturnih sprememb, ki jih povzroči elektroporacija, in ki prerazporedijo znotrajcelično tekočino v zunajcelični prostor, s čimer se poveča volumen tekočine, dostopne za elektroosmozni transport. Pri višjih jakostih DC toka (100 in 200 mA) se je ta sinergijski učinek zmanjšal. Pri 200 mA so vzorci, obdelani zgolj z DC, nekoliko presegli tiste, ki so prejeli kombinacijo PEF in DC, kar kaže na obrat trenda, opaženega pri nižjih tokih. Ta rezultat lahko pripišemo povečanemu segrevanju med aplikacijo visokih tokov, zlasti v bližini anode, kjer lahko pride do izsuševanja. V elektroporiranem tkivu, kjer so membrane že oslabiljene, to spodbuja hitro izgubo vode in sčasoma zmanjšuje elektroosmozno učinkovitost. Poleg tega smo pri PEF-obdelanih vzorcih pogosteje opazili napetostne nestabilnosti, kar je lahko vplivalo na sposobnost generatorja, da ohrani stalen tok, in upočasnilo EOF.



Slika III.8: Odziv tkiva krompirja na tlačno obremenitev pri različnih jakostih enosmernega toka (DC). (a) Krivulje deformacije (izražene kot odstotek začetne višine vzorca), povprečene preko petih ponovitev ($N = 5$). Krivulje prikazujejo deformacijo po začetni fazi predobremenitve, dolgi 30 s, in nato trajno kompresijo, oboje pod konstantno silo 10 N. V pogojih z uporabo PEF je bilo pri času 0 s uporabljenih 8 pulzov (amplituda 1000 V, trajanje 100 μ s, ponavljalna frekvenca 1 s^{-1}), medtem ko je bil v pogojih z DC uporabljen konstanten tok (25, 50, 100 ali 200 mA), ki je bil vklopljen od 15 s dalje. Električni obdelavi sta bili izvedeni preko dveh vzporednih elektrod iz nerjavečega jekla, oddaljenih 6 mm. (b) Prikaz z grafikoni kvantilov prikazuje deformacijo po 150 s in (c) končno deformacijo po 330 s (konec preizkusa).

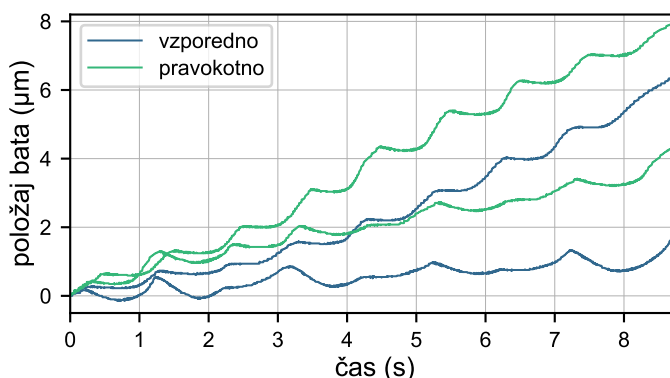
Nato smo raziskali, kako različni amplitudi PEF pulzov (150 V v primerjavi z 1000 V) vplivata na deformacijo vzorcev krompirja, z in brez naknadne aplikacije enosmernega toka. Pulzi z amplitudo 150 V so povzročili bistveno večjo deformacijo kot zgolj obremenitev, vendar precej manjšo kot pulzi z 1000 V, kar kaže na učinek elektroporacije odvisen od amplitude. Pri 150 V je bila permeabilizacija membran verjetno le delna in nezadostna za večje povečanje deformacije, medtem ko so pulzi z 1000 V povzročili obsežnejšo elektroporacijo, večji premik vode in povečano stisljivost tkiva [118]. V kombinaciji s 100 mA enosmernim to-

kom sta obe amplitudi PEF povzročili večjo deformacijo kot PEF sam. Končna deformacija je bila bistveno večja pri amplitudi PEF 1000 V kot pri 150 V, kar po-
udarja vlogo permeabilizacije membran pri olajševanju elektroosmoznega gibanja
tekočine.

Zanimivo je, da je bila končna deformacija v pogojih samo enosmernega toka
primerljiva z deformacijo pri kombinaciji PEF 150 V z DC, vendar nekoliko
manjša kot pri kombinaciji PEF 1000 V z DC, čeprav razlika ni bila statistično
značilna. Odsotnost jasnih razlik je verjetno posledica heterogenosti vzorcev ra-
stlinskega tkiva, zlasti v pogojih brez homogenizacije, ki jo povzroči PEF. Naši
rezultati so skladni s predhodnimi raziskavami [117], ki so pokazale, da se preraz-
poreditev vode v krompirjevem tkivu povečuje z jakostjo električnega polja. Na
splošno rezultati kažejo, da lahko elektroporacija bistveno okrepi deformacijo, ki
jo povzroča elektroosmoza, zlasti pri višjih napetostih, kjer obsežnejše strukturne
spremembe omogočajo lažji transport tekočine.

Elektroosmozo smo raziskali tudi v prašičji skeletni mišici, kjer smo enosmerni
tok aplicirali tako v vzporedni kot v pravokotni usmeritvi glede na mišična vlakna.
Čeprav statistično značilnih razlik nismo opazili, je bila deformacija pri enosmer-
nem toku običajno večja kot pri zgolj mehanski obremenitvi, kar nakazuje možen
prispevek elektroosmoze. V primerjavi z rastlinskim tkivom je bil skupni vpliv
elektroosmoze na deformacijo manjši, verjetno zaradi odsotnosti turgorskega tlaka
in bolj zapletene strukture živalskega tkiva [119].

Za nadaljnjo raziskavo vloge elektroosmoze smo aplicirali osem PEF pulzov,
pri čemer smo lahko opazili stopničasto pomikanje bata tako pri vzporedni kot
pri pravokotni usmeritvi glede na mišična vlakna (Slika III.9). To zaznano giba-
nje kaže na električno povzročeno gibanje tekočine in potrjuje prisotnost pojava
elektroosmoze tudi v živalskem tkivu, kljub njegovi strukturni kompleksnosti. Ta
opazanja so še posebej pomembna za živilsko industrijo, kjer bi lahko že zmerna
elektroosmozna aktivnost prispevala k toplotni in električni homogenizaciji na
mikroskopski ravni ter s tem izboljšala enakomernost obdelave.



Slika III.9: Podroben prikaz pomika bata med dovajanjem osmih PEF pulzov (amplituda 1000 V, trajanje 100 μ s, ponavljalna frekvenca 1 s^{-1}) pod konstantno tlačno obremenitvijo 10 N, ki prikazuje elektroosmozne učinke. Prikazani so podatki za dva posamezna ponovitvena vzorca za vsako orientacijo, pri čemer je bila deformacija merjena v smeri vzporedno in pravokotno na mišična vlakna. Električni pulzi so bili aplicirani preko vzporednih elektrod iz nerjavečega jekla, oddaljenih 6 mm.

Elektroosmozne učinke smo raziskali tudi v agaroznih fantomih. Kljub odsotnosti celičnih struktur in turgorskega tlaka so fantomi pod vplivom enosmernega toka pokazali bistveno večjo deformacijo kot zgolj mehansko obremenjeni vzorci. Ta deformacija je bila izključno posledica elektroosmoze skozi porozno mrežo gela, kar potrjuje primernost agaroze kot poenostavljenega sistema za izolirano preučevanje elektroosmozne prispevka h gibanju tekočin.

Mehanske učinke elektroporacije smo v tej študiji obravnavali z uporabo teksturne analize rastlinskega in živalskega tkiva, kar je zagotovilo eksperimentalne dokaze o deformacijah, povzročenih z elektroporacijo in elektroosmozo. To predstavlja pomemben korak k razumevanju, kako masni transport, sprožen z električnim poljem, vpliva na strukturo tkiva. V tej študiji smo pokazali, da elektroporacija poveča deformacijo pri kompresiji, zlasti v predhodno obdelanem tkivu, kar kaže na povečano gibljivost vode in spremenjene viskoelastične lastnosti elektroporiranega biološkega tkiva. Ti rezultati so v skladu z izhodiščnim ciljem ocene mehanskih sprememb pod vplivom električnega polja. Delo odpira možnosti za nadaljnje raziskave, ki bi lahko vključevale podrobnejšo viskoelastično karakterizacijo, čeprav že trenutni rezultati predstavljajo pomemben napredek v tej smeri.

Povzamemo lahko, da je elektroosmoza pomemben mehanizem za transport tekočin med elektroporacijo, zlasti v rastlinskem tkivu, kjer deluje sinergijsko z izgubo turgorja, povzročeno z elektroporacijo. Čeprav je bil prispevek elektroosmoze v živalskem tkivu manj izrazit, neposredno zaznani elektroosmozni tok med dovajanjem pulzov potrjuje njeno prisotnost. Uporaba agaroznih fantomov je pojav potrdila tudi v poenostavljenem sistemu, ki ne vsebuje celic, kar poudarja uporabnost tovrstnih tkivnih fantomov v mehanističnih raziskavah elektroosmoze.

IV Zaključek

Ta doktorska disertacija je bila usmerjena v poglobitev razumevanja kompleksnih bioelektričnih in fizikalno-kemijskih mehanizmov, ki so prisotni pri terapijah, temelječih na elektroporaciji. Rezultati, predstavljeni v petih izvirnih znanstvenih člankih, poudarjajo tako potencial kot omejitve obstoječih modelnih in eksperimentalnih pristopov k preučevanju pojavov, povezanih z elektroporacijo. Skupaj poudarjajo pomen integracije eksperimentalnih in računalniških metod za boljše ovrednotenje odzivov tkiva ter za optimizacijo elektroporacijskih obravnav z namenom izboljšane učinkovitosti in ponovljivosti.

Študije, osredotočene na skeletno mišico, so pokazale, da ima anizotropija ključno vlogo pri oblikovanju električnega odziva in pri vplivu na izid elektroporacije. Razvit je bil večnivojski model, s katerim smo ovrednotili vpliv usmerjenosti mišičnih vlaken na porazdelitev električnega polja in geometrijo lezij, pri čemer so bili rezultati potrjeni z *in vivo* poskusi in slikovnimi analizami. Poleg tega je MRI-študija pokazala, da so poti toka v skeletni mišici anizotropne in odvisne od usmerjenosti apliciranega električnega polja, kar poudarja pomen mišične zgradbe za izid elektroporacije. Impedančna spektroskopija, izvedena na izrezanem mišičnem tkivu, je dodatno pokazala, da so anizotropne električne lastnosti prisotne vsaj 24 ur *post-mortem*, kar potrjuje uporabnost *ex vivo* tkiva za karakterizacijo in eksperimentalno potrditev ter zmanjšuje potrebo po uporabi živih živalskih modelov. Ti izsledki skupaj predstavljajo osnovo za modeliranje anizotropije v aplikacijah elektroporacije, ki vključujejo skeletno mišico.

Vzporedno je študija o spremembah pH, povzročenih z elektroporacijo, poudarila pomen upoštevanja elektrokemičnih reakcij na meji med elektrodo in elektrolitom. Računalniški model, ki temelji na Nernst–Planckovem sistemu enačb,

je natančno napovedal razvoj pH front med elektroporacijo. Model smo eksperimentalno potrdili z namensko izdelanim optičnim slikovnim sistemom, ki smo ga kalibrirali za pretvorbo barvnega odtenka v vrednosti pH. Rezultati poudarjajo, da lahko tudi pri običajno uporabljenih parametrih pulzov pride do izrazitih sprememb pH, kar lahko zmanjša učinkovitost zdravljenja in prispeva k poškodbam tkiva v okolici tretiranega območja.

Zadnja študija se je osredotočila na elektroosmozo, mehanizem, ki je v biomedicinskih aplikacijah pogosto prezrt. Poskusi na rastlinskih, živalskih in agaroznih vzorcih so potrdili, da električno povzročeno gibanje tekočine prispeva k deformaciji tkiva pod obremenitvijo. V tkivu krompirja se je elektroosmoza izkazala kot prevladujoč mehanizem, pri čemer je PEF-inducirana permeabilizacija membran dodatno okrepila deformacijo, zlasti pri nižjih tokovih. V skeletni mišici je bil prispevek elektroosmoze k deformaciji manjši, predvsem zaradi odsotnosti turgorskega tlaka, vendar so opaženi stopničasti premiki bata med dovajanjem pulzov predstavljali neposreden vizualni dokaz elektroosmoznega toka tudi v strukturno kompleksnem *post-mortem* živalskem tkivu.

Rezultati, predstavljeni v tej disertaciji, v celoti poudarjajo pomen vključevanja ustreznih bioelektričnih in fizikalno-kemijskih mehanizmov, kot so anizotropija, elektrokemične reakcije in elektroosmozni tok, tako v eksperimentalne protokole, kot v modele. Čeprav niso vsi mehanizmi pomembni za vsako aplikacijo, je njihova vključitev ključna pri raziskovanju tkiv z urejeno strukturo, kot je skeletna mišica, ali pri uporabi pulznih protokolov, ki verjetno sprožajo elektrokemične učinke.

Pojave, na katere smo se osredotočili v sklopu doktorske disertacije – električno anizotropijo, elektrokemične spremembe pH, elektroosmozni tok in z njim povezane mehanske učinke – smo raziskali s ciljno usmerjenimi in temeljitimi eksperimentalnimi ter modelnimi pristopi. Vsak od teh mehanizmov ima ključno vlogo pri oblikovanju izidov elektroporacijskih obravnav. Čeprav so bili obravnavani ločeno, rezultati jasno kažejo na potrebo po integriranem modelskem okviru, ki bi te učinke združil v celovito simulacijsko okolje.

Zato je treba pričujoče delo razumeti kot osnovo, ki jo bo v prihodnosti mogoče nadgraditi z modeli pragov ireverzibilne elektroporacije in segrevanja tkiva. Ra-

zvoj tako obsežnega večfizikalnega simulacijskega okvira bi pomenil pomemben korak naprej pri razumevanju in izkoriščanju celotnega potenciala tehnologij, temelječih na elektroporaciji.

Takšen celovit model bi lahko služil za oceno območij reverzibilne in ireverzibilne elektroporacije, za prepoznavanje območij, na katere vplivajo elektrokemične spremembe, kot so spremembe pH, ter za napovedovanje območij, kjer pride do prerazporeditve tekočin ali mehčanja tkiva. Z vključitvijo anizotropne strukture tkiva, časovnega razvoja prevodnosti membran, elektroosmoze, toplotnih učinkov in dinamike masnega transporta, bi bilo mogoče razviti celovito napoved terapijskega izida. To bi omogočilo optimizirano načrtovanje terapij tako na področju biomedicine kot tudi v prehrambeni industriji.

V Izvirni prispevki k znanosti

Večnivojsko numerično modeliranje in eksperimentalna potrditev anizotropije skeletne mišice

Skeletna mišica izkazuje anizotropne električne lastnosti, ki pomembno vplivajo na izid terapij, temelječih na elektroporaciji, vendar do sedaj ni bila izvedena podrobna in sistematična potrditev teh lastnosti. V tem prispevku smo razvili celovite večnivojske numerične modele anizotropije skeletne mišice ter jih temeljito preverili z več eksperimentalnimi metodami, vključno z analizo lezij *in vivo*, in MRI-slikanjem gostote toka ter impedančno spektroskopijo *ex vivo*. Kvantitativne analize so pokazale ključen vpliv usmerjenosti mišičnih vlaken na porazdelitev električnega polja, geometrijo lezije in tokovne poti med elektroporacijo. Pokazali smo, da je prag za ireverzibilno elektroporacijo neodvisen od usmerjenosti vlaken. Naši združeni eksperimentalni in simulacijski rezultati močno podpirajo zaključek, da anizotropno električno obnašanje v skeletni mišici v prvi vrsti izhaja iz izolativnih lastnosti celičnih membran, ki pomembno zavirajo tok v smeri pravokotno na mišična vlakna. Ti potrjeni modeli predstavljajo ključno osnovo za izboljšanje natančnosti in učinkovitosti elektroporacijskih protokolov, prilagojenih anizotropnemu biološkemu tkivu.

Eksperimentalno potrjen numerični model pH sprememb, povzročenih z elektroporacijskimi pulzi

Elektroporacija sproži elektrokemične reakcije na mejah med elektrodama in tkivom, kar povzroči izrazite lokalne spremembe pH. Za natančno napovedovanje in karakterizacijo teh sprememb med in po dovajanju elektroporacijskih pulzov smo razvili celovit mehanistični računski model. Za potrditev modela smo vzpostavili inovativen eksperimentalni sistem, ki je temeljil na agaroznih gelih, ki so vsebovali

pH indikatorje, kar je omogočilo sprotno spremljanje razvoja pH front. Študija je podala nove kvantitativne vpoglede v dinamiko pH sprememb, povzročenih z elektroporacijo, in še posebej izpostavila njihov možen vpliv na terapije, občutljive na spremembe pH, kot je npr. genska elektrotransfekcija. Eksperimentalno potrjen model predstavlja dragoceno orodje za usmerjanje oblikovanja geometrije elektrod in optimizacijo parametrov pulzov z namenom zmanjšanja nezaželenih elektrokemičnih učinkov ter izboljšanja končnega izida zdravljenja.

Eksperimentalna karakterizacija elektroosmoznega toka v tkivih pri PEF in DC pogojih

Elektroosmozni tok (EOF), mehanizem električno inducirane prenosa tekočine, je trenutno relativno neraziskan v kontekstu elektroporacije. Sistematično smo karakterizirali EOF v rastlinskih, živalskih in nadomestnih tkivih. Eksperimentalna analiza je omogočila neposredno vizualizacijo in kvantitativno potrditev elektroosmoznega toka ter poudarila njegov pomemben vpliv na deformacijo tkiva in prerazporeditev tekočine. Študija je dodatno pokazala sinergijsko delovanje med s pulzi povzročeno permeabilizacijo celičnih membran in naknadnim elektroosmoznim tokom. Ti izsledki poudarjajo pomen upoštevanja elektroosmoze pri razvoju elektroporacijskih protokolov ter nudijo nove vpoglede za izboljšanje aplikacij v biomedicini in živilski industriji.

**Mechanisms of electroporation
and physicochemical factors of
importance to
electroporation-based therapies**

1 Introduction

1.1 The phenomenon of electroporation

Electroporation is a biophysical phenomenon in which short high-voltage electrical pulses temporarily disrupt the integrity of cell membranes. These pulses create transient hydrophilic pores in the membrane, significantly increasing membrane permeability. Such permeability changes facilitate the entry or exit of molecules (or ions) such as drugs, nucleic acids and proteins into or out of the cells. Whether electroporation leads to reversible membrane permeabilisation, or permanent cell damage depends primarily on the amplitude, duration and repetition rate of the applied electrical pulses. If the pulse intensity is relatively moderate, the cell membranes recover after treatment, resulting in reversible electroporation. Conversely, pulses with higher intensity lead to permanent damage to the membranes and subsequent cell death, which is referred to as irreversible electroporation [1], [2], [3], [4]. A simple schematic representation of the electroporation phenomenon is shown in Figure 1.1.

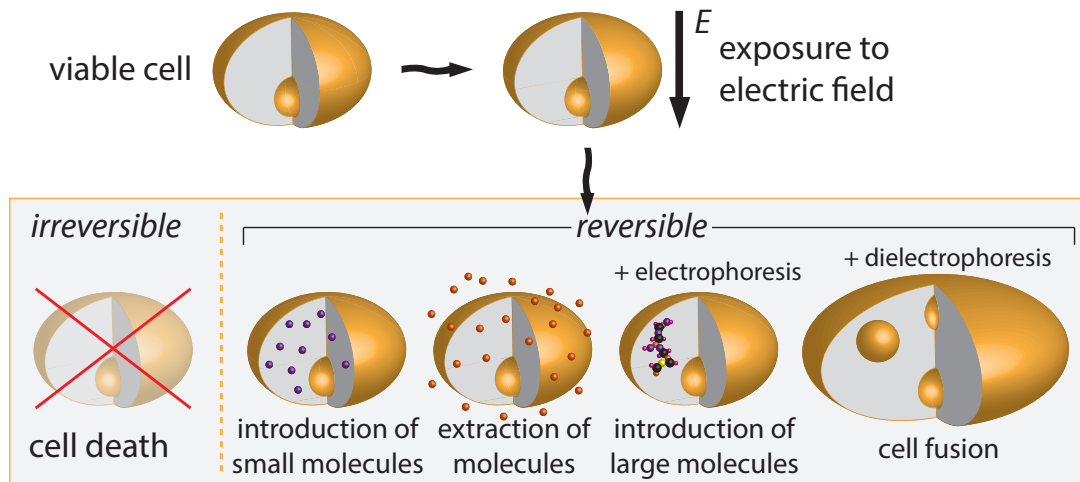


Figure 1.1: A schematic representation of the electroporation phenomenon, illustrating the possible outcomes depending on the pulse parameters (amplitude, shape, duration) [9].

1.2 Applications of electroporation

Both reversible and irreversible electroporation have found wide application in various fields, particularly in biomedicine [6], biotechnology [7], environmental science [8] and food processing [9]. In biomedicine, reversible electroporation is used for therapeutic applications such as gene electrotransfer. As it enables the efficient introduction of genetic material into cells, it plays a key role in gene therapy and vaccination strategies [10], [11], [12]. In addition, reversible electroporation is used in electrochemotherapy to improve the intracellular delivery of chemotherapeutic agents. By increasing the uptake of the drug into the tumour cells, it enables more effective local treatment while potentially reducing the need for high systemic doses [13], [14], [15].

Irreversible electroporation, on the other hand, has established itself as an effective method of tumour ablation which, due to its non-thermal mechanism, is able to selectively destroy malignant cells while preserving the integrity of the surrounding healthy tissue [16], [17], [18], [19], [20]. Irreversible electroporation has also become increasingly important in cardiology for the treatment of cardiac arrhythmias, particularly atrial fibrillation. Ablation using irreversible electropo-

ration is used to isolate the pulmonary veins, effectively disrupting the arrhythmic conduction pathways. In this context, the technology is referred to as pulsed field ablation (PFA) [21], [22], [23], [24], [25].

In addition to medicine, electroporation has also found application in the food industry, where it is usually termed pulsed electric field (PEF). In the food industry, PEF is often used as a pre-treatment technique to improve various mass transfer processes. It can improve juice yield [9], support more efficient drying through faster water release [26], increase the bioaccessibility of valuable bioactive compounds [27], [28], and help to reduce the concentrations of unwanted or harmful toxicants [29], [30]. In addition, PEF is being explored as a tool in food preservation methods such as cryopreservation, where it facilitates the penetration of cryoprotectants into cellular structures, preserving the food texture and flavour by preventing the harmful formation of ice crystals [31].

1.3 Electrical properties of tissues

The result of electroporation treatments depends not only on the pulse parameters but is also significantly influenced by the intrinsic electrical properties of the tissue. Biological tissues exhibit complex electrical behaviour, which is determined by their composition, structural organisation, and the distribution of charged particles. The interplay of these factors influences the distribution of electric fields and the propagation of currents in tissue, leading to considerable variability between different tissue types [32], [33], [34], [35], [36], [37]. In general, extracellular spaces conduct electricity more effectively due to the abundance of free ions, whereas cell membranes with their significantly lower conductivity act as barriers that limit current flow [38], [39]. The electrical properties of tissue also vary significantly with frequency, reflecting different physiological mechanisms that are active in different frequency ranges [35], [37]. A thorough understanding of these complex behaviours is essential for the optimisation of electroporation protocols.

Techniques such as electrical impedance spectroscopy (EIS) are instrumental for the detailed characterisation of the electrical properties of tissues, providing

comprehensive insights into their resistive and capacitive properties over a broad frequency spectrum [40], [41], [42], [43], [44], [45]. Further valuable information can be obtained from real-time monitoring of voltage and current waveforms during the application of electroporation pulses, providing dynamic data on how tissue conductivity evolves during treatment [46], [47]. In addition, advanced imaging techniques such as magnetic resonance-based current density imaging (CDI) can significantly improve our understanding of how electrical current flows in biological tissue during electroporation [48], [49], [50], [51].

1.3.1 Skeletal muscle anisotropy

Skeletal muscle tissue is of great interest in electroporation research, mainly because it is often chosen as a target for gene electrotransfer due to its ability to effectively express proteins and secrete them into the bloodstream [52], [53], [54]. A key factor influencing the electrical behaviour of skeletal muscle is anisotropy, which refers to the directionality of its electrical properties [55], [56], [57]. This anisotropy arises primarily from the structured orientation of muscle fibres within an intricate network of connective tissue layers, such as endomysium, perimysium, and epimysium [58], [59]. Each skeletal muscle fibre is enveloped by a plasma membrane, the sarcolemma, which, together with the surrounding connective tissue, forms insulating barriers that restrict the movement of ions. These insulating layers effectively impede the flow of electrical current perpendicular to the fibre orientation [60]. Consequently, skeletal muscle exhibits significant directional differences in electrical conductivity, with conductivity along the muscle fibres generally being higher than across them, which is particularly noticeable at low frequencies [35], [37].

The directional variations of conductivity have a significant influence on the spatial distribution of electric fields in skeletal muscle tissue and thus have a direct impact on the outcome of electroporation-based treatments. A comprehensive understanding of anisotropic electrical behaviour is therefore crucial for accurately predicting how electric fields interact with muscle tissue, optimising electroporation-based applications and improving treatment precision in biomedical applications.

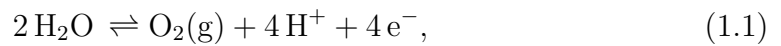
1.4 Additional phenomena accompanying electroporation

Electroporation is accompanied by additional secondary phenomena that can influence tissue response and mass transport. Some of these, such as tissue heating due to Joule losses, have been extensively studied [62], [63], [64], [65], [66], [67], while others are less well understood. Tissue damage caused by pH changes due to electrochemical reactions [68], [69] and the role of electroosmosis [70], [71], [72] in mass transport during electroporation are among the effects that remain less understood but are increasingly recognised as critical and therefore require further investigation.

1.4.1 Electrochemical effects of pulsed fields

Electrochemical effects of pulsed electric fields are important phenomena accompanying electroporation, significantly impacting the local tissue environment. These electrochemical effects result primarily from water electrolysis reactions that occur at the electrode–tissue interface when electrical pulses are delivered to biological tissue. Water electrolysis at the electrodes generates substantial localised pH gradients: acidic conditions develop at the anode, whereas alkaline conditions develop at the cathode [68], [69], [73], [74], [75].

The main electrochemical reactions responsible for these pH changes during pulse delivery are oxidation reactions (electron loss) at the anode and reduction reactions (electron gain) at the cathode. Water and chloride ions are oxidised at the anode, producing hydrogen ions and the gases oxygen and chlorine [76], [77], [78]:



These reactions lead to the formation of acidic pH fronts around the anode. Conversely, water molecules are reduced at the cathode, producing hydroxide ions and hydrogen gas, which leads to alkaline pH fronts [79]:



Electrochemically induced pH changes have critical implications for electroporation-based therapies [80], [81], [82], [83]. In gene electrotransfer applications, for example, maintaining physiologically compatible pH conditions is essential to preserve the integrity of plasmid DNA and ensure effective transfection. Significant pH changes can damage the genetic material and impair cell viability, thereby compromising therapeutic efficacy [84], [85], [86].

In contrast, in tumour treatment, the pH gradients are intentionally induced in order to improve the therapeutic outcomes. In electrochemical tumour therapy, controlled low-level direct current is used to create a localised acidic and alkaline environment that causes the targeted death of tumour cells [76], [77], [87], [88], [89]. A newer approach that combines electroporation with electrolysis, an approach referred to as E2, exploits these localised pH changes to enhance tissue ablation by promoting intracellular uptake of electrolytic reaction products through permeabilised membranes [90], [91], [92], [93]. Studies suggest that comparable ablation volumes to conventional irreversible electroporation with high-voltage pulses can also be achieved with a greater number of low-voltage pulses, further emphasising the role of electrochemically induced pH changes in tissue damage and treatment outcomes [94]. Understanding the electrochemical effects of electroporation is therefore crucial for optimising electroporation protocols and minimising unintended tissue damage in clinical and experimental applications.

1.4.2 Electric field-induced fluid motion

Another phenomenon that is often overlooked in electroporation research is electroosmosis, despite its potential to significantly affect the transport of fluids and solutes in biological tissue when exposed to electric fields. Electroosmosis refers to the movement of fluid, typically water, through porous biological media in response to an applied electric field. This movement is caused by electrokinetic interactions at charged solid–liquid interfaces, where the formation of an electrical double layer leads to a displacement of ions. As the ions migrate under the influence of the electric field, they exert a drag force on the surrounding fluid, resulting in a net flow [72]. The superficial electroosmotic velocity u_{EOS} in porous

media is given by:

$$u_{\text{EOS}} = \frac{\varepsilon_w \zeta \varepsilon}{\eta \lambda^2} \nabla \phi, \quad (1.4)$$

where ε_w is the permittivity of water (F/m), ζ is the zeta potential (V) at the charged interfaces, ε is the porosity of the medium, η is the dynamic viscosity (Pa·s) of the fluid, λ is the tortuosity (dimensionless), which describes the complexity of the fluid pathways, and $\nabla \phi$ is the gradient of the electric potential (V/m) [95]. The zeta potential is particularly critical, as it determines the direction and magnitude of the electroosmotic flow based on the charge at the solid–liquid interface [96].

Most biological tissues exhibit a negative zeta potential, which means that fluid normally moves from the anode to the cathode [97], [98], [99]. In plant-based applications, PEF treatments can improve electroosmotic dehydration by increasing membrane permeability and promoting water release. This offers improved energy efficiency and reduced reliance on conventional thermal drying, with potential benefits for both product quality and environmental impact [71], [100].

In biomedicine, the electroosmotic flow can significantly influence treatment outcomes. In tumour treatment, for example, electroosmosis enhances fluid migration from the anode to the cathode, intensifying local dehydration and amplifying the destructive effects of localised pH shifts [101], [102], [103]. Electroosmotic effects are also promising in targeted drug delivery, particularly through electrokinetic, convection-enhanced delivery. This technique utilises electric fields to direct therapeutic agents to deep and otherwise inaccessible regions, including the brain. It allows for more precise and less invasive administration with lower infusion pressures than conventional methods [104], [105]. Thus, electroosmosis offers an opportunity to better control mass transport during electroporation. Further research into its mechanisms and effects is important to improve treatment precision and efficiency in both food and biomedical applications.

1.5 Aims of the dissertation

The overarching aim of this dissertation is to advance electroporation-based therapies by improving the fundamental mechanistic understanding of its underpinnings through validated numerical models of selected physicochemical and anatomical factors that influence treatment outcomes. Three main lines of investigation are pursued herein: skeletal muscle anisotropy, electrochemically induced pH changes, and electric field-driven fluid transport (i.e., electroosmosis). Each of these phenomena bears significant implications for treatment efficiency, safety, and translational potential.

The first aim was to investigate the role of skeletal muscle electrical anisotropy and its implications for electroporation outcomes. While it is well established that the conductivity of muscle varies with fibre orientation, the specific effects on the electric field and current distribution and the resulting biological response had not yet been comprehensively characterised. To address this, a multiscale modelling approach was used, starting at the level of individual fibres and extending to complex, anatomically inspired muscle geometries. These models were validated through comparisons with lesion patterns observed *in vivo* and by MRI-based current density imaging. In addition, impedance spectroscopy was used to assess the anisotropic electrical properties of muscle over time after death, while numerical simulations were used to interpret and confirm experimentally observed changes related to *post-mortem* tissue degradation. A key objective was to determine whether excised *post-mortem* muscle could serve as a surrogate for *in vivo* conditions, thereby reducing the need for animal testing. The three studies contributing to this aim provided important insights into the influence of muscle fibre orientation on treatment outcomes, anisotropic current pathways, and temporal changes in tissue conductivity following death.

The second aim was to investigate the electrochemical pH changes that occur during and after electroporation, focussing on protocols relevant to gene electrotransfer, which typically uses relatively long monophasic pulse waveforms. A mechanistic computational model was developed to predict the formation and propagation of acidic and alkaline pH fronts generated by water electrolysis reactions at the electrodes. This model was validated using agarose gels in which pH

indicators were embedded, with dynamic pH mapping enabled by a calibrated imaging system. The aim was to establish a reliable experimental protocol to capture the spatial and temporal pH dynamics and to evaluate how these electrochemical effects might influence the safety and efficacy of electroporation-based treatments.

The third aim was to investigate electroosmosis as a concomitant effect of electroporation and to evaluate its significance in various biological matrices. The electroosmotic flow was investigated experimentally in plant tissue (potato tubers), animal muscle, and agarose phantoms. In plant tissue, the role of pulsed electric field (PEF) pretreatment in supporting electroosmotic dehydration by promoting the release of intracellular fluid was investigated. In animal muscle, experiments on freshly excised tissue were conducted to investigate the role of electroosmosis in mass transport in contexts relevant to food processing and biomedicine. Agarose phantoms were also evaluated as surrogate materials for studying electroosmotic effects under controlled conditions.

Through the insights gained by following these three strands of inquiry, this dissertation contributes to a deeper understanding of the key phenomena that influence the outcomes of electroporation-based therapies. Together they form a foundation for improving treatment design, optimisation, and applicability in both experimental and clinical contexts.

2 Research papers

The research work carried out during the doctoral studies is presented in five original scientific papers, published in or submitted to international peer-reviewed journals. This chapter begins with a brief overview of each paper, while the full methodology and results are detailed within the respective publications, which form the main content of this chapter.

The first paper, *A multiscale computational model of skeletal muscle electroporation validated using in situ porcine experiments*, addresses the role of skeletal muscle anisotropy in electroporation. The study investigates how the orientation of the electric field, which is applied either parallel or perpendicular to the muscle fibres, influences the extent of irreversible electroporation in skeletal muscle. First, a numerical model was developed to simulate electroporation at the level of a single muscle fibre and to determine how conductivity changes during electroporation. These changes were then generalised to a model of skeletal muscle as a bulk tissue. *In vivo* experiments were performed on porcine skeletal muscle in which electroporation lesions were created and segmented to allow direct comparison with the numerical predictions. The calculated electric field distributions were compared with experimentally obtained *in vivo* lesions using the Sørensen–Dice similarity coefficient to determine the threshold above which irreversible damage occurs.

The second paper, *Electrical pathways through the intricate network of skeletal muscle fibres: insights from MRI-validated numerical modelling*, builds on the first study by increasing the anatomical complexity of the model. Rather than treating the muscle as a homogeneous bulk tissue, this study incorporates individual muscle fibres to provide a more detailed representation of the tissue structure.

The study investigates the current flow at two orientations of the applied electric field, parallel and perpendicular to the muscle fibres. Experimentally observed current flow patterns were obtained using a magnetic resonance-based technique called current density imaging (CDI), which enables non-invasive mapping of current distributions within biological tissue. These were then compared with numerical simulations to assess how well the model captures anisotropic electrical conduction in skeletal muscle.

The third paper, *Skeletal muscle death from the perspective of electrical impedance as evidenced by experiment and mathematical modelling*, investigates how skeletal muscle anisotropy changes over time after death. The study combines impedance spectroscopy with numerical modelling to track changes in electrical properties *post-mortem*. By measuring the impedance at different time points, we investigated how the directional conductivity of muscle tissue evolves during physiological degradation. The numerical model is used to interpret and support experimental findings, offering insight into the mechanisms driving these changes. In addition, the feasibility of experimenting on excised muscle tissue is explored, suggesting that *ex vivo* studies may in some cases provide an alternative to experiments on live animals, thereby reducing both the ethical and economic burden.

The fourth paper, *An experimentally validated numerical model of pH changes in surrogate tissue induced by electroporation pulses*, investigates the electrochemical processes that occur during the delivery of electroporation pulses, in particular those used in gene electrotransfer protocols. We developed a comprehensive mechanistic computational model to predict the pH changes in tissue during and after the application of electrical pulses. The model focuses on the effects of water electrolysis at the electrode–tissue interface, which leads to the formation of acidic and alkaline pH fronts. Experimental validation was performed using agarose gels embedded with pH indicators, prepared with different buffer systems to evaluate how buffer capacity influences pH evolution. A video recording system was developed and calibrated to monitor these changes in real time. The aim of this approach was to establish reproducible experimental procedures and confirm the ability of the model to accurately predict the spatial and temporal pH dynamics during electroporation.

The fifth paper, *On the importance of electroosmosis in pulsed electric field treatment of food matrices*, investigates the electroosmotic flow (EOF) in plant and animal tissues under pulsed electric field (PEF) and direct current (DC) conditions. Texture analysis was used to study electroosmotic flow in potato tubers, with particular focus on whether PEF pretreatment facilitates the release of intracellular fluid and serves as a prerequisite for effective electroosmotic dehydration. In animal tissue, experiments were performed on freshly excised skeletal muscle to assess the role of electroosmosis in mass transport, which is relevant for both food processing and biomedical applications. In addition, agarose phantoms were investigated as potential surrogate materials for the study of electroosmotic phenomena under well-controlled experimental conditions. These investigations provide experimental insight into the often-overlooked contribution of electroosmosis to solute and fluid transport during electroporation-based treatments.

2.1 Paper 1

Title: **A multiscale computational model of skeletal muscle electroporation validated using *in situ* porcine experiments**

Authors: **Rok Šmerc**, David A. Ramirez, Samo Mahnič-Kalamiza, Janja Dermol-Černe, Daniel C. Sigg, Lars M. Mattison, Paul A. Iaizzo, and Damijan Miklavčič

Publication: *IEEE Transactions on Biomedical Engineering*, vol. 60, no. 6, pp. 1826-1837, June 2023

Impact factor: 4.4 (2023)

Quartile: Q2

Rank: 36/123 (Biomedical engineering)

DOI: <https://doi.org/10.1109/TBME.2022.3229560>

A Multiscale Computational Model of Skeletal Muscle Electroporation Validated Using *In Situ* Porcine Experiments

Rok Šmerc , David A. Ramirez , Samo Mahnič-Kalamiza , Janja Dermol-Černe , Daniel C. Sigg , Lars M. Mattison, Paul A. Iaizzo , and Damijan Miklavčič 

Abstract—Objective: The goal of our study was to determine the importance of electric field orientation in an anisotropic muscle tissue for the extent of irreversible electroporation damage by means of an experimentally validated mathematical model. **Methods:** Electrical pulses were delivered to porcine skeletal muscle *in vivo* by inserting needle electrodes so that the electric field was applied in direction either parallel or perpendicular to the direction of the muscle fibres. Triphenyl tetrazolium chloride staining was used to determine the shape of the lesions. Next, we used a single cell model to determine the cell-level conductivity during electroporation, and then generalised the calculated conductivity changes to the bulk tissue. Finally, we compared the experimental lesions with the calculated field strength distributions using the Sørensen-Dice similarity coefficient to find the contours of the electric field strength threshold beyond which irreversible damage is thought to occur. **Results:** Lesions in the parallel group were consistently smaller and narrower than lesions in the perpendicular group. The determined irreversible threshold of electroporation for the selected pulse protocol was 193.4 V/cm with a standard deviation of 42.1 V/cm, and was not dependent on field orientation. **Conclusion:** Muscle anisotropy is of significant importance when considering electric field distribution in electroporation applications. **Significance:** The paper presents an important advancement in building up from the current understanding of single cell electroporation to an *in silico* multiscale model of bulk muscle tissue. The model accounts for anisotropic electrical conductivity and has been validated through experiments *in vivo*.

Index Terms—Electric field strength distribution, electroporation, irreversible electroporation threshold, multiscale numerical model, pulsed field ablation, skeletal muscle anisotropy.

I. INTRODUCTION

ELECTROPORATION, electropermeabilisation, pulsed electric field (PEF) treatment, and pulsed field ablation (PFA) are terms used to describe the same phenomenon in different fields of research and applications. When a biological cell is exposed to an external electric field of sufficient amplitude, its membrane becomes transiently permeable to ions and molecules for which it is otherwise poorly permeable or not permeable at all (reversible electroporation). The exposure may lead to cell death, in which case the phenomenon is called irreversible electroporation [1], [2], [3]. Electroporation is used in various fields of biomedicine, biotechnology, as well as in food processing [4], [5], [6], [7], [8], [9], [10].

One of the important applications of electroporation in biomedicine is gene electrotransfer (GET) [11]. In GET, the phenomenon of electroporation is used to introduce genetic material (usually plasmid DNA) into cells to achieve a desired therapeutic effect. Skeletal muscle is the most commonly used target tissue for gene therapy and DNA vaccination due to its ability to express genes and secrete proteins into the bloodstream. Since skeletal muscle cells do not divide, gene expression is sustained for several months after GET [12], [13], [14]. Another increasingly important application of electroporation in biomedicine is treatment of cardiac arrhythmias, particularly of atrial fibrillation, by ablation of pulmonary vein tissue using irreversible electroporation [10], [15], [16], [17], [18]. The specific structure of skeletal and cardiac muscles dictates an anisotropic electrical conductivity, leading to a fibre-orientation dependent electric field distribution upon pulse application [19], [20], [21]. The electrical conductivity of skeletal muscle in the direction of its fibres was found to be higher than the electrical conductivity in the direction perpendicular to the fibres [22], [23], [24], [25], [26], [27]. Anisotropic electrical conductivity has also been observed in cardiac muscle [28]. It has been reported previously that the (reversible) threshold of electroporation depends on the direction of the applied electric field with respect to the direction of the muscle fibres – lower pulse amplitudes were required for

Manuscript received 3 June 2022; revised 24 August 2022 and 11 November 2022; accepted 4 December 2022. Date of publication 3 February 2023; date of current version 19 May 2023. This work was supported in part by the Slovenian Research Agency (ARRS) through the Research Program Electroporation-Based Technologies and Treatments under Grant P2-0249, and in part by the Medtronic, Inc. (Corresponding author: Damijan Miklavčič.)

Rok Šmerc, Samo Mahnič-Kalamiza, and Janja Dermol-Černe are with the Faculty of Electrical Engineering, University of Ljubljana, Slovenia.

David A. Ramirez and Paul A. Iaizzo are with the Department of Surgery, University of Minnesota, USA.

Daniel C. Sigg and Lars M. Mattison are with the Cardiac Ablation Solutions, Medtronic, Inc., USA.

Damijan Miklavčič is with the Faculty of Electrical Engineering, University of Ljubljana, 1000 Ljubljana, Slovenia (e-mail: damijan.miklavcic@fe.uni-lj.si).

This article has supplementary downloadable material available at <https://doi.org/10.1109/TBME.2022.3229560>, provided by the authors.

Digital Object Identifier 10.1109/TBME.2022.3229560

parallel orientation: 80 V/cm versus perpendicular orientation: 200 V/cm [29]. Interestingly, a tissue that is not intrinsically anisotropic, such as the liver tissue, can become anisotropic after electroporation [30]. Anisotropy can also have a significant influence in PEF applications in the food industry, such as meat and fish processing [31]. Namely, many food plant tissues exhibit anisotropic properties, e.g. asparagus [32].

It is also known that electroporation at the cell level *in vitro* depends on the cell geometry and the orientation of the cell in the electric field [33], [34], [35], [36], whereas the preferential orientation for electroporation depends also on pulse duration and amplitude [37]. Electroporation leads to an increase in membrane conductivity, which results in bulk tissue conductivity increase [38], [39], [40], [41]. The orientation of muscle fibres is not constant throughout the muscle, which is most pronounced within the cardiac muscle, where the orientation of cardiomyocytes varies not only spatially through the heart, but also from the epicardial to the endocardial side [42]. Therefore, muscle is considered a heterogeneous tissue, which can considerably affect the success of muscle gene transfection and cardiac ablation. The increase in bulk tissue conductivity due to or during electroporation has been described previously and was used to control pulse delivery, thus limiting the damage induced due to electroporation [43]. It has been described by various functional dependencies of conductivity as a function of local electric field [44], [45], but until recently was not explicitly linked to changes in membrane conductivity. The conductivity of the cell membrane and consequently the conductivity of the cell is increased in the direction of the electric field of the delivered electroporative pulses, i.e., it can be said that electroporation induces or increases the anisotropy of the tissue [30]. Previously, a skin structure with different cell shapes and packing densities was presented and numerically compared with skin impedance measurements [46], [47], [48], which also provided the basis to connect membrane electroporation to the increase in tissue conductivity due to electroporation [49].

Hitherto, the increase in anisotropy of conductivity due to electroporation has not been well described. Namely, electroporation in one direction contributes to the change of conductivity in all directions, not only in the direction of the applied electric field / electroporation. We have therefore constructed skeletal muscle tissue from cells, similar to how it was demonstrated for skin keratinocytes in dense suspensions in the models of Huclova et al. This approach allows to connect the micro- to the macro-scale of electroporation, and to deduce about membrane changes backwards, i.e. from measurements made at the tissue scale, we can in principle infer the degree of membrane permeabilisation required to achieve the observed changes in the bulk tissue conductivity [50].

The anatomic features and physiological functioning of skeletal muscle has been well described in the literature [51], [52], [53]. When targeting skeletal muscle for electroporation, we need to consider the given architecture of the muscle cells and their relative lengths. Muscle cells are multinucleated and can have lengths ranging from millimetres to over 10 cm [54]. Each muscle fibre itself is surrounded by a connective tissue known as endomysium. These fibres, or myofibres, then form clusters

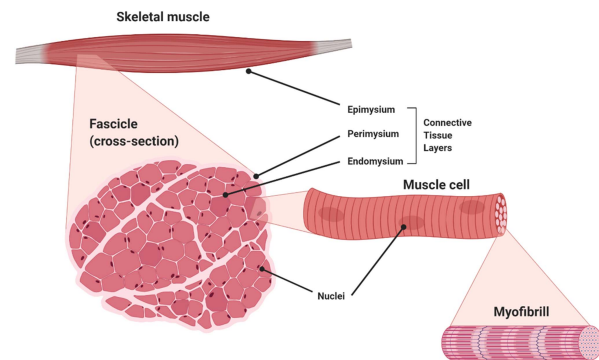


Fig. 1. Skeletal muscle structure: The skeletal muscle is organised into various substructures, with connective tissue layers separating those structures. The major muscle is surrounded by a connective tissue layer called epimysium. The muscle contains a large number of fascicles (shown as a cross-section) which is surrounded by a tissue layer called perimysium. Each fascicle contains a number of individual muscle cells surrounded by a tissue layer called endomysium. Each muscle cell is multinucleated, and contains myofibrils, composed of the contractile muscle proteins actin and myosin.

known as fascicles, which are again wrapped in additional connective tissue, the perimysium. Finally, the fascicles are then enveloped in another layer of connective tissue known as the epimysium, and the skeletal muscle such as the *vastus lateralis* is surrounded by a final layer of connective tissue, the perimysium (Fig. 1). These structures were described and imaged with high-resolution MRI with histology images [55]. Each connective tissue layer presents a complex system with differing densities and compositions [56]. To compound to the complexity of the skeletal muscle, there are nerve fibres and blood vessels intertwined throughout these connective tissue layers.

Our study consisted of two parts, an experimental and a numerical part, initially separated but then intertwined (see Fig. S1 in the Supplementary Materials). In the experimental part of the study, we performed *in vivo* experiments in the skeletal muscle tissue of pigs. We delivered electrical pulses to the tissue, inserting needle electrodes in two different orientations with respect to the muscle fibres. In the first group, the direction of the applied electric field was parallel to the direction of the muscle fibres (later referred to as parallel orientation), and in the second group, the direction of the applied electric field was perpendicular to the direction of the muscle fibres (perpendicular orientation). We then used triphenyl tetrazolium chloride (TTC) staining to determine the shape of the lesion for each application of pulses. TTC stains living cells in bright red while dead tissue appears white/pale. The white compound is enzymatically reduced to red TPF (1,3,5-triphenylformazan) in living tissues due to the activity of various dehydrogenases. This stain enables determination of the irreversibly ablated region, i.e. the lesion [57].

In the numerical part of the study, we built a multiscale numerical model of skeletal muscle. We first used a single-cell model to determine cell-level conductivity during electroporation. Next, we implemented these results into a bulk model of the tissue.

We then combined the experimental and numerical parts of the study in such a way that we used our numerical model to simulate the *in vivo* experiments and determined irreversible threshold of electroporation for each experiment by comparing the numerical, i.e. model results to the shape of the experimental lesion.

The purpose and main objective of the study is two-faceted. Firstly, we aimed to show how bulk tissue properties, specifically anisotropy, can be deduced from a single-cell model, i.e., to demonstrate an approach of building muscle tissue from its basic constituents, the muscle fibres. This fibre to tissue scaleup consists specifically of observing electrical properties of bulk muscle based on electrical characteristics of single cells both before treatment, and then as altered due to electroporation. Secondly, we aimed at both validating the model by comparing TTC-stained lesions in shape and size to numerically calculated electric field distributions, as well as quantifying the irreversible electroporation threshold of muscle tissue *in vivo* for specific pulse parameters. We made no *a priori* assumptions regarding the threshold in terms of its dependence on field-to-fibre orientation, i.e., we built no assumptions into the model that the threshold is dependent on field-to-fibre orientation. From this point of view the study is also an attempt at determining whether anisotropic electrical properties of muscle tissue will lead to an orientation-dependent irreversible field strength threshold on the level of a single cell, or, are the orientation-dependent lesions shapes and sizes a result of electric field distribution in an electrically anisotropic medium.

II. MATERIALS AND METHODS

A. In Vivo Experiments

In situ preclinical porcine models have been shown to be a reliable and widely used for translational ablation studies, including those for assessing the effect of electroporation therapies [58]. Further, the porcine *vastus lateralis* muscle has been shown to elicit reproducible lesion sizes and depths and thus was considered as a viable model for preclinical ablation studies [59].

Adult male Yorkshire pigs (75–85 kg) were used. All animals received humane care in compliance with the ‘Principles of Laboratory Animal Care’, formulated by the National Society for Medical Research, and The Guide for the Care of Laboratory Animals, published by the National Institutes of Health. This research protocol was approved by the University of Minnesota’s Institutional Animal Care and Use Committee (IACUC protocol number: #2006-38201 A; last approval date: 28 January 2022).

The pigs were sedated with methohexital (20–50 mg/kg as needed), then intubated and mechanically ventilated. Anaesthesia was maintained using isoflurane (>2 %) and a 2:1 air-to-oxygen mixture. The heart rate and blood pressure of each animal were monitored continuously (SpaceLabs, WA, USA) and properly maintained. Their core temperatures (rectal temperatures, YSI thermocouples, City, State) were monitored and maintained between $38 \pm 0.5^\circ\text{C}$, external convective warming (BairHugger, 3 M, USA) was utilised as needed. Next, the *vastus lateralis* muscles of each pig were carefully exposed. To do so, the skin was cut using electric cautery adjacent to the muscle so

not to impair function and the remaining connective tissue and fascia was blunt dissected to leave the muscle fibres exposed (see Fig. S2a in the Supplementary Materials). Thus there were no tissues adjacent to the treated muscle present that could affect the electric field distribution within the treated muscle tissue and its conductivity. The microstructure of the tissue also has no significant influence on the distribution of the electric field on a macroscopic level and can therefore be neglected, but it does influence the distribution of the electric field on a microscopic level / locally [45], [60]. As can be observed in Fig. S2a in the Supplementary Materials, the fascicles and muscle fibres of the *vastus lateralis* run parallel to the long axis of this muscle (origin to insertion). The muscle and fibres are on average 10 cm long and 4.5 cm wide, and the fascicles are about 4 mm in diameter.

Electroporation was performed by delivering 48 pulses with a pulse width of 100 μs in 6 trains of 8 pulses each, with a pulse repetition rate of 1000 s^{-1} in each train, and a pause of 2 seconds between trains. Custom built pulse generator was used. The pulses of four different amplitudes (600 V, 800 V, 1000 V, and 1200 V) were delivered through two needle electrodes with a diameter of 0.70 mm and an centre-to-centre distance of 8.0 mm. The total length of the electrodes was 8 mm, with the upper 1 mm insulated, i.e. 7 mm was the length of the non-insulated part of the electrodes, to ensure that the active part of the electrodes inserted into the tissue was the same for each experiment performed. The decision to use only 2 needle electrodes was based on the literature [50] showing that 2 needle electrodes provide an adequate gradient of electric field, have a well-defined geometry and at the same time minimise trauma to the tissue. This electrode geometry also allows comparison with other relevant studies, e.g. [61], and allows easy determination of orientation with respect to the muscle fibres. The 2 needle electrode geometry also maximises the number of possible lesions per muscle and thus minimises the number of animals needed for experiments. The electrodes were placed so that the direction of the electric field was as parallel or perpendicular as possible to the direction of the muscle fibres. Each electrode position was at least 5 cm apart and the types of ablation deliveries were randomised before each day’s experiment. All voltage and current measurements were acquired with an oscilloscope (Keysight MSOS104 A, California, USA) recording at 1 GHz. High voltage differential probes (Keysight N2891 A) with an attenuation ratio of 1000:1 were fed into the oscilloscope. The probes were clamped directly onto a specialised space within the needle electrode holder. Muscle contractions were visually observed with all pulse deliveries and for the electrodes placed with the varied fibre orientations. From these observations, we could not detect any differences in contraction response between muscle stimulations with the varied electrode placements. As expected, the greater applied pulse amplitude induced visibly larger contractions: i.e., more muscle tissue was activated.

Following pulse delivery, all lesions were allowed to mature for 1.5 hours before the animal was euthanised via cardioplegia delivery. Immediately post-mortem the *vastus lateralis* muscles were isolated and removed and taken to a dissection table where the most superficial layer was sectioned off. This was done to allow the staining agent to penetrate the muscle cells, as

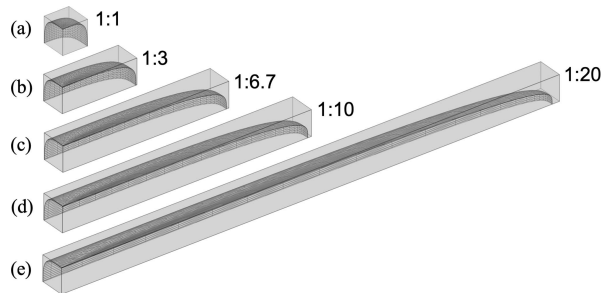


Fig. 2. Geometry of the muscle cells in the unit cells for $r_{\text{short-to-r}_{\text{long}}$ ratio of (a) 1:1, (b) 1:3, (c) 1:6.7, (d) 1:10, and (e) 1:20.

connective tissue and fascia interfere with the TTC stain. The tissue was then placed in a solution of 5 % 2,3,5-Triphenyltetrazolium chloride (TTC) at 37 °C for 3.5 minutes. The stained tissue was then imaged and processed with ImageJ (NIH) in preparation for computational analysis (see Fig. S2b in the Supplementary Materials).

B. Single-Cell Numerical Model

Calculations of cell-level conductivity during electroporation were performed in Comsol Multiphysics v6.0 (Comsol Inc., Sweden). We used a unit-cell approach as described in [46] and applied for cell electroporation previously [49]. First, we constructed a 3D cuboidal biological cell in Matlab R2022a (MathWorks, USA) using the superformula [62] ((1)-(9) in [46]) and parameters for a cuboidal cell (Table I in [46]). The constructed cell was saved in a drawing interchange format (.dxf file) and imported to Comsol using the Import function under Geometry with the CAD module. The imported biological cell was then scaled to obtain the desired geometry (r_{long} and r_{short} , Table S-I in the Supplementary Materials, and Fig. 2) of a single muscle cell. A unit cell around the muscle cell was constructed as a block. Its geometry was adapted so that the volume fraction of the biological cell was 76 %. This value is lower than that of the actual muscle tissue [63], but it is the highest value that can be achieved with the geometry used without impractically increasing the computational cost. The effect of the volume fraction value used in the model on the calculated cell-level conductivity results is further addressed in the Results and discussion section. Because of the symmetry of the model, only 1/8 of the model was calculated to decrease the computational cost.

For the calculation of electroporation, we coupled the Weak Form Boundary PDE (partial differential equation) and the Electric Current interface in the same way as described in [49] with the parameters [47], [64], [65] summarised in Table S-I in the Supplementary Materials. The Weak Form Boundary PDE was used to calculate the change in pore density, while the Electric Currents were used to calculate the Laplace equation. Eight square 100 μs long pulses with a rise- and fall-time of 1 μs were applied either in parallel or perpendicular direction with respect to the direction of the long axis of the muscle cell to two

opposite boundaries with a pulse repetition rate of 1000 s^{-1} . The other boundaries were set as electrically insulated. The muscle cell membrane was modelled as a contact impedance boundary condition and its conductivity (σ_m) increased due to the change in pore density (N):

$$\sigma_m = \sigma_{m0} + N(2\pi r_p^2 \sigma_p d_m) / (\pi r_p + 2d_m) \quad (1)$$

(parameters described in Table S-I in the Supplementary Materials). Pore formation was calculated with the asymptotic pore equation with fixed pore radii, which then increased the membrane conductivity, as described in [49], [65]. The transmembrane voltage (U_m) was calculated as the difference between the potential on the inside and the outside of the cell membrane. For calculation of electrical conductivity of the unit cell, two additional Laplace equations were added to the model via the Electric Current interfaces, one for calculation of the electrical conductivity in the direction of the long axis of the muscle cell (later referred to as parallel conductivity), and the other for calculation of the electrical conductivity in the direction perpendicular to the long axis of the muscle cell (perpendicular conductivity). In both, a fixed voltage of 1 V (V_{test}) was applied throughout the whole course of simulation. The voltage of 1 V used had no influence on the results of the electroporation part of the model, as these additional interfaces were used exclusively for the calculation of the two conductivities and were not coupled to the primary Electric Current interface.

First, a stationary study was run to initialise the parameters of the two physical interfaces, used for calculations of the conductivities. Then, a time-domain study was performed for all included physical interfaces to model the pore formation and calculate the corresponding conductivity change. The simulation time was 30 seconds with denser time points during the pulse application, which is sufficient to observe the closing of the pores, as well as the faster dynamics during the pulse application.

Unit cell conductivity was obtained by using the currents caused by V_{test} and calculated within the two corresponding Electric Current interfaces. These two currents were obtained by calculating a boundary integral of a normal current density across a cross-section (y - z plane for the parallel current and x - z plane for the perpendicular current, see Fig. S3 in the Supplementary Materials for the coordinate system orientation). Taking into account the geometry of the cross-section, i.e. of the unit cell (d_x , d_y , d_z) as well as the applied voltage (V_{test}), the conductivity of the muscle cell during and after pulse application was determined in S/m and used in further calculations. The results of these calculations are shown in Fig. 3 for the two cases where the direction of the electric field is either parallel or perpendicular with respect to the direction of the long axis of the muscle cell, and for both cases, the conductivity both in direction parallel or perpendicular with respect to the direction of the long axis of the muscle cell is given.

To summarise: In the numerical model of a single cell that serves as a means of bulk tissue properties determination, the pulses are applied to the unit cell directly by prescribing the appropriate initial and boundary conditions to the surfaces of the unit cell, and the geometry of the electrodes is not involved. The results of this model, specifically the electric conductivity

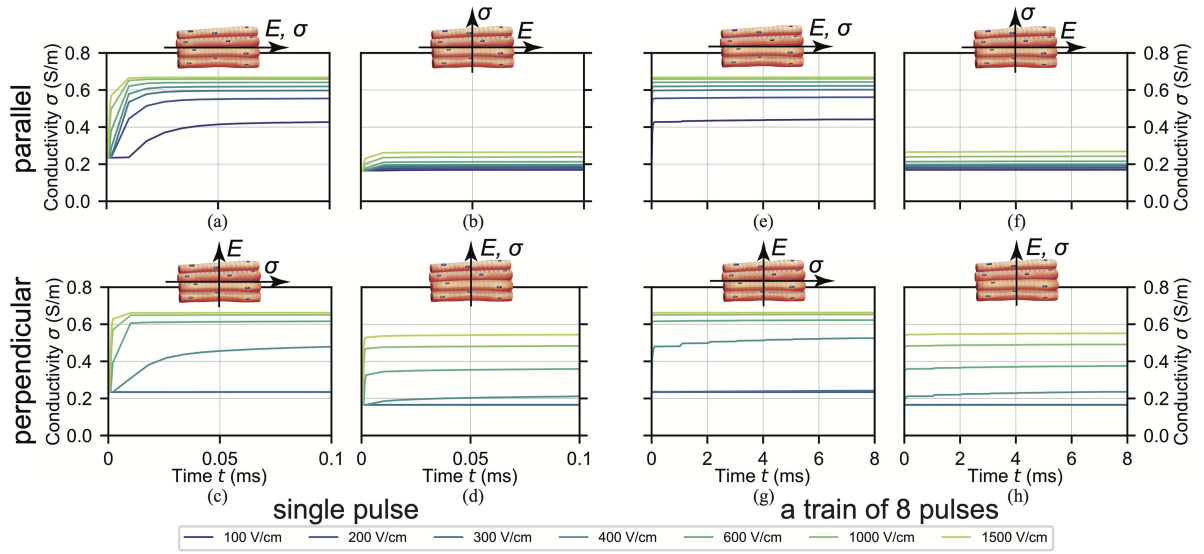


Fig. 3. Conductivity at the cell-level during electroporation, calculated by using the unit-cell approach. The results are shown for a single 100 μ s pulse in (a)–(d), and for a train of eight 100 μ s long pulses with a pulse repetition rate of 1000 s^{-1} in (e)–(h), for different values of the applied electric field. In (a), (b), (e), and (f) the electric field was applied in direction parallel with respect to the direction of the long axis of the muscle cell (parallel orientation), and in (c), (d), (g), and (h) in direction perpendicular with respect to the direction of the long axis of the muscle cell (perpendicular orientation). In (a), (c), (e), and (g) the results are shown for conductivity in direction parallel with respect to the direction of the long axis of the muscle cell (parallel conductivity), and in (b), (d), (f), and (h) for conductivity in direction perpendicular with respect to the direction of the long axis of the muscle cell (perpendicular conductivity). Note the different time scales in (a)–(d) and (e)–(h).

distribution in and around the cell, is then fed into a bulk model of tissue where the electrodes are modelled (as needle electrodes) and the bulk tissue properties used to calculate the electric field distribution in bulk tissue.

C. Bulk Tissue Numerical Model

The bulk tissue model of the skeletal muscle, used for the calculations of the distribution of the electric field during the delivery of the electroporation pulses was built in Comsol Multiphysics v6.0 (Comsol Inc., Sweden). The geometric representation of the skeletal muscle tissue in the model was a cuboid with dimensions of 40 mm \times 40 mm \times 10 mm, with the muscle fibres assumed to be aligned along the x -axis in the model. Two needle electrodes with the same dimensions as used in the experiments (i.e., diameter of 0.70 mm, insertion length in the tissue of 7 mm, and the centre-to-centre distance between the two electrodes of 8.0 mm) were added to the model. In each simulation, the direction of the applied electric field with respect to the muscle fibres was the same as it was in each experiment. In the model we used the Electric Current physics interface with a time domain study.

Based on the results of the single-cell model, shown in Fig. 3, we defined interpolation functions of electrical conductivity for use in our bulk tissue model. We used sequential linear interpolation. We defined four interpolation functions: two for the case when the electric field is applied in direction parallel with respect to the direction of the muscle fibres (parallel orientation), and

two for the case when the electric field is applied in direction perpendicular with respect to the direction of the muscle fibres (perpendicular orientation). For each of these two cases, we defined one function for the conductivity in direction parallel with respect to the direction of the muscle fibres (parallel conductivity), and another function for the conductivity in direction perpendicular with respect to the direction of the muscle fibres (perpendicular conductivity) – all four functions are shown in Fig. 4 for a single 100 μ s pulse. In this way, we have included electrical conductivity in the model as a function of time and also as a function of the distribution of the magnitude of the electric field. However, since the distribution of the electric field in the bulk tissue model is also a function of space, this means the conductivity in our bulk tissue model is defined as a function of time and also as a function of space, separately for the value of the conductivity in direction parallel with respect to the direction of the muscle fibres, and for the value of the conductivity in direction perpendicular with respect to the direction of the muscle fibres.

The four conductivity functions defined above can be used for the case when the electric field is applied in direction either exactly parallel or exactly perpendicular with respect to the direction of the muscle fibres. However, for an arbitrary orientation of the applied electric field φ with respect to the direction of the muscle fibres (see Fig. 4(e) for a schematic representation of φ with respect to the muscle fibres), we need to define additional functions by combining the above defined four. To define the electrical conductivity in direction parallel with respect to the

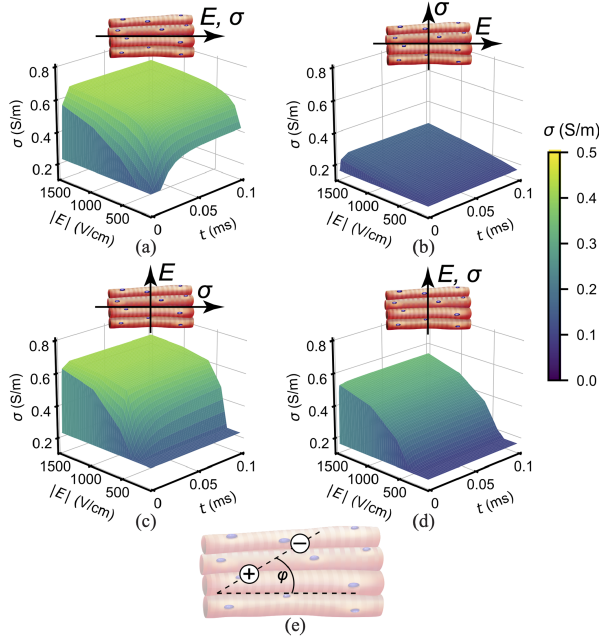


Fig. 4. Conductivity as a function of time and the magnitude of the electric field, in different directions with respect to the muscle fibres, used in the bulk-tissue model. The functions were defined by using the results of the unit-cell model (Fig. 3) and sequential linear interpolation. For clarity, the functions are only shown for the first pulse. In (a) and (b) the direction of the applied electric field was parallel with respect to the direction of the muscle fibres (parallel orientation), and in (c) and (d) perpendicular with respect to the direction of the muscle fibres (perpendicular orientation). In (a) and (c) the functions for the conductivity in direction parallel with respect to the direction of the muscle fibres are shown (parallel conductivity), and in (b) and (d) the functions for the conductivity in direction perpendicular with respect to the direction of the muscle fibres (perpendicular conductivity). A schematic representation of the orientation of the electrodes with respect to the direction of the muscle fibres is given in (e).

direction of the muscle fibres, we used (2):

$$\sigma_{\parallel}^{\varphi} = \sigma_{\parallel} \cdot \cos^2 \varphi + \sigma_{\perp} \cdot \sin^2 \varphi, \quad (2)$$

and to define the electrical conductivity in direction perpendicular with respect to the direction of the muscle fibres, we used (3):

$$\sigma_{\perp}^{\varphi} = \sigma_{\perp} \cdot \cos^2 \varphi + \sigma_{\parallel} \cdot \sin^2 \varphi, \quad (3)$$

wherein the subscript index indicates the direction of the applied electric field with respect to the direction of the muscle fibres, the superscript index indicates the direction of conductivity with respect to the direction of the muscle fibres, and the superscript φ indicates the case when the electric field is applied in an arbitrary orientation φ [Fig. 4(e)] with respect to the direction of the muscle fibres. We used the bulk tissue model described above to calculate the spatio-temporal distribution of the electric field in the tissue for each experiment. To reduce the computational cost, we used only a single train of eight 100 μ s long pulses in our simulations, as the results in Fig. 3 show that the calculated conductivity reaches a plateau during the first pulse train for all values of the electric field.

D. Irreversible Electroporation Threshold Determination

On each image of the lesion obtained from the *in vivo* experiments, we marked four pixels: two representing the location of the two needle electrodes and the other two defining the direction of the muscle fibres. We used these markings to determine the actual orientation of the electrodes with respect to the muscle fibres φ , and to manipulate the images so that they could later be compared with each other and also be compared with the calculated electric field distributions. We magnified and rotated each image so that the electrode locations were always at the same coordinates: $(-4.0 \text{ mm}, 0)$ and $(4.0 \text{ mm}, 0)$, since the centre-to-centre distance between the two electrodes is 8.0 mm. We then used our bulk tissue model to calculate the time-dependent electric field distribution in the muscle tissue for a single train of 8 pulses with a pulse width of 100 μ s and a pulse delivery rate of 1000 s^{-1} . We performed the same number of *in silico* simulations as was the number of the *in vivo* experiments: in each of the simulations, we used the actual orientation of the electrodes with respect to the muscle fibres φ as determined from the lesion images, and used the same voltage as in the experiments. For each simulation, we generated contour images of the electric field distribution at the end of the 8th pulse in the same manner as the lesion images (i.e., with the electrode positions at the same coordinates). We generated a separate image for each value of the electric field. We chose range of values from 100 V/cm to 350 V/cm to ensure that the irreversible threshold value was within expected range and used a step size of 1 V/cm. To determine the value of the irreversible threshold of electroporation for each of the experiments performed, we calculated the Sørensen-Dice similarity coefficient for each of the generated contour images using the following equation [66]:

$$DSC = \frac{2|X \cap Y_i|}{|X| + |Y_i|}, \quad (4)$$

where X is the actual lesion image and Y_i is the i^{th} calculated contour image. We chose the value of the electric field from the contour image that had the highest Sørensen-Dice similarity coefficient with the actual lesion image from one of the experiments as the value of the irreversible threshold of electroporation for that particular experiment. For calculations of Sørensen-Dice similarity coefficients we used Matlab R2022a (MathWorks, USA). The flowchart of the methodology of the present study is shown in Fig. S1 in the Supplementary Materials.

III. RESULTS AND DISCUSSION

Electric pulses delivered *in vivo* in parallel or perpendicular orientation with respect to the direction of the muscle fibres yielded markedly different lesions both in size and shape (Fig. 5, Table I). The lesions from the parallel orientation group were consistently smaller than the lesions from the perpendicular orientation group at each of the voltages used [Fig. 5(c)]. This also applies to the lesion width [dimension n in Fig. 5(e)], but not to the lesion length [dimension m in Fig. 5(d)]. We were able to distinguish between two very characteristic and morphologically disparate lesion types when the field is delivered in direction parallel to the muscle fibres [Figs. 5(a), 6(a–d)] as opposed to

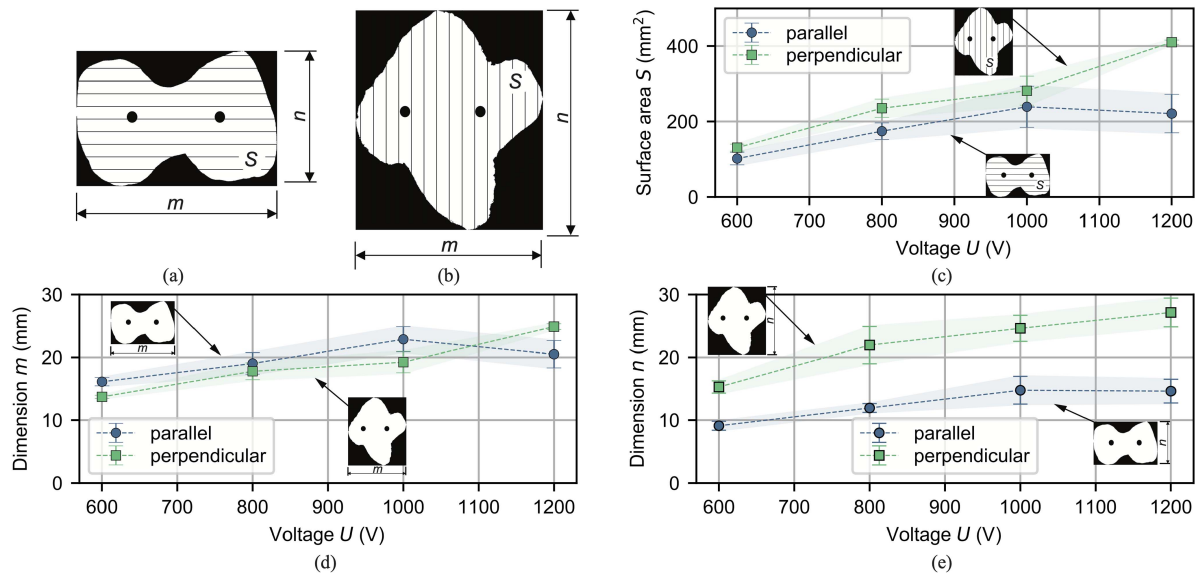


Fig. 5. Comparison of the surface area S and the dimensions m and n of parallel (i.e., the electric field was applied in direction parallel with respect to the direction of the muscle fibres) and perpendicular (i.e., the electric field was applied in direction perpendicular with respect to the direction of the muscle fibres) lesions. The explanation of the symbols S , m , and n is shown schematically in (a) for an example of a parallel lesion, and in (b) for an example of a perpendicular lesion. In (c), (d) and (e) the comparisons of the surface S , the dimension m , and the dimension n for parallel and perpendicular lesions are given, respectively. Error bars represent mean value \pm standard deviation.

TABLE I
VOLTAGE, ORIENTATION OF THE ELECTRODES WITH RESPECT TO THE MUSCLE FIBRES, DETERMINED VALUE OF THE IRREVERSIBLE ELECTROPORATION THRESHOLD WITH CORRESPONDING CALCULATED SORESENSEN-DICE SIMILARITY COEFFICIENT, DIMENSIONS OF THE LESIONS, AND CALCULATED AND MEASURED ELECTRIC CURRENT AT THE END OF THE 8TH PULSE OF THE 1ST TRAIN FOR EACH OF THE EXPERIMENTS PERFORMED

	U (V)	φ (°)	$E_{i,irrev}$ (V/cm)	DSC (/)	S (mm ²)	m (mm)	n (mm)	I_{calc} (A)	I_{meas} (A)
parallel orientation	600	5.02	214	0.82	110.61	15.54	9.58	1.97	3.09
	600	10.93	252	0.82	82.08	16.84	8.28	1.96	3.12
	600	12.45	206	0.91	111.58	16.00	9.46	1.95	3.77
	800	0.31	175	0.88	171.99	20.30	11.14	2.69	4.15
	800	2.23	132	0.83	185.60	20.08	12.66	2.69	3.92
	800	2.34	157	0.87	191.10	19.28	12.14	2.69	/
	800	3.23	162	0.89	185.47	19.46	12.50	2.69	5.28
	800	10.90	215	0.81	137.03	16.08	11.26	2.68	7.68
	1000	0.55	134	0.90	282.60	24.84	14.68	3.41	/
	1000	0.81	185	0.82	184.06	22.60	12.04	3.41	3.85
	1000	1.99	175	0.81	206.87	23.60	13.52	3.41	5.65
	1000	4.42	130	0.88	280.71	23.48	17.20	3.41	/
	1000	8.10	134	0.89	300.70	23.60	17.60	3.41	/
	1000	29.72	267	0.88	180.05	19.06	13.54	3.41	11.70
	1200	0.51	168	0.91	263.32	22.94	14.76	4.13	/
	1200	1.54	156	0.83	271.55	21.78	16.80	4.13	7.46
perpendicular orientation	1200	1.67	194	0.86	233.52	21.01	15.52	4.13	/
	1200	4.58	291	0.87	153.33	17.38	11.68	4.13	/
	1200	9.39	258	0.86	183.47	19.38	14.38	4.13	5.66
	600	68.65	247	0.86	124.21	13.94	15.06	1.81	2.36
	600	80.04	242	0.87	125.81	13.44	14.44	1.80	2.99
	600	82.41	197	0.87	141.17	13.78	16.36	1.80	2.36
	800	74.67	222	0.91	207.50	17.14	18.58	2.70	3.78
	800	75.40	171	0.90	247.28	16.90	24.10	2.70	3.55
	800	85.22	175	0.90	251.16	19.34	23.16	2.70	7.47
	1000	72.52	185	0.86	254.74	17.34	25.34	3.60	4.76
	1000	74.28	170	0.92	319.73	20.40	25.96	3.61	8.35
	1000	82.54	178	0.91	309.14	20.92	25.62	3.63	5.76
	1000	88.70	236	0.89	243.25	18.32	21.52	3.64	4.42
	1200	78.31	182	0.88	406.05	24.56	28.76	4.55	6.12
	1200	88.28	186	0.89	414.10	25.20	25.52	4.58	7.03

perpendicular [Figs. 5(b), 6(e-h)]. The orientation we refer to as parallel results in what has been previously observed [61] and is the typical, expected shape of a two-needle electrode delivery reversible/irreversible electroporation area in electrically homogeneous (i.e. isotropic) material [50] [Fig. 6(a-d)]. Quite differently to the parallel, in the perpendicular direction of electric field with respect to the direction of muscle fibres, the irreversibly damaged area extends far out and away from the line connecting the electrodes, and this extension seems to be most prominent along the plane bisecting the line connecting the two electrodes [Fig. 6(e-h)]. This may seem counter-intuitive, since the electric field right in the middle between the two electrodes is normally the lowest (for parallel orientation or in homogeneous, isotropic tissue [50]), however, the strong anisotropy in tissue electrical conductivity seems to result in the electric field strongly extending into this central plane between the electrodes.

As outlined in the Materials and Methods section, the multi-scale approach allows for calculating both the initial as well as electric field strength-dependent muscle tissue conductivity in both the parallel to fibres and perpendicular to fibres orientation (both of which then need to be further analysed with respect to the direction in which the electric field is being generated). This is given in brief by (2) and (3), and by interpolating the electric field-dependent conductivity evolution curves as given in Fig. 4, we can determine (simulate) the electric field strength distribution (and current density, if desired) for an arbitrary placement of electrodes in tissue and an arbitrary voltage applied to the electrodes. This is possible as long as the pulse protocol

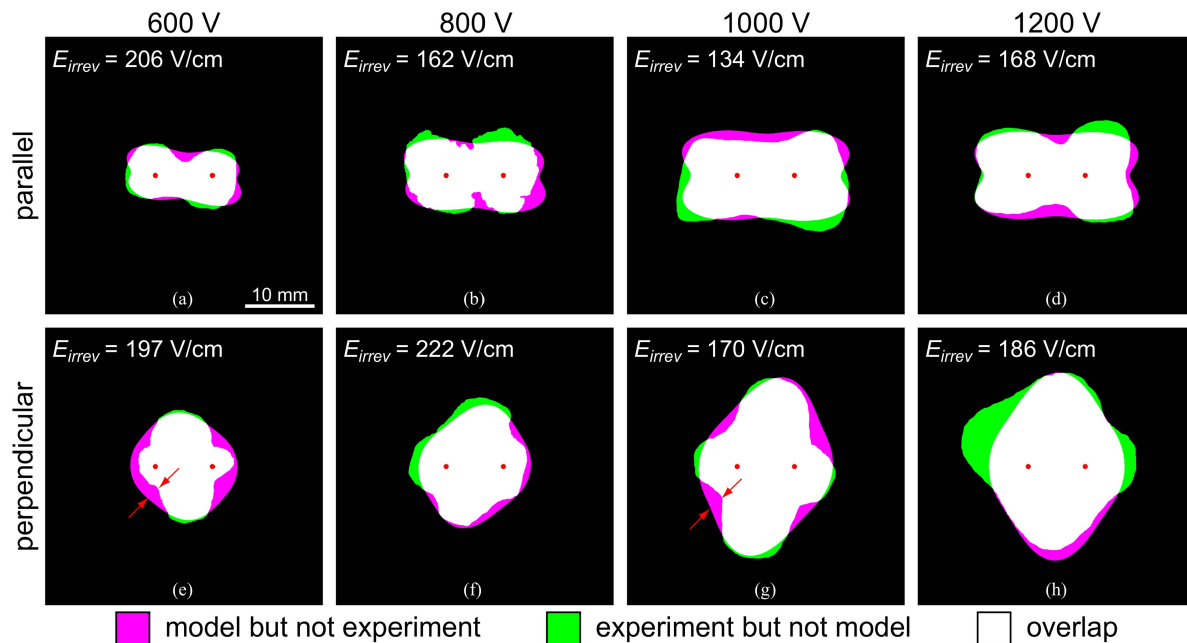


Fig. 6. Comparison of the experimentally-obtained lesions with the results of the numerical model. One sample is shown for each experimental group; parallel orientation (i.e., the electric field was applied in direction parallel with respect to the direction of the muscle fibres) in (a) – (d), and perpendicular orientation (i.e., the electric field was applied in direction perpendicular with respect to the direction of the muscle fibres) in (e) – (h); the voltage used in the experiments was 600 V in (a) and (e), 800 V in (b) and (f), 1000 V in (c) and (g), and 1200 V in (d) and (h). The value of determined irreversible threshold is given for each sample presented. The arrows mark the discrepancy in the morphology of the calculated as compared to the experimentally determined lesion shape.

that is simulated matches that for which the evolution of conductivity was calculated (see Fig. 3). The resulting calculated electric field distribution can be compared to the appropriately oriented and magnified lesion image, and using an appropriate surface matching algorithm, we can determine the field strength value for which the calculated lesion shape best matches the experimental one. We refer to this process as thresholding in continuation. In Fig. 6 and Table I, we present the results of thresholding for eight representative lesions with their optimally matched calculated electric field thresholds. We can observe that the shape of the calculated distribution closely matches experimentally obtained lesion shape.

There is however some discrepancy in the morphology of the calculated as compared to the experimentally determined lesion shape that our model cannot explain through merely modelling electric field distribution, and we attribute this discrepancy to a yet unidentified mechanism or phenomenon related to either complex muscle anatomy, or cell death, or the damaged cell staining mechanism. This discrepancy is most obvious in Fig. 6(e) and (g) (marked with red arrows), where we can observe a rather sharp change in continuity of the lesion edge in several places along the lesion's circumference.

The comparison between experimentally determined lesions and calculated electric field distributions allows us to determine the effective irreversible electroporation field strength threshold for this particular muscle and pulse protocol. Results are given in Fig. 7 and Table I. According to the theory of electroporation [3],

this irreversible threshold should not depend on the voltage applied to the electrodes. Indeed, Fig. 7(c) clearly demonstrates that the determined field strength threshold is independent of the applied voltage on the electrodes be it either 600, 800, 1000 or 1200 V, with an average value of 193.4 V/cm and a standard deviation of 42.1 V/cm [Fig. 7(a)]. This scatter may seem large, however, in view of the enormous number of variables difficult to control for in the *in vivo* experiments, this is perhaps surprisingly small (the coefficient of variation is 21.8 %). Moreover, there is no statistically significant difference in the average threshold if comparing parallel and perpendicular orientation of applied electric field with respect to the direction of the muscle fibres [Fig. 7(b)]. This is in line with theoretical expectation, as we do not expect the orientation to influence the sensitivity of the cell to electroporation-induced damage and its capability of recovery following electroporation. The different lesion shape (and size!) that can be observed between the parallel and perpendicular orientation can thus be explained largely by the difference in distribution of the electric field (and current density) during pulse delivery as resulting from anisotropy in electrical conductivity, without resort to introduction of additional complexity such as orientation-dependent irreversible electroporation threshold. The determined value of the irreversible electroporation threshold of 193.4 V/cm is much lower than the one reported previously (i.e. 450 V/cm in [29]). This is not surprising since we used a much higher number of pulses (48 compared to 8), knowing that membrane electroporation depends on the number of pulses

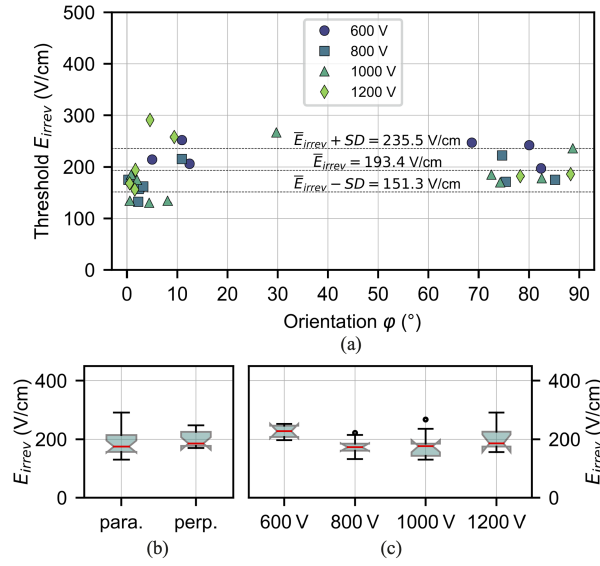


Fig. 7. (a) The determined values of the irreversible threshold of each experiment (E_{irrev}) plotted against the orientation of the electrodes with respect to the direction of the muscle fibres (ϕ), with marked mean value of the threshold with standard deviation. (b) The result of the one-way ANOVA test for the data from (a) divided into two groups, the parallel and the perpendicular. The result of the one-way ANOVA test shows no statistically significant difference in the threshold for the two groups. The p -value of the test is 0.55. (c) The result of the one-way ANOVA test for the data from (a) divided into four groups, 600 V, 800 V, 1000 V, and 1200 V. The result of the one-way ANOVA test shows no statistically significant difference in the threshold for the four groups. The p -value of the test is 0.08.

applied [67]. In addition, the experimental conditions differed considerably (e.g. type of electrodes, pulse repetition rate).

In Fig. 8 we present the anisotropy ratio, that is the ratio between the conductivity in direction parallel with respect to the direction of the muscle fibres and the conductivity in direction perpendicular with respect to the direction of the muscle fibres, as a function of the elongation of the cell, or more precisely, of the cell diameter (fixed) as opposed to its length (varied) at the end of the 8th pulse of the first train. By presenting this analysis/dependence we wish to justify the particular r_{short} -to- r_{long} cell dimension ratio that we chose and used for all the simulations of conductivity evolution, i.e. 1:6.7, as representing a sufficiently anisotropic cell geometry (in other words, a sufficiently long cell to represent a unit of muscle fibre from the electrical conductivity perspective) that does result in an appropriate degree of anisotropy of bulk muscle, facilitating the subsequent lesion shape analysis and thresholding processes. Fig. 8 illustrates that elongating the cell further, to ratios of 1:10 or 1:20, does not significantly impact the conductivity anisotropy ratio at the end of the 8th (i.e. the last) pulse in the train.

We also analysed the impact of varying the volume fraction and the elongation of the unit-cell on the initial, pre-electroporation conductivity of tissue in both parallel and perpendicular direction with respect to the direction of the long axis of the muscle fibre. Results of this analysis are given in Fig. S4 in the Supplementary Materials. While the dependence on volume

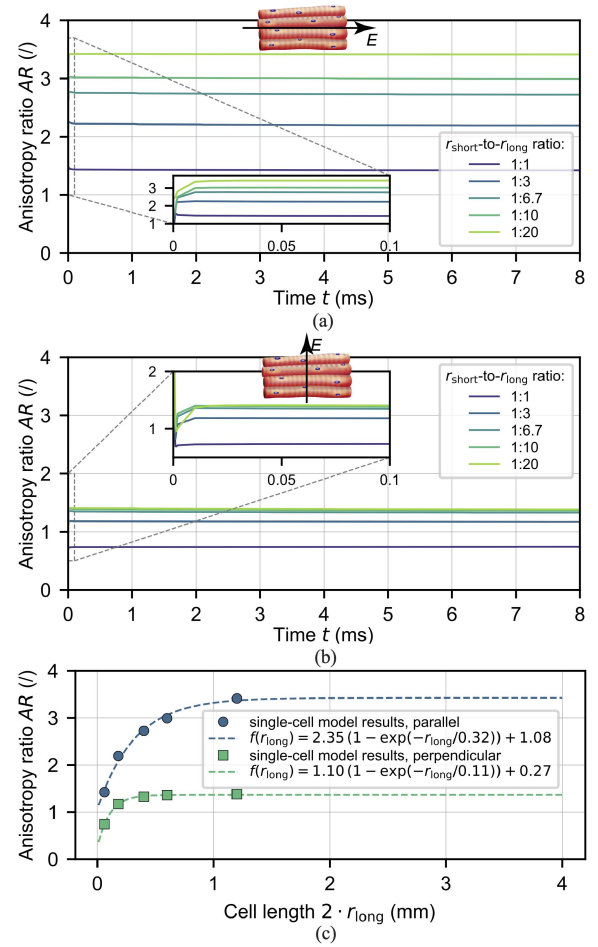


Fig. 8. The effect of the geometry of the cell (r_{short} -to- r_{long} ratio), used in the unit-cell model, on the calculated anisotropy ratio (defined as $AR = \sigma_{||}/\sigma_{\perp}$). The results are shown for a train of eight 100 μ s long pulses with a pulse delivery rate of 1000 s^{-1} . The magnitude of the applied electric field was 1000 V/cm. In (a) the electric field was applied in direction parallel with respect to the direction of the long axis of the muscle cell (parallel orientation), and in (b) in direction perpendicular with respect to the direction of the long axis of the muscle cell (perpendicular orientation). The insets show the anisotropy ratio during the first pulse. In (c), the unit-cell model results of anisotropy ratio at the end of the 8th pulse for the parallel and the perpendicular orientation are given, together with the result of fitting an exponential function ($f(r_{long}) = a(1 - \exp(-r_{long}/b)) + c$) of r_{long} to the unit-cell model results of anisotropy ratio.

fraction is of negligible importance (Fig. S4b), the same cannot be said of the geometrical diameter-to-length ratio of the unit cell (Fig. S4a).

Fig. 9 shows the number of pores formed on 1/8 of the muscle cell membrane as calculated with the unit cell model. At electric field values below 400 V/cm, more pores are formed when the electric field is applied in direction parallel to the muscle fibres than when it is applied in direction perpendicular to them, whereas at field values above 400 V/cm, more pores are formed in perpendicular orientation, which may explain

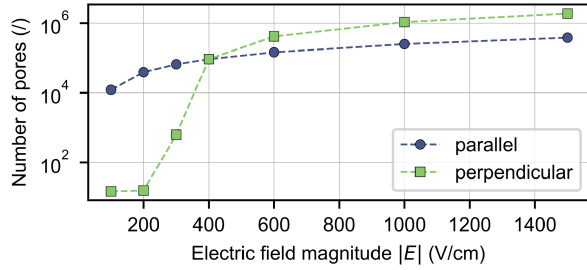


Fig. 9. Number of pores on 1/8 of the muscle cell membrane, as calculated with the unit-cell model for the parallel and the perpendicular orientation of the applied electric field with respect to the direction of the long axis of the muscle cell.

different orientation sensitivity reported in the literature [36], [37].

The calculated values of electric current ranged from 1.97 A to 4.58 A, while the measured currents (of the first pulse train) ranged from 3.09 A to 11.70 A (all values are listed in Table I). The measured currents were consistently higher than the calculated ones. This may be due to unaccounted for phenomena related to high-voltage pulse delivery to *in vivo* animal tissue, which is far more complex than a mere assembly of unit cells [68]. The mean values of the measured electric current for each applied voltage are shown graphically in Fig. S5 in the Supplementary Materials. In spite of large scatter of measured currents – which is not surprising – higher voltages applied resulted in larger currents measured. When comparing the current of the first pulse in different trains, there is no statistically significant difference between the current values at all voltages, which allowed us to model only one train of pulses, rather than six delivered experimentally, to reduce computational cost.

Through comparison of model results and *in vivo* experimental results, we believe to have successfully demonstrated the power of this approach in explaining especially the particular lesion shape that results from the highly geometrically asymmetrical muscle cell and consequential anisotropic properties of muscle tissue. Our study's main results include the determination of the field strength threshold required for irreversible electroporation of porcine skeletal muscle cells using the specific pulse protocol that was used, and the finding that the field-to-fibre orientation does not seem to affect the irreversible field strength threshold. We have thus successfully demonstrated that it is not the susceptibility of individual cells to damage caused by the magnitude of the electric field strength, but rather the anisotropic electric properties of tissue that result in the disparately shaped lesions whose shape strongly depends on field-to-fibre orientation.

The reader should beware our study concerns a single type of tissue, i.e., the porcine *vastus lateralis* skeletal muscle, and was performed in both the numerical as well as experimental part employing a specific electroporation (pulse) protocol. The obtained threshold in both magnitude and its non-dependence on field-to-fibre orientation must be interpreted in this light. Changing the muscle tissue type (e.g. cardiac muscle) or pulse

protocol (e.g. pulse length, repetition rate, number, etc.) will most likely result in different thresholds and necessitates a repeat of the numerical study, with, ideally, a validation in form of experimental *in vivo* work. Furthermore, the calculated temporal evolution of conductivity during electroporation, calculated using the unit cell approach (Fig. 3), does not show the immediate drop in conductivity after the pulse that was observed in the experiments [69]. The reason for this shortcoming is that our unit-cell model is based on the models of Huclova et al. [46], and does not account for all the dynamics of recovery in conductivity. We were therefore unable to account for the immediate drop in conductivity after the pulse in the current developmental phase of our multiscale model.

We would also like to emphasise that in our study we used the values for intracellular (0.55 S/m) and extracellular (1.2 S/m) conductivity at the upper end of the ranges available in the literature. We chose these values to achieve comparable currents in the numerical electrical model to those observed *in vivo*. However, we also performed a parametric study in which we modelled with lower conductivity values; as low as 0.3 S/m for intracellular and 1.0 S/m for extracellular conductivity. We found that the impact on the main result of the study (i.e., the determined irreversible electric field strength threshold) was negligible. The threshold values for lower conductivity values differed no more than 5 % from the values obtained using the higher conductivity (i.e., 0.55 and 1.2 S/m). In absolute numbers, this means the average value when using lower conductivity resulted in a change in the irreversible threshold from 193.4 to 197.7 V/cm. Moreover, we can offer some theoretical support for the use of the higher-conductivity values for the extracellular space with negligible consequences on the calculated field strength thresholds by reasoning that the extracellular conductivity is of significant importance only when close to the tissue conductivity, i.e., when the tissue / cell suspension consists of only a few cells. This was extensively studied and demonstrated, for instance, in [70], where the authors compared the results of the FEM simulations with the analytical results of Maxwell, Rayleigh, Tobias, and Bruggeman. Their results of normalised effective conductivity versus the volume fraction (Fig. 5 in the aforementioned study) show that the effective conductivity at a cell volume fraction of 0 (where there are no cells in the medium) is equal to the extracellular conductivity, and then steadily decreases with increasing cell volume fraction. The effective (bulk tissue) conductivity amounts to only about 20 % of the extracellular conductivity at a cell volume fraction of cells of 0.76, which is the volume fraction used in our study. Thus, at a relatively high-volume fraction of 0.76, the intracellular conductivity has a much stronger influence of the bulk tissue conductivity as does the extracellular; meaning that even if we had overestimated the extracellular conductivity, the impact of such an overestimation should not be critical to the validity of the model-based data and derived conclusions.

IV. CONCLUSION

This paper presents a fresh attempt at implementing the very first steps in building a comprehensive model of electroporated

skeletal muscle tissue by accounting for its anisotropy. We chose the ground-up multiscale approach to the study of macroscopic conductivity and its changes due to electroporation, whereby we try to deduce electrical properties and irreversible damage observed at the macroscale based on properties of single elongated muscle cells and their behaviour under exposure to electric field.

While we cannot – at this stage of development – claim the model is all-embracing and complete, as there are indications that unaccounted for phenomena and mechanisms exists that need to be either further elucidated and explained, and then included as co-factors into the model (e.g. the dynamics of current, mechanisms of cell death, etc.), we nevertheless believe it has the capability of serving as the basic proof of concept for this particular multiscale approach, and thus strongly warrants and invites further validation, exploration, elaboration, and consequentially exploitation.

ACKNOWLEDGMENT

RŠ, SMK, JDČ and DM would like to thank their colleague Bor Kos for his help with the image processing algorithm/code.

REFERENCES

- [1] E. Neumann and K. Rosenheck, "Permeability changes induced by electric impulses in vesicular membranes," *J. Membrane Biol.*, vol. 10, no. 1, pp. 279–290, Dec. 1972.
- [2] T. Kotnik, G. Pucihar, and D. Miklavčič, "The cell in the electric field," in *Clinical Aspects of Electroporation*, S. T. Kee, J. Gehl, and E. W. Lee, Eds. Berlin, Germany: Springer, 2011, pp. 19–29.
- [3] T. Kotnik et al., "Membrane electroporation and electroporation: Mechanisms and models," *Annu. Rev. Biophys.*, vol. 48, no. 1, pp. 63–91, May 2019.
- [4] S. Haberl et al., "Cell membrane electroporation-Part 2: The applications," *IEEE Elect. Insul. Mag.*, vol. 29, no. 1, pp. 29–37, Jan./Feb. 2013.
- [5] M. L. Yarmush et al., "Electroporation-based technologies for medicine: Principles, applications, and challenges," *Annu. Rev. Biomed. Eng.*, vol. 16, no. 1, pp. 295–320, Jul. 2014.
- [6] T. Kotnik et al., "Electroporation-based applications in biotechnology," *Trends Biotechnol.*, vol. 33, no. 8, pp. 480–488, Aug. 2015.
- [7] S. Mahnič-Kalamiza, E. Vorobiev, and D. Miklavčič, "Electroporation in food processing and biorefinery," *J. Membrane Biol.*, vol. 247, no. 12, pp. 1279–1304, Dec. 2014.
- [8] B. Geboers et al., "High-Voltage electrical pulses in oncology: Irreversible electroporation, electrochemotherapy, gene electrotransfer, electrofusion, and electroimmunotherapy," *Radiology*, vol. 295, no. 2, pp. 254–272, 2020.
- [9] G. Saldaña et al., "Microbiological aspects related to the feasibility of PEF technology for food pasteurization," *Crit. Rev. Food Sci. Nutr.*, vol. 54, no. 11, pp. 1415–1426, Nov. 2014.
- [10] A. Sugrue et al., "Irreversible electroporation for catheter-based cardiac ablation: A systematic review of the preclinical experience," *J. Interventional Cardiac Electrophysiol.*, vol. 55, no. 3, pp. 251–265, Sep. 2019.
- [11] S. Sachdev et al., "Revisiting the role of pulsed electric fields in overcoming the barriers to in vivo gene electrotransfer," *Bioelectrochemistry*, vol. 144, Apr. 2022, Art. no. 107994.
- [12] L. M. Mir et al., "High-efficiency gene transfer into skeletal muscle mediated by electric pulses," *Proc. Nat. Acad. Sci.*, vol. 96, no. 8, pp. 4262–4267, Apr. 1999.
- [13] E. Sokołowska and A. U. Błachnio-Zabielska, "A critical review of electroporation as a plasmid delivery system in mouse skeletal muscle," *Int. J. Mol. Sci.*, vol. 20, no. 11, Jun. 2019, Art. no. 2776.
- [14] R. Heller and L. C. Heller, "Gene electrotransfer clinical trials," in *Advances in Genetics*, vol. 89. New York, NY, USA: Elsevier, 2015, pp. 235–262.
- [15] M. T. Stewart et al., "Intracardiac pulsed field ablation: Proof of feasibility in a chronic porcine model," *Heart Rhythm*, vol. 16, no. 5, pp. 754–764, May 2019.
- [16] V. Y. Reddy et al., "Pulsed field ablation for pulmonary vein isolation in atrial fibrillation," *J. Amer. College Cardiol.*, vol. 74, no. 3, pp. 315–326, Jul. 2019.
- [17] F. D. Ramirez et al., "Emerging technologies for pulmonary vein isolation," *Circulation Res.*, vol. 127, no. 1, pp. 170–183, Jun. 2020.
- [18] A. Verma et al., "First-in-human experience and acute procedural outcomes using a novel pulsed field ablation system: The PULSED AF pilot trial," *Circulation: Arrhythmia Electrophysiol.*, vol. 15, no. 1, Jan. 2022, Art. no. e010168.
- [19] S. Čorović et al., "The influence of skeletal muscle anisotropy on electroporation: In vivo study and numerical modeling," *Med. Biol. Eng. Comput.*, vol. 48, no. 7, pp. 637–648, Jul. 2010.
- [20] A. Suzuki et al., "Impact of myocardial fiber orientation on lesions created by a novel heated saline-enhanced radiofrequency needle-tip catheter: An MRI lesion validation study," *Heart Rhythm: Official J. Heart Rhythm Soc.*, vol. 18, no. 3, pp. 443–452, 2021.
- [21] L. Zang et al., "Effect of anisotropic electrical conductivity induced by fiber orientation on ablation characteristics of pulsed field ablation in atrial fibrillation treatment: A computational study," *J. Cardiovasc. Develop. Dis.*, vol. 9, no. 10, Sep. 2022, Art. no. 319.
- [22] B. R. Epstein and K. R. Foster, "Anisotropy in the dielectric properties of skeletal muscle," *Med. Biol. Eng. Comput.*, vol. 21, no. 1, pp. 51–55, Jan. 1983.
- [23] K. R. Foster and H. P. Schwan, "Dielectric properties of tissues and biological materials: A critical review," *Crit. Rev. Biomed. Eng.*, vol. 17, no. 1, pp. 25–104, 1989.
- [24] C. Gabriel, S. Gabriel, and E. Corthout, "The dielectric properties of biological tissues: I. literature survey," *Phys. Med. Biol.*, vol. 41, no. 11, pp. 2231–2249, Nov. 1996.
- [25] S. Gabriel, R. W. Lau, and C. Gabriel, "The dielectric properties of biological tissues: II. measurements in the frequency range 10 Hz to 20 GHz," *Phys. Med. Biol.*, vol. 41, no. 11, pp. 2251–2269, Nov. 1996.
- [26] S. Gabriel, R. W. Lau, and C. Gabriel, "The dielectric properties of biological tissues: III. parametric models for the dielectric spectrum of tissues," *Phys. Med. Biol.*, vol. 41, no. 11, pp. 2271–2293, Nov. 1996.
- [27] B. Karki et al., "Evaluation of a multi-electrode bioimpedance spectroscopy tensor probe to detect the anisotropic conductivity spectra of biological tissues," *Meas. Sci. Technol.*, vol. 25, no. 7, Jul. 2014, Art. no. 075702.
- [28] J.-Z. Tsai et al., "In-vivo measurement of swine myocardial resistivity," *IEEE Trans. Biomed. Eng.*, vol. 49, no. 5, pp. 472–483, May 2002.
- [29] S. Čorović, L. M. Mir, and D. Miklavčič, "In vivo muscle electroporation threshold determination: Realistic numerical models and in vivo experiments," *J. Membrane Biol.*, vol. 245, no. 9, pp. 509–520, Sep. 2012.
- [30] M. E. Mezeme et al., "Assessing how electroporation affects the effective conductivity tensor of biological tissues," *Appl. Phys. Lett.*, vol. 101, no. 21, Nov. 2012, Art. no. 213702.
- [31] B. Gómez et al., "Application of pulsed electric fields in meat and fish processing industries: An overview," *Food Res. Int.*, vol. 123, pp. 95–105, Sep. 2019.
- [32] A. Janositz, J. Semrau, and D. Knorr, "Impact of PEF treatment on quality parameters of white asparagus (*Asparagus officinalis* L.)." *Innov. Food Sci. Emerg. Technol.*, vol. 12, no. 3, pp. 269–274, Jul. 2011.
- [33] P. X. de Oliveira, R. A. Bassani, and J. W. M. Bassani, "Lethal effect of electric fields on isolated ventricular myocytes," *IEEE Trans. Biomed. Eng.*, vol. 55, no. 11, pp. 2635–2642, Nov. 2008.
- [34] B. Valič et al., "Effect of electric field induced transmembrane potential on spheroidal cells: Theory and experiment," *Eur. Biophys. J.*, vol. 32, no. 6, pp. 519–528, Oct. 2003.
- [35] D. W. Hunter et al., "In vitro cell selectivity of reversible and irreversible electroporation in cardiac tissue," *Circulation: Arrhythmia Electrophysiol.*, vol. 14, no. 4, Apr. 2021, Art. no. e008817.
- [36] S. Chaigne et al., "Reversible and irreversible effects of electroporation on contractility and calcium homeostasis in isolated cardiac ventricular myocytes," *Circulation: Arrhythmia Electrophysiol.*, vol. 15, Oct. 2022, Art. no. e011131.
- [37] J. Dermol-Cerne et al., "Short microsecond pulses achieve homogeneous electroporation of elongated biological cells irrespective of their orientation in electric field," *Sci. Rep.*, vol. 10, no. 1, Dec. 2020, Art. no. 9149.
- [38] M. E. Mezeme et al., "A numerical analysis of multicellular environment for modeling tissue electroporation," *Appl. Phys. Lett.*, vol. 100, no. 14, Apr. 2012, Art. no. 143701.

- [39] M. F. Lorenzo et al., "Rapid impedance spectroscopy for monitoring tissue impedance, temperature, and treatment outcome during electroporation-based therapies," *IEEE Trans. Biomed. Eng.*, vol. 68, no. 5, pp. 1536–1546, May 2021.
- [40] M. Pavlin and D. Miklavčič, "The effective conductivity and the induced transmembrane potential in dense cell system exposed to DC and AC electric fields," *IEEE Trans. Plasma Sci.*, vol. 37, no. 1, pp. 99–106, Jan. 2009.
- [41] J. Langus et al., "Dynamic finite-element model for efficient modelling of electric currents in electroporated tissue," *Sci. Rep.*, vol. 6, no. 1, Sep. 2016, Art. no. 26409.
- [42] P. Agger et al., "Anatomically correct assessment of the orientation of the cardiomyocytes using diffusion tensor imaging," *NMR Biomed.*, vol. 33, no. 3, Mar. 2020, Art. no. e4205.
- [43] D. Cukjati et al., "Real time electroporation control for accurate and safe in vivo non-viral gene therapy," *Bioelectrochemistry*, vol. 70, no. 2, pp. 501–507, May 2007.
- [44] S. Čorović et al., "Modeling of electric field distribution in tissues during electroporation," *BioMed. Eng. OnLine*, vol. 12, no. 1, Dec. 2013, Art. no. 16.
- [45] H. Cindric et al., "Numerical mesoscale tissue model of electrochemotherapy in liver based on histological findings," *Sci. Rep.*, vol. 12, no. 1, Dec. 2022, Art. no. 6476.
- [46] S. Huclova, D. Erni, and J. Fröhlich, "Modelling effective dielectric properties of materials containing diverse types of biological cells," *J. Phys. D: Appl. Phys.*, vol. 43, no. 36, Sep. 2010, Art. no. 365405.
- [47] S. Huclova, D. Erni, and J. Fröhlich, "Modelling and validation of dielectric properties of human skin in the MHz region focusing on skin layer morphology and material composition," *J. Phys. D: Appl. Phys.*, vol. 45, no. 2, Jan. 2012, Art. no. 025301.
- [48] S. Huclova and J. Fröhlich, "Towards a realistic dielectric tissue model: A multiscale approach," in *Proc. IEEE Annu. Int. Conf. IEEE Eng. Med. Biol. Soc.*, 2010, pp. 6813–6816.
- [49] J. Dermol-Černe and D. Miklavčič, "From cell to tissue properties—modeling skin electroporation with pore and local transport region formation," *IEEE Trans. Biomed. Eng.*, vol. 65, no. 2, pp. 458–468, Feb. 2018.
- [50] D. Miklavčič et al., "A validated model of in vivo electric field distribution in tissues for electrochemotherapy and for DNA electrotransfer for gene therapy," *Biochimica et Biophysica Acta (BBA) - Gen. Subjects*, vol. 1523, no. 1, pp. 73–83, 2000.
- [51] S. D'Arpa et al., "Variability and reliability of the vastus lateralis muscle anatomy," *Acta Chirurgica Belgica*, vol. 116, no. 4, pp. 203–212, Jul. 2016.
- [52] S. Methenitis et al., "Intramuscular fiber conduction velocity and muscle fascicle length in human vastus lateralis," *Appl. Physiol., Nutr. Metab.*, vol. 44, no. 2, pp. 133–138, 2019.
- [53] V. Tayfur et al., "Anatomy of vastus lateralis muscle flap," *J. Craniofacial Surg.*, vol. 21, no. 6, pp. 1951–1953, Nov. 2010.
- [54] A. Sharifnezhad, R. Marzilger, and A. Arampatzis, "Effects of load magnitude, muscle length and velocity during eccentric chronic loading on the longitudinal growth of vastus lateralis muscle," *J. Exp. Biol.*, vol. 217, pp. 2726–2733, 2014.
- [55] E. C. de Almeida Araujo, "Adaptation of proof of concepts into quantitative NMR methods: Clinical application for the characterization of alterations observed in the skeletal muscle tissue in neuromuscular disorders," Ph.D. dissertation, Université Paris Sud - Paris XI, Paris, France, 2014.
- [56] A. Rehfeld, M. Nylander, and K. Karnov, *Compendium of Histology: A Theoretical and Practical Guide*. Berlin, Germany: Springer, 2017.
- [57] M. C. Fishbein et al., "Early phase acute myocardial infarct size quantification: Validation of the triphenyl tetrazolium chloride tissue enzyme staining technique," *Amer. Heart J.*, vol. 101, no. 5, pp. 593–600, 1981.
- [58] A. Singal et al., "Effects of ablation (radio frequency, cryo, microwave) on physiologic properties of the human vastus lateralis," *IEEE Trans. Biomed. Eng.*, vol. 65, no. 10, pp. 2202–2209, Oct. 2018.
- [59] A. Verma et al., "Assessing the relationship of applied force and ablation duration on lesion size using a diamond tip catheter ablation system," *Circulation: Arrhythmia Electrophysiol.*, vol. 14, 2021, Art. no. e009541.
- [60] F. H. Cornelis et al., "Peri-tumoral metallic implants reduce the efficacy of irreversible electroporation for the ablation of colorectal liver metastases," *CardioVascular Interventional Radiol.*, vol. 43, no. 1, pp. 84–93, Jan. 2020.
- [61] E. Ben-David et al., "Irreversible electroporation: Treatment effect is susceptible to local environment and tissue properties," *Radiology*, vol. 269, no. 3, 2013, Art. no. 738–747.
- [62] J. Gielis, "A generic geometric transformation that unifies a wide range of natural and abstract shapes," *Amer. J. Botany*, vol. 90, no. 3, pp. 333–338, Mar. 2003.
- [63] S. Hindel et al., "Validation of blood volume fraction quantification with 3D gradient echo dynamic contrast-enhanced magnetic resonance imaging in porcine skeletal muscle," *PLoS One*, vol. 12, no. 1, Jan. 2017, Art. no. e0170841.
- [64] T. Kotnik, D. Miklavčič, and T. Slivnik, "Time course of transmembrane voltage induced by time-varying electric fields: a method for theoretical analysis and its application," *Bioelectrochemistry Bioenergetics*, vol. 45, no. 1, pp. 3–16, Mar. 1998.
- [65] L. Rems et al., "Cell electrofusion using nanosecond electric pulses," *Sci. Rep.*, vol. 3, no. 1, Dec. 2013, Art. no. 3382.
- [66] A. Carass et al., "Evaluating white matter lesion segmentations with refined Sørensen-Dice analysis," *Sci. Rep.*, vol. 10, no. 1, Dec. 2020, Art. no. 8242.
- [67] G. Pucihar et al., "Equivalent pulse parameters for electroporation," *IEEE Trans. Biomed. Eng.*, vol. 58, no. 11, pp. 3279–3288, Nov. 2011.
- [68] U. Pliquett et al., "High electrical field effects on cell membranes," *Bioelectrochemistry*, vol. 70, no. 2, pp. 275–282, May 2007.
- [69] A. Ivorra et al., "In vivo electrical conductivity measurements during and after tumor electroporation: Conductivity changes reflect the treatment outcome," *Phys. Med. Biol.*, vol. 54, no. 19, pp. 5949–5963, Oct. 2009.
- [70] M. Pavlin, T. Slivnik, and D. Miklavcic, "Effective conductivity of cell suspensions," *IEEE Trans. Biomed. Eng.*, vol. 49, no. 1, pp. 77–80, Jan. 2002.

Supplementary Materials for

A multiscale computational model of skeletal muscle electroporation validated using *in situ* porcine experiments

Rok Šmerc, David A. Ramirez, Samo Mahnič-Kalamiza, Janja Dermol-Černe, Daniel C. Sigg, Lars M. Mattison, Paul A. Iazzo, Damijan Miklavčič

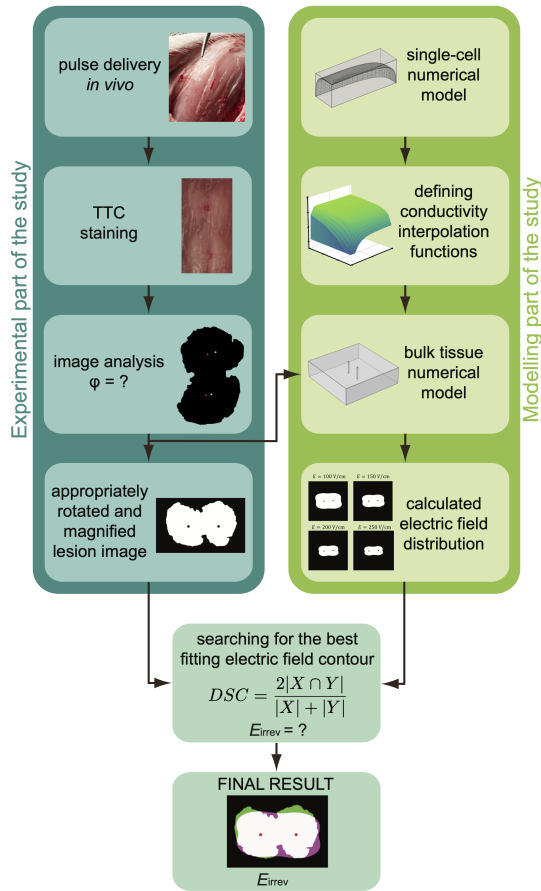


Fig. S1. Flowchart of the methodology of the study presented. The study consisted of two parts. In the experimental part, we delivered electrical pulses to the skeletal muscle tissue of pigs *in vivo*, inserting the needle electrodes in two different orientations with respect to the muscle fibres. We then used TTC staining to determine the shape of the irreversibly ablated region for each experiment. In the numerical part of the study, we built a multiscale numerical model of the skeletal muscle, which we later used to simulate the *in vivo* experiments and determine the irreversible threshold of electroporation for each experiment by comparing the model results to the shape of the experimental lesion.

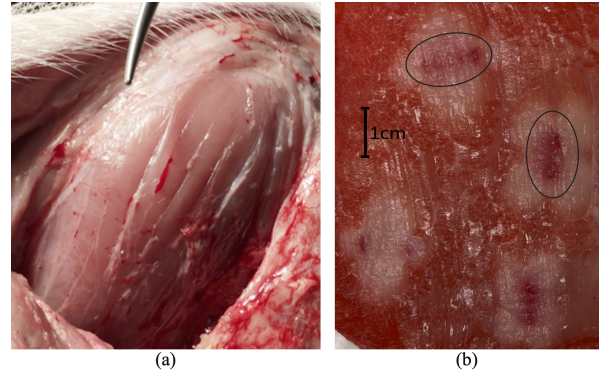


Fig. S2. (a) Exposed porcine *vastus lateralis* tissue. Fibre bundles and fascia delineate orientation. (b) Stained thigh tissue. The light colour indicates ablated tissue. Some evidence of haematoma is observed from the electrode insertion (circled).

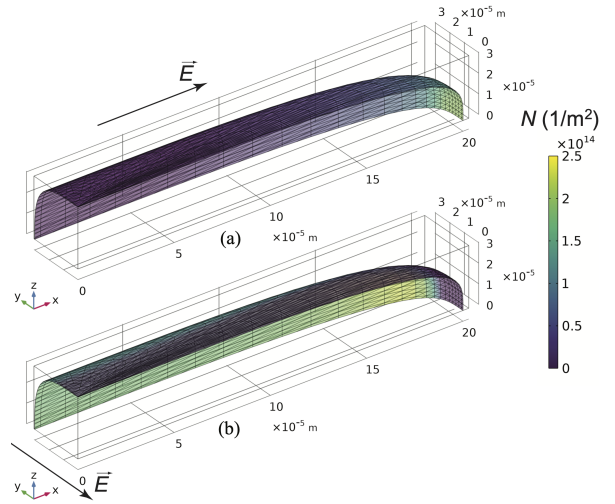


Fig. S3. Pore density distribution at the end of the 8th pulse of the first train. An example for the magnitude of the applied electric field of 1000 V/cm. In (a) the electric field was applied in direction parallel with respect to the direction of the long axis of the muscle cell (parallel orientation), and in (b) in direction perpendicular with respect to the direction of the long axis of the muscle cell (perpendicular orientation).

TABLE S-I

PARAMETERS USED IN THE SINGLE CELL MODEL [R1]–[R3].

Name	Expression	Description
d_m	7 nm	Membrane thickness
ε_i	80	Intracellular permittivity
ε_e	80	Extracellular permittivity
ε_m	5	Membrane permittivity
σ_i	0.55 S/m	Intracellular conductivity
σ_{m0}	$3 \cdot 10^{-7}$ S/m	Initial membrane conductivity
σ_e	1.2 S/m	Extracellular conductivity
r_p	$0.76 \cdot 10^{-9}$ m	Pore radius
α	$10^9 \text{m}^{-2} \text{s}^{-1}$	
U_{ep}	0.258 V	Characteristic voltage of electroporation
N_0	$1.5 \cdot 10^9 \text{m}^{-2}$	Equilibrium pore density when $ITV = 0$ V
q	2.46	Electroporation constant
σ_p	$(\sigma_e - \sigma_i) / \log(\sigma_e / \sigma_i)$	Pore conductivity
r_{long}	200 μm^a	Radius of the muscle cell in x -direction
r_{short}	30 μm , 90 μm , 300 μm , 600 μm^b	Radius of the muscle cell in y - and z -direction
V_{est}	1 V	Voltage, applied for calculation of conductivity
d_x	$1.015 r_{long}$	Depth of the unit cell for 76 % volume fraction
d_y, d_z	$1.015 r_{short}$	Width and height of the unit cell for 76 % volume fraction

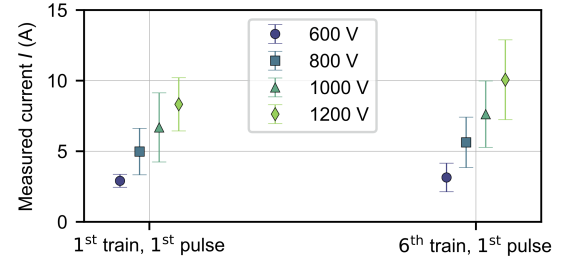
^a For calculations with different electric fields^b For calculations of the effect of geometry

Fig. S5. Mean value of measured electric current during *in vivo* experiments for each applied voltage. Current values were taken at the end of the pulse. Error bars represent mean value \pm standard deviation.

REFERENCES

- [R1] S. Huclova, D. Erni, and J. Fröhlich, “Modelling and validation of dielectric properties of human skin in the MHz region focusing on skin layer morphology and material composition,” *Journal of Physics D: Applied Physics*, vol. 45, no. 2, p. 025301, Jan. 2012.
- [R2] T. Kotnik, D. Miklavčič, and T. Slivnik, “Time course of transmembrane voltage induced by time-varying electric fields—a method for theoretical analysis and its application,” *Bioelectrochemistry and Bioenergetics*, vol. 45, no. 1, pp. 3–16, Mar. 1998.
- [R3] L. Rems, M. Ušaj, M. Kanduđer, M. Reberšek, D. Miklavčič, and G. Pučihar, “Cell electrofusion using nanosecond electric pulses,” *Scientific Reports*, vol. 3, no. 1, p. 3382, Dec. 2013.

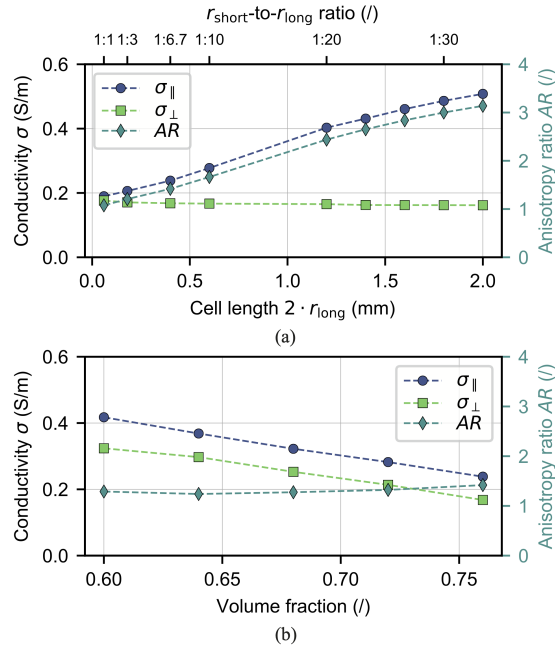


Fig. S4. (a) The effect of the geometry of the cell (r_{short} -to- r_{long} ratio), used in the unit-cell model, on the calculated conductivity and anisotropy ratio (defined as $AR = \sigma_{||} / \sigma_{\perp}$) for non-electroporated cells. (b) The effect of the volume fraction, used in the unit-cell model, on the calculated conductivity and anisotropy ratio for non-electroporated cells.

2.2 Paper 2

Title: **Electrical pathways through the intricate network of skeletal muscle fibres: Insights from MRI-validated numerical modelling**

Authors: **Rok Šmerc**, Marko Stručić, Matej Kranjc, Igor Serša, Damijan Miklavčič, and Samo Mahnič-Kalamiza

Publication: *IEEE Transactions on Biomedical Engineering*, 2025

Impact factor: 4.5 (2024)

Quartile: Q2

Rank: 38/124 (Biomedical engineering)

DOI: <https://doi.org/10.1109/TBME.2025.3572353>

Electrical Pathways Through the Intricate Network of Skeletal Muscle Fibres: Insights From MRI-Validated Numerical Modelling

Rok Šmerc , Marko Stručić , Matej Kranjc , Igor Serša , Damijan Miklavčič ,
and Samo Mahnič-Kalamiza 

Abstract—Objective: Skeletal muscles exhibit pronounced anisotropy due to their highly oriented fibre structure, a property that significantly influences the spatial distribution of tissue mechanical and electrical properties. Understanding this anisotropy is critical for advancing biomedical applications such as electrical stimulation, bioelectric impedance analysis, and novel therapeutic interventions such as pulsed field ablation (PFA). **Methods:** We developed a numerical model incorporating realistic skeletal muscle fibre geometry at the microscale to elucidate the origins of the experimentally observed anisotropy at the bulk tissue level. To validate the model, we evaluated the skeletal muscle anisotropy using current density imaging (CDI), a magnetic resonance-based technique. **Results:** The developed numerical model identifies the origins of the observed anisotropy in bulk tissue. Experimental CDI measurements validate the model, confirming that the observed current anisotropy arises from the intrinsic properties of individual muscle fibres and their organization within the tissue. Remarkably, this anisotropy persists several – even up to 48 – hours *post-mortem*, suggesting a structural basis that transcends the level of muscle cell membranes. **Conclusion:** The integration of CDI with advanced modelling provides a powerful framework for understanding and leveraging skeletal muscle anisotropy in both imaging and therapeutic applications. **Significance:** Our study provides an experimentally validated model of skeletal muscle that is relevant to biomedical applications involving electrical treatments. It also invites further experimentation using tissues immediately after harvesting, demonstrating potential use of *ex vivo* tissues as models of *in vivo* tissue, reducing the need for experimentation with live animals and the

associated ethical burden.

Index Terms—Current density magnetic resonance imaging, current density distribution, *ex vivo* animal tissue, numerical modelling, skeletal muscle anisotropy.

I. INTRODUCTION

MANY biological tissues, such as the brain, skeletal muscle, and cardiac muscle, exhibit pronounced anisotropic properties [1]–[6] that significantly influence both the current flow and the electric field distribution within them when exposed to externally applied electric fields [7]–[11]. This anisotropy arises from the structural organisation of these tissues, which leads to direction-dependent electrical and other physical properties (e.g. rates of mass and heat transfer). For example, the alignment of muscle fibres in the skeletal and cardiac muscle or the complex cellular architecture of the brain are the main causes of these anisotropic properties, which should be considered in therapeutic applications [12]–[19].

The aforementioned tissues are often selected as target tissues in treatments involving externally applied electric fields [20]–[24]. One such example is the treatment of cardiac arrhythmias, particularly atrial fibrillation, by pulmonary vein isolation, a method commonly referred to as pulsed field ablation [25]–[29]. Another common application is gene electrotransfer, with skeletal muscle being the most common target tissue [30]–[32]. These therapies are based on a biophysical phenomenon called electroporation, whereby short, high-amplitude electrical pulses are delivered to biological cells or tissues, transiently permeabilising the cell membranes [33]. The increased membrane permeability facilitates the transport of ions and molecules across the membrane, thereby enabling the introduction of drugs, nucleic acids, and other molecules into the cells or their release from the cells [33]–[36]. Depending on pulse parameters, the phenomenon can be reversible, allowing cells to survive after membrane re-sealing, or irreversible, causing cell death [33], with both types increasingly used in biomedicine, biotechnology, and food processing [36]–[42]. Moreover, electrical stimulation of skeletal muscle tissue is often associated with delivery of high-voltage electrical pulses and is usually accompanied by an undesirable side effect causing pain and discomfort [43], which is therefore aimed to be minimised. Therefore, research

Manuscript received ... This work was supported by Slovenian Research and Innovation Agency (ARIS) through University of Ljubljana's internal funding for Start-up Research Programmes, grant P2-0249 Electroporation-based technologies and treatments, grant P1-0060 Experimental biophysics of complex systems and imaging in biomedicine, and the funding for Junior Researcher to Marko Stručić. This study was conducted within the Infrastructure Programme: Network of research infrastructure centres at the University of Ljubljana (MRIC UL IP-0510), specifically within infrastructural centre Cellular Electrical Engineering (I0-0022), also funded by the Slovenian Research and Innovation Agency (ARIS). (Rok Šmerc and Marko Stručić are co-first authors.) (Corresponding author: Samo Mahnič-Kalamiza.)

Rok Šmerc, Marko Stručić, Matej Kranjc, Damijan Miklavčič, and Samo Mahnič-Kalamiza are with the University of Ljubljana, Faculty of Electrical Engineering, Slovenia (e-mail: rok.smerc@fe.uni-lj.si; marko.strucic@fe.uni-lj.si; matej.kranjc@fe.uni-lj.si; damijan.miklavcic@fe.uni-lj.si; samo.mahnic-kalamiza@fe.uni-lj.si). Igor Serša is with the Jožef Stefan Institute, Slovenia (e-mail: igor.sersa@ijs.si).

Digital Object Identifier ...

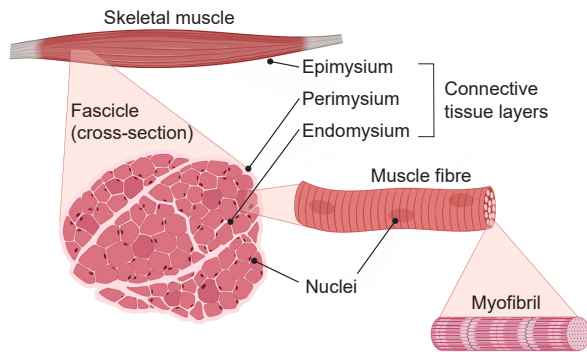


Fig. 1. The structure of skeletal muscle. The skeletal muscle is divided into various substructures, which are separated by layers of connective tissue. The entire muscle is covered by a layer of connective tissue, the epimysium. Within the muscle there are several fascicles (shown in cross-section), each of which is enveloped by the perimysium. Each fascicle consists of several muscle fibres that are enveloped by the endomysium. The muscle fibres are multinucleated and contain myofibrils. Reused from [8], licensed under CC BY 4.0.

into tissue anisotropy is crucial for optimising therapeutic procedures and outcomes. We would like to emphasise that, although this work is motivated by the relevance of anisotropic properties in tissues targeted by electroporation-based therapies, it does not directly investigate membrane permeabilisation or treatment efficacy. Instead, the study focuses on how structural anisotropy in skeletal muscle affects current density distribution during pulse application – a factor that may influence the efficacy of such procedures.

Skeletal muscle is a fibrous tissue enveloped by a layer of connective tissue, the epimysium. Within the muscle there are several fascicles with a diameter of 1–10 mm, which are separated by another layer of connective tissue, the perimysium. Each fascicle consists of several muscle fibres with a diameter of 20–100 μm , which are separated by the endomysium, the innermost layer of connective tissue (Fig. 1) [44]–[47]. Each layer of connective tissue forms a complex structure with varying density and composition. To further increase the complexity of skeletal muscle, nerve fibres and blood vessels are closely interwoven with these layers of connective tissue [48]. Muscle fibres are polynucleated cells ranging in length from millimetres to several tens of centimetres and contain myofibrils, which consist of the contractile muscle proteins [49]. The muscle fibres are specialised to contract in response to signals from associated nerve endings called motor endplates. The fibres transmit these signals by propagating the action potential along their sarcolemma [50]. The primary carriers of electrical charge in biological tissues are ions. Their movement is restricted by insulating structures such as the sarcolemma and connective tissue layers (e.g. epi-, peri-, and endomysium), leading to electrical anisotropy, especially at low frequencies [6], [51].

Since many biological tissues have heterogeneous structures, which can result in anisotropic properties, it is important to obtain spatial information on their electrical properties, such as conductivity distribution maps, or alternatively, the distribution of current density or electric field within the

tissue when exposed to an external electric field [52]. The heterogeneous distribution of conductivity has already been observed, e.g., in tumour or brain tissue [53]–[56]. In CDI, the magnetic field change is recorded in a phase of an MR image, which is then used to calculate the corresponding magnetic field created by the currents, and finally from these the current density using Ampere’s law [57]. Since its introduction in 1989, CDI has become a versatile method for study electrical conductivity properties in DC [58], AC [59], and RF [60] frequency ranges of various biological samples [61]–[63] or materials [64].

In this study, we investigate the origins of electrical anisotropy in skeletal muscle using a combination of numerical modelling and experimental validation. The work follows from our previously published study [8] and continues the multi-scale approach whereby the bulk properties of tissue follow from properties of individual constituents and their geometrical organisation. Although our earlier work addresses muscle anisotropy by comparing lesion sizes resulting from electric fields applied in different orientations relative to muscle fibres, such outcome-based validation remains indirect, as it does not explicitly confirm the modelled electrical behaviour arises from the geometrical organisation and biophysical properties of individual muscle fibres. To address this, we developed a three-dimensional model based on anatomically realistic muscle fibre architecture and used current density imaging (CDI), a magnetic resonance-based method, for experimental validation. The model was specifically designed to disentangle the contributions of muscle microstructure, such as fibre alignment and membrane electrical impedance, from other confounding variables. By comparing parallel and perpendicular electrode orientations in both the model and experiments, we aim to explain how skeletal muscle structure alone governs current flow and anisotropic behaviour within tissue. This approach offers new insights into tissue-scale electrical properties, with implications for electrical therapies, bioimpedance measurements, and treatments or diagnostics based thereon.

II. MATERIALS AND METHODS

A. Numerical Computations

The numerical model was built and solved with the COMSOL Multiphysics software environment (version 6.2, COMSOL AB, Stockholm, Sweden) using the finite element method. A three-dimensional geometry was used to approximate the experimental muscle tissue sample, with slightly reduced dimensions to increase computational efficiency of the simulations. The tissue was modelled as a cylinder with a diameter of 20 mm and a height of 0.5 mm, whereas the muscle fibres were represented as cylinders with a diameter of 60 μm spanning the entire domain. The geometry was designed so that the volume fraction of the muscle fibres was 78 %, which falls within the range typically reported in the literature for the muscle tissue [65]. The plasma membranes, whose thickness is several orders of magnitude smaller than that of the other dimensions, were not included explicitly but were instead modelled using a Contact Impedance boundary condition. Specifically, the contact impedance values were

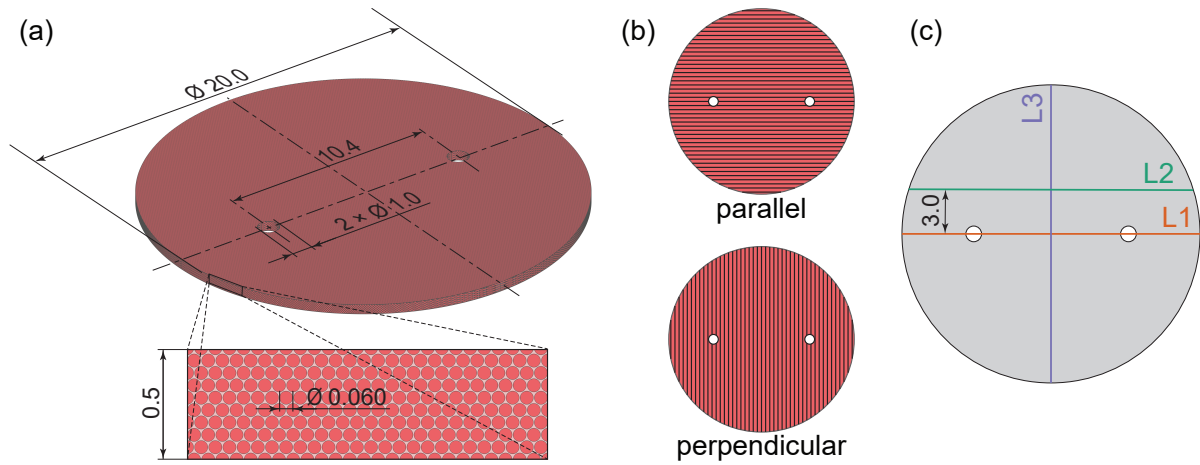


Fig. 2. (a) Geometry and dimensions of the muscle tissue sample as modelled in COMSOL Multiphysics. Note that all dimensions are in mm. (b) The two orientations of the inserted electrodes relative to the orientation of the muscle fibres: in the parallel orientation, the electrodes are positioned so that the direction of the applied electric field is parallel to the muscle fibres; in the perpendicular orientation, the field is perpendicular to the fibre orientation. (c) The three lines (L1, L2, L3) selected for detailed analysis of the current density distribution in both the numerical simulations and the experimental measurements.

derived from the ratio of the membranes' thickness to their conductivity, effectively capturing the essential resistive effect of the membranes while avoiding the computational expense of resolving the submicrometre geometry. This ensures that the contribution of the membranes to the current flow is preserved without significantly increasing the complexity of the finite element mesh. The geometry, including all dimensions, is shown in Fig. 2a. The electrodes were inserted into the tissue in two different orientations relative to the muscle fibre alignment (see Fig. 2b). In the parallel orientation, the electrodes were positioned so that the direction of the applied electric field was parallel to the muscle fibres. In perpendicular orientation, the electric field was perpendicular to the fibre orientation. The model was solved using the Electric Currents physics interface with a stationary study. This approach was appropriate because the CDI technique captures the cumulative effect of the electric current on the MR signal phase and thus represents the time-averaged current density over the duration of the applied pulse. Therefore, a stationary study provides a suitable approximation of the experimentally observed behaviour. A voltage of 100 V was applied, matching the amplitude used in the experimental setup. The model was discretised with approximately 19.5 million finite elements. The primary goal of the simulation was to calculate the current density distribution, represented as a vector field, for both the parallel and perpendicular orientations. The current density distribution was then analysed in more detail along three specific lines L1, L2, and L3 (see Fig. 2c). The current density at each specific line was normalised by the maximum value of the current densities from both the parallel and perpendicular orientations for that particular line, ensuring the ratio between the two orientations was maintained. The parameters and their corresponding values used in the model are listed in Table I. Note that the conductivity of the cell plasma membranes was adjusted by approximately two orders of magnitude from

TABLE I
PARAMETERS AND THEIR CORRESPONDING VALUES USED IN THE NUMERICAL MODEL [65]–[67].

Parameter	Value	Description
f	0.78	Volume fraction of fibres
σ_i	0.55 S/m	Intracellular conductivity
σ_e	1.20 S/m	Extracellular conductivity
σ_m	2.5×10^{-5} S/m	Membrane conductivity
t_m	7 nm	Membrane thickness

typical values found in literature to account for the at least partial disintegration of the membranes within 48 hours from the muscle tissue extraction. This is due to the experiments being performed *ex vivo*, 48 hours *post-mortem*, in which time the skeletal muscle membranes are expected to undergo a certain degree of (gradual) disintegration. The post-processing of the simulation results was performed using Python.

B. Experimental Study

Samples of porcine muscle tissue were acquired 2 hours *post-mortem* from the biceps femoris and trapezius muscles. We chose muscles with a uniform alignment of fibres to be able to ensure consistency in the orientation of the applied electric field, whether parallel or perpendicular to the fibres. The tissue was obtained from a slaughterhouse that operates in accordance with Slovenian law. Sections measuring 10 cm \times 10 cm \times 10 cm were excised from both sites, cooled to 4 °C and stored for 48 hours for transport to the experimental facility. Smaller cylindrical samples (20 mm in height and 26 mm in diameter) were then cut from these sections to fit into a custom-made acrylic glass container for MRI analysis. The samples were cut so that the muscle fibres were aligned perpendicular to the axis of the cylinder and no visible fascia

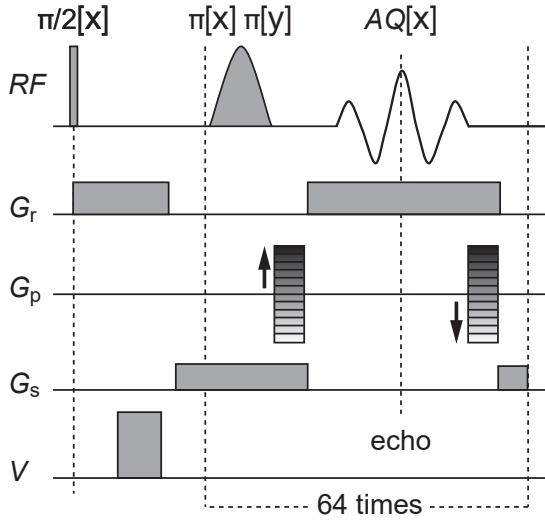


Fig. 3. Two-shot RARE pulse sequence for monitoring the current density distribution during external electrical pulse delivery. The sequence begins with a non-selective 90° radiofrequency (RF) excitation pulse, immediately followed by the current encoding part with an $800\ \mu\text{s}$, $100\ \text{V}$ electrical pulse (V). Signal acquisition is then performed using the single-shot RARE scheme with readout (G_r), phase-encoding (G_p), and slice-selection (G_s) magnetic field gradients. Due to the phase shifts induced by the electrical pulse, the sequence is repeated twice, first with refocussing pulses of phase 0° and then of phase 90° with respect to the phase of the excitation pulse, and the corresponding two acquired signals are co-added [69].

was present. Prior to the experiments, the tissue samples were allowed to warm up to room temperature. The samples were divided into two groups based on the orientation of the applied electric field. In the parallel orientation, the direction of the applied field was parallel to the muscle fibres, whereas in the perpendicular orientation it was perpendicular to the fibres (Fig. 2b). For each of the two orientations, three samples were prepared from each of the biceps femoris and trapezius muscles, resulting in a total of twelve samples. Two platinum-iridium alloy (90:10 w%) needle electrodes with a diameter of $1\ \text{mm}$ were inserted into the centre of the sample, with a centre-to-centre distance of $10.4\ \text{mm}$. A single short electrical pulse with an amplitude of $100\ \text{V}$ and a duration of $800\ \mu\text{s}$ was delivered between the electrodes using a laboratory prototype pulse generator (University of Ljubljana, Ljubljana, Slovenia), based on an H-bridge digital amplifier with $1\ \text{kV}$ MOSFETs (DE275-102N06A, IXYS, Milpitas, CA, USA) [68].

A two-shot rapid acquisition with relaxation enhancement (RARE) pulse sequence imaging was used to perform the CDI (Fig. 3). Each sequence contained the aforementioned $800\ \mu\text{s}$, $100\ \text{V}$ electrical pulse, delivered immediately after the initial $\pi/2$ radiofrequency (RF) pulse [69], [70]. Data acquisition was performed using an NMR/MRI system (Tecmag, Houston, TX, USA) connected to a $2.35\ \text{T}$ horizontal bore superconducting magnet ($100\ \text{MHz}$ proton MR frequency, Oxford Instruments, Abingdon, UK). The system was equipped with gradient hardware capable of delivering maximum gradient pulses of $250\ \text{mT/m}$ (Bruker, Ettlingen, Germany). The spectrometer

featured programmable TTL outputs for controlling peripheral devices, one of which triggered the external electrical pulses on the pulse generator and synchronised them with the imaging sequence. The imaging parameters included a $30\ \text{mm}$ field of view, a 64×64 imaging matrix, an inter-echo delay of $2.64\ \text{ms}$, a RARE factor of 64 and an echo time of $20\ \text{ms}$.

The lower sensitivity limit of CDI is inversely proportional to the presence of noise in the phase image, whereas the upper sensitivity limit depends on the product of the delivered current (I) and the total duration of the applied electric pulses (t_c). Since the phase signal-to-noise ratio (SNR) is not significantly affected by the application of electrical pulses, the sensitivity of the CDI can only be improved by increasing the amplitude or duration of these pulses. To increase CDI sensitivity and enable current density detection at lower current levels, we extended the pulse duration to $800\ \mu\text{s}$. However, further increasing the pulse duration beyond this point would have a negative effect on the overall SNR. This is because in spin-echo-based imaging sequences, the MR signal decays exponentially with time due to T_2 relaxation, following the relationship $\text{SNR} \propto \exp(-T_E/T_2)$, where T_E is the echo time. A longer pulse duration would increase the T_E and thus reduce the signal strength and therefore the lower sensitivity limit of the CDI.

One might note the substantial difference between the Larmor frequency ($\sim 100\ \text{MHz}$ at $2.35\ \text{T}$) and the lower characteristic frequency ($\sim 1.25\ \text{kHz}$) of an $800\ \mu\text{s}$ pulse. However, electric pulses induce a phase shift in the NMR signal that is proportional to the time integral of the applied current. This phase shift is retained throughout the imaging sequence and appears in the phase of the resulting MR image. Importantly, the CDI technique captures the cumulative effect of the electrical current on the phase of the MR signal, i.e. it reflects the time-averaged current density over the duration of the pulse. As such, CDI is independent of the Larmor frequency or the frequency content of the applied pulses and depends only on the pulse duration and amplitude.

After data acquisition, the imaged slices were reconstructed using ImageJ (version 1.53, National Institutes of Health, Bethesda, MD, USA). The slices were then realigned to standardise the electrode positions and ensure consistent alignment to facilitate comparison between slices during post-processing. Following reconstruction and alignment, the images were imported into MATLAB (version R2024a, MathWorks Inc., Natick, MA, USA) to reconstruct the current density vector fields. The samples were divided into two groups: one in which the electrodes were positioned so that the direction of the applied electric field was parallel to the muscle fibres, and the other in which the field was perpendicular to the fibre orientation. No distinction was made between the biceps femoris and trapezius muscle samples, as both are skeletal muscles that show no marked differences in properties. The current density data for all samples were then determined along the three specified lines L1, L2, and L3, as shown in Fig. 2c, and each subsequently normalised by the maximum current density value from each individual experiment (twelve samples in total, six for each orientation). For each line, the set of voxels nearest to the defined path was selected for analysis,

with the width of the line corresponding to a single voxel to ensure that no information was lost by averaging across multiple voxels.

C. Statistical Methods

No statistical tests were carried out for the numerical results, as each simulation result is deterministic and consistently reproducible under identical conditions.

For the experimental results, vector fields were presented for each electrode orientation (parallel and perpendicular). These were not averaged to preserve the details of the fields and avoid potential loss of information. In the analysis of current density along the three selected lines (L1, L2, and L3; Fig. 2c), the data from six samples in each orientation group (parallel and perpendicular) were averaged across each location along the lines L1, L2, and L3, with the results presented as mean values with standard deviations to illustrate the variability within each group.

To assess the statistical differences between the parallel and perpendicular orientations, data at each spatial coordinate (position) along the observation lines were first tested for normality using the Shapiro-Wilk test, and for homogeneity of variances using the Brown-Forsythe test. Because unequal variances were observed at some positions, Welch's *t*-test (two-tailed, unpaired, and not assuming equal variances) was performed at each position. In addition, a false discovery rate (FDR) correction using the Benjamini-Hochberg method was applied to control false positives. The resulting *p*-values were used to identify segments where statistically significant differences ($p < 0.05$) occurred. The electrode regions along line L1 were excluded from the statistical tests.

III. RESULTS

The result of current density imaging (CDI) is a vector field in a slice of three-dimensional tissue that ascribes a vector of electric current with its amplitude and direction to each voxel. The most common method of visualising this vector field is given in Fig. 4. This method allows visualising the areas of highest current density but is not the most suitable for performing quantitative comparison and analysis. To the latter, an analysis of only the amplitude of the current density vector is more suited, but since we thereby lose the directionality information, we analysed the amplitude only along selected dissection planes/lines as defined in Fig. 5.

Fig. 4 shows the current density distribution in the muscle tissue samples, represented as vector fields. Both simulation results (Fig. 4a and 4c) and experimental results (Fig. 4b and 4d) are shown, comparing parallel (Fig. 4a and 4b) and perpendicular (Fig. 4c and 4d) orientations. For the experimental data, three exemplary replicates out of six are shown for each orientation. No distinction was made between the biceps femoris and trapezius muscle samples, as both are skeletal muscles that exhibit no marked differences in properties. In the simulation results for the parallel orientation (Fig. 4a), the current flows predominantly along the shortest path between the electrodes. In contrast, for the perpendicular orientation (Fig. 4c), the current is more evenly distributed across the tissue section with

no clear preferred path, indicating a less preferential flow. The experimental results show similar behaviour. In the parallel orientation (Fig. 4b), most of the current flows predominantly along the shortest path between the electrodes, consistent with the simulations. However, in the perpendicular orientation (Fig. 4d), the current flow is deflected in the direction of the muscle fibres rather than favouring the shortest path, similar to the modelling results (Fig. 4c). A corresponding visualisation of the spatial distribution of normalised current density amplitude is provided in the Supplementary Materials (Fig. S1).

The normalised current density distribution along three selected lines (L1, L2, and L3) for the parallel and perpendicular electrode orientation is compared in Fig. 5. Both simulation (Fig. 5a, 5c, and 5e) and experimental (Fig. 5b, 5d, and 5f) data are shown. For the experimental data, twelve samples (six for each orientation, including both biceps femoris and trapezius muscle samples) were analysed and compared. No distinction was made between the biceps femoris and trapezius muscle samples, as both are skeletal muscles that exhibit no marked differences in properties. An alternative version of Fig. 5 is included in the Supplementary Materials as Fig. S2, showing the same mean values, but with shaded regions representing the full range (minimum to maximum) across samples instead of standard deviations.

For line L1, the simulation results (Fig. 5a) show that the current density between the electrodes is higher in the parallel orientation than in the perpendicular orientation, indicating that current flows preferentially along the shortest path between the electrodes. The experimental results confirm this observation. The statistical analysis revealed a significant difference ($p < 0.05$) between the two orientations in a 1.8 mm wide region at the centre of the observation line (Fig. 5b).

For line L2, the simulation results (Fig. 5c) indicate that the current density is more evenly distributed along the line in the parallel orientation, with a slightly lower amplitude compared to the perpendicular orientation. The experimental results (Fig. 5d) show similar distribution but no statistically significant differences between the parallel and perpendicular orientations.

For line L3, the simulation results (Fig. 5e) show a pronounced peak in current density at the centre of the line in the parallel orientation, again suggesting that the current flows preferentially along the shortest path between the electrodes. In contrast, in the perpendicular orientation, the current is more evenly distributed along the entire line. The experimental results (Fig. 5f) show a similar trend for the parallel orientation, with a pronounced peak in the centre of the line. However, for the perpendicular orientation, the experimental results show that the current is deflected in the direction of the muscle fibres, either above or below the line connecting the electrodes, resulting in a minimum of current density in the mid-line region. Because this deflection varies from sample to sample, shifting above the electrode axis in some cases and below in others, averaging the results of all six experiments leads to an artificial appearance with two peaks and a dip in the centre. This is not due to two distinct current paths, but rather the result of averaging variable deflection patterns. The statistical

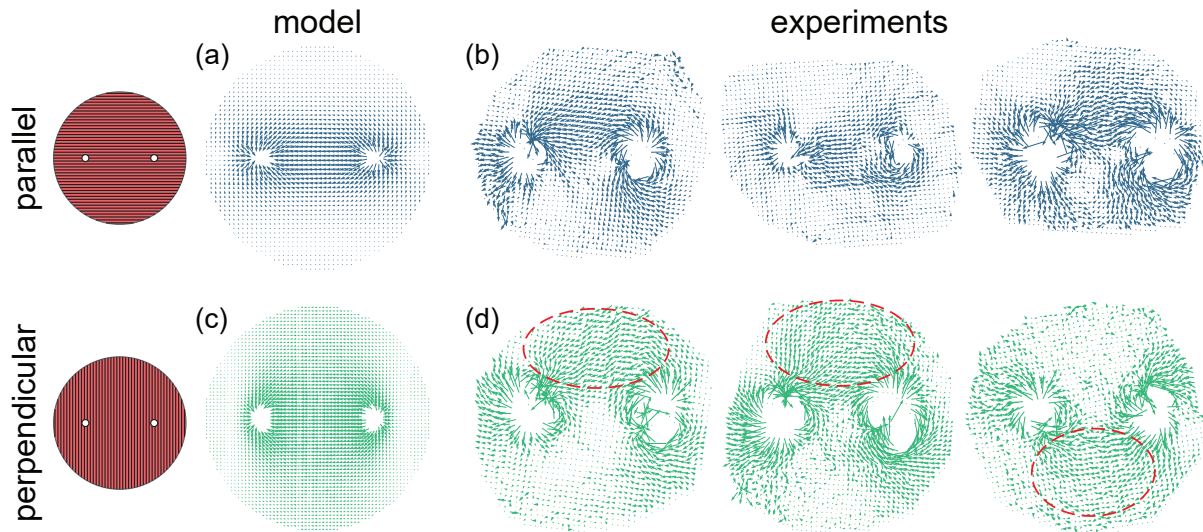


Fig. 4. Vector fields (amplitude and direction) representing the current density distribution in the muscle tissue samples. The simulation results are presented in (a) and (c), and the experimental results, representing three exemplary replicates out of six from each orientation in (b) and (d). In (a) and (b) the electrode orientation was parallel (i.e., the electric field was applied in a direction parallel with respect to the direction of the muscle fibres) and in (c) and (d) it was perpendicular (i.e., the electric field was applied in a direction parallel with respect to the direction of the muscle fibres). Red dashed ellipses show the displacement of the current away from the central area between the electrodes, as the current flow is deflected in the direction of the muscle fibres.

analysis revealed a significant difference ($p < 0.05$) between the two orientations in a 2.3 mm wide region at the centre of the observation line.

IV. DISCUSSION

The present study follows from our previously published work [8]. The multiscale numerical model described therein models tissue anisotropy by accounting for membrane permeabilisation of individual constituent cells that are represented as heavily elongated cuboidal cells [71]–[73]. Elongated as they may be, these individual cells modelled in the multiscale model of a skeletal muscle are still far from being true to the anatomical structure of an actual muscle fibre extending from several millimetres to tens of centimetres in length. In the newly developed model, the skeletal muscle tissue comprises many thin cylinders representing individual muscle fibres of realistic dimensions. We thus remain true to the adage of building a model from the ground up (i.e., a multiscale numerical model) whilst observing behaviour and properties on the macro scale (i.e., in bulk tissue). Due to the increased anatomical complexity of the model, particularly the inclusion of individual muscle fibres in the bulk tissue, it was necessary to reduce the numerical complexity to ensure computational feasibility. To achieve this, we employed a static approach rather than a dynamic time-domain simulation. Furthermore, we opted not to account for the changes in electrical material properties that may occur in the tissue due to membrane permeabilisation. However, these decisions should not be considered as limitations, as the primary aim of our work was to investigate the intrinsic anisotropy of skeletal muscle tissue, in particular its initial properties before such changes would occur. We wish to emphasise that the specific experimental

parameters used in this study (i.e., a single 800 μ s pulse at 100 V, resulting in the maximum theoretical 100 V/cm voltage-to-distance ratio as an estimate of the peak electric field strength) were selected to remain below the established electroporation thresholds for skeletal muscle tissue under similar conditions. Due to electrode geometry (needle electrodes), most of the tissue experienced well under 100 V/cm, since our intent was to study the intrinsic anisotropy of the tissue without significantly altering its structure or electrical properties due to membrane permeabilisation. In our case, the tissue used was *ex vivo* and 48 hours *post-mortem*, meaning cell membranes were already partially disintegrated. This likely diminished the contribution of active membrane resistance to overall anisotropy, shifting the observed anisotropic behaviour more toward structural and extracellular matrix properties (e.g., alignment of collagenous structures). We therefore expect that any membrane permeabilisation effects at these low field strengths had minimal additional influence on the observed anisotropy.

To experimentally validate the model, we performed current density imaging (CDI) experiments on *ex vivo* porcine muscle tissue. An electric pulse was delivered to observe the current flow in tissue. We positioned the electrodes in two specific orientations: one in which the applied electric field was parallel to the muscle fibres and one in which it was perpendicular to them. This arrangement allowed a comprehensive investigation of the anisotropic properties of the tissue. The purpose of this was to explore the anisotropy through advanced numerical modelling and to experimentally validate the model's predictions visualising the current flow within the tissue by means of CDI.

Main results of our study are current density distributions

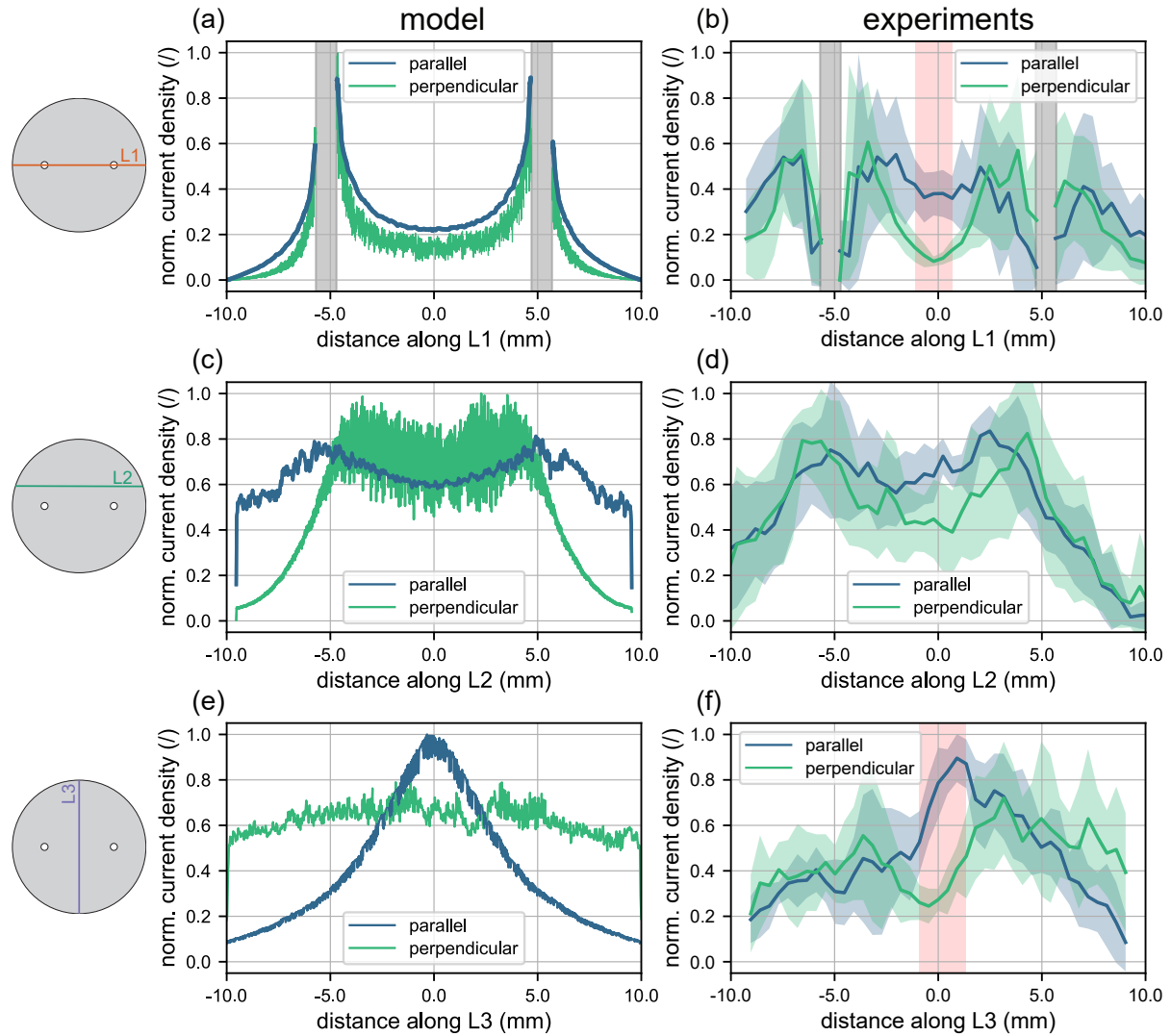


Fig. 5. Detailed comparison of the normalised current density distribution along the three selected lines of observation for the parallel (i.e., the electric field was applied in a direction parallel with respect to the direction of the muscle fibres) and perpendicular (i.e., the electric field was applied in a direction perpendicular with respect to the direction of the muscle fibres) groups. The results along the line L1 are shown in (a) and (b), along the line L2 in (c) and (d), and along the line L3 in (e) and (f). The simulation results are shown in (a), (c), and (e), whereas the experimental results are shown in (b), (d), and (f). In (a) and (b), the grey shaded regions indicate the position of the electrodes. In (b), (d), and (f), the results are given as mean values \pm standard deviations (shaded areas), with $N = 6$. The red shaded regions in (b) and (f) indicate segments along the observation lines where a statistically significant difference ($p < 0.05$) was observed between the parallel and perpendicular groups.

for the experimentally obtained data on muscle tissue and their counterparts obtained via numerical modelling. Both were analysed for the case of parallel and perpendicular direction between the electric field and main axis of the muscle fibres. The model was constructed following our previous work [8] with the aim of providing a theoretical background and offer a possible mechanism for the observed anisotropy, and the experimental part of the study validates the premises on which the model is built through a good correlation between vector fields and amplitudes in current density obtained in both ways.

The results underline the anisotropic behaviour of muscle

tissue under electric fields, which is evident both in the modelling and in the experimental data. The deflection of the current flow in the perpendicular orientation (Fig. 4d) is likely caused by the resistance posed by tissue structures with a much lower electrical conductivity than the intra- and extracellular conductivities, such as sarcolemma or connective tissue layers, at the level of the muscle fibres. These structures impede the flow of current in directions perpendicular to the longitudinal axis of the fibres. An alternative view of this behaviour, highlighting, for example, the difference between the first sample in Fig. 4b and the last in Fig. 4d, is provided in the

Supplementary Materials (Fig. S1), which displays the spatial distribution of current density amplitude across all samples. In contrast to the perfectly symmetrical flow patterns observed in the model, the experimental results show asymmetries in the current flow. These discrepancies likely arise from inherent tissue heterogeneities, such as local variations in the density of muscle fibres or composition of connective and adipose tissue, or other structural components (e.g. vessels, capillaries, nerves). Such heterogeneities create pathways with different resistances, influencing the preferential current flow observed in the experiments. The keen reader will have noticed a strong apparent divergence of the current field at both electrodes in the experimental results, occurring at the anode as well as the cathode. The direction of the current vectors near the electrodes at the electrode-tissue boundary and between the electrodes and the edge of the tissue shows inconsistent behaviour, which is an artefact of the CDI reconstruction algorithm that has problems with reconstructing the direction of current at the electrode-tissue interface, and which we were not able to fully mitigate in post-processing. Please note that the directionality (but not the amplitude, which remains unaffected) of the vector fields in these boundary regions is not reliable.

The results from Fig. 5 confirm the findings on the anisotropic behaviour of muscle tissue observed in Fig. 4 and allow quantitative comparison of results obtained by modelling and by CDI. In the parallel orientation, both the simulations and the experimental results consistently show a higher current density along the shortest path in the region between the electrodes. This supports the idea that the current flows preferentially along this path due to the muscle tissue structure, i.e., fibre composition and orientation. The lack of apparent differences in the experimental results for line L2 could be due to *post-mortem* changes in the tissue, as we used *ex vivo* tissue samples 48 hours *post-mortem*. These changes may have affected the tissue properties so that the differences between the parallel and perpendicular orientations were less pronounced. Changes such as membrane disintegration may have affected the observed results, resulting in no clear differences between the orientations. To support this hypothesis, we note that electrical impedance measurements (as of yet unpublished, preliminary experimental data obtained in a separate, conceptually related study) performed on similar muscle tissue at different *post-mortem* time points (3 h, 24 h, and 72 h) showed a clear decline in anisotropy over time. These results suggest that structural degradation, particularly of cell membranes, can diminish the degree of tissue anisotropy. A potential avenue for future work would be to repeat the CDI measurements on fresher tissue or across multiple *post-mortem* intervals to directly correlate anisotropy loss with time-dependent microstructural changes.

The deflection of current flow in the perpendicular orientation observed in the experimental results, particularly in line L3, again suggests that tissue heterogeneity plays a role in controlling current flow. In contrast to the symmetrical flow patterns observed in the simulations, the experimental results seem to exhibit a preferential current path that deviates from the shortest path between the two electrodes. We propose

that the observed pattern likely results from the formation of preferential current paths during the experiment, which emerge from minute, spatially varying differences in tissue conductivity; for example, due to slight differences in hydration, fibre alignment, or local membrane degradation. Such heterogeneities can seed current redistribution, where slightly more conductive regions near one electrode facilitate higher current densities early on in a particular direction at a non-zero (and possibly substantial) angle with respect to the shortest path between the two electrodes. Once this preferential path is established, the non-linear dependence of conductivity on field strength may reinforce this route as the current continues to flow, effectively amplifying the initial asymmetry into a consistent directional pattern. We have observed something quite similar very early on in our MRI-based experiments, on agarose phantoms [74].

The experimental results indicate that the skeletal muscle tissue exhibits anisotropy even days after excision. This suggests that the observed anisotropic properties are not solely a function of the plasma membrane of living cells but may also be attributed to the collagenous composition of the muscle structures. This inherent anisotropy could be due to the orientation and structure of collagen and other extracellular matrix components, but also intracellular structures such as actin and myosin in the sarcomere (as the membrane is already disintegrated), that contribute to the overall resistance to current flow in muscle tissue. These structural components remain in the tissue after death and form the basis for the anisotropic behaviour, even after the disintegration of the cell membranes. We should at this point clarify that while our computational model assumes that muscle tissue anisotropy arises predominantly from the relative conductivities of the intracellular and extracellular spaces and the resistive effect of the cell membrane, the experimental data were acquired from *ex vivo* tissue 48 hours *post-mortem*. By this time, the structural and functional integrity of the plasma membranes is likely compromised to a significant extent. As such, the experimentally observed anisotropy is probably governed less by the membrane resistance and more by the properties and spatial organisation of the extracellular matrix and remaining intracellular architecture. This implies that although the model parameters (e.g., membrane conductivity, intracellular and extracellular conductivity) provide a computationally robust framework for simulating anisotropic current flow, they may not fully correspond to the mechanistic properties governing anisotropy under the experimental conditions. Nevertheless, the consistency between simulated and experimental data indicates that the model remains valuable for probing the structural determinants of tissue anisotropy, even if the biophysical meaning of certain parameters must be interpreted with caution in the context of *post-mortem* tissue.

To evaluate the robustness of the experimental results, we investigated the influence of line positioning (particularly the line L2) and the selected width (i.e., the number of voxels) of the lines L1, L2, and L3 on the current density distributions. The position of line L2 had no significant influence on the results when its distance from line L1 varied slightly (within ± 1 mm). However, when L2 was moved closer to L1 (to within

1 mm), the amplitude of the parallel current density became higher than that of the perpendicular orientation. Conversely, the perpendicular current density increased relative to the parallel orientation when L2 was moved further away from L1 towards the edge of the sample.

If the width of the lines was increased to three voxels, this had no significant effect on the results, except for minor local deviations at certain points. We chose to use a line width of a single voxel, in order to avoid the potential loss of detail that could result from averaging across a larger width, which could blur spatial variations and reduce the accuracy of the current density distribution along the lines. We believe this approach ensures that the results reflect the actual variations in current density with minimal smoothing or distortion, thereby providing a more accurate representation of the anisotropic properties of the tissue.

It is also important to consider other factors that could influence the results of the model. One of these is the role of muscle fibre volume fraction and the possible effects of membrane permeabilisation near the electrodes. In our previous work [8], we have already investigated the influence of muscle fibre volume fraction on the anisotropy rate in skeletal muscle tissue. As described in the Supplementary Material of [8], the influence of volume fraction on the anisotropy rate was found to be negligible, although it affected the absolute values of conductivity in the parallel and perpendicular orientations. This indicates that the results of the current model are not significantly dependent on the volume fraction of the muscle fibres.

Factors such as variations in muscle fibre density and orientation, as well as the presence of different tissue types, including connective and adipose tissue, vessels, capillaries, and nerves, could influence electrical properties and current flow. These factors are not explicitly accounted for in the model, which could have led to the observed discrepancies between the model's predictions and experimental results. Furthermore, the model assumes a uniform tissue geometry. Although this simplifies the representation of muscle tissue, it cannot fully capture the natural heterogeneity that exists *in vivo*.

Despite providing valuable insights into the anisotropic behaviour of muscle tissue, certain limitations must be considered when interpreting the results. The first limitation is that the experiments were performed 48 hours *post-mortem*. By this time, the plasma membranes have at least partially disintegrated. This means that the tissue does not show the same behaviour as fresh tissue, which may limit the transferability of the results to *in vivo* conditions.

Another potential limitation is the possibility of the alteration of tissue electrical properties due to permeabilisation of membranes near the electrodes. In our study, we used a single pulse of 800 μ s duration and a low amplitude of 100 V, which should not induce significant changes except possibly in the immediate vicinity of the electrodes. Although it may be beneficial to include membrane permeabilisation in the model to account for potential changes in the electrical properties of the tissue, as has been done previously [8], [71]–[73], this would significantly increase the computational

complexity of the simulations. Given the state of the tissue under the experimental conditions (disintegrated membranes at 48 hours *post-mortem*), such effects are expected to have minimal impact on the results.

V. CONCLUSION

In conclusion, our study presents three key contributions to understanding skeletal muscle tissue and its material properties.

Firstly, our geometrically complex yet simplified model, with minimal degrees of freedom in material properties, illustrates how muscle anisotropy arises from the muscles' structure. The model serves as a strong foundation for further development, including incorporating living (*in vivo*) cell membranes whose permeability and conductivity could be modelled as treatment-dependent.

Secondly, our findings confirm that muscle tissue anisotropy can be effectively studied via electric current using state-of-the-art magnetic resonance imaging methods, such as CDI. While the necessary equipment is available only to select research groups, established methods in the literature provide a pathway for further experimentation provided the necessary equipment is acquired.

Thirdly, our results suggest that skeletal muscle tissue retains a detectable degree of anisotropy even days post-excision, indicating that this property may not be solely dependent on the plasma membrane of living cells but also (in part, at least) on the collagenous composition and internal structures like actin- and myosin-containing sarcomeres.

These promising experimental results encourage further studies on freshly harvested tissues (minutes to a couple of hours *post-mortem*) to explore the plasma membrane's role in bulk anisotropy.



REFERENCES

- [1] B. R. Epstein and K. R. Foster, "Anisotropy in the dielectric properties of skeletal muscle," *Med. Biol. Eng. Comput.*, vol. 21, no. 1, pp. 51–55, Jan. 1983.
- [2] K. R. Foster and H. P. Schwan, "Dielectric properties of tissues and biological materials: A critical review," *Crit Rev Biomed Eng.*, vol. 17, no. 1, pp. 25–104, 1989.
- [3] C. Gabriel, S. Gabriel, and E. Corthout, "The dielectric properties of biological tissues: I. Literature survey," *Phys. Med. Biol.*, vol. 41, no. 11, pp. 2231–2249, Nov. 1996.
- [4] S. Gabriel, R. W. Lau, and C. Gabriel, "The dielectric properties of biological tissues: II. Measurements in the frequency range 10 Hz to 20 GHz," *Phys. Med. Biol.*, vol. 41, no. 11, pp. 2251–2269, Nov. 1996.
- [5] —, "The dielectric properties of biological tissues: III. Parametric models for the dielectric spectrum of tissues," *Phys. Med. Biol.*, vol. 41, no. 11, pp. 2271–2293, Nov. 1996.
- [6] D. Miklavčič, N. Pavšelj, and F. X. Hart, "Electric Properties of Tissues," in *Wiley Encyclopedia of Biomedical Engineering*, 1st ed., M. Akay, Ed. Wiley, Apr. 2006.
- [7] S. Čorović *et al.*, "The influence of skeletal muscle anisotropy on electroporation: In vivo study and numerical modeling," *Med Biol Eng Comput.*, vol. 48, no. 7, pp. 637–648, Jul. 2010.
- [8] R. Šmerc *et al.*, "A Multiscale Computational Model of Skeletal Muscle Electroporation Validated Using *In Situ* Porcine Experiments," *IEEE Trans. Biomed. Eng.*, vol. 70, no. 6, pp. 1826–1837, Jun. 2023.
- [9] F. Xie and C. W. Zemlin, "Effect of Twisted Fiber Anisotropy in Cardiac Tissue on Ablation with Pulsed Electric Fields," *PLoS ONE*, vol. 11, no. 4, p. e0152262, Apr. 2016.
- [10] B. Kos *et al.*, "Determination of lethal electric field threshold for pulsed field ablation in ex vivo perfused porcine and human hearts," *Front. Cardiovasc. Med.*, vol. 10, p. 1160231, Jun. 2023.

- [11] L. Molinari, M. Zaltieri, C. Massaroni, S. Filippi, A. Gizzi, and E. Schena, "Multiscale and Multiphysics Modeling of Anisotropic Cardiac RFCA: Experimental-Based Model Calibration via Multi-Point Temperature Measurements," *Front. Physiol.*, vol. 13, p. 845896, Apr. 2022.
- [12] M. Takaza, K. M. Moerman, J. Gindre, G. Lyons, and C. K. Simms, "The anisotropic mechanical behaviour of passive skeletal muscle tissue subjected to large tensile strain," *Journal of the Mechanical Behavior of Biomedical Materials*, vol. 17, pp. 209–220, Jan. 2013.
- [13] A. E. Knight *et al.*, "Full Characterization of *in vivo* Muscle as an Elastic, Incompressible, Transversely Isotropic Material Using Ultrasonic Rotational 3D Shear Wave Elasticity Imaging," *IEEE Trans. Med. Imaging*, vol. 41, no. 1, pp. 133–144, Jan. 2022.
- [14] D. Maji *et al.*, "Enhancing *In Vivo* Electroporation Efficiency through Hyaluronidase: Insights into Plasmid Distribution and Optimization Strategies," *Pharmaceutics*, vol. 16, no. 4, p. 547, Apr. 2024.
- [15] M. Couade *et al.*, "In Vivo Quantitative Mapping of Myocardial Stiffening and Transmural Anisotropy During the Cardiac Cycle," *IEEE Trans. Med. Imaging*, vol. 30, no. 2, pp. 295–305, Feb. 2011.
- [16] A. Suzuki *et al.*, "Impact of myocardial fiber orientation on lesions created by a novel heated saline-enhanced radiofrequency needle-tip catheter: An MRI lesion validation study," *Heart Rhythm*, vol. 18, no. 3, pp. 443–452, Mar. 2021.
- [17] V. Kovalev and F. Kruggel, "Texture Anisotropy of the Brain's White Matter as Revealed by Anatomical MRI," *IEEE Trans. Med. Imaging*, vol. 26, no. 5, pp. 678–685, May 2007.
- [18] Y. Feng, R. J. Okamoto, R. Namani, G. M. Genin, and P. V. Bayly, "Measurements of mechanical anisotropy in brain tissue and implications for transversely isotropic material models of white matter," *Journal of the Mechanical Behavior of Biomedical Materials*, vol. 23, pp. 117–132, Jul. 2013.
- [19] R. W. Carlsen and N. P. Daphalapurkar, "The Importance of Structural Anisotropy in Computational Models of Traumatic Brain Injury," *Front. Neurol.*, vol. 6, Feb. 2015.
- [20] J. M. McMahon and D. J. Wells, "Electroporation for Gene Transfer to Skeletal Muscles: Current Status," *BioDrugs*, vol. 18, no. 3, pp. 155–165, 2004.
- [21] J. De Vry *et al.*, "In vivo electroporation of the central nervous system: A non-viral approach for targeted gene delivery," *Progress in Neurobiology*, vol. 92, no. 3, pp. 227–244, Nov. 2010.
- [22] P. D. Fisher *et al.*, "Adipose tissue: A new target for electroporation-enhanced DNA vaccines," *Gene Ther.*, vol. 24, no. 12, pp. 757–767, Dec. 2017.
- [23] F. H. Wittkamp, R. Van Es, and K. Neven, "Electroporation and its Relevance for Cardiac Catheter Ablation," *JACC: Clinical Electrophysiology*, vol. 4, no. 8, pp. 977–986, Aug. 2018.
- [24] E. Sokolowska and A. U. Blachnio-Zabielska, "A Critical Review of Electroporation as A Plasmid Delivery System in Mouse Skeletal Muscle," *IJMS*, vol. 20, no. 11, p. 2776, Jun. 2019.
- [25] A. Sugrue *et al.*, "Irreversible electroporation for catheter-based cardiac ablation: A systematic review of the preclinical experience," *J Interv Card Electrophysiol*, vol. 55, no. 3, pp. 251–265, Sep. 2019.
- [26] A. Verma *et al.*, "First-in-Human Experience and Acute Procedural Outcomes Using a Novel Pulsed Field Ablation System: The PULSED AF Pilot Trial," *Circ. Arrhythmia and Electrophysiology*, vol. 15, no. 1, p. e010168, Jan. 2022.
- [27] V. Y. Reddy *et al.*, "Pulsed Field or Conventional Thermal Ablation for Paroxysmal Atrial Fibrillation," *N Engl J Med*, vol. 389, no. 18, pp. 1660–1671, Nov. 2023.
- [28] A. Verma *et al.*, "Pulsed Field Ablation for the Treatment of Atrial Fibrillation: PULSED AF Pivotal Trial," *Circulation*, vol. 147, no. 19, pp. 1422–1432, May 2023.
- [29] K.-R. J. Chun *et al.*, "State-of-the-art pulsed field ablation for cardiac arrhythmias: Ongoing evolution and future perspective," *Europace*, vol. 26, no. 6, p. euae134, Jun. 2024.
- [30] L. M. Mir *et al.*, "High-efficiency gene transfer into skeletal muscle mediated by electric pulses," *Proc. Natl. Acad. Sci. U.S.A.*, vol. 96, no. 8, pp. 4262–4267, Apr. 1999.
- [31] G. Tevz *et al.*, "Gene Electroporation into Murine Skeletal Muscle: A Systematic Analysis of Parameters for Long-term Gene Expression," *Technol Cancer Res Treat*, vol. 7, no. 2, pp. 91–101, Apr. 2008.
- [32] D. C. Hughes, J. P. Hardee, D. S. Waddell, and C. A. Goodman, "CORP: Gene delivery into murine skeletal muscle using *in vivo* electroporation," *Journal of Applied Physiology*, vol. 133, no. 1, pp. 41–59, Jul. 2022.
- [33] T. Kotnik, L. Rems, M. Tarek, and D. Miklavčič, "Membrane Electroporation and Electroporomeabilization: Mechanisms and Models," *Annu. Rev. Biophys.*, vol. 48, no. 1, pp. 63–91, May 2019.
- [34] T. Kotnik, G. Pucihar, and D. Miklavčič, "The Cell in the Electric Field," in *Clinical Aspects of Electroporation*, S. T. Kee, J. Gehl, and E. W. Lee, Eds. New York, NY: Springer New York, 2011, pp. 19–29.
- [35] T. Polajzer, T. Jarm, and D. Miklavcic, "Analysis of damage-associated molecular pattern molecules due to electroporation of cells *in vitro*," *Radiology and Oncology*, vol. 54, no. 3, pp. 317–328, Jul. 2020.
- [36] B. Geboers *et al.*, "High-Voltage Electrical Pulses in Oncology: Irreversible Electroporation, Electrochemotherapy, Gene Electroporation, Electrofusion, and Electroimmunotherapy," *Radiology*, vol. 295, no. 2, pp. 254–272, May 2020.
- [37] S. Haberl, D. Miklavcic, G. Sersa, W. Frey, and B. Rubinsky, "Cell membrane electroporation-Part 2: The applications," *IEEE Electr. Insul. Mag.*, vol. 29, no. 1, pp. 29–37, Jan. 2013.
- [38] M. L. Yarmush, A. Golberg, G. Serša, T. Kotnik, and D. Miklavčič, "Electroporation-Based Technologies for Medicine: Principles, Applications, and Challenges," *Annu. Rev. Biomed. Eng.*, vol. 16, no. 1, pp. 295–320, Jul. 2014.
- [39] T. Kotnik, W. Frey, M. Sack, S. Haberl Meglič, M. Peterka, and D. Miklavčič, "Electroporation-based applications in biotechnology," *Trends in Biotechnology*, vol. 33, no. 8, pp. 480–488, Aug. 2015.
- [40] S. Mahnič-Kalamiza, E. Vorobiev, and D. Miklavčič, "Electroporation in Food Processing and Biorefinery," *J Membrane Biol*, vol. 247, no. 12, pp. 1279–1304, Dec. 2014.
- [41] G. Saldaña, I. Álvarez, S. Condón, and J. Raso, "Microbiological Aspects Related to the Feasibility of PEF Technology for Food Pasteurization," *Critical Reviews in Food Science and Nutrition*, vol. 54, no. 11, pp. 1415–1426, Nov. 2014.
- [42] S. Sachdev, T. Potočnik, L. Rems, and D. Miklavčič, "Revisiting the role of pulsed electric fields in overcoming the barriers to *in vivo* gene electroporation," *Bioelectrochemistry*, vol. 144, p. 107994, Apr. 2022.
- [43] A. Cvetkoska, A. Maček-Lebar, P. Trdina, D. Miklavčič, and M. Reberšek, "Muscle contractions and pain sensation accompanying high-frequency electroporation pulses," *Sci Rep*, vol. 12, no. 1, p. 8019, May 2022.
- [44] V. Tayfur, O. Magden, M. Edizer, and A. Atabey, "Anatomy of Vastus Lateralis Muscle Flap," *Journal of Craniofacial Surgery*, vol. 21, no. 6, pp. 1951–1953, Nov. 2010.
- [45] S. D'Arpa, F. Toia, E. Brenner, C. Melloni, F. Moschella, and A. Cordova, "Variability and reliability of the vastus lateralis muscle anatomy," *Acta Chirurgica Belgica*, vol. 116, no. 4, pp. 203–212, Jul. 2016.
- [46] S. Methenitis, A.-N. Stasinaki, N. Zaras, K. Spengos, N. Karandreas, and G. Terzis, "Intramuscular fibre conduction velocity and muscle fascicle length in human vastus lateralis," *Appl. Physiol. Nutr. Metab.*, vol. 44, no. 2, pp. 133–138, Feb. 2019.
- [47] E. C. de Almeida Araujo, "Adaptation of Proof of Concepts Into Quantitative NMR Methods: Clinical Application for the Characterization of Alterations Observed in the Skeletal Muscle Tissue in Neuromuscular Disorders," Ph.D. dissertation, Université Paris Sud - Paris XI, Paris, France, 2014.
- [48] A. Rehfeld, M. Nylander, and K. Karnov, *Compendium of Histology: A Theoretical and Practical Guide*. Cham: Springer International Publishing, 2017.
- [49] A. Sharifnezhad, R. Marzilger, and A. Arampatzis, "Effects of load magnitude, muscle length and velocity during eccentric chronic loading on the longitudinal growth of vastus lateralis muscle," *Journal of Experimental Biology*, p. jeb.100370, Jan. 2014.
- [50] J. Feher, "Contractile Mechanisms in Skeletal Muscle," in *Quantitative Human Physiology*. Elsevier, 2017, pp. 305–317.
- [51] J. Malmivuo and R. Plonsey, *Bioelectromagnetism Principles and Applications of Bioelectric and Biomagnetic Fields*. Oxford University Press, Oct. 1995.
- [52] M. Kranjc, F. Bajd, I. Sersa, and D. Miklavcic, "Magnetic Resonance Electrical Impedance Tomography for Monitoring Electric Field Distribution During Tissue Electroporation," *IEEE Trans. Med. Imaging*, vol. 30, no. 10, pp. 1771–1778, Oct. 2011.
- [53] L. T. Muftuler, M. J. Hamamura, O. Birgul, and O. Nalcioğlu, "In vivo MRI electrical impedance tomography (MREIT) of tumors," *Technol Cancer Res Treat*, vol. 5, no. 4, pp. 381–387, Aug. 2006.
- [54] Y. Wang *et al.*, "Mapping electrical properties heterogeneity of tumor using boundary informed electrical properties tomography (BIEPT) at 7T," *Magnetic Resonance in Med*, vol. 81, no. 1, pp. 393–409, Jan. 2019.
- [55] H. J. Kim *et al.*, "In Vivo electrical conductivity imaging of a canine brain using a 3 T MREIT system," *Physiol. Meas.*, vol. 29, no. 10, pp. 1145–1155, Oct. 2008.
- [56] M. Åström, J.-J. Lemaire, and K. Wårdell, "Influence of heterogeneous and anisotropic tissue conductivity on electric field distribution in deep

- brain stimulation," *Med Biol Eng Comput*, vol. 50, no. 1, pp. 23–32, Jan. 2012.
- [57] G. Scott, M. Joy, R. Armstrong, and R. Henkelman, "Sensitivity of magnetic-resonance current-density imaging," *Journal of Magnetic Resonance (1969)*, vol. 97, no. 2, pp. 235–254, Apr. 1992.
- [58] M. Joy, G. Scott, and M. Henkelman, "In vivo detection of applied electric currents by magnetic resonance imaging," *Magnetic Resonance Imaging*, vol. 7, no. 1, pp. 89–94, Jan. 1989.
- [59] U. Mikac, F. Demšar, K. Beravs, and I. Serša, "Magnetic resonance imaging of alternating electric currents," *Magnetic Resonance Imaging*, vol. 19, no. 6, pp. 845–856, Jul. 2001.
- [60] G. C. Scott, M. L. G. Joy, R. L. Armstrong, and R. M. Henkelman, "RF Current Density Imaging in Homogeneous Media," *Magnetic Resonance in Med*, vol. 28, no. 2, pp. 186–201, Dec. 1992.
- [61] K. Beravs, D. White, I. Serša, and F. Demsar, "Electric current density imaging of bone by MRI," *Magnetic Resonance Imaging*, vol. 15, no. 8, pp. 909–915, Jan. 1997.
- [62] I. Serša, K. Beravs, N. J. F. Dodd, S. Zhao, D. Miklavčič, and F. Demsar, "Electric current density imaging of mice tumors," *Magnetic Resonance in Med*, vol. 37, no. 3, pp. 404–409, Mar. 1997.
- [63] R. Yoon, T. DeMonte, K. Hasanov, D. Jorgenson, and M. Joy, "Measurement of thoracic current flow in pigs for the study of defibrillation and cardioversion," *IEEE Trans. Biomed. Eng.*, vol. 50, no. 10, pp. 1167–1173, Oct. 2003.
- [64] E. Kossel and R. Kimmich, "Flow measurements below 50 Mm: NMR microscopy experiments in lithographic model pore spaces," *Magnetic Resonance Imaging*, vol. 23, no. 2, pp. 397–400, Feb. 2005.
- [65] J. Pingel, H. M. Kjer, F. Biering-Sørensen, R. Feidenhans'l, and T. B. Dyrby, "3D synchrotron imaging of muscle tissues at different atrophic stages in stroke and spinal cord injury: A proof-of-concept study," *Sci Rep*, vol. 12, no. 1, p. 17289, Oct. 2022.
- [66] T. Kotnik, D. Miklavčič, and T. Slivnik, "Time course of transmembrane voltage induced by time-varying electric fields—a method for theoretical analysis and its application," *Bioelectrochemistry and Bioenergetics*, vol. 45, no. 1, pp. 3–16, Mar. 1998.
- [67] L. Rems, M. Ušaj, M. Kanduđer, M. Reberšek, D. Miklavčič, and G. Pucihar, "Cell electrofusion using nanosecond electric pulses," *Sci Rep*, vol. 3, no. 1, p. 3382, Nov. 2013.
- [68] J. Dermol-Cerne *et al.*, "Plasma membrane depolarization and permeabilization due to electric pulses in cell lines of different excitability," *Bioelectrochemistry*, vol. 122, pp. 103–114, Aug. 2018.
- [69] I. Serša, M. Kranjc, and D. Miklavčič, "Current density imaging sequence for monitoring current distribution during delivery of electric pulses in irreversible electroporation," *BioMed Eng OnLine*, vol. 14, no. S3, p. S6, Dec. 2015.
- [70] I. Serša, "Auxiliary phase encoding in multi spin-echo sequences: Application to rapid current density imaging," *Journal of Magnetic Resonance*, vol. 190, no. 1, pp. 86–94, Jan. 2008.
- [71] S. Huclova, D. Erni, and J. Fröhlich, "Modelling effective dielectric properties of materials containing diverse types of biological cells," *J. Phys. D: Appl. Phys.*, vol. 43, no. 36, p. 365405, Sep. 2010.
- [72] —, "Modelling and validation of dielectric properties of human skin in the MHz region focusing on skin layer morphology and material composition," *J. Phys. D: Appl. Phys.*, vol. 45, no. 2, p. 025301, Jan. 2012.
- [73] J. Dermol-Cerne and D. Miklavcic, "From Cell to Tissue Properties—Modeling Skin Electroporation With Pore and Local Transport Region Formation," *IEEE Trans. Biomed. Eng.*, vol. 65, no. 2, pp. 458–468, Feb. 2018.
- [74] M. Essone Mezeme, M. Kranjc, F. Bajd, I. Serša, C. Brosseau, and D. Miklavčič, "Assessing how electroporation affects the effective conductivity tensor of biological tissues," *Appl. Phys. Lett.*, vol. 101, no. 21, p. 213702, Nov. 2012.

Supplementary Materials for Electrical Pathways Through the Intricate Network of Skeletal Muscle Fibres: Insights From MRI-Validated Numerical Modelling

Rok Šmerc , Marko Stručić , Matej Kranjc , Igor Serša , Damijan Miklavčič ,
and Samo Mahnič-Kalamiza 

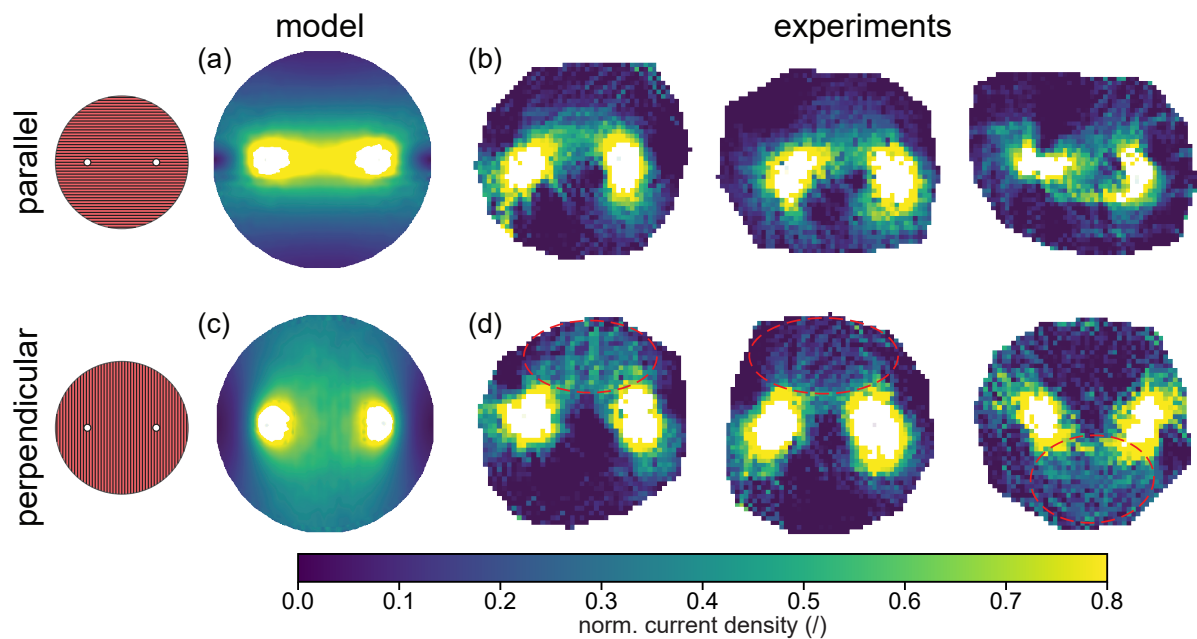


Fig. S1: Spatial distribution of normalised current density amplitude in the muscle tissue samples. The simulation results are presented in (a) and (c), and the experimental results, representing three exemplary replicates out of six from each orientation in (b) and (d). In (a) and (b) the electrode orientation was parallel (i.e., the electric field was applied in a direction parallel with respect to the direction of the muscle fibres) and in (c) and (d) it was perpendicular (i.e., the electric field was applied in a direction perpendicular with respect to the direction of the muscle fibres). Red dashed ellipses show the displacement of the current away from the central area between the electrodes, as the current flow is deflected in the direction of the muscle fibres.

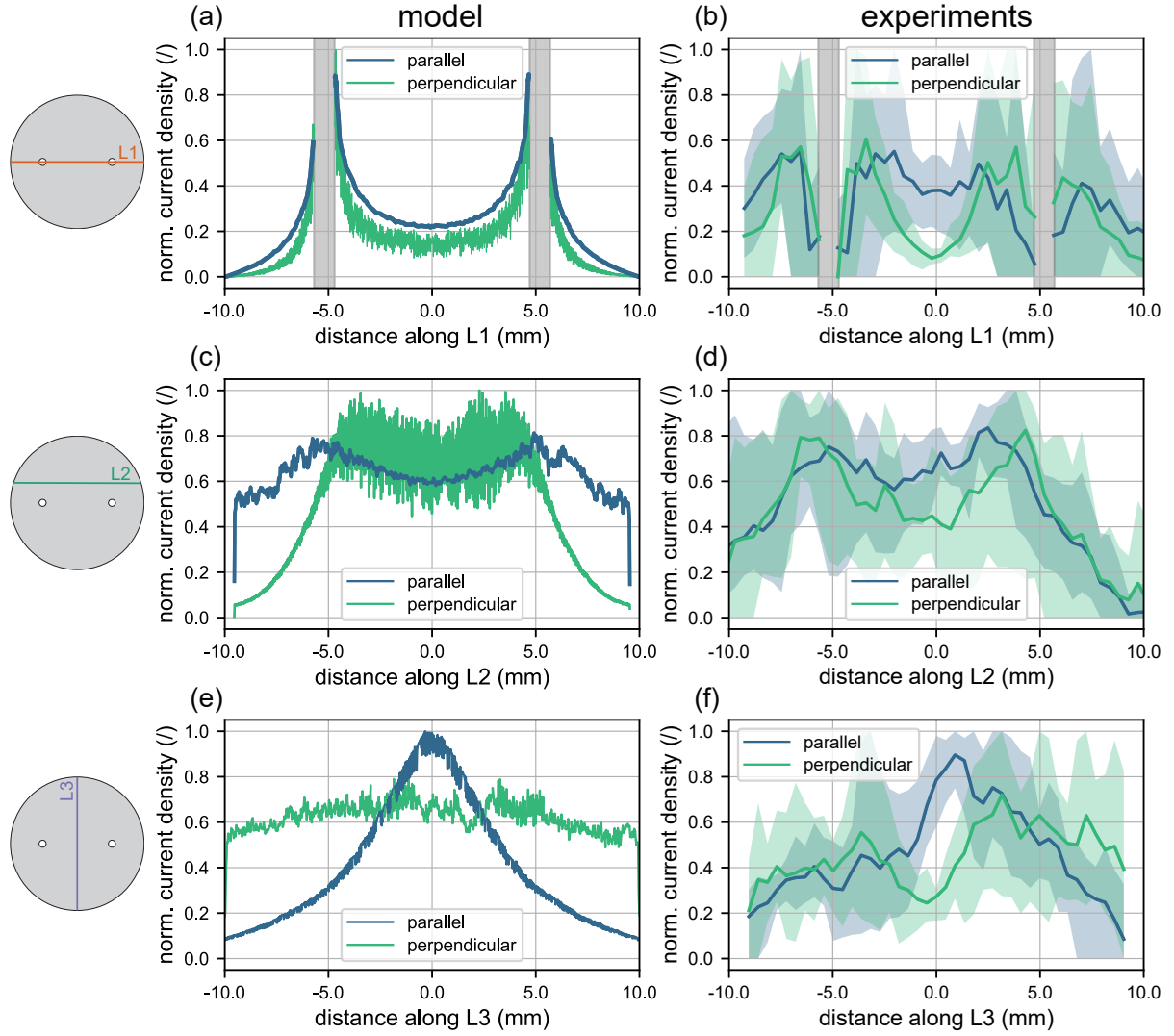


Fig. S2: Detailed comparison of the normalised current density distribution along the three selected lines of observation for the parallel (i.e., the electric field was applied in a direction parallel with respect to the direction of the muscle fibres) and perpendicular (i.e., the electric field was applied in a direction perpendicular with respect to the direction of the muscle fibres) groups. The results along the line L1 are shown in (a) and (b), along the line L2 in (c) and (d), and along the line L3 in (e) and (f). The simulation results are shown in (a), (c), and (e), whereas the experimental results are shown in (b), (d), and (f). In (a) and (b), the grey shaded regions indicate the position of the electrodes. In (b), (d), and (f), the results are given as mean values, with shaded areas representing the range between the minimum and maximum values, with $N = 6$.

2.3 Paper 3

Title: **Skeletal muscle death from the perspective of electrical impedance as evidenced by experiment and numerical modelling**

Authors: **Rok Šmerc**, Damijan Miklavčič, and Samo Mahnič-Kalamiza

Publication: *Computers in Biology and Medicine*

Impact factor: 6.3 (2024)

Quartile: Q1

Rank: 22/124 (Biomedical engineering)

Status: under review

Skeletal muscle death from the perspective of electrical impedance as evidenced by experiment and numerical modelling

Rok Šmerc, Damijan Miklavčič, Samo Mahnič-Kalamiza*

University of Ljubljana, Faculty of Electrical Engineering, Tržaška cesta 25, SI-1000 Ljubljana, Slovenia

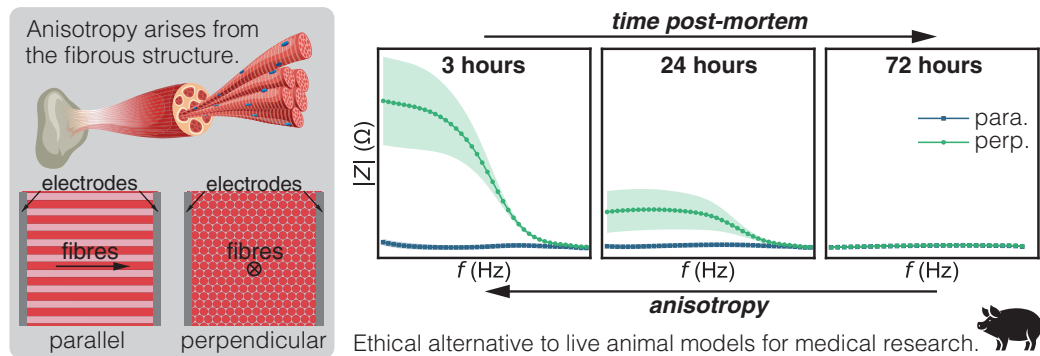
Abstract

Understanding the biophysical changes in skeletal muscle tissue during the minutes to hours post-excision or following irreversible damage is critical for biomedical applications and food processing. Muscle tissue, composed of myofibrillar and sarcoplasmic proteins, water, lipids, and connective tissue, forms a complex network of interactions that persists as it degrades post-mortem. This study investigates skeletal muscle death through ex vivo experimental measurements on porcine muscle, supported by a novel numerical model that builds the muscle up from individual fibres. Skeletal muscle tissue was found to exhibit strong anisotropy in electrical conductivity due to its structure. It demonstrates much lower conductivity perpendicular to muscle fibres compared to parallel with them owing to its limited plasma membrane conductivity. We explore how post-mortem changes, including increased membrane permeability during membrane decomposition, and external interventions like electroporation, alter these anisotropic properties. Our findings have implications for biomedicine, including treatments targeting muscle tissue, such as pulsed field ablation for cardiac arrhythmias. In food production, the study informs applications of pulsed electric fields to modify meat structure and texture. By integrating experimental and theoretical approaches, this work provides new insights into the electrochemical and structural dynamics of skeletal muscle during and after death.

Keywords: tissue electrical impedance; ex vivo animal tissue; numerical modelling; skeletal muscle anisotropy; electroporation.

Graphical abstract

SKELETAL MUSCLE ANISOTROPY THROUGH EXPERIMENTAL AND NUMERICAL IMPEDANCE SPECTROSCOPY



*Corresponding author. E-mail address: samo.mahnic-kalamiza@fe.uni-lj.si (S. Mahnič-Kalamiza).

Highlights:

- Dead skeletal muscle continues to exhibit anisotropy of its electrical impedance.
- We present a numerical model describing muscle cell plasma membrane deterioration.
- Electroporation affirms that cell membrane decay is the origin of anisotropy change.
- Dependence of electrical impedance is modelled by varying one membrane parameter.

1 Introduction

Biological tissues exhibit complex electrical properties that are determined by their composition, structure, and the distribution of ions and polar molecules within. These properties influence the behaviour of electric fields and current flow in tissue and vary greatly between different tissues and tissue constituents [1–6]. For example, extracellular spaces typically exhibit higher conductivity due to the presence of free ions, whereas cell membranes, with their significantly lower electrical conductivity, act as insulating barriers that impede current flow [7, 8]. In addition, tissue properties are frequency-dependent, with different structures and processes characterising the electrical response of tissue across various frequency ranges [4, 6]. Understanding these properties is fundamental for interpreting the behaviour of tissues under electrical stimulation, which is essential for both clinical applications and the development or optimisation of biomedical technologies. These applications include electrical stimulation therapies [9–12], diagnostic imaging techniques [13, 14], and electroporation-based treatments [15–17].

Electroporation is a biophysical phenomenon where short, high-voltage electrical pulses temporarily permeabilise cell membranes, allowing ions and molecules, such as drugs or nucleic acids, to enter/exit the cells. Depending on the pulse parameters, electroporation can be reversible, where cells recover after the membrane resealing, or irreversible, which leads to cell death [18–20]. Both reversible and irreversible electroporation are used in a wide variety of fields, from biomedicine and biotechnology to the food industry [16, 17, 21–25]. Reversible electroporation is commonly used for gene electrotransfer or drug delivery, with skeletal muscle being the predominant target [26–28]. In contrast, pulsed field ablation, a treatment modality that is based on irreversible electroporation, is advancing the treatment of cardiac arrhythmias, particularly atrial fibrillation, through pulmonary vein isolation [29–32]. The end goal of pulsed field ablation is to irreversibly damage the target tissue, resulting in cessation of conduction of electrical signals that cause arrhythmias. It is therefore of great interest and importance to the success of this treatment that we understand the mechanisms of muscle cell death, as well as how electroporation affects the target tissue properties such as electrical impedance, as this impedance will govern current flow (and electric field distribution) through the target tissue post-treatment.

In the food processing industry, the phenomenon of electroporation falls under the umbrella of a wider, more encompassing term *pulsed electric fields* treatment, which is more related to the method of altering the tissue rather than the phenomenon of increased membrane permeability itself, since it is with intense electrical pulses used to pre-treat various food matrices that the intended disruption of cell membranes, microorganisms, or enzymes is achieved resulting in a desired effect. The treatment, well established for processing of plant materials, is also being examined for its potential in the meat industry for e.g. tenderisation, as it can improve meat tenderness by disrupting muscle fibres and enzymatic activity [33], enhancing drying and curing [34], and for improving quality by reducing cooking time and improving texture during sous-vide processing [35]. However, there are many open questions as to the exact mechanisms by which pulsed electric fields affect muscle tissue. This void is exacerbated by large biological diversity in the raw material (animal species, tissue type and origin, etc.) and a plethora of possible combinations of treatment parameters, both electrical and other physical conditions (e.g.

temperature, time post-mortem, etc.) [33, 36]. This variability and wide-open parameter space produce a need to not only characterise the treated material from the electrical perspective to ensure success and homogeneity of the treatment by pulsed electric fields, but also to provide means of detecting and quantifying the effects of the treatment in the target tissue.

Regardless of whether we are interested in the response of muscle tissue to electric fields for purposes of biomedical or food processing applications, it is important to note that both skeletal and cardiac muscles exhibit directional differences in their electrical properties, a property known as anisotropy [37–39]. The anisotropy in skeletal and cardiac muscles arises from the alignment of the muscle fibres, which are embedded in a complex network of connective tissue layers [40, 41]. These layers, together with the insulating sarcolemma, form a unique arrangement that restricts the movement of ions in certain directions, resulting in different electrical properties that vary depending on fibre orientation, especially at low frequencies [42]. Electrical conductivity is usually higher in the direction of the muscle fibres than across them [4, 6]. Interestingly, even tissues that are not intrinsically anisotropic, such as liver tissue, can develop anisotropic properties after electroporation [43]. The characterisation of anisotropic behaviour is important for understanding how electrical stimuli influence the tissue response.

Electrical impedance spectroscopy (EIS) is a powerful technique for characterising the electrical properties of biological tissue over a wide frequency range. By applying a small alternating current (AC) and measuring the resulting voltage, EIS provides information on both the resistive and capacitive properties of tissues [44–46]. Through analysis of the impedance spectrum important insights into how tissues respond to external electrical stimuli are provided, aiding in the evaluation of treatment outcomes. Furthermore, EIS can be effectively used to characterise anisotropic tissue properties, distinguishing electrical behaviour along and across the fibre axis [3, 4, 47]. Its non-invasive and real-time capabilities make it an indispensable tool in both clinical and research settings, enabling the exploration of the intricate relationship between tissue structure, composition, and electrical properties. In addition, EIS enables the evaluation of dynamic changes in tissue properties, such as those induced by electroporation [48–51] or occurring post-mortem [52–54]. There is even an established methodology of assessing the integrity of the cell membranes using EIS – the P_y parameter of meat quality, which relates the degree of meat degradation post-mortem to the meat quality properties such as drip/cooking/frying loss, pH, colour, etc. [55].

In addition to EIS, there are alternative methods for assessing the electrical properties of tissue, such as analysing voltage and current waveforms recorded during the application of electrical pulses. Monitoring these electrical signals in real time provides valuable insight into changes in membrane properties during electroporation [56, 57]. Current dynamics during the application of high-voltage pulses have been shown to be indicative of electroporation processes, further highlighting the potential of this approach to characterise tissue responses. While less frequently employed, these analyses complement EIS by providing additional information on tissue behaviour during and after electroporation [58, 59].

The aim of the present study was threefold: first, to assess whether skeletal muscle anisotropy can be shown by impedance spectroscopy measurements in ex vivo tissue post-mortem, second, to validate the experimental results by numerical modelling with emphasis on the permeability of the plasma membrane, and third, to show whether loss of integrity of the skeletal muscle cell plasma membrane resulting from phospholipase activity and other degradation processes can be likened, in effect, to increasing cell membrane permeability by electroporation. We sought to assess the feasibility of characterising the anisotropic properties of the tissue ex vivo, several hours post-mortem, when cellular and structural changes may alter the electrical behaviour of the tissue. In addition, we analysed the current dynamics during the application of high-voltage pulses to complement the impedance data, allowing for a more comprehensive analysis of tissue responses. The primary key objective was to demonstrate that muscle tissue can serve as a reliable model for in vivo tissue even a few hours post-mortem. This offers an alternative to

experiments with living animals and in turn reduces the ethical burden of animal testing in medical research. The secondary key objective was to demonstrate that i) electroporation as a mechanism of increasing cell membrane permeability (and current conductivity) and ii) breaking down of the structural components of the membrane through phospholipase activity leading to membrane thinning and increased permeability [60], both impact the muscle anisotropy in the same sense, thus demonstrating that the muscle cell plasma membrane is indeed the structure responsible for anisotropy of living muscle tissue electrical impedance.

2 Materials and methods

2.1 Experimental setup

The experimental setup for the impedance spectroscopy experiments comprised an LCR metre, a pulse generator, an oscilloscope, a treatment chamber, and a PC running LabVIEW for data acquisition and control. The LCR metre (model E4980A, Keysight Technologies, Santa Rosa, CA, USA) was used to perform impedance measurements, while the laboratory prototype pulse generator (HV-LV) [56] was used to deliver high-voltage electroporation pulses. The oscilloscope (model HDO6104A-MS, LeCroy, Chestnut Ridge, NY, USA), equipped with voltage (model HVD3206A, LeCroy, Chestnut Ridge, NY, USA) and current (model CP031A, LeCroy, Chestnut Ridge, NY, USA) probes, was used to monitor and verify the electrical pulses generated by the pulse generator. A custom-built acrylic treatment chamber with a diameter of 26 mm was used to house the tissue samples during the experiments. The chamber was equipped with two pairs of custom-made stainless-steel electrodes spaced 6 mm apart, which were used both for delivering the high-voltage electroporation pulses and for impedance measurements. These electrodes were configured for 4-electrode impedance measurements to ensure accurate and reliable data acquisition. Stainless steel was selected for electrode material as it provides sufficient stability and durability for high-voltage pulsing and is safe to use, since, in the 4-electrode configuration employed, the influence of electrode polarisation is minimised, making the use of non-polarisable materials such as platinum unnecessary. A switch box was integrated into the setup to allow seamless switching between the LCR metre and pulse generator connections to the electrodes. The PC running LabVIEW (version LabVIEW 2020, National Instruments, Austin, TX, USA) controlled the data acquisition and enabled automated measurement procedures and real-time data monitoring. A photograph of the experimental setup with the individual components is shown in Figure 1.

2.2 Preparation of muscle tissue samples

The muscle tissue used in the experiments was obtained from the trapezius muscle of a pig (*Sus scrofa domesticus*), which was harvested within a half-hour after death. The tissue was sourced from a slaughterhouse that operates according to Slovenian law. To ensure consistency of the impedance measurements, a muscle with a uniform orientation of the fibres was selected. This allowed a reliable comparison of impedance measurements in both parallel and perpendicular orientations relative to the fibres. After harvesting, the tissue was cooled to 4 °C to preserve its structure and properties. Before each series of experiments, which were conducted at three different time points (3 hours, 24 hours, and 72 hours post-mortem), the tissue samples were allowed to warm up to room temperature. A sharp cork borer was used to manually cut discs of 26 mm diameter from the tissue sample. The thickness of the discs was 6 mm. Two types of samples were prepared: one set was cut so that the impedance measurements could be performed along the muscle fibres (parallel orientation), and the other set was prepared so that the measurements could be performed across the muscle fibres (perpendicular orientation).

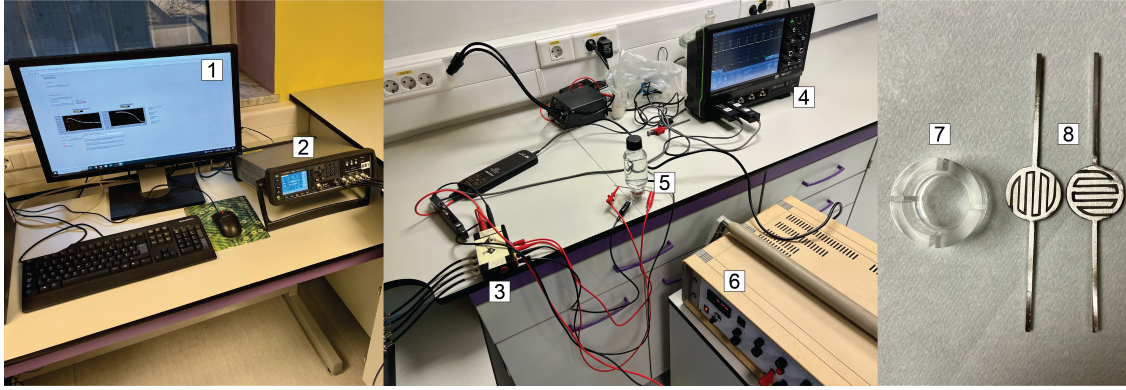


Figure 1: Experimental setup for impedance spectroscopy experiments. The setup consists of (1) a PC running LabVIEW for data acquisition and control, (2) an LCR metre for performing impedance measurements, (3) a switch box that allows switching between the connections of the LCR metre and the pulse generator to the electrodes, (4) an oscilloscope with voltage and current probes for signal monitoring, (5) a treatment chamber with two pairs of electrodes and a tissue sample between the pairs, (6) a laboratory prototype pulse generator, (7) a treatment chamber made of acrylic glass, and (8) two pairs of stainless steel electrodes used for 4-electrode impedance measurements within the treatment chamber.

2.3 Impedance spectroscopy and pulse dynamics analysis

Impedance spectroscopy measurements were conducted on untreated muscle tissue at three different post-mortem time points: 3 hours, 24 hours, and 72 hours. These baseline measurements were performed to characterise the electrical properties of the tissue in both parallel and perpendicular orientations relative to the muscle fibres. At each time point, six replicates of the experiment were performed ($N = 6$) to ensure statistical reliability. Absolute impedance and phase angle were measured in the frequency range from 20 Hz to 2 MHz, with a sinusoidal voltage of 100 mV peak applied to one pair of electrodes. This pair served as the current source and sink, while the other pair was used to measure the voltage drop, as customarily configured in 4-electrode impedance analysis. The selected frequency range allowed for characterisation of the tissue's electrical properties over a broad range and reflected the maximum measurement capability of the LCR meter used (Keysight E4980A).

Following the baseline impedance measurements, electroporation pulses were applied to the tissue samples at the 3-hour and 24-hour post-mortem time points, but not at 72-hour post-mortem (see Discussion for an explanation). The impedance measurements were recorded again within 2 seconds after pulse delivery (allowing for the time to switch the electrodes from the generator to the LCR meter). Electroporation was performed using eight rectangular pulses, each with a duration of 100 μs , an amplitude of either 200 V or 400 V, and a pulse repetition rate of 1 s^{-1} . Pulse amplitudes were selected to induce different degrees of electroporation, with 200 V producing moderate effects and 400 V resulting in more extensive membrane permeabilisation. The ratio of the impedance magnitude after electroporation ($|Z_{\text{post}}|$) to the impedance magnitude before electroporation ($|Z_{\text{pre}}|$) was calculated for each sample to quantify the effect of electroporation on the impedance of the tissue. Results are expressed as mean \pm standard deviations.

In addition, the pulse dynamics during the electroporation pulses were analysed. The normalised electrical current difference (ΔI_{norm}) was calculated to quantify the change in current during the first delivered pulse, similar to the approach used previously [61]. We defined ΔI_{norm} as the difference between the final current (I_f) at $t = 95 \mu\text{s}$ (determined as the average value of the current between 94.5 and 95.5 μs to eliminate measurement noise) and the initial current

(I_i) at $t = 5 \mu\text{s}$ (average value of the current between 4.5 and 5.5 μs), divided by the initial current (I_i), as shown in the following equation:

$$\Delta I_{\text{norm}} = \frac{I_f - I_i}{I_i} \quad (1)$$

We chose the current as recorded at 5 μs as the initial current to allow for all the transients in the current waveform (e.g. capacitive spike at the start of the pulse) to completely fade consistently for all pulses. The sample that represents the final current value (at 95 μs) was chosen to consistently capture the highest current value before the pulse starts to decrease in amplitude.

To assess the statistical significance of the results, Student's t -test was used to compare the current differences at different orientations and time points. All statistical analysis and data processing were performed using Python.

2.4 Numerical modelling

The simulations were conducted using COMSOL Multiphysics software (version 6.3, COMSOL AB, Stockholm, Sweden), employing the finite element method (FEM). To optimise computational efficiency, a simplified three-dimensional geometry was designed to approximate the experimental muscle tissue sample. The tissue was modelled as a cubic domain with dimensions of 1 mm per side, while the muscle fibres were represented as cylindrical structures extending over the entire domain, each with a diameter of 60 μm (see Figure 2a). The volume fraction of the muscle fibres was set at 78%, which corresponds to typical values reported in the literature for skeletal muscle tissue [62]. In our previous work [63], we showed that variations in volume fraction had no significant effect on the anisotropy rate, supporting the use of a fixed value in the model.

Since the cell plasma membranes are several orders of magnitude thinner than the other modelled dimensions, they were not explicitly included in the geometry. Instead, their electrical effect was incorporated through a boundary condition that represents the membrane as a thin resistive-capacitive layer. This condition relates the transmembrane current density to the local transmembrane voltage and accounts for both membrane conductivity and permittivity. The membrane's thickness was used together with its electrical properties to define the specific impedance of the boundary.

The numerical model is based on the quasi-static approximation and solves the Laplace equation:

$$\nabla \cdot (\sigma \nabla \varphi) = 0 \quad (2)$$

for the electric potential φ , with σ representing the conductivity in the intracellular, extracellular, and membrane regions.

The electrodes were positioned in two different orientations with respect to the muscle fibre alignment (see Figure 2b). In the parallel orientation, the electrodes were placed so that the impedance was measured along the direction of the muscle fibres, whereas in the perpendicular orientation, the impedance was measured perpendicular to the fibre orientation. The simulations were performed in the frequency domain to compute the steady-state electric potential distribution across the model at each frequency. This allowed us to determine the frequency-dependent impedance of the tissue, enabling direct comparison with the experimental measurements in the 20 Hz to 2 MHz range. The finite element mesh comprised approximately 1.9 million elements, with second order (quadratic) Lagrange elements used for potential discretisation. A mesh convergence check was performed to ensure numerical stability, confirming that the computed impedance values remained consistent with finer mesh resolutions.

The main objective of the simulations was to calculate the impedance in both parallel and perpendicular orientations at 3 hours and 24 hours post-mortem experimental conditions, when

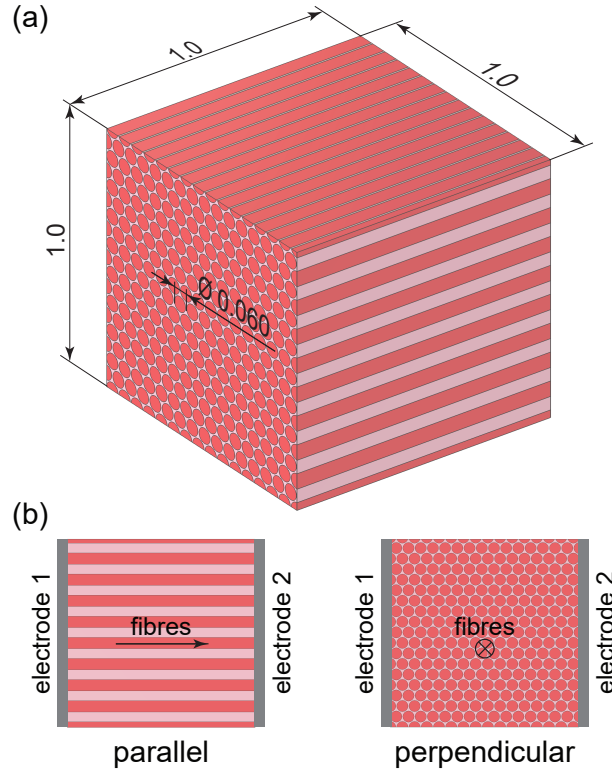


Figure 2: (a) Geometry and dimensions of the muscle tissue model in COMSOL Multiphysics. Note that all dimensions are in mm. (b) The two orientations of the electrodes relative to the orientation of the muscle fibres: in the parallel orientation, the electrodes are positioned so that the impedance is measured in the direction parallel to the muscle fibres; in the perpendicular orientation, the impedance is measured perpendicular to the fibre orientation.

the anisotropy is still observed. A parametric study was conducted to evaluate the effect of varying plasma membrane conductivities on the impedance predictions of the model. Membrane conductivities were adjusted to simulate changes in tissue properties over time. The results for the different membrane conductivities were then compared with the experimental measurements at 3 hours and 24 hours post-mortem. The best-fit conductivity values for the membranes at each time point were determined using the least mean squares method. The impedance values obtained from the model were adjusted to take into account the differences in dimensions between the model and the experimental setup. The calculated impedance was adjusted using the following equation:

$$|Z_{\text{adjusted}}| = |Z_{\text{model}}| \cdot \frac{k_1}{k_2} \quad (3)$$

where $|Z_{\text{adjusted}}|$ is the adjusted impedance, $|Z_{\text{model}}|$ is the impedance calculated by the model, k_1 is a factor that accounts for the difference in electrode spacing between the experimental and model geometries, and k_2 is a factor that accounts for the difference in the electrode surface areas between the experiments and the model. While only the ratio k_1/k_2 affects the impedance scaling, we define the two factors separately to preserve a clear connection to the distinct geometric differences between the model and experimental setups. This adjustment ensures that the model impedance results are directly comparable with experimental measurements.

The parameters used in the model and their corresponding values are listed in Table 1. The relative permittivity of the membranes was increased compared to the typically used values for the relative permittivity of the membranes in order to take into account the connective tissue

layers surrounding the muscle fibres, which were not explicitly included in the geometry of the model. Membrane conductivity was not modelled as a function of transmembrane voltage. Instead, it was treated as a constant parameter within each simulation, and varied only across different simulations to reflect changes in membrane integrity due to post-mortem degradation. This adjustment was important to better represent the electrical properties of the tissue and to ensure that the model reflected the experimentally observed impedance changes. It is important to note that while COMSOL Multiphysics was used for simulations, the underlying model is fundamentally based on well-known principles of bioelectricity and can be reproduced using any numerical method that solves the quasi-static Laplace equation with the same boundary conditions and parameter settings applied. In summary, the novelty of our modelling approach lies in representing muscle tissue at the level of individual fibres. This structural model allows for anisotropy to emerge naturally from the geometry and electrical properties of the fibres, rather than relying on homogenised bulk tissue properties, providing direct insight into how changes in membrane conductivity influence macroscopic impedance behaviour. The post-processing of the simulation results was performed using Python.

Table 1: Parameters and their corresponding values used in the numerical model [64–67].

Parameter	Value	Description
f	0.78	Volume fraction of fibres
σ_i	0.80 S/m	Intracellular conductivity
σ_e	1.80 S/m	Extracellular conductivity
σ_m	varied	Membrane conductivity
ε_i	70	Intracellular relative permittivity
ε_e	80	Extracellular relative permittivity
ε_m	30	Membrane relative permittivity
t_m	4 nm	Membrane thickness
k_1	6	Adjustment factor (electrode spacing)
k_2	179.71	Adjustment factor (electrode area)

3 Results and discussion

3.1 Impedance of untreated skeletal muscle

The frequency-dependent impedance of untreated skeletal muscle was measured at three post-mortem time points to assess the changes in the electrical properties of the tissue over time, focusing on the anisotropy between the two orientations with respect to the muscle fibres: the parallel (i.e., the impedance was measured in the direction parallel to the muscle fibres) and the perpendicular (i.e., the impedance was measured in the direction perpendicular to the muscle fibres).

At 3 hours post-mortem, significant differences in skeletal muscle impedance can be observed between the parallel and perpendicular orientations (Figure 3a), with the perpendicular orientation exhibiting more than 10 times higher impedance at lower frequencies. This pronounced anisotropy is due to the fibrous structure of skeletal muscle and the preservation of cell plasma membranes shortly (at minimum 3 hours) after death, resulting in significantly different impedance characteristics between the two orientations.

By 24 hours post-mortem, the anisotropy remains, but the difference between the two orientations decreases, with the impedance in the perpendicular orientation being only about three times higher than in the parallel orientation (Figure 3b). This reduction indicates the onset of cell degradation, including membrane disintegration, although the fibrous structure of the

muscle still contributes to some anisotropy.

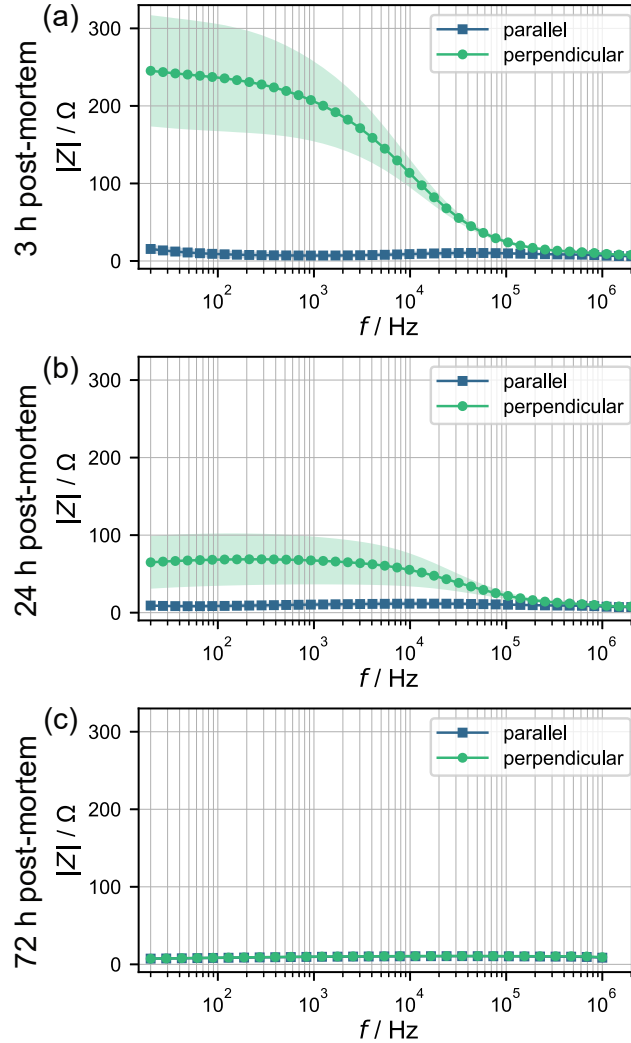


Figure 3: Frequency-dependent absolute impedance of untreated skeletal muscle in the parallel (i.e., the impedance was measured in the direction parallel to the muscle fibres) and the perpendicular (i.e., the impedance was measured in the direction perpendicular to the muscle fibres) orientations at (a) 3 hours post-mortem, (b) 24 hours post-mortem, and (c) 72 hours post-mortem. The results are given as mean values \pm standard deviations (shaded areas), with $N = 12$.

At 72 hours post-mortem, there are no obvious differences in impedance between the two orientations (Figure 3c). The impedance is equal in both directions and lower than at earlier time points, reflecting the loss of the muscle's structural integrity. These results highlight the progressive degradation of skeletal muscle tissue over time and the corresponding changes in electrical impedance, with the anisotropic behaviour in the early post-mortem stages attributed to the preservation of muscle structure and membranes, and the reduction in anisotropy corresponding to tissue breakdown. Interestingly, in our previous study [Šmerc et al., article submitted for publication, manuscript is available to reviewers upon request], where we looked at muscle anisotropy *ex vivo* using CDI (an MRI-based method of mapping current pathways in tissue), we have shown that 48 hours post-mortem the electric current distribution still exhibits some anisotropy. Those CDI measurements have shown that current flows differently depending on

whether it is injected into tissue perpendicularly or parallel to the muscle fibres (two needle electrodes were used, rather than plate electrodes). This would seem to indicate that there is still some anisotropy present 48 hours post-mortem, however, as we have shown with impedance measurements, all anisotropy is completely undetectable a day later, 72 hours post-mortem.

The observed anisotropy in impedance measurements at 3 hours post-mortem is consistent with findings reported in the literature, which collect data from various *ex vivo* skeletal muscle studies, some of which were conducted immediately after incision [3, 4, 6]. Although different methods were used in these studies, the anisotropic behaviour observed in this work is consistent with the literature, supporting the feasibility of using post-mortem muscle tissue as a reliable model for *in vivo* tissue.

3.2 Electroporation-induced changes in skeletal muscle impedance

The effect of electroporation on the electrical properties of skeletal muscle tissue was investigated by measuring the frequency-dependent impedance before ($|Z_{\text{pre}}|$) and after ($|Z_{\text{post}}|$) electroporation, with the impedance ratio ($|Z_{\text{post}}|/|Z_{\text{pre}}|$) serving as a measure of the electroporation-induced changes. Electroporation was performed using 8 rectangular pulses, each with a duration of 100 μs , with amplitudes of 200 V or 400 V, and at a pulse repetition rate of 1 s^{-1} . The results for both 3 hours and 24 hours post-mortem are shown in Figure 4. We chose not to perform electroporation experiments 72 hours post-mortem since, as is evident in Figure 3c, there is no observable anisotropy even in intact tissue.

At 3 hours post-mortem, the impedance ratio showed marked changes in the response to electroporation in both the parallel and perpendicular orientations. Following the application of 200 V pulses, the impedance decreased by about 10 % in the parallel orientation (Figure 4a) and by about 15 % in the perpendicular orientation (Figure 4b), as shown in Figure 4c. This modest reduction indicates that pulses with an amplitude of 200 V are not sufficient to induce major changes in the electrical properties of muscle tissue. However, increasing the amplitude to 400 V resulted in a much stronger effect. In the parallel orientation, the impedance decreased by up to 20 % (Figure 4d), while in the perpendicular orientation the decrease was about 60 % (Figure 4e), as can be seen from the impedance ratio (Figure 4f). These larger decreases at higher amplitudes indicate that the 400 V pulses caused significant electroporation, disrupting plasma membranes and significantly altering the electrical properties of the tissue.

At 24 hours post-mortem, the impedance changes were less pronounced, likely due to tissue degradation. In the parallel orientation, 200 V pulses caused minimal impedance changes, with no significant reduction observed (Figure 4g). However, in the perpendicular orientation, a reduction of a similar magnitude to that observed in the samples collected 3 hours post-mortem was still observed (Figure 4h), as shown in Figure 4i. When the amplitude was increased to 400 V, the changes in the parallel orientation were again minimal (Figure 4j). In contrast, the impedance in the perpendicular orientation decreased by approximately 30 % (Figure 4k), as shown in Figure 4l, demonstrating a weaker but still observable effect compared to the 3 hours post-mortem. This reduction in the magnitude of the impedance change 24 hours post-mortem suggests that as the tissue degrades, its susceptibility to electroporation decreases, likely due to the degradation of cellular structures and plasma membranes.

Although the observed changes in impedance after electroporation (Figures 4a, 4b, 4d, 4e, 4g, 4h, 4j, 4k) appear small and statistically insignificant in most cases, except for the perpendicular orientation with 400 V pulses (Figure 4e), it is important to note that electroporation consistently decreased tissue impedance in each pair of before-after measurements. The relatively large standard deviations observed are attributable to variability between different tissue samples.

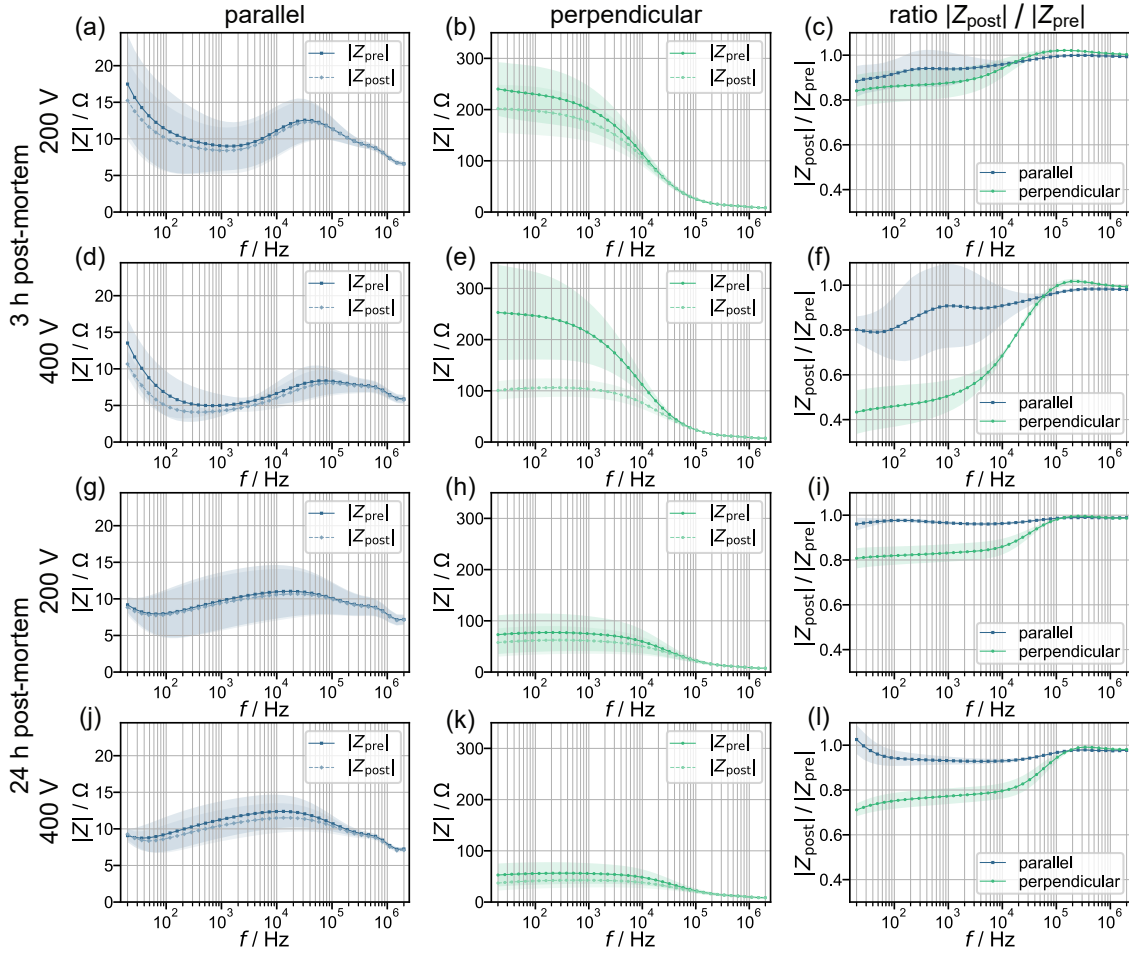


Figure 4: Frequency-dependent absolute impedance of untreated skeletal muscle (i.e., before electroporation; $|Z_{\text{pre}}|$), treated skeletal muscle (i.e., within 2 s after electroporation; $|Z_{\text{post}}|$), and their ratio ($|Z_{\text{post}}|/|Z_{\text{pre}}|$), measured in the parallel (i.e., the impedance was measured in the direction parallel to the muscle fibres) and the perpendicular (i.e., the impedance was measured in the direction perpendicular to the muscle fibres) orientations. Electroporation was performed using 8 rectangular pulses, each with a duration of 100 μs , an amplitude of either 200 V or 400 V, and a pulse repetition rate of 1 s^{-1} . The results for 3 hours post-mortem are shown in (a–f), and for 24 hours post-mortem in (g–l). The amplitude of the applied pulses was 200 V in (a–c, g–i) and 400 V in (d–f, j–l). The absolute impedance of untreated and treated skeletal muscle, measured in the parallel orientation, is shown in (a, d, g, j), and in the perpendicular orientation in (b, e, h, k). The impedance ratio ($|Z_{\text{post}}|/|Z_{\text{pre}}|$) is shown in (c, f, i, l). The results are given as means \pm standard deviations (shaded areas), with $N = 6$. Note the different ordinate scales for absolute impedance measured in the parallel (a, d, g, j) and perpendicular (b, e, h, k) orientations.

The observed results indicate that the efficacy of electroporation on skeletal muscle impedance is time-dependent, with a stronger effect at earlier post-mortem stages when tissue integrity is better preserved. At 3 hours post-mortem, electroporation with 400 V pulses resulted in a significant decrease in impedance, particularly in the perpendicular orientation. This significant decrease in the perpendicular orientation can be attributed to the orientation of the muscle fibres and cell plasma membranes relative to the applied electric field. In the perpendicular orientation, the membranes lie in the path of the electric field and are directly electroporated, which leads to significant impedance changes. In contrast, in the parallel orientation, the membranes are

aligned along the field and do not present a significant barrier, resulting in smaller impedance changes. At 24 hours post-mortem, the effect of electroporation was significantly attenuated, reflecting the progressive loss of tissue structure and functionality as well as reduced membrane integrity.

The observed anisotropic effects on impedance changes after electroporation provide a mechanistic explanation for the differences in lesion shapes observed in skeletal [63] and cardiac [68] muscles when electric fields are applied in different orientations. Electroporation in the perpendicular orientation resulted in significantly greater impedance decrease, indicating more extensive cell plasma membrane disruption compared to the parallel orientation. This is consistent with the structural arrangement of the muscle fibres, where the membranes are more exposed to the electric field in the perpendicular orientation, leading to greater conductivity changes. In the parallel orientation, the field is aligned with the fibres, bypassing membranes and causing less disruption. These differences have a direct influence on permeabilisation (e.g. in DNA delivery by electroporation) and on lesion formation in electroporation-based ablation procedures. Lesions in the parallel orientation are narrower and less extensive, while lesions in the perpendicular orientation are larger and more widespread.

Existing models often assume the same factor of conductivity increase for both parallel and perpendicular orientations and maintain a constant anisotropy ratio (the ratio of parallel to perpendicular conductivity) before and after electroporation [32, 68–71]. Even though these models are focused on cardiac muscle, we can reasonably assume that our findings from skeletal muscle are at least partially transferable to cardiac muscle, as both tissues exhibit anisotropic properties due to their fibrous structure. We have observed that the impedance is much less affected by electroporation in the parallel orientation, suggesting that the factor of conductivity increase should be much lower in the parallel orientation than in the perpendicular orientation. This also means that the anisotropy ratio after electroporation should not be the same as before electroporation. Incorporating these findings into numerical models could increase their accuracy and enable better predictions about the distribution of the electric field and the formation of lesions.

3.3 Electric current dynamics during electroporation

The dynamics of the electric current during electroporation were evaluated by analysing the normalised electric current difference (ΔI_{norm}), which we defined as the difference between the final (I_f ; at $t = 95 \mu\text{s}$) and initial (I_i ; at $t = 5 \mu\text{s}$) current values of the first pulse delivered, normalised to the initial current value (I_i ; see Figure 5a). This parameter reflects the changes in electrical conductivity induced directly by electroporation. The results for the parallel and perpendicular orientations at 3 hours and 24 hours post-mortem are shown in Figures 5b and 5c, respectively. The alternative comparison, focusing on comparing 3 hours post-mortem versus 24 hours post-mortem, is shown for 200 V and 400 V pulses in Figures 5d and 5e, respectively.

At 3 hours post-mortem (Figure 5b), the normalised current difference showed significant differences between the parallel and perpendicular orientations, with the perpendicular orientation consistently exhibiting higher values. For 200 V pulses, the median normalised current difference in the parallel orientation was 0.12, while it was 0.29 in the perpendicular orientation ($p = 1.73 \times 10^{-5}$). A similar trend was observed for 400 V pulses, where the median of the normalised current difference was 0.04 in the parallel orientation and increased to 0.11 in the perpendicular orientation ($p = 1.58 \times 10^{-4}$).

At 24 hours post-mortem (Figure 5c), the values of the normalised current difference were significantly lower, indicating the influence of tissue degradation on the electroporation dynamics. For 200 V pulses, the median normalised current difference in the parallel orientation had decreased to 0.04, with respect to 0.12 in the perpendicular orientation. For 400 V pulses, the medians were 0.03 in the parallel orientation and 0.06 in the perpendicular orientation. Statistical analysis confirmed significant differences between the two orientations for both 200 V

($p = 6.68 \times 10^{-4}$) and 400 V ($p = 1.66 \times 10^{-4}$).

When comparing the normalised current difference between 3 hours and 24 hours post-mortem (Figure 5d and 5e), significant differences were found in most cases. For 200 V pulses (Figure 5d), significant differences were observed in both orientations (parallel: $p = 6.12 \times 10^{-3}$; perpendicular: $p = 8.34 \times 10^{-6}$). For 400 V pulses (Figure 5e), however, there was a significant difference in the perpendicular orientation ($p = 4.13 \times 10^{-4}$), while this was not the case for the parallel orientation ($p = 8.37 \times 10^{-2}$). These results suggest that the progressive degradation of cell plasma membranes over time reduces the tissue's ability to undergo electroporation.

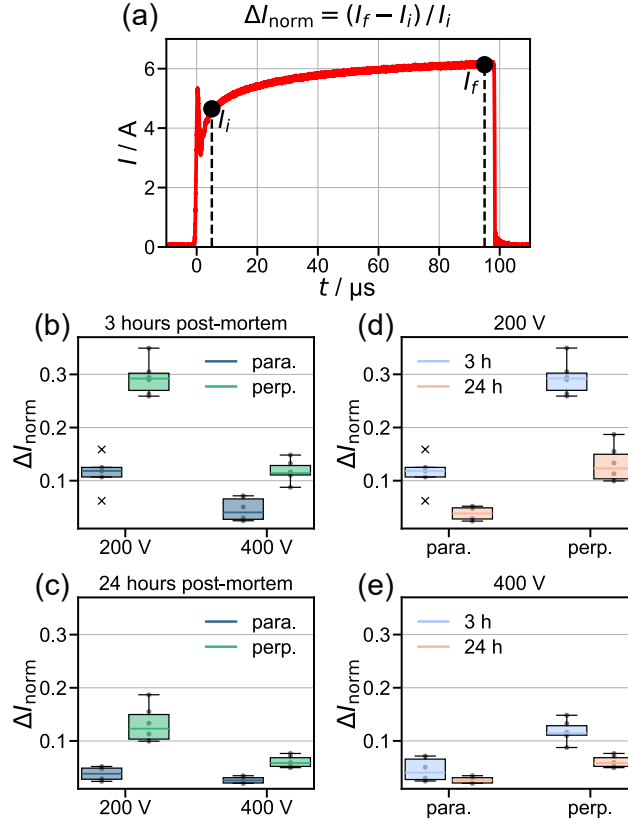


Figure 5: (a) The definition of the normalised electric current difference (ΔI_{norm}), calculated as the difference between the final (I_f ; at $t = 95 \mu\text{s}$) and the initial (I_i ; at $t = 5 \mu\text{s}$) current values of the first electroporation pulse delivered, divided by the initial current value (I_i). The calculated normalised electric current for the parallel (i.e., the impedance was measured in the direction parallel to the muscle fibres) and the perpendicular (i.e., the impedance was measured in the direction perpendicular to the muscle fibres) orientations at (b) 3 hours post-mortem and (c) 24 hours post-mortem. Electroporation was performed using 8 rectangular pulses, each with a duration of $100 \mu\text{s}$, an amplitude of either 200 V or 400 V, and a pulse repetition rate of 1 s^{-1} . The results are presented as boxplots, with the median marked by the centre line, the box representing the interquartile range (IQR), and the whiskers extending to the most extreme values within $1.5 \times \text{IQR}$. Outliers, which are marked as individual points, are values beyond $1.5 \times \text{IQR}$. $N = 6$.

The differences observed between the orientations can be attributed to the role of the cell plasma membranes in determining the tissue's electrical response. In the perpendicular orientation, the membranes act as significant barriers to current flow, and their electroporation leads to greater conductivity changes. In contrast, in the parallel orientation, the current bypasses the membranes, resulting in smaller changes in conductivity.

The differences between the 3-hour and 24-hour post-mortem samples illustrate the influence of tissue degradation. At 3 hours post-mortem, the better-preserved tissue structure and membrane integrity allow a more pronounced electroporation. In contrast, the degradation of cellular and extracellular components 24 hours post-mortem impairs membrane function, resulting in a lower ability of the tissue to undergo electroporation and a smaller change in current dynamics.

These results emphasise the critical role of tissue orientation and integrity in determining the electrical response during electroporation. The perpendicular orientation showed more pronounced changes in conductivity, and the effects were more pronounced at earlier stages and became less significant as the tissue degraded.

3.4 Numerical modelling results and comparison with experimental measurements

Figure 6 compares the modelling results with the experimentally determined frequency-dependent impedance of the untreated skeletal muscle in both the parallel and perpendicular orientations. The modelling results for 3 hours and 24 hours post-mortem are shown in Figures 6b and 6d, respectively, while the experimental data are shown in Figures 6a and 6c, respectively.

The best fit of the experimental data in the perpendicular orientation was obtained using the least mean squares method, which yielded a membrane conductivity of $\sigma_m = 5 \times 10^{-7}$ S/m for the 3 hours post-mortem samples (Figure 6b). The other curves, shown in lighter hues, correspond to different membrane conductivity values ranging from 1×10^{-8} S/m to 1×10^{-6} S/m, illustrating how the impedance changes with variations in membrane conductivity.

For the 24-hour post-mortem data (Figure 6d), the best fit to the experimental results was achieved with a membrane conductivity of $\sigma_m = 1 \times 10^{-4}$ S/m. The other curves correspond to membrane conductivity values between 0.6×10^{-4} S/m and 1.4×10^{-4} S/m. The effect of the membrane conductivity on the parallel orientation is negligible at both time points.

In general, the modelling results are in agreement with the experimental data, suggesting that the numerical model accurately reflects the general trends of the frequency-dependent impedance of the untreated skeletal muscle. However, a slight difference is observed between the experimental and modelling results, particularly in the parallel orientation and at higher frequencies in the perpendicular orientation, where the impedance values are higher in the modelling results. This discrepancy suggests that the intra- and extracellular conductivities of the tissue sample in our experiments were likely higher than the values used in the model, which could explain the observed differences at these frequencies.

The numerical modelling results obtained provide a useful framework for understanding the experimental impedance data, particularly the changes observed over time as the tissue degrades. The sensitivity of the model to membrane conductivity is consistent with the experimental observations of post-mortem tissue degradation [55] and supports the idea that membrane integrity plays a critical role in determining the electrical properties of skeletal muscle.

It is also important to consider the uncertainty in the conductivity and permittivity values of the individual tissue constituents, i.e., intracellular space, extracellular space, and membranes, used in the model. The data for these tissue constituents are not precisely known and may vary due to tissue heterogeneity and post-mortem changes. The values used in the model are based on literature, which may not fully capture the variations due to tissue heterogeneity and post-mortem changes. Additionally, the values in literature also vary considerably. This uncertainty in the material properties could contribute to the observed discrepancies between the experimental and modelling results, which seem especially evident at higher frequencies where the calculated impedance is higher than the experimental one, suggesting that the values of intra- and extracellular conductivities used in the model are too low. Nevertheless, the model provides a useful framework for understanding the overall trends in the impedance data, with sensitivity to membrane conductivity being consistent with the experimental observations of post-mortem tissue degradation.

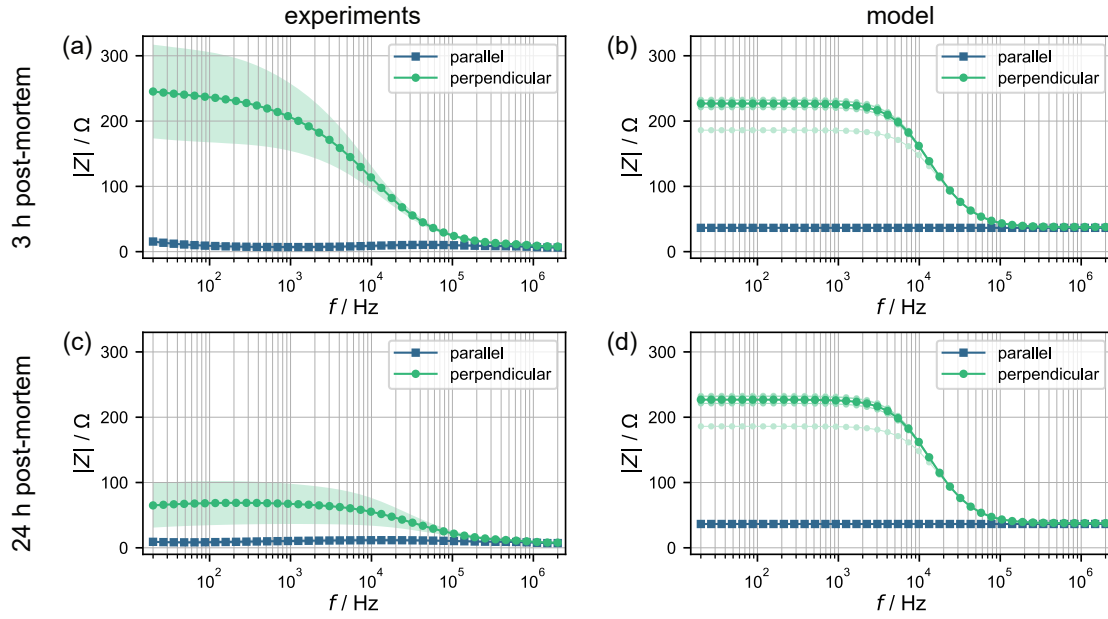


Figure 6: Frequency-dependent absolute impedance of untreated skeletal muscle in the parallel (i.e., the impedance was measured in the direction parallel to the muscle fibres) and the perpendicular (i.e., the impedance was measured in the direction perpendicular to the muscle fibres) orientations. The experimentally determined impedance is shown in (a, c), while the corresponding modelling results are shown in (b, d). The results for 3 hours post-mortem are shown in (a, b), and for 24 hours post-mortem in (c, d). The experimental results are given as mean values \pm standard deviations (shaded areas), with $N = 12$. In (b), the best fit of the perpendicular orientation to the corresponding experimental data (shown in green) corresponds to a membrane conductivity of $\sigma_m = 5 \times 10^{-7}$ S/m. The other curves (shown in lighter hue) correspond to membrane conductivity values, from the highest to the lowest impedance, of 1×10^{-8} S/m, 1×10^{-7} S/m, 1×10^{-6} S/m, and 5×10^{-6} S/m, respectively. In (d), the best fit of the perpendicular orientation to the corresponding experimental data (shown in green) corresponds to a membrane conductivity of $\sigma_m = 1 \times 10^{-4}$ S/m. The other curves (shown in lighter hue) correspond to membrane conductivity values, from the highest to the lowest impedance, of 0.6×10^{-4} S/m, 0.8×10^{-4} S/m, 1.2×10^{-4} S/m, and 1.4×10^{-4} S/m, respectively. The influence of the membrane conductivity on the parallel results is negligible.

The reader should note that possible routes towards generalising the model and the experimental approach must consider that muscle tissues of different animal species, in general, degrade at different rates. These rates have been approximately determined for animals of interest as sources of meat and span a vast range; the fastest rates of decay (fish, chicken) can be up to an order of magnitude apart from the slowest (beef, lamb, deer) [72]. Our study did also not consider techniques of tissue conservation or preservation that have been developed mainly for the purposes of prolonging the viability of organs in organ donor programmes. Using some of those approaches, it should be feasible to considerably extend the window of usefulness of excised tissue samples from just a couple of hours to possibly several days [73].

4 Conclusions

We primarily set up our study to assess if it is possible to investigate anisotropy in skeletal muscle tissue *ex vivo* using impedance spectroscopy on an excised muscle, post-mortem. If an

animal is slaughtered in the process of meat production for human consumption, the experiment does not require sacrificing an animal expressly for scientific purposes. Our study suggests that perhaps some of the live animal experiments, where and if deemed suitable, could be replaced by ex vivo work, thereby reducing the moral and economic cost of animal experimentation. The approach certainly beats potato models that are currently used when animal experimentation is not feasible or justifiable [74].

Secondly, we built a model to validate the experimental results where we constructed a structured bundle of muscle fibres in silico and showed that anisotropy in electrical impedance is a direct result of skeletal muscle geometry if we account for typical intra- and extracellular conductivities of muscle cells and – most importantly – the low conductivity of the living cell plasma membrane.

And thirdly, we have shown through comparison of muscle anisotropy changes resulting from tissue dying and thus undergoing degradation processes versus those resulting from increasing cell membrane permeability by electroporation that these processes both affect the membrane permeability in a similar way, resulting in a like decrease in muscle anisotropy. We have thus shown that a single variable – i.e. the (im)permeability of the muscle cell membrane for ions – is responsible for the observed bulk tissue anisotropy in electrical impedance of skeletal muscle.

Possible limitations of the model and the experimental study mainly stem from its lack of comprehensiveness. The study should be understood as a proof of concept. Much work remains in characterising the dynamics of skeletal muscle electric impedance anisotropy changes for different muscle origins (species of animal, type of muscle, ...) and handling of the tissue after excision (temperature, preservation solution, ...). We relegate these endeavours to future work.

CRedit authorship contribution statement

Rok Šmerc: Conceptualization, Methodology, Software, Validation, Formal analysis, Investigation, Resources, Writing – Original Draft, Writing – Review & Editing, Visualization. **Damijan Miklavčič:** Writing – Review & Editing, Supervision, Funding acquisition. **Samo Mahnič-Kalamiza:** Conceptualization, Methodology, Investigation, Resources, Writing – Original Draft, Writing – Review & Editing, Supervision.

Declaration of Competing Interest

Damijan Miklavčič is the inventor and author of several patents pending and granted, is receiving royalties, and is consulting for several companies and organizations, which are active in electroporation and electroporation-based technologies and therapies. Other authors report no conflict of interest.

Acknowledgements

This work was supported by the Slovenian Research and Innovation Agency (ARIS) through University of Ljubljana's internal funding for Start-up Research Programmes and grant P2-0249 Electroporation-based technologies and treatments. This study was conducted within the Infrastructure Programme: Network of research infrastructure centres at the University of Ljubljana (MRIC UL IP-0510), specifically within infrastructural centre Cellular Electrical Engineering (I0-0022), also funded by the Slovenian Research and Innovation Agency (ARIS).

References

- [1] S. Grimnes, Bioimpedance and bioelectricity basics, 3rd ed, Academic Press, London, U.K, 2015.
- [2] K.R. Foster, H.P. Schwan, Dielectric properties of tissues and biological materials: a critical review, *Crit Rev Biomed Eng* 17 (1989) 25–104.

- [3] C. Gabriel, S. Gabriel, E. Corthout, The dielectric properties of biological tissues: I. Literature survey, *Phys. Med. Biol.* 41 (1996) 2231–2249. <https://doi.org/10.1088/0031-9155/41/11/001>
- [4] S. Gabriel, R.W. Lau, C. Gabriel, The dielectric properties of biological tissues: II. Measurements in the frequency range 10 Hz to 20 GHz, *Phys. Med. Biol.* 41 (1996) 2251–2269. <https://doi.org/10.1088/0031-9155/41/11/002>
- [5] S. Gabriel, R.W. Lau, C. Gabriel, The dielectric properties of biological tissues: III. Parametric models for the dielectric spectrum of tissues, *Phys. Med. Biol.* 41 (1996) 2271–2293. <https://doi.org/10.1088/0031-9155/41/11/003>
- [6] D. Miklavčič, N. Pavšelj, F.X. Hart, Electric Properties of Tissues, in: M. Akay (Ed.), *Wiley Encyclopedia of Biomedical Engineering*, 1st ed., Wiley, 2006. <https://doi.org/10.1002/9780471740360.ebs0403>
- [7] D.A. Dean, T. Ramanathan, D. Machado, R. Sundararajan, Electrical impedance spectroscopy study of biological tissues, *Journal of Electrostatics* 66 (2008) 165–177. <https://doi.org/10.1016/j.elstat.2007.11.005>
- [8] M.B. Lee, G.-H. Jahng, H.J. Kim, E.J. Woo, O.I. Kwon, Extracellular electrical conductivity property imaging by decomposition of high-frequency conductivity at Larmor-frequency using multi-b-value diffusion-weighted imaging, *PLoS ONE* 15 (2020) e0230903. <https://doi.org/10.1371/journal.pone.0230903>
- [9] H.S. Mayberg, A.M. Lozano, V. Voon, et al., Deep Brain Stimulation for Treatment-Resistant Depression, *Neuron* 45 (2005) 651–660. <https://doi.org/10.1016/j.neuron.2005.02.014>
- [10] R. Banan Sadeghian, M. Ebrahimi, S. Salehi, Electrical stimulation of microengineered skeletal muscle tissue: Effect of stimulus parameters on myotube contractility and maturation, *J Tissue Eng Regen Med* 12 (2018) 912–922. <https://doi.org/10.1002/term.2502>
- [11] D. Serrano-Muñoz, H. Beltran-Alacreu, D. Martín-Caro Álvarez, et al., Effectiveness of Different Electrical Stimulation Modalities for Pain and Masticatory Function in Temporomandibular Disorders: A Systematic Review and Meta-Analysis, *The Journal of Pain* 24 (2023) 946–956. <https://doi.org/10.1016/j.jpain.2023.01.016>
- [12] R.M. Dorrian, C.F. Berryman, A. Lauto, A.V. Leonard, Electrical stimulation for the treatment of spinal cord injuries, *Front. Cell. Neurosci.* 17 (2023) 1095259. <https://doi.org/10.3389/fncel.2023.1095259>
- [13] Y. Chen, C.-P. Liang, Y. Liu, et al., Review of advanced imaging techniques, *Journal of Pathology Informatics* 3 (2012) 22. <https://doi.org/10.4103/2153-3539.96751>
- [14] S. Hussain, I. Mubeen, N. Ullah, et al., Modern Diagnostic Imaging Technique Applications and Risk Factors in the Medical Field: A Review, *BioMed Research International* 2022 (2022) 5164970. <https://doi.org/10.1155/2022/5164970>
- [15] R.V. Davalos, L.M. Mir, B. Rubinsky, Tissue Ablation with Irreversible Electroporation, *Ann Biomed Eng* 33 (2005) 223–231. <https://doi.org/10.1007/s10439-005-8981-8>
- [16] M.L. Yarmush, A. Golberg, G. Serša, T. Kotnik, D. Miklavčič, Electroporation-Based Technologies for Medicine: Principles, Applications, and Challenges, *Annu. Rev. Biomed. Eng.* 16 (2014) 295–320. <https://doi.org/10.1146/annurev-bioeng-071813-104622>

-
- [17] B. Geboers, H.J. Scheffer, P.M. Graybill, et al., High-Voltage Electrical Pulses in Oncology, *Radiology* 295 (2020) 254–272. <https://doi.org/10.1148/radiol.2020192190>
 - [18] Kotnik, T., Pucihar, G., & Miklavčič, D. (2011). The Cell in the Electric Field. In S. T. Kee, J. Gehl, & E. W. Lee (Eds.), *Clinical Aspects of Electroporation* (pp. 19–29). Springer New York. 10.1007/978-1-4419-8363-3_3
 - [19] T. Kotnik, L. Rems, M. Tarek, D. Miklavčič, Membrane Electroporation and Electroporabilization: Mechanisms and Models, *Annu. Rev. Biophys.* 48 (2019) 63–91. <https://doi.org/10.1146/annurev-biophys-052118-115451>
 - [20] T. Batista Napotnik, T. Polajžer, D. Miklavčič, Cell death due to electroporation – A review, *Bioelectrochemistry* 141 (2021) 107871. <https://doi.org/10.1016/j.bioelechem.2021.107871>
 - [21] S. Haberl, D. Miklavcic, G. Sersa, et al., Cell membrane electroporation-Part 2: the applications, *IEEE Electr. Insul. Mag.* 29 (2013) 29–37. <https://doi.org/10.1109/MEI.2013.6410537>
 - [22] S. Sachdev, T. Potočnik, L. Rems, D. Miklavčič, Revisiting the role of pulsed electric fields in overcoming the barriers to in vivo gene electrotransfer, *Bioelectrochemistry* 144 (2022) 107994. <https://doi.org/10.1016/j.bioelechem.2021.107994>
 - [23] T. Kotnik, W. Frey, M. Sack, et al., Electroporation-based applications in biotechnology, *Trends in Biotechnology* 33 (2015) 480–488. <https://doi.org/10.1016/j.tibtech.2015.06.002>
 - [24] S. Mahnič-Kalamiza, E. Vorobiev, D. Miklavčič, Electroporation in Food Processing and Biorefinery, *J Membrane Biol* 247 (2014) 1279–1304. <https://doi.org/10.1007/s00232-014-9737-x>
 - [25] G. Saldaña, I. Álvarez, S. Condón, J. Raso, Microbiological Aspects Related to the Feasibility of PEF Technology for Food Pasteurization, *Crit Rev Food Sci Nutr* 54 (2014) 1415–1426.
 - [26] L.M. Mir, M.F. Bureau, J. Gehl, R. Rangara, D. Rouy, J.-M. Caillaud, P. Delaere, D. Branellec, B. Schwartz, D. Scherman, High-efficiency gene transfer into skeletal muscle mediated by electric pulses, *Proc. Natl. Acad. Sci. U.S.A.* 96 (1999) 4262–4267. <https://doi.org/10.1073/pnas.96.8.4262>
 - [27] G. Tevz, D. Pavlin, U. Kamensek, S. Kranjc, S. Mesojednik, A. Coer, G. Sersa, M. Cemazar, Gene Electrotransfer into Murine Skeletal Muscle: A Systematic Analysis of Parameters for Long-term Gene Expression, *Technol Cancer Res Treat* 7 (2008) 91–101. <https://doi.org/10.1177/153303460800700201>
 - [28] D.C. Hughes, J.P. Hardee, D.S. Waddell, C.A. Goodman, CORP: Gene delivery into murine skeletal muscle using in vivo electroporation, *J. Appl. Physiol.* 133 (2022) 41–59. <https://doi.org/10.1152/jappphysiol.00088.2022>
 - [29] V.Y. Reddy, E.P. Gerstenfeld, A. Natale, W. Whang, F.A. Cuoco, et al., Pulsed Field or Conventional Thermal Ablation for Paroxysmal Atrial Fibrillation, *N Engl J Med* 389 (2023) 1660–1671. <https://doi.org/10.1056/NEJMoa2307291>
 - [30] A. Verma, D.E. Haines, L.V. Boersma, N. Sood, A. Natale, et al., Pulsed Field Ablation for the Treatment of Atrial Fibrillation: PULSED AF Pivotal Trial, *Circulation* 147 (2023) 1422–1432. <https://doi.org/10.1161/CIRCULATIONAHA.123.063988>

- [31] K.-R.J. Chun, D. Miklavčič, K. Vlachos, S. Bordinon, D. Scherr, et al., State-of-the-art pulsed field ablation for cardiac arrhythmias: ongoing evolution and future perspective, *Europace* 26 (2024) euae134. <https://doi.org/10.1093/europace/euae134>
- [32] D. Miklavčič, A. Verma, P.R.P. Krahm, J. Štublar, B. Kos, et al., Biophysics and electrophysiology of pulsed field ablation in normal and infarcted porcine cardiac ventricular tissue, *Sci Rep* 14 (2024) 32063. <https://doi.org/10.1038/s41598-024-83683-y>
- [33] Z.F. Bhat, J.D. Morton, S.L. Mason, A.E.-D.A. Bekhit, Current and future prospects for the use of pulsed electric field in the meat industry, *Crit Rev Food Sci Nutr* 59 (2019) 1660–1674. <https://doi.org/10.1080/10408398.2018.1425825>
- [34] L. Astráin-Redín, J. Raso, G. Cebrián, I. Álvarez, Potential of Pulsed Electric Fields for the preparation of Spanish dry-cured sausages, *Sci Rep* 9 (2019) 16042. <https://doi.org/10.1038/s41598-019-52464-3>
- [35] R. Karki, I. Oey, P. Bremer, S.Y. Leong, P. Silcock, Effect of Pulsed Electric Fields (PEF) Pre-Treatment on the Quality of Sous Vide (SV) Processed Beef Short Ribs and Optimisation of PEF and SV Process Parameters Using Multiple Polynomial Regression Model, *Food Bioprocess Technol* 16 (2023) 216–231. <https://doi.org/10.1007/s11947-022-02932-y>
- [36] I. Tomasevic, V. Heinz, I. Djekic, N. Terjung, Pulsed electric fields and meat processing: latest updates, *Italian Journal of Animal Science* (2023). <https://www.tandfonline.com/doi/abs/10.1080/1828051X.2023.2206834>
- [37] B.R. Epstein, R.G. Settle, K.R. Foster, Anisotropic impedance properties of skeletal muscle, in: *Bioengineering*, Elsevier, 1981: pp. 139–143. <https://doi.org/10.1016/B978-0-08-027207-8.50034-5>
- [38] M.S. Spach, W.T. Miller, E. Miller-Jones, R.B. Warren, R.C. Barr, Extracellular potentials related to intracellular action potentials during impulse conduction in anisotropic canine cardiac muscle., *Circ Res* 45 (1979) 188–204. <https://doi.org/10.1161/01.RES.45.2.188>
- [39] D.B. Geselowitz, R.C. Barr, M.S. Spach, W.T. Miller, The impact of adjacent isotropic fluids on electrograms from anisotropic cardiac muscle. A modeling study., *Circ Res* 51 (1982) 602–613. <https://doi.org/10.1161/01.RES.51.5.602>
- [40] V. Tayfur, O. Magden, M. Edizer, A. Atabey, Anatomy of Vastus Lateralis Muscle Flap, *J Craniofac Surg* 21 (2010) 1951–1953. <https://doi.org/10.1097/SCS.0b013e3181f4ee7f>
- [41] A. Rehfeld, M. Nylander, K. Karnov, *Compendium of Histology: A Theoretical and Practical Guide*, Springer, Cham, 2017. <https://doi.org/10.1007/978-3-319-41873-5>
- [42] J. Malmivuo, R. Plonsey, *Bioelectromagnetism: Principles and Applications of Bioelectric and Biomagnetic Fields*, Oxford University Press, 1995. <https://doi.org/10.1093/acprof:oso/9780195058239.001.0001>
- [43] M. Essone Mezeme, M. Kranjc, F. Bajd, I. Serša, C. Brosseau, D. Miklavčič, Assessing how electroporation affects the effective conductivity tensor of biological tissues, *Appl. Phys. Lett.* 101 (2012) 213702. <https://doi.org/10.1063/1.4767450>
- [44] Q. Castellví, B. Mercadal, A. Ivorra, Assessment of Electroporation by Electrical Impedance Methods, in: D. Miklavčič (Ed.), *Handbook of Electroporation*, Springer International Publishing, Cham, 2017: pp. 671–690. [10.1007/978-3-319-32886-7_164](https://doi.org/10.1007/978-3-319-32886-7_164)

- [45] A. Mercanzini, P. Colin, J.-C. Bensadoun, A. Bertsch, P. Renaud, In Vivo Electrical Impedance Spectroscopy of Tissue Reaction to Microelectrode Arrays, *IEEE Trans. Biomed. Eng.* 56 (2009) 1909–1918. <https://doi.org/10.1109/TBME.2009.2018457>
- [46] H.S. Magar, R.Y.A. Hassan, A. Mulchandani, Electrochemical Impedance Spectroscopy (EIS): Principles, Construction, and Biosensing Applications, *Sensors* 21 (2021) 6578. 10.3390/s21196578
- [47] O. Kangasmaa, I. Laakso, Estimation method for the anisotropic electrical conductivity of in vivo human muscles and fat between 10 kHz and 1 MHz, *Phys. Med. Biol.* 67 (2022) 225002. 10.1088/1361-6560/ac9a1e
- [48] A. Ivorra, B. Rubinsky, In vivo electrical impedance measurements during and after electroporation of rat liver, *Bioelectrochemistry* 70 (2007) 287–295. 10.1016/j.bioelechem.2006.10.005
- [49] S. Laufer, A. Ivorra, V.E. Reuter, B. Rubinsky, S.B. Solomon, Electrical impedance characterization of normal and cancerous human hepatic tissue, *Physiol. Meas.* 31 (2010) 995–1009. 10.1088/0967-3334/31/7/009
- [50] A. Silve, A. Guimerà Brunet, B. Al-Sakere, A. Ivorra, L.M. Mir, Comparison of the effects of the repetition rate between microsecond and nanosecond pulses: Electroporomeabilization-induced electro-desensitization?, *Biochim. Biophys. Acta Gen. Subj.* 1840 (2014) 2139–2151. 10.1016/j.bbagen.2014.02.011
- [51] T. García-Sánchez, A. Azan, I. Leray, J. Rosell-Ferrer, R. Bragós, L.L.M. Mir, Interpulse multifrequency electrical impedance measurements during electroporation of adherent differentiated myotubes, *Bioelectrochemistry* 105 (2015) 123–135. 10.1016/j.bioelechem.2015.05.018
- [52] T.A. Whitman, J.C. Forrest, M.T. Morgan, M.R. Okos, Electrical measurement for detecting early postmortem changes in porcine muscle, *J. Anim. Sci.* 74 (1996) 80. 10.2527/1996.74180x
- [53] C.E. Byrne, D.J. Troy, D.J. Buckley, Postmortem changes in muscle electrical properties of bovine *M. longissimus dorsi* and their relationship to meat quality attributes and pH fall, *Meat Sci.* 54 (2000) 23–34. 10.1016/S0309-1740(99)00055-8
- [54] X. Zhao, H. Zhuang, S.-C. Yoon, Y. Dong, W. Wang, W. Zhao, Electrical Impedance Spectroscopy for Quality Assessment of Meat and Fish: A Review on Basic Principles, Measurement Methods, and Recent Advances, *J. Food Qual.* 2017 (2017) 6370739. 10.1155/2017/6370739
- [55] U. Pliquet, M. Altmann, F. Pliquet, L. Schöberlein, Py—a parameter for meat quality, *Meat Sci.* 65 (2003) 1429–1437. 10.1016/S0309-1740(03)00066-4
- [56] M. Pavlin, K. Flisar, M. Kandušer, The Role of Electrophoresis in Gene Electrotransfer, *J. Membr. Biol.* 236 (2010) 75–79. 10.1007/s00232-010-9276-z
- [57] Y. Lv, X. Cheng, S. Chen, H. Liu, Y. Wang, C. Yao, B. Rubinsky, Analysis of the Electric Field-Dependent Current During Electroporation Pulses, *IEEE Access* 8 (2020) 93850–93856. 10.1109/ACCESS.2020.2995151
- [58] D. Cukjati, D. Batiuskaite, F. André, D. Miklavčič, L.M. Mir, Real time electroporation control for accurate and safe in vivo non-viral gene therapy, *Bioelectrochemistry* 70 (2007) 501–507. 10.1016/j.bioelechem.2006.11.001

- [59] J. Langus, M. Kranjc, B. Kos, T. Šuštar, D. Miklavčič, Dynamic finite-element model for efficient modelling of electric currents in electroporated tissue, *Sci. Rep.* 6 (2016) 26409. 10.1038/srep26409
- [60] K.A. Poulsen, J.F. Young, P. Theil, M. Kolko, N. Oksbjerg, I.H. Lambert, Role of phospholipase A2 in the induction of drip loss in porcine muscle, *J. Agric. Food Chem.* 55 (2007) 1970–1976. 10.1021/jf062341n
- [61] J. Genovese, M. Kranjc, I. Serša, M. Petracci, P. Rocculi, D. Miklavčič, S. Mahnič-Kalamiza, PEF-treated plant and animal tissues: Insights by approaching with different electroporation assessment methods, *Innovative Food Science & Emerging Technologies* 74 (2021) 102872. 10.1016/j.ifset.2021.102872
- [62] J. Pingel, H.M. Kjer, F. Biering-Sørensen, R. Feidenhans'l, T.B. Dyrby, 3D synchrotron imaging of muscle tissues at different atrophic stages in stroke and spinal cord injury: a proof-of-concept study, *Sci. Rep.* 12 (2022) 17289. 10.1038/s41598-022-21741-z
- [63] R. Šmerc, D.A. Ramirez, S. Mahnič-Kalamiza, J. Dermol-Černe, D.C. Sigg, L.M. Mattison, P.A. Iaizzo, D. Miklavčič, A Multiscale Computational Model of Skeletal Muscle Electroporation Validated Using In Situ Porcine Experiments, *IEEE Trans. Biomed. Eng.* 70 (2023) 1826–1837. 10.1109/TBME.2022.3229560
- [64] T. Kotnik, D. Miklavčič, T. Slivnik, Time course of transmembrane voltage induced by time-varying electric fields—a method for theoretical analysis and its application, *Bioelectrochemistry and Bioenergetics* 45 (1998) 3–16. 10.1016/S0302-4598(97)00093-7
- [65] L. Rems, M. Ušaj, M. Kandušer, M. Reberšek, D. Miklavčič, G. Pucihar, Cell electrofusion using nanosecond electric pulses, *Sci. Rep.* 3 (2013) 3382. 10.1038/srep03382
- [66] M. Scuderi, J. Dermol-Černe, T. Batista Napotnik, S. Chaigne, O. Bernus, D. Benoist, D.C. Sigg, L. Rems, D. Miklavčič, Characterization of Experimentally Observed Complex Interplay between Pulse Duration, Electrical Field Strength, and Cell Orientation on Electroporation Outcome Using a Time-Dependent Nonlinear Numerical Model, *Biomolecules* 13 (2023) 727. 10.3390/biom13050727
- [67] Tissue Frequency Chart IT'IS Foundation, (n.d.). <https://itis.swiss/virtual-population/tissue-properties/database/tissue-frequency-chart/> (accessed December 19, 2024).
- [68] B. Kos, L. Mattison, D. Ramirez, H. Čindrič, D.C. Sigg, P.A. Iaizzo, M.T. Stewart, D. Miklavčič, Determination of lethal electric field threshold for pulsed field ablation in ex vivo perfused porcine and human hearts, *Front. Cardiovasc. Med.* 10 (2023) 1160231. 10.3389/fcvm.2023.1160231
- [69] S. Čorović, L.M. Mir, D. Miklavčič, In Vivo Muscle Electroporation Threshold Determination: Realistic Numerical Models and In Vivo Experiments, *J. Membr. Biol.* 245 (2012) 509–520. 10.1007/s00232-012-9432-8
- [70] S. Corovic, I. Lackovic, P. Sustaric, T. Sustar, T. Rodic, D. Miklavcic, Modeling of electric field distribution in tissues during electroporation, *BioMed Eng OnLine* 12 (2013) 16. 10.1186/1475-925X-12-16
- [71] L. Zang, K. Gu, X. Ji, H. Zhang, S. Yan, X. Wu, Effect of Anisotropic Electrical Conductivity Induced by Fiber Orientation on Ablation Characteristics of Pulsed Field Ablation in Atrial Fibrillation Treatment: A Computational Study, *JCDD* 9 (2022) 319. 10.3390/jcdd9100319

- [72] M. Greaser, W. Guo, Postmortem Muscle Chemistry, in: 2012: pp. 63–78. 10.1201/b11479-7
- [73] S. Freitas-Ribeiro, R.L. Reis, R.P. Pirraco, Long-term and short-term preservation strategies for tissue engineering and regenerative medicine products: state of the art and emerging trends, *PNAS Nexus* 1 (2022) pgac212. 10.1093/pnasnexus/pgac212
- [74] A. Narkar, A. Kaboudian, Y. Ardeshirpour, M. Casciola, T. Feaster, K. Blinova, In Vitro Assay Development to Study Pulse Field Ablation Outcome Using Solanum Tuberosum, *IJMS* 25 (2024) 8967. 10.3390/ijms25168967

2.4 Paper 4

Title: **An experimentally validated numerical model of pH changes in surrogate tissue induced by electroporation pulses**

Authors: **Rok Šmerc**, Damijan Miklavčič, and Samo Mahnič-Kalamiza

Publication: *Electrochimica Acta*, vol. 511: 145363, January 2025

Impact factor: 5.6 (2024)

Quartile: Q1

Rank: 11/44 (Electrochemistry)

DOI: <https://doi.org/10.1016/j.electacta.2024.145363>



Contents lists available at ScienceDirect

Electrochimica Acta

journal homepage: www.journals.elsevier.com/electrochimica-acta

An experimentally validated numerical model of pH changes in surrogate tissue induced by electroporation pulses

Rok Šmerc, Damijan Miklavčič, Samo Mahnič-Kalamiza*

University of Ljubljana, Faculty of Electrical Engineering, Tržaška cesta 25, SI-1000 Ljubljana, Slovenia

ARTICLE INFO

Keywords:

Electrochemistry
Mathematical model
Electroporation
pH front
Agarose gel phantoms
Hydrolysis

ABSTRACT

Electroporation often leads to electrochemical reactions at the electrode-electrolytic solution interface, particularly when using monophasic pulses of considerable duration (typically on the order of several microseconds or longer) that cause not only capacitive charging of the double-layer, but also faradaic charge transfer between the electrodes and the solution. Applications, where the electrochemical changes are to be either avoided or actively exploited to benefit the treatment, range from gene electrotransfer to electrolytic ablation of tissue. Through numerical modelling and experimental validation, our study explores the extent of pH changes induced by faradaic currents in a surrogate tissue. A mechanistic multiphysics model of pH changes was developed based on first principles, incorporating hydrolysis reactions at the anode and cathode, and the Nernst-Planck model of ion transport. The model was validated using agarose gel tissue phantoms designed to simulate unbuffered and buffered (mimicking in vivo tissue buffering capacity) conditions. An imaging system with pH-sensitive dyes was developed and used to visualise and quantify pH front formation and migration. The model predictions qualitatively aligned well with experimental data, differentiating pH front behaviour between unbuffered and buffered media. However, the quantitative accuracy in predicting the temporal and spatial evolution of the pH fronts can be further improved. Experimental observations emphasise the need for more advanced models. Nevertheless, the developed model provides a sound theoretical foundation for predicting pH changes due to high-voltage electric pulse delivery, such as encountered in electroporation-based treatments and therapies.

1. Introduction

Electroporation is a biophysical phenomenon in which short, high-voltage electric pulses are used to transiently permeabilise the cell plasma membrane, facilitating the transport of ions and molecules across the membrane, and is often used to introduce various drugs and nucleic acids into the cells [1–3]. This phenomenon has shown great promise in various fields of biomedicine, biotechnology, and food processing [4–10]. Electroporation can be either reversible or irreversible, depending on the amplitude and duration of the pulses. Reversible electroporation temporarily disrupts the cell membrane and is utilised, for example, in gene electrotransfer and drug delivery [11,12]. Irreversible electroporation, on the other hand, leads to cell death and is used in tissue ablation, particularly in tumour treatment, and more recently also in the treatment of cardiac arrhythmias, particularly atrial fibrillation [10,13–17].

Electroporation in tissue is achieved by applying high-voltage (often accompanied by high-current) electric pulses via electrodes. These high-

voltage (high-current) pulses also cause heating in the tissue and electrochemical reactions at the electrode-electrolyte interface [18,19]. While electroporation and tissue heating have been extensively studied, the changes in pH and their effects are still relatively unexplored [20–23]. In tissue, pH changes are caused by the electrolysis of water, i. e., hydrolysis. Hydrolysis leads to significant pH changes at the electrode-electrolyte or electrode-electrolytic solution interface, resulting in extreme local pH changes [24–27]. The pH changes in tissue may be important in e.g. gene electrotransfer, where control of pH conditions is crucial for maintaining the stability of plasmid DNA. Extreme pH changes can negatively affect transfection efficiency by, in the most extreme case, denaturing the plasmid DNA, but also affecting cell viability [28,29]. For successful gene expression, it is thus critical to minimise pH changes, and thus plasmid DNA and tissue damage [12,29,30].

Conversely, pH changes were recognised as the main mechanism of action in the electrochemical treatment of tumours. This approach uses low-level DC to establish acidic and alkaline environments and cause

* Corresponding author at: University of Ljubljana, Faculty of Electrical Engineering, Laboratory of Biocybernetics, Tržaška cesta 25, SI-1000 Ljubljana Slovenia.
E-mail address: samo.mahnic-kalamiza@fe.uni-lj.si (S. Mahnič-Kalamiza).

<https://doi.org/10.1016/j.electacta.2024.145363>

Received 22 August 2024; Received in revised form 28 October 2024; Accepted 15 November 2024

Available online 16 November 2024

0013-4686/© 2024 The Author(s). Published by Elsevier Ltd. This is an open access article under the CC BY-NC license (<http://creativecommons.org/licenses/by-nc/4.0/>).

cell death [31–36]. Recently, it has been suggested that the combined use of electroporation and electrolysis, termed E2, enhances cell death and consequently tissue ablation by allowing the electrolytic products to enter into the cell through a permeabilised cell membrane, thereby reducing the required charge and treatment duration [37–40]. Furthermore, it was shown that ablation volumes comparable to conventional irreversible electroporation (using high-voltage pulses) can also be achieved with a larger number of low-voltage pulses, suggesting that electrolysis and pH changes contribute significantly to cell death [41]. On the other hand, the use of sub-microsecond electric pulses in electrochemotherapy has shown that these pulses reduce heating and electrochemical reactions, although requiring higher concentrations of chemotherapeutic agents for similar cytotoxic effects [42]. Additionally, sub-microsecond electric pulses have been shown to be effective in gene electrotransfer [29,43], a therapy that would also benefit from the reduced heating and electrochemical reactions associated with sub-microsecond pulses.

Computational models show that pulse amplitude and polarity significantly influence the dissolution of metal electrodes, highlighting the importance of optimising these parameters. Recent studies using a multiphysics approach have further explored the electrochemical effects and electrode material alterations in electroporation, giving important insights into the underlying mechanisms [18,44]. Furthermore, magnetic resonance imaging and electrical impedance tomography have been used to monitor pH changes during electrolysis in real-time [45,46]. Understanding the significance of pH changes is also crucial in the field of pulsed electric field (PEF) treatments of foods as they affect the inactivation of microbes, enzymes, and cause electrode corrosion. By optimising the pulse waveforms, undesirable electrochemical reactions can be minimised [47,48]. Finally, multiphysics modelling has provided insight into the effects of pulse frequency and medium composition on metal release from the electrodes, enabling optimisation of PEF treatment conditions to reduce electrode degradation [49].

Pioneering work in modelling electrochemical treatments was done by Eva Nilsson et al. for both the unbuffered and buffered electrolytes. Their models are based on the Nernst-Planck system of equations [24,25,32,33]. Subsequent studies have made important contributions by investigating pH-front interaction in tissue, the optimal dose-response relationship, innovative electrode configurations, protein denaturation dynamics, and comprehensive 2D modelling [50–56]. However, these models specifically address the electrical conditions typical of the electrochemical treatment of tumours, in which direct currents of low amplitudes are applied over a longer period, often up to several hours [34]. In contrast, electroporation uses short, high-amplitude pulses, which require careful setup of the numerical methods of resolving the model, as the pulses of high amplitude in both voltage (and often current) make the simulation inherently unstable. Consequently, recent studies have focused on the computational modelling of pH changes during electroporation. Electroporation has been shown to create significant and immediate formation of pH fronts that can lead to tissue damage if not controlled [26,57,58]. It has also been suggested that pH fronts are the primary cause of muscle damage in gene electrotransfer protocols [27,59]. Additionally, a dose-response model linking pulse dosage to tissue damage was developed [60]. Overall, these studies highlight the crucial role of modelling in optimising and understanding electrochemical processes involved in the treatment.

The aim of our study was thus to build a comprehensive mechanistic computational model of pH changes in tissue during and after the application of electric pulses with parameters typical of electroporation as used in gene electrotransfer (milliseconds-duration monophasic pulses). The developed model was validated by experiments using agarose gels to which various pH indicators were added to monitor pH changes. In addition, a video recording system was developed and calibrated to allow for a direct comparison between the experimental results and the model calculations. The aim of this approach was to establish reliable reproducible experimental protocols and to validate the computational

model and ensure its accuracy and applicability in predicting pH changes during electroporation.

2. Materials and methods

2.1. Governing equations and transport mechanisms

The Nernst-Planck equation system, which describes the transport of ionic species and the distribution of the electric potential in the electrolyte, was used as a framework for the model. Two configurations were analysed: an unbuffered model and a buffered model, based on previous work [24,25,27,32,33]. For the unbuffered model, the system consists of equations for the concentration of ions in a four-component electrolyte, where the components are hydrogen (H^+), hydroxide (OH^-), chloride (Cl^-), and sodium ions (Na^+), along with an equation for the spatial distribution of the electric potential (ϕ). The system, therefore, consists of five coupled partial differential equations. These equations consider two mechanisms of ion transport, namely diffusion, which is driven by concentration gradients, and migration, which is driven by the gradient of the electric potential. Convection is considered negligible and is therefore not considered in the model. This assumption is likely valid under in vivo conditions due to the phenomenon of the vascular lock, wherein electroporation pulses cause a temporary and localised cessation of perfusion, effectively immobilising the pH-altering products within the treated area [61]. The buffered model contains a bicarbonate buffer which expands the electrolyte to a seven-component system by adding bicarbonate (HCO_3^-) and carbonate ions (CO_3^{2-}), and carbon dioxide (CO_2) to the components of the unbuffered model. This leads to a system of eight coupled partial differential equations, introducing additional complexity and numerical stability challenges.

The mass balance of the ions of species i is defined as

$$\frac{\partial c_i}{\partial t} = -\nabla \cdot \mathbf{N}_i + R_i, \quad (1)$$

where c_i is the ion concentration of species i , t is the time, R_i is the production of species i by chemical reactions in the electrolyte, and \mathbf{N}_i is the molar flux of ions of species i , defined as

$$\mathbf{N}_i = -D_i \nabla c_i - \frac{z_i}{|z_i|} u_i c_i \nabla \phi, \quad (2)$$

where D_i is the ion diffusion coefficient of the species i , z_i is the charge of the species i , u_i is the ion mobility of the species i , and ϕ is the electric potential in the electrolyte. The first term in Eq. (2) describes the mechanism of diffusion, and the second term describes electrophoresis, i.e., the migration of charged species due to the electric field. Ion mobility and the diffusion coefficient are linked by the Nernst-Einstein equation

$$D_i = \frac{RT}{|z_i|F} u_i, \quad (3)$$

where T is the temperature, R the universal gas constant, and F the Faraday constant. The last differential equation used is the equation for the conservation of electric charge

$$\nabla \cdot \left(\sum_{i=1}^N |z_i| u_i c_i \nabla \phi \right) + \sum_{i=1}^N z_i D_i \nabla^2 c_i = 0. \quad (4)$$

Note: the upper bound N of summation in Eq. (4) depends on whether the buffer is considered: $N = 4$ in the unbuffered model and $N = 7$ in the buffered model, respectively. Finally, the condition of electroneutrality must be considered

$$\sum_{i=1}^N z_i c_i = 0. \quad (5)$$

During pulse delivery, oxidation (i.e., electron loss) takes place at the anode and reduction (i.e., electron gain) at the cathode. When platinum is used as an electrode material in biological tissue, the anodic reactions consist mainly of the production of oxygen and chlorine gases, while hydrogen gas is released at the cathode. The main reactions at the anode are therefore oxygen and chlorine evolution



while the main reaction at the cathode is hydrogen evolution



In the case of the unbuffered model, only one chemical reaction is considered, the water autoprotolysis reaction



In the buffered model, however, three additional chemical reactions are considered



Appendix A provides the additional equations that define the production of ionic species, as well as the boundary and initial conditions for the numerical model.

2.2. Computational approach

The system of equations defined above was solved using the finite element method in the COMSOL Multiphysics (COMSOL Inc., Sweden) software environment, utilising the Tertiary Current Distribution, Nernst-Planck physics interface. A one-dimensional geometry was chosen as it represents a reasonable approximation of the experimental system as described below. In particular, the experimental setup was such that the electric field is mainly oriented parallel to the line connecting the anode with the cathode. This simplification to one dimension captures the essential physics of the problem without unnecessarily elevating the degree of computational complexity, since ion transport occurs predominantly along this axis. Consequently, variations in the two directions perpendicular to the main axis have a negligible effect on the overall results. This geometry was represented in the model as a line of 14.3 mm in length, which corresponds to the edge-to-edge distance between the electrodes in the experiments. The anodic boundary conditions were set at $x = 0$ mm, and the cathodic boundary conditions at $x = 14.3$ mm. The geometry was discretised into 14,924 mesh elements, employing cubic shape functions for both concentration and electric potential discretisation. The chosen pulse waveform consisted of 8 rectangular pulses with a duration of 10 ms each, delivered at a repetition rate of 1 s^{-1} . Two different amplitudes were used for the pulses: 200 V and 400 V, corresponding to 140 V/cm and 280 V/cm voltage-to-distance ratio, respectively. The simulations were performed using time-dependent studies in COMSOL Multiphysics, with the solver settings optimised to ensure convergence and accuracy. The values of all parameters required for the simulations are listed in Table 1. Post-processing of the simulation results was performed using Python.

2.3. Experimental setup

The experimental setup comprised a camera system, a pulse generator, an oscilloscope, and a PC. A Basler Ace ACA1920–155UC camera, which is capable of recording at 100 frames per second with a resolution

Table 1
Parameters and their corresponding values used in the models [24,25,62].

Parameter	Value	Unit	Description
$c_{\text{H}^+}^0$	$1.0 \cdot 10^{-4}$ (unbuffered) / $10^{-4.4}$ (buffered)	mol m^{-3}	Initial concentration of H^+
$c_{\text{OH}^-}^0$	$1.0 \cdot 10^{-4}$ (unbuffered) / $10^{-3.2}$ (buffered)	mol m^{-3}	Initial concentration of OH^-
$c_{\text{Na}^+}^0$	160	mol m^{-3}	Initial concentration of Na^+
$c_{\text{Cl}^-}^0$	160 (unbuffered) / 132.9 (buffered)	mol m^{-3}	Initial concentration of Cl^-
$c_{\text{HCO}_3^-}^0$	27.0	mol m^{-3}	Initial concentration of HCO_3^-
$c_{\text{CO}_3^{2-}}^0$	$4.4 \cdot 10^{-2}$	mol m^{-3}	Initial concentration of CO_3^{2-}
$c_{\text{CO}_2}^0$	1.3	mol m^{-3}	Initial concentration of CO_2
D_{H^+}	$12.50 \cdot 10^{-9}$	$\text{m}^2 \text{ s}^{-1}$	Diffusion coefficient of H^+
D_{OH^-}	$7.05 \cdot 10^{-9}$	$\text{m}^2 \text{ s}^{-1}$	Diffusion coefficient of OH^-
D_{Na^+}	$1.78 \cdot 10^{-9}$	$\text{m}^2 \text{ s}^{-1}$	Diffusion coefficient of Na^+
D_{Cl^-}	$2.72 \cdot 10^{-9}$	$\text{m}^2 \text{ s}^{-1}$	Diffusion coefficient of Cl^-
$D_{\text{HCO}_3^-}$	$1.49 \cdot 10^{-9}$	$\text{m}^2 \text{ s}^{-1}$	Diffusion coefficient of HCO_3^-
$D_{\text{CO}_3^{2-}}$	$2.46 \cdot 10^{-9}$	$\text{m}^2 \text{ s}^{-1}$	Diffusion coefficient of CO_3^{2-}
D_{CO_2}	$2.71 \cdot 10^{-9}$	$\text{m}^2 \text{ s}^{-1}$	Diffusion coefficient of CO_2
$k_{w,f}$	$1.5 \cdot 10^8$	$\text{m}^3 \text{ mol}^{-1} \text{ s}^{-1}$	Forward rate constant of water autoprotolysis reaction
$k_{w,b}$	$6.79 \cdot 10^{-5}$	s^{-1}	Backward rate constant of water autoprotolysis reaction
$k_{b1,f}$	310	$\text{m}^3 \text{ mol}^{-1} \text{ s}^{-1}$	Forward rate constant of 1st buffer reaction
$k_{b1,b}$	$4.62 \cdot 10^{-6}$	$\text{m}^3 \text{ mol}^{-1} \text{ s}^{-1}$	Backward rate constant of 1st buffer reaction
$k_{b2,f}$	20	$\text{m}^3 \text{ mol}^{-1} \text{ s}^{-1}$	Forward rate constant of 2nd buffer reaction
$k_{b2,b}$	$6.08 \cdot 10^{-4}$	s^{-1}	Backward rate constant of 2nd buffer reaction
$k_{b3,f}$	$1.5 \cdot 10^8$	$\text{m}^3 \text{ mol}^{-1} \text{ s}^{-1}$	Forward rate constant of 3rd buffer reaction
$k_{b3,b}$	$5.81 \cdot 10^7$	s^{-1}	Backward rate constant of 3rd buffer reaction
$j_{\text{H}^+}^0$	$1 \cdot 10^{-6}$	A m^{-2}	Exchange current density of oxygen evolution reaction
$j_{\text{Cl}^-}^0$	10	A m^{-2}	Exchange current density of chlorine evolution reaction
$j_{\text{H}_2}^0$	1	A m^{-2}	Exchange current density of hydrogen evolution reaction
E_{I}^{eq}	1.229	V	Equilibrium potential difference of oxygen evolution reaction
$E_{\text{II}}^{\text{eq}}$	1.36	V	Equilibrium potential difference of chlorine evolution reaction
$E_{\text{III}}^{\text{eq}}$	−0.828	V	Equilibrium potential difference of hydrogen evolution reaction

of 1920×1200 pixels, was employed to capture the rate of change in colour across the gel(s). The camera was equipped with a Basler C10-3514-8M-S f35 mm lens and was mounted on a Kaiser Copylizer executive LED – Kaiser 5215 stand, which features an illuminated base to ensure consistent lighting conditions throughout each experiment. The laboratory prototype pulse generator (HV-LV) [63] was used to deliver the pulses. The oscilloscope (HDO6104A-MS, LeCroy, USA) with voltage (HVD3206A, LeCroy, USA) and current (CP031A, LeCroy, USA) probes were used to monitor and verify the electric pulses generated by the pulse generator. The camera was connected to a PC, with which the video recordings of the experiments were recorded and saved. A photo of the experimental setup is shown in Fig. 1.

2.4. Camera system calibration experiments

The aim of the camera system calibration experiments was to develop a function capable of converting the colour information captured by the camera during the agarose gel experiments into numerical pH values for each pixel. A total of 27 different buffer solutions were prepared by mixing various weak acids with their conjugate bases, resulting in buffers with pH values between 1.0 and 13.0. Each buffer solution was verified using a calibrated pH metre to ensure accuracy. Three millilitres of each buffer solution were pipetted into a small Petri dish with a diameter of 34 mm. Then, 0.3 ml of a universal pH indicator solution was added to each Petri dish. The universal pH indicator was prepared with the following concentrations: 0.012 % methyl red, 0.06 % bromothymol blue, and 0.010 % phenolphthalein disodium salt. This indicator was chosen for its ability to display a wide range of colours and thus distinguish a broad spectrum of pH values. To facilitate the calibration experiments, the addition of agarose was omitted, as preliminary experiments showed that the agarose in the concentration used (i.e., 0.6 %) had no influence on the colour hue of the solutions. The solutions were then photographed with the camera system. Consistent lighting conditions were maintained throughout the experiments. The captured photographs were analysed to calculate the average RGB (red, green, blue) values of the pixels for each Petri dish. These RGB values were then converted into the HSV (hue, saturation, value) colour system, focusing on the hue component. The hue component, representing the angle on a 360-degree colour wheel corresponding to the perceived colour, was derived from the RGB values using the following formula:

$$h_{\text{RGB}} = \text{atan2}(\sqrt{3} \cdot (G - B), 2R - G - B). \quad (13)$$

Once the hue values corresponding to each pH value were determined, a calibration curve was established for the camera system by fitting a function to this data. The fitted function was a sum of three

sigmoid functions. This function was chosen because the universal pH indicator consists of three components, each corresponding to a distinct colour transition zone.

2.5. Agarose gel experiments

For the experiments with agarose gel, mini Petri dishes with a diameter of 34 mm were used, each of which was fitted with a 4.5 mm thick 3D-printed insert with a 15.3 mm long and 3 mm wide channel. This geometry was chosen because it can be accurately simulated with a one-dimensional model in our numerical simulations. The design of the insert is depicted in Fig. 2a. To simulate the comparable rate of diffusion and electrophoresis (i.e., the migration of charged species due to the electric field) to that of biological tissue, an agarose gel with the agarose concentration of 0.6 % was used [64]. The experiments were performed with three different media to assess their effects on pH changes: unbuffered medium, bicarbonate buffer, and HEPES buffer. The concentrations for the unbuffered medium (i.e., the NaCl solution) and the bicarbonate buffer solution were chosen to match the concentrations in our simulations (see Table 1). The concentration for the HEPES buffer was chosen to have the same molarity as the bicarbonate buffer, resulting in a concentration of 0.6434 % HEPES, with NaCl added to match the conductivity of the bicarbonate buffer. The corresponding concentrations for all three media were mixed in distilled water. The CO₂ was added to the bicarbonate buffer solution by infusing the distilled water with CO₂ using cartridges of pressurised CO₂ delivered using a pressure regulator, releasing gas into the water during the time required for the water to reach a desired pH level. To prepare the agarose phantoms, 0.6 % agarose powder was dissolved in each of the prepared solutions, heated in the microwave until completely dissolved, and then mixed with 10 % of the volume of the universal pH indicator solution. The resulting liquid agarose solutions were pipetted into the channels of the 3D-printed inserts in the Petri dishes and allowed to cool and solidify into a gel. In the experiments, a pulse waveform consisting of 8 rectangular pulses with a duration of 10 ms each and a repetition rate of 1 s^{-1} was delivered to the agarose gel phantoms. The amplitude of the pulses was either 200 V or 400 V (same as in the model, described in subsection 2.3). This pulse protocol was selected because of its suitability as a protocol for gene electrotransfer. Shorter pulse durations, e.g. in the microsecond range, would limit the observable pH changes, while the use of a larger number of shorter pulses (e.g. 800 pulses of 100 μs each, providing an equivalent on-time to eight 10 ms pulses) would make numerical calculations very challenging. The electrodes were made of 90–10 platinum-iridium alloy, with a diameter of 1 mm and an edge-to-edge distance of 14.3 mm. Three replicates were performed for

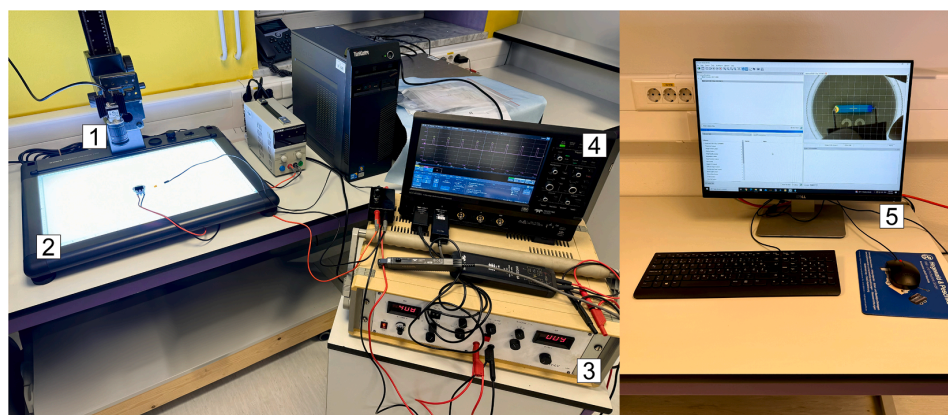


Fig. 1. Experimental setup for agarose gel experiments composed of a camera with a macro lens (1) mounted on a camera stand with an illuminated base (2), a laboratory prototype pulse generator (3), an oscilloscope with voltage and current probes (4), and a PC for recording the experiments (5).

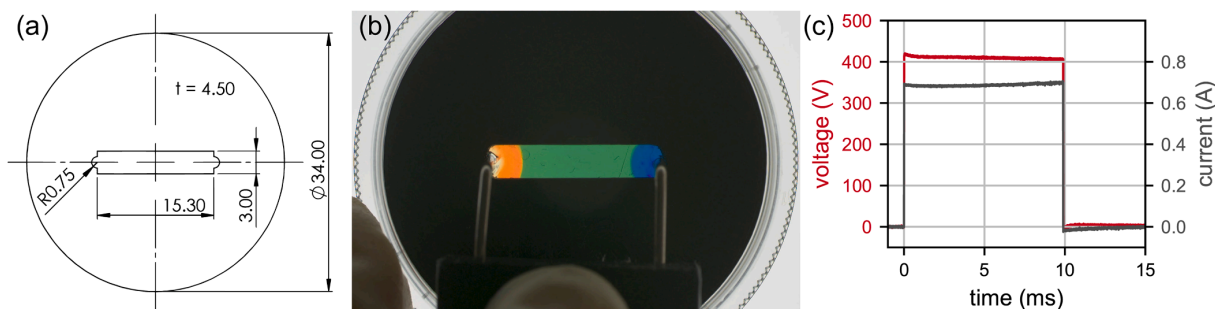


Fig. 2. (a) Design of the 4.5 mm thick 3D-printed insert with a 15.3 mm long and 3 mm wide channel used for agarose gel experiments. Note that all dimensions are in mm. (b) A representative agarose gel experiment performed in a mini Petri dish with the 3D-printed insert. (c) A recorded pulse from an agarose gel experiment.

each experimental condition and the experiments were recorded using the camera system. A representative agarose gel experiment performed in a mini Petri dish with the 3D-printed insert is shown in Fig. 2b, and a recorded pulse (voltage and current) from one of the experiments is shown in Fig. 2c. The post-processing of the experimental data was performed using Python.

3. Results and discussion

3.1. Camera system calibration

Fig. 3 shows the fitted function composed of three sigmoid functions (constituents of Eq. (14)) that relates the colour hue to the pH value and illustrates how the colour hue values vary across different pH levels. The hue values of the captured colours range from about 20 for pH values below 4 to about 260 for pH values above 10. The function demonstrates a useful range from pH 4 to pH 10, within which the hue values are sufficiently distinct for reliable differentiation. This function is crucial for the interpretation of agarose gel experiments, as it allows accurate colour-based pH values determination within the specified range. Outside the pH range of 4 to 10, the colour values are too similar and, therefore, cannot be reliably distinguished. The calibration curve shown in Fig. 3 is defined by the following equation

$$\text{hue}(\text{pH}) = 20.20 + \frac{36.25}{1 + \exp(-\text{pH} \cdot 2.94 + 13.63)} + \frac{135.84}{1 + \exp(-\text{pH} \cdot 3.17 + 22.22)} + \frac{62.32}{1 + \exp(-\text{pH} \cdot 3.29 + 30.72)} \quad (14)$$

Eq. (14) consists of a constant offset and three additive sigmoidal

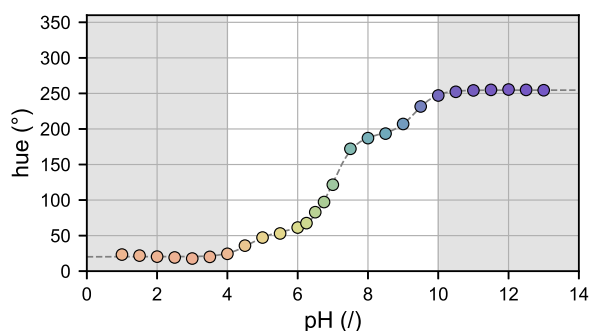


Fig. 3. The calibration curve of the hue value (in degrees) as a function of pH. Note that the usable range for this function is from pH 4 to pH 10, as the hue values outside this range are too similar and, therefore, cannot be reliably distinguished.

constituents of the form $c_1/(1 + \exp(-(c_2 \cdot \text{pH} + c_3)))$. Each of these three terms corresponds to a colour transition of the respective constituent pH indicator forming the universal pH indicator solution. Finding an inverse of the function in Eq. (14) would lead to a poorly defined function at the boundaries, so we solve numerically for pH given a particular hue, thus enabling temporal and spatial determination of the pH value in an agarose gel, i.e., for every pixel of the acquired image at a specific time during observation. Thus, the system allows for accurate (limited by the resolution of the imaging system and motion artifacts) mapping of pH changes in the agarose phantoms and tracking of the pH changes in time during an experiment.

The calibration curve should be obtained for each individual laboratory setup and setting to ensure accurate pH reconstruction. Variations in the experimental environment, such as differences in camera type, model, and settings, as well as lighting conditions, can significantly affect the recorded colour hue and consequently the derived pH values. In addition, temperature variations can affect the diffusion coefficients and conductivity, which can affect the formation and diffusion of pH fronts. It is therefore advisable to maintain a stable temperature during the experiments to minimise the variability in obtained results.

3.2. Computational modelling results

The extent to which the pH fronts travelled from the electrodes over time was examined to compare the results of the unbuffered and buffered models. These results are shown in Fig. 4a–c for the unbuffered model and in Fig. 4d–f for the buffered model. Different criteria to define pH fronts were established: Fig. 4a and d portray the entire region of altered pH and track the pH changes around the baseline pH (7.0 in the unbuffered model and 7.4 in the buffered model) within a pH value tolerance of ± 0.05 . In Fig. 4b and e, the fronts are tracked for pH values deviating by ± 1.5 from the baseline value. Fig. 4c and f illustrate the range where tissue damage could potentially occur due to extreme pH values (pH below 4.0 at the anode and above 10.6 at the cathode) [60, 65]. The last time point (i.e., at 60 s) corresponds to the experimental results shown in Figs. 5 and 6. The pH fronts in the unbuffered model were approximately twice as large (depending on the definition of the observed pH fronts) as those in the buffered model. In the unbuffered model, the pH fronts are larger at the anode than at the cathode, whereas the opposite is true in the buffered model. This discrepancy could be explained by the fact that the bicarbonate buffer, as prepared and used in our experiments (as opposed to in a living organism), is better at neutralising acidic pH changes, resulting in smaller pH fronts at the anode than at the cathode in the buffered model. The change in the slope of the curve (marked with an arrow) observed at 7.01 s coincides with the delivery of the final pulse in the sequence of eight pulses. During the pulse delivery, pH-altering species are produced and electrophoretically driven away from the electrodes. After the delivery of the last pulse, this electric field-driven migration and production cease. From here on the species diffuse freely at a slower rate compared to the electrophoretic

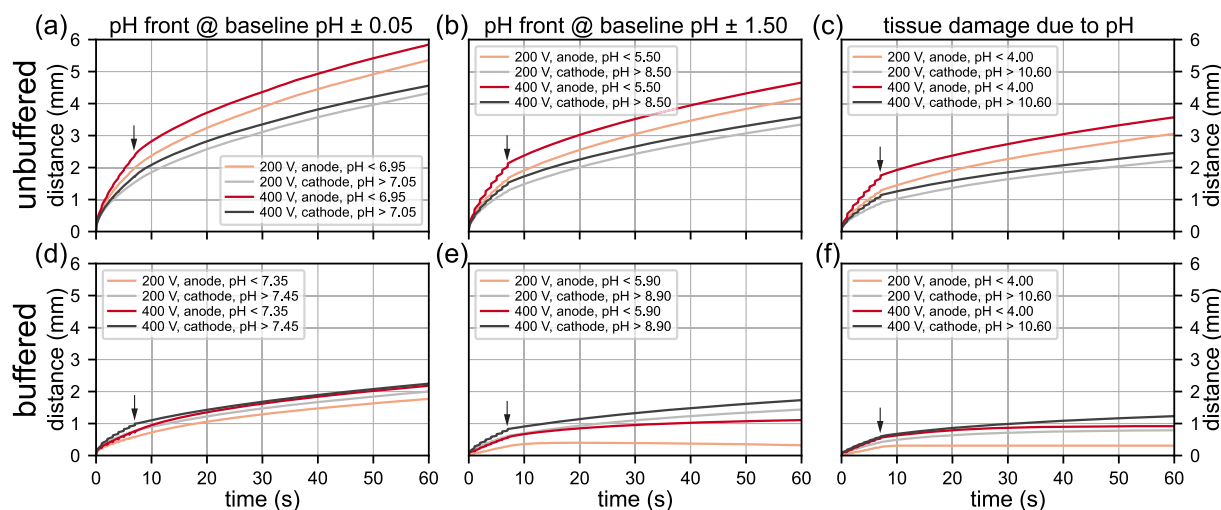


Fig. 4. The time course of the migration of the pH fronts from the anodes and cathodes in both the unbuffered (a-c) and the buffered model (d-f) for two amplitudes of the rectangular pulse waveform, 200 V and 400 V, with different criteria for defining the pH fronts. Note that the baseline pH is different in the unbuffered and the buffered model due to different initial ion concentrations; it is 7.0 in the unbuffered and 7.4 in the buffered model. Arrows indicate the ends of the pulse deliveries at 7.01 s.

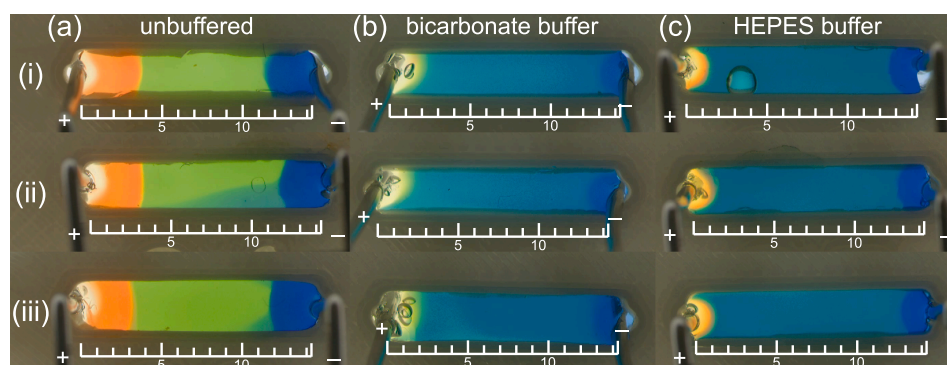


Fig. 5. Three replicates (i, ii, iii) of agarose gel experiments for 8 rectangular pulses with a duration of 10 ms, amplitude of 400 V, and a pulse repetition rate of 1 s^{-1} , performed in (a) the unbuffered medium, (b) the bicarbonate buffer medium, and (c) in the HEPES buffer medium. In order to also investigate the effect of diffusion, a time of 60 s from the delivery of the first pulse was selected for the analysis. Note that the scale bar dimensions are expressed in mm.

drag that occurred during the pulses. This transition explains the noticeable change in the slope in the pH front profiles.

3.3. Experimental observations

For each experimental condition (3 different media and 2 different pulse amplitudes), 3 repetitions of the agarose gel experiments were performed. To also capture the effect of diffusion of ionic species after pulse delivery in our investigation, the agarose gel phantoms were analysed 60 s after the start of the pulse delivery (the time point corresponding to the end time point in the graphs shown in Fig. 4). Snapshots extracted from the recorded videos at this time point are shown for the pulse amplitude of 400 V in Fig. 5a for the unbuffered medium, in Fig. 5b for the bicarbonate buffer medium, and in Fig. 5c for the HEPES buffer medium – 3 replicates for each medium. The experimental observations indicated a low variance (high reproducibility) between replicates (i, ii, iii). As expected, a significantly more extensive area of altered pH is observed in the unbuffered medium. However, while the buffer capabilities of the two buffers were comparable (due to being prepared to match in molarity), slight detectable differences between

the two buffers were nevertheless observed (Fig. 5b and c). The acidic pH front has a much less extreme pH value in the bicarbonate buffer, even though the front is slightly larger than in the HEPES buffer. Additionally, the delineation between the altered and the baseline pH is much sharper in the HEPES buffer than in the bicarbonate buffer.

The high amplitude of the pulses, both in voltage (and current), is critical, since the rate of hydrolysis and, thus, the amount of produced pH-altering species, is directly proportional to the faradaic charge transfer between the electrode(s) and the electrolytic solution. This transferred charge is, quantitatively, the temporal integral of the ohmic current flowing through the electrolyte solution (i.e., the generator current minus the capacitive current charging and discharging the double-layer capacitance). Due to these high currents flowing through the electrolytic solution (cell suspension, tissue) in electroporation, the resulting pH changes can be substantial, and their quantification is important.

The experimentally determined pH fronts for 8 rectangular pulses with a duration of 10 ms each, delivered at a repetition rate of 1 s^{-1} are shown in Fig. 6 for three different media: the unbuffered medium, the bicarbonate-buffered medium, and the HEPES-buffered medium

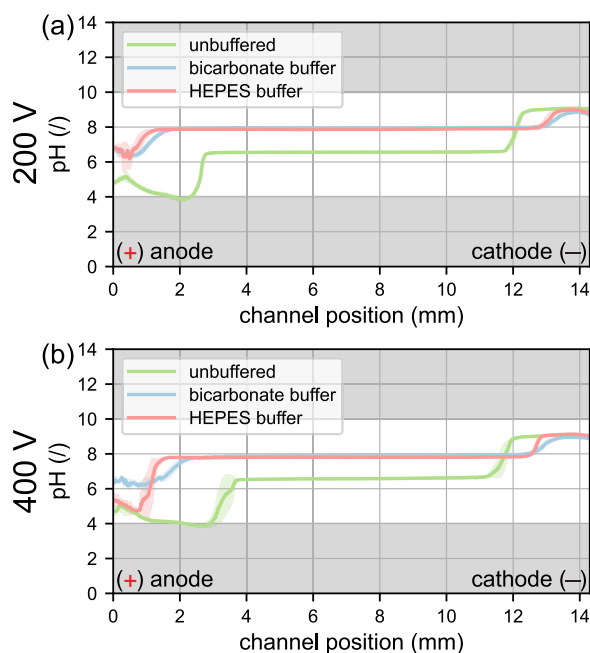


Fig. 6. Experimentally determined pH distributions for 8 rectangular pulses with a duration of 10 ms and a pulse repetition rate of 1 s^{-1} for experiments conducted in unbuffered medium, in bicarbonate-buffered medium, and HEPES-buffered medium. The amplitude of the pulses was 200 V in (a), and 400 V in (b). The shaded areas represent the standard deviations of the averaged values. The results are shown for a time of 60 s to also capture the effect of diffusion in the analysis. The anode is located on the left side (at 0 mm), and the cathode on the right side (at 14.3 mm).

determined 60 s after the start of the pulse delivery. The pulse amplitudes were set to 200 V in Fig. 6a and 400 V in b. In these experiments, the anode was positioned at 0 mm (left side) and the cathode at 14.3 mm (right side). The pH distributions were calculated by averaging the values over the three replicates of the central 50 pixels of the channel width across its entire length, covering the area between the electrodes. The standard deviations of the averaged values are represented by the lightly shaded areas surrounding the averaged values (curves) in Fig. 6. Notably, the pH fronts in the unbuffered medium are approximately twice as large as those observed in the buffered media. There is also a clear difference in baseline pH values between the unbuffered and buffered media, as the baseline pH value of the unbuffered media is around 7.0, and that of the buffered media around 7.4. As expected, the pH fronts are significantly larger at higher pulse amplitudes. At 200 V pulses, the pH fronts in the bicarbonate and HEPES buffers are quite similar. At 400 V pulses, however, the pH values in the HEPES buffer are more extreme, although the affected regions are smaller compared to those in the bicarbonate buffer. This difference is particularly evident near the anode.

3.4. Comparison of modelling and experimental results

The comparison of the calculated and experimentally determined pH fronts for 8 rectangular pulses each of a duration of 10 ms and a pulse repetition rate of 1 s^{-1} is shown in Fig. 7, determined as before at the 60-second time-point. The experimentally determined pH distributions were calculated by averaging the values of the central 50 pixels of the channel width across its entire length, covering the area between the electrodes, from each of the three replicates performed under identical conditions. The anode was positioned at 0 mm (left side) and the cathode at 14.3 mm (right side). Fig. 7a and b show the results for pulses

with the amplitude of 200 V, while Fig. 7c and d show the results for 400 V pulses. The results for the unbuffered medium are shown in Fig. 7a and c, while the results for the bicarbonate-buffered medium are shown in Fig. 7b and d. At the anode side of the unbuffered medium, good agreement between the experimental and simulation results is observed from about 2 mm for an amplitude of 200 V and from about 3 mm for an amplitude of 400 V. However, closer examination reveals an unexpected increase in pH values near the anode in the experimental data, which is unrealistic. This discrepancy is likely due to pH values falling in the undetectable range of our calibration function (shaded in grey in Fig. 3). Also, Fig. 5a shows a lack of colouration near the anode, suggesting that the pH indicator fails to function accurately at these extreme pH values. At the cathode, the experimental pH values are lower than those predicted by the simulations. For the buffered medium, the agreement between simulation and experiment is generally good, with particularly accurate predictions on the anode side.

The simulations predict larger areas of altered pH compared to the experiments, possibly due to an overestimation of the diffusion coefficients (for diffusion in water) in the model (Table 1). Because the model overestimates pH front propagation, the diffusion coefficient values for all species were reduced to 50 % of those listed in Table 1. The simulation results with lower values of the diffusion coefficients are shown in Fig. 7 with dashed lines. These simulation results show improved agreement with the experimental results, particularly for the unbuffered medium at a pulse amplitude of 400 V, but also at 200 V. In the buffered medium, the revised model demonstrates better agreement on the cathode side, albeit slightly less accurate than the model with higher diffusion coefficient on the anode side. Overall, the results indicate that the use of lower diffusion coefficients in the model leads to better agreement with the experimental data, suggesting that the original coefficients (for diffusion in water) may have been overestimated in our case. In our numerical simulations we used a highly refined mesh that effectively reduces the effect of numerical viscosity – a phenomenon where unwanted diffusion effects occur due to the discretisation inherent in numerical simulations. This highly refined mesh ensures that any potential effects of numerical viscosity are negligible and enables accurate representation of the physical processes involved. Further work in varying various species' diffusion coefficients may lead to a better description/prediction of the model with respect to the experiments. It also needs to be considered that tissue diffusion coefficients may differ from those in the agarose gel, potentially limiting the accuracy of the model.

During model development and experimentation with numerical simulations under different pulse parameters and conditions, we have been able to replicate the complex pH front behaviour dependent on pulse protocol parameters (pulse duration and pulse repetition rate). Namely, that the front advances during pulse application and retracts somewhat in the pause between the pulses in the case of the buffered medium. These simulation results corroborate experimental observations obtained in tissue *in vivo*, such as reported in [27]. However, since pH front retraction can only be observed in the model for pulses delivered at voltages much lower than those we employed in our study, and only for the case of the buffered medium, we opted to keep the discussion and validation of the model as general as possible, and we relegate the analysis at border conditions and the comparison and study of applicability of the model to *in vivo* work to future work.

4. Conclusions

The aim of the study was to develop a comprehensive mechanistic computational model of the pH changes in tissue during and after pulse application in electroporation applications by means of combined numerical modelling and experimentation. Numerically obtained results were combined with experiments to (1) quantitatively corroborate and validate the model premises by direct comparison of simulation results to a geometrically equivalent/accurate representation of simulated

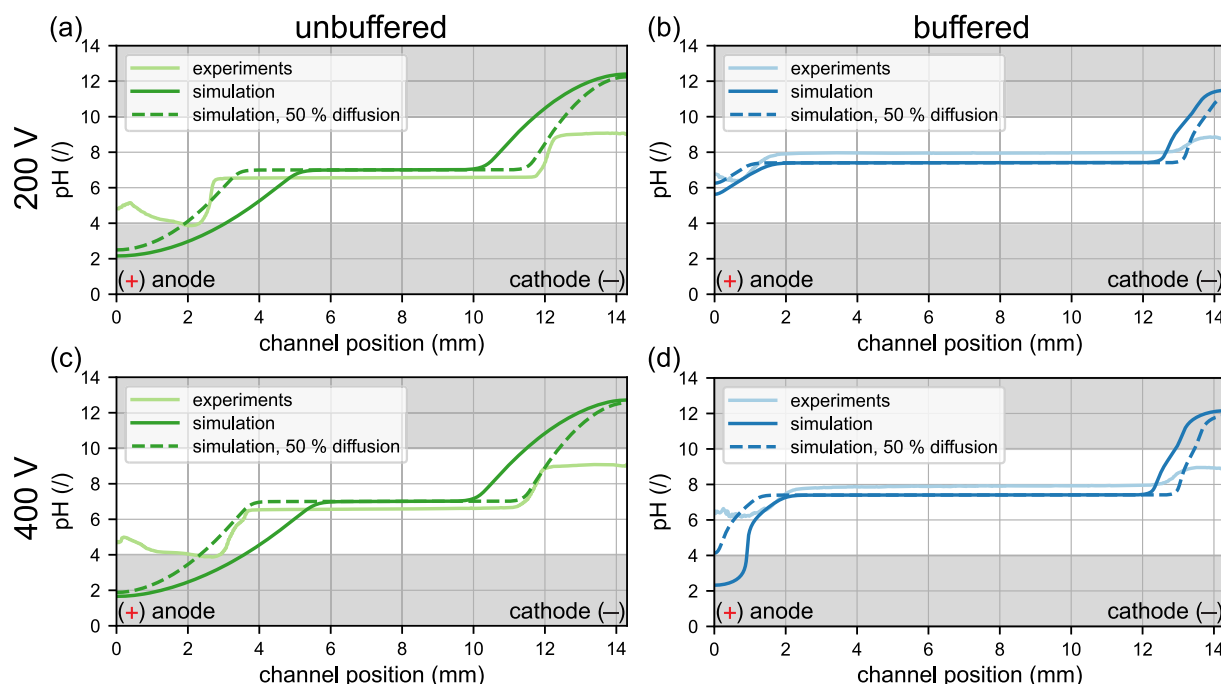


Fig. 7. Comparison of the calculated and experimentally determined pH distributions for 8 rectangular pulses with a duration of 10 ms and a pulse repetition rate of 1 s^{-1} . The amplitude of the pulses was 200 V in (a) and (b), and 400 V in (c) and (d). The results for the unbuffered medium are shown in (a) and (c), while the results for the buffered medium are shown in (b) and (d). The results are shown for a time of 60 s to also include the effect of diffusion in the analysis. The dashed lines represent the results of the models where the diffusion coefficients were reduced to 50 % of the values given in Table 1. The anode is located on the left (at 0 mm), and the cathode on the right (at 14.3 mm).

conditions in vitro, and to (2) obtain insight through experimentation into how accurate and comprehensive the model is in terms of the electrochemical phenomena it manages to capture.

The model is powerful enough to capture the effects of individual pulses and the dynamics of pH front evolution (migration, advancement, retraction) during the pause between the pulses. This is possible due to its construction as a dynamic time-domain model, which accounts for passive diffusion, active field-driven migration of species, and their production and annihilation according to the chemical reaction rates. This high degree of spatio-temporal resolution of the model comes not only with advantages such as deeper insight and understanding of the interplay of the various contributing factors and mechanisms affecting pH front formation and migration, but also with the disadvantage of high numerical complexity and instability, which renders the model difficult for practical use. Future work will focus on improving the robustness of the model in the sense of computational stability.

The results of our work show that the model generates a relatively accurate prediction of the pH front changes within an unbuffered and a buffered media but falls short in terms of absolute accuracy. This can be attributed to inaccurate values of some of the parameters obtained from literature i.e., from already established models in the field. The discrepancy and the need for optimisation in searching for correct ("best-fit") parameter values, as demonstrated by reducing diffusion coefficients (see Fig. 7), warrants further examination and experimentation to determine the origin of the discrepancy – it lies either in the source of the parameters that were adopted for the model, or in a crucial omission from the model in its construction. Either way, experimental observations clearly show there is a need to develop even more complex versions of this electrochemical model, e.g., one that would be capable of accounting for not only diffusion and electrokinetic mechanisms of

mass transfer of pH-altering species during pulse application but possibly also for the effect of other mechanisms such as electroosmosis and the interaction between the medium and the pH indicator, both of which have not been examined in our study.

CRediT authorship contribution statement

Rok Šmerc: Writing – review & editing, Writing – original draft, Visualization, Validation, Software, Methodology, Investigation, Formal analysis. **Damijan Miklavčič:** Writing – review & editing, Supervision, Project administration, Funding acquisition, Conceptualization. **Samo Mahnič-Kalamiza:** Writing – review & editing, Writing – original draft, Supervision, Methodology, Investigation, Conceptualization.

Declaration of competing interest

Damijan Miklavčič is the inventor of several patents pending and granted, is receiving royalties, and is consulting for several companies and organizations, which are active in electroporation and electroporation-based technologies and therapies. Other authors report no conflict of interest.

Acknowledgements

The authors acknowledge the support of the Slovenian Research and Innovation Agency (ARIS) under grant P2-0249 Electroporation-based technologies and treatments. This study was conducted within the Infrastructure Programme: Network of research infrastructure centres at the University of Ljubljana (MRIC UL IP-0510), also funded by the Slovenian Research and Innovation Agency (ARIS).

Appendix A. Equations for ionic species production, boundary, and initial conditions

The production of Na^+ and Cl^- ions is zero in both the unbuffered and buffered models

$$R_{Na^+} = R_{Cl^-} = 0. \quad (A.1)$$

In the unbuffered model, the H^+ and OH^- ions can be produced and consumed through the water autoprotolysis reaction

$$R_{H^+} = R_{OH^-} = k_{w,b} c_{H_2O} - k_{w,f} c_{H^+} c_{OH^-}, \quad (A.2)$$

where $k_{w,b}$ and $k_{w,f}$ are the rate constants of water autoprotolysis reactions in the backward and forward directions, respectively. In the buffered model, the production and consumption of the species H^+ , OH^- , HCO_3^- , CO_3^{2-} , and CO_2 are determined according to the water autoprotolysis reaction and the buffer reactions

$$R_{H^+} = k_{w,b} \cdot c_{H_2O} + k_{b1,b} \cdot c_{CO_2} \cdot c_{H_2O} - k_{w,f} \cdot c_{H^+} \cdot c_{OH^-} - k_{b1,f} \cdot c_{H^+} \cdot c_{HCO_3^-}, \quad (A.3)$$

$$R_{OH^-} = -k_{b2,f} \cdot c_{CO_2} \cdot c_{OH^-} + k_{b2,b} \cdot c_{HCO_3^-} - k_{b3,f} \cdot c_{HCO_3^-} \cdot c_{OH^-} + k_{b3,b} \cdot c_{CO_3^{2-}} + k_{w,b} \cdot c_{H_2O} - k_{w,f} \cdot c_{H^+} \cdot c_{OH^-}, \quad (A.4)$$

$$R_{HCO_3^-} = k_{b1,b} \cdot c_{CO_2} \cdot c_{H_2O} - k_{b1,f} \cdot c_{H^+} \cdot c_{HCO_3^-} + k_{b2,f} \cdot c_{CO_2} \cdot c_{OH^-} - k_{b2,b} \cdot c_{HCO_3^-} - k_{b3,f} \cdot c_{HCO_3^-} \cdot c_{OH^-} + k_{b3,b} \cdot c_{CO_3^{2-}}, \quad (A.5)$$

$$R_{CO_2} = -k_{b2,f} \cdot c_{CO_2} \cdot c_{OH^-} + k_{b2,b} \cdot c_{HCO_3^-} + k_{b1,f} \cdot c_{H^+} \cdot c_{HCO_3^-} - k_{b1,b} \cdot c_{CO_2} \cdot c_{H_2O}, \quad (A.6)$$

$$R_{CO_3^{2-}} = k_{b3,f} \cdot c_{HCO_3^-} \cdot c_{OH^-} - k_{b3,b} \cdot c_{CO_3^{2-}}. \quad (A.7)$$

At the electrode surface, the molar flux of the ionic species involved in the electrode reactions is linked to the charge transport of the electrochemical reactions [32,33]. The boundary conditions at the anode surface are therefore

$$N_{H^+} \cdot \mathbf{n} = -\frac{j_I}{F}, \quad (A.8)$$

$$N_{Cl^-} \cdot \mathbf{n} = \frac{j_{II}}{F}, \quad (A.9)$$

where \mathbf{n} is the unit normal vector, F is the Faraday constant, j_I is the current density contribution due to oxygen evolution reaction, and j_{II} is the current density contribution due to chlorine evolution reaction, given by Butler-Volmer equations

$$j_I = j_I^0 \left(\exp \left(-\frac{F(\phi + E_I^{eq})}{2 R T} \right) - \frac{c_{H^+}}{c_{H^+}^0} \exp \left(\frac{F(\phi + E_I^{eq})}{2 R T} \right) \right), \quad (A.10)$$

$$j_{II} = j_{II}^0 \left(\frac{c_{Cl^-}}{c_{Cl^-}^0} \exp \left(-\frac{F(\phi + E_{II}^{eq})}{2 R T} \right) - \exp \left(\frac{F(\phi + E_{II}^{eq})}{2 R T} \right) \right), \quad (A.11)$$

where j_i^0 is the exchange current density of the reaction i , and E_i^{eq} is the standard electrode potential of the reaction i . For all the other ionic species, the molar flux at the anode surface is equal to zero, thus

$$N_{OH^-} \cdot \mathbf{n} = N_{Na^+} \cdot \mathbf{n} = 0 \quad (A.12)$$

in the unbuffered model, and

$$N_{OH^-} \cdot \mathbf{n} = N_{Na^+} \cdot \mathbf{n} = N_{HCO_3^-} \cdot \mathbf{n} = N_{CO_2} \cdot \mathbf{n} = N_{CO_3^{2-}} \cdot \mathbf{n} = 0 \quad (A.13)$$

in the buffered model. At the cathode surface, the boundary condition is

$$N_{OH^-} \cdot \mathbf{n} = \frac{j_{III}}{F}, \quad (A.14)$$

where j_{III} is the current density contribution due to hydrogen evolution reaction

$$j_{III} = j_{III}^0 \left(\left(\frac{c_{OH^-}}{c_{OH^-}^0} \right)^2 \exp \left(-\frac{3F(\phi + E_{III}^{eq})}{2 R T} \right) - \exp \left(\frac{F(\phi + E_{III}^{eq})}{2 R T} \right) \right) \quad (A.15)$$

For all the other ionic species, the molar flux at the cathode surface is equal to zero, thus

$$N_{H^+} \cdot \mathbf{n} = N_{Na^+} \cdot \mathbf{n} = N_{Cl^-} \cdot \mathbf{n} = 0 \quad (A.16)$$

in the unbuffered model, and

$$N_{H^+} \cdot \mathbf{n} = N_{Na^+} \cdot \mathbf{n} = N_{Cl^-} \cdot \mathbf{n} = N_{HCO_3^-} \cdot \mathbf{n} = N_{CO_2} \cdot \mathbf{n} = N_{CO_3^{2-}} \cdot \mathbf{n} = 0 \quad (A.17)$$

in the buffered model. Since there are initially no concentration gradients in the electrolyte, the initial conditions are

$$\nabla c_i = 0 \text{ at } t = 0, \quad (\text{A.18})$$

$$c_i = c_i^0. \quad (\text{A.19})$$

Data availability

Data will be made available on request.

References

- [1] E. Neumann, K. Rosenheck, Permeability changes induced by electric impulses in vesicular membranes, *J. Membran Biol.* 10 (1972) 279–290, <https://doi.org/10.1007/BF01867861>.
- [2] T. Kotnik, G. Pucihar, D. Miklavčič, The cell in the electric field, in: S.T. Kee, J. Gehl, E.W. Lee (Eds.), *Clinical Aspects of Electroporation*, Springer New York, New York, NY, 2011, pp. 19–29, https://doi.org/10.1007/978-1-4419-8363-3_3.
- [3] T. Kotnik, L. Rems, M. Tarek, D. Miklavčič, Membrane electroporation and electroporation: mechanisms and models, *Annu. Rev. Biophys.* 48 (2019) 63–91, <https://doi.org/10.1146/annurev-biophys-052118-115451>.
- [4] S. Haberl, D. Miklavčič, G. Sersa, W. Frey, B. Rubinsky, Cell membrane electroporation-Part 2: the applications, *IEEE Electr. Insul. Mag.* 29 (2013) 29–37, <https://doi.org/10.1109/MEI.2013.6410537>.
- [5] M.L. Yarmush, A. Golberg, G. Sersa, T. Kotnik, D. Miklavčič, Electroporation-based technologies for medicine: principles, applications, and challenges, *Annu. Rev. Biomed. Eng.* 16 (2014) 295–320, <https://doi.org/10.1146/annurev-bioeng-071813-104622>.
- [6] T. Kotnik, W. Frey, M. Sack, S. Haberl Meglič, M. Peterka, D. Miklavčič, Electroporation-based applications in biotechnology, *Trend. Biotechnol.* 33 (2015) 480–488, <https://doi.org/10.1016/j.tibtech.2015.06.002>.
- [7] S. Mahnič-Kalamiza, E. Vorobiev, D. Miklavčič, Electroporation in food processing and biorefinery, *J. Membran. Biol.* 247 (2014) 1279–1304, <https://doi.org/10.1007/s00232-014-9737-x>.
- [8] G. Saldana, I. Alvarez, S. Condón, J. Raso, Microbiological aspects related to the feasibility of PEF technology for food pasteurization, *Crit. Rev. Food Sci. Nutr.* 54 (2014) 1415–1426, <https://doi.org/10.1080/10408398.2011.638995>.
- [9] S. Sachdev, T. Potočník, L. Rems, D. Miklavčič, Revisiting the role of pulsed electric fields in overcoming the barriers to in vivo gene electrotransfer, *Bioelectrochemistry* 144 (2022) 107994, <https://doi.org/10.1016/j.bioelechem.2021.107994>.
- [10] B. Geboers, H.J. Scheffer, P.M. Graybill, A.H. Ruarus, S. Nieuwenhuizen, R.S. Puijk, P.M. Van Den Tol, R.V. Davalos, B. Rubinsky, T.D. De Grujil, D. Miklavčič, M. R. Meijerink, High-voltage electrical pulses in oncology: irreversible electroporation, electrochemotherapy, gene electrotransfer, electrofusion, and electroimmunotherapy, *Radiology* 295 (2020) 254–272, <https://doi.org/10.1148/radiol.2020192190>.
- [11] R. Heller, L.C. Heller, Gene electrotransfer clinical trials. *Advances in Genetics*, Elsevier, 2015, pp. 235–262, <https://doi.org/10.1016/bs.adgen.2014.10.006>.
- [12] C. Rosazza, S. Haberl Meglič, A. Zumbusch, M.-P. Rols, D. Miklavčič, Gene Electrotransfer, A mechanistic perspective, *CGT* 16 (2016) 98–129, <https://doi.org/10.2174/1566523216666160331130040>.
- [13] A. Sugrue, V. Vaidya, C. Witt, C.V. DeSimone, O. Yasin, E. Maor, A.M. Killu, S. Kapa, C.J. McLeod, D. Miklavčič, S.J. Asirvatham, Irreversible electroporation for catheter-based cardiac ablation: a systematic review of the preclinical experience, *J. Interv. Card. Electrophysiol.* 55 (2019) 251–265, <https://doi.org/10.1007/s10840-019-00574-3>.
- [14] A. Verma, L. Boersma, D.E. Haines, A. Natale, F.E. Marchlinski, P. Sanders, H. Calkins, D.L. Packer, J. Hummel, B. Onal, S. Rosen, K.-H. Kuck, G. Hindricks, B. Wilmsore, First-in-human experience and acute procedural outcomes using a novel pulsed field ablation system: the PULSED AF pilot trial, *Circ. Arrhythm. Electrophysiol.* 15 (2022) e010168, <https://doi.org/10.1161/CIRCEP.121.010168>.
- [15] V.Y. Reddy, E.P. Gerstenfeld, A. Natale, W. Whang, F.A. Cuoco, C. Patel, S. E. Mountantonakis, D.N. Gibson, J.D. Harding, C.R. Ellis, K.A. Ellenbogen, D. B. DeLurgio, J. Osorio, A.B. Achyutha, C.W. Schneider, A.S. Mugglin, E. M. Albrecht, K.M. Stein, J.W. Lehmann, M. Mansour, Pulsed field or conventional thermal ablation for paroxysmal atrial fibrillation, *N. Engl. J. Med.* 389 (2023) 1660–1671, <https://doi.org/10.1056/NEJMoa2307291>.
- [16] A. Verma, D.E. Haines, L.V. Boersma, N. Sood, A. Natale, F.E. Marchlinski, H. Calkins, P. Sanders, D.L. Packer, K.-H. Kuck, G. Hindricks, B. Onal, J. Cerkvenik, H. Tada, D.B. DeLurgio, on behalf of the PULSED AF investigators, pulsed field ablation for the treatment of atrial fibrillation: PULSED AF pivotal trial, *Circulation* 147 (2023) 1422–1432, <https://doi.org/10.1161/CIRCULATIONAHA.123.063988>.
- [17] K.-R.J. Chun, D. Miklavčič, K. Vlachos, S. Bordignon, D. Scherr, P. Jais, B. Schmidt, State-of-the-art pulsed field ablation for cardiac arrhythmias: ongoing evolution and future perspective, *Europace* 26 (2024) euae134, <https://doi.org/10.1093/europace/eaue134>.
- [18] S. Mahnič-Kalamiza, D. Miklavčič, Scratching the electrode surface: insights into a high-voltage pulsed-field application from in vitro & in silico studies in indifferent fluid, *Electrochim. Acta* 363 (2020) 137187, <https://doi.org/10.1016/j.electacta.2020.137187>.
- [19] P.A. Garcia, R.V. Davalos, D. Miklavčič, A numerical investigation of the electric and thermal cell kill distributions in electroporation-based therapies in tissue, *PLoS ONE* 9 (2014) e103083, <https://doi.org/10.1371/journal.pone.0103083>.
- [20] C. Rossmanna, D. Haemmerich, Review of temperature dependence of thermal properties, dielectric properties, and perfusion of biological tissues at hyperthermic and ablation temperatures, *Crit. Rev. Biomed. Eng.* 42 (2014) 467–492, <https://doi.org/10.1615/CritRevBiomedEng.2015012486>.
- [21] E.M. Dunki-Jacobs, P. Philips, R.C.G. Martin II, Evaluation of thermal injury to liver, pancreas and kidney during irreversible electroporation in an in vivo experimental model, *Brit. J. Surg.* 101 (2014) 1113–1121, <https://doi.org/10.1002/bjs.9536>.
- [22] K.N. Aycok, R.V. Davalos, Irreversible electroporation: background, theory, and review of recent developments in clinical oncology, *Bioelectricity* 1 (2019) 214–234, <https://doi.org/10.1089/bioe.2019.0029>.
- [23] P. Agnass, E. Van Veldhuisen, M.J.C. Van Gemert, C.W.M. Van Der Geld, K.P. Van Lienden, T.M. Van Gulik, M.R. Meijerink, M.G. Besselink, H.P. Kok, J. Crezee, Mathematical modeling of the thermal effects of irreversible electroporation in vitro, in vivo, and clinical use: a systematic review, *Int. J. Hypertherm.* 37 (2020) 486–505, <https://doi.org/10.1080/02656736.2020.1753828>.
- [24] E. Nilsson, J. Berendson, E. Fontes, Impact of chlorine and acidification in the electrochemical treatment of tumours, *J. Appl. Electrochem.* 30 (2000) 1321–1333, <https://doi.org/10.1023/A:1026560806158>.
- [25] E. Nilsson, E. Fontes, Mathematical modelling of physicochemical reactions and transport processes occurring around a platinum cathode during the electrochemical treatment of tumours, *Bioelectrochemistry* 53 (2001) 213–224, [https://doi.org/10.1016/S0302-4598\(01\)00097-6](https://doi.org/10.1016/S0302-4598(01)00097-6).
- [26] P. Turjanski, N. Olaiz, F. Maglietti, S. Michinski, C. Suárez, F.V. Molina, G. Marshall, The role of pH fronts in reversible electroporation, *PLoS ONE* 6 (2011) e17303, <https://doi.org/10.1371/journal.pone.0017303>.
- [27] M. Marino, N. Olaiz, E. Signori, F. Maglietti, C. Suárez, S. Michinski, G. Marshall, pH fronts and tissue natural buffer interaction in gene electrotransfer protocols, *Electrochim. Acta* 255 (2017) 463–471, <https://doi.org/10.1016/j.electacta.2017.09.021>.
- [28] X. Wang, H.J. Lim, A. Son, Characterization of denaturation and renaturation of DNA for DNA hybridization, *Environ. Health. Toxicol.* 29 (2014) e2014007, <https://doi.org/10.5620/eh.2014.29.e2014007>.
- [29] T. Potočník, S. Sachdev, T. Polajžer, A. Maček Lebar, D. Miklavčič, Efficient gene transfection by electroporation—in vitro and in silico study of pulse parameters, *Appl. Sci.* 12 (2022) 8237, <https://doi.org/10.3390/app12168237>.
- [30] T. Potočník, A. Maček Lebar, Š. Kos, M. Reberšek, E. Pirč, G. Sersa, D. Miklavčič, Effect of experimental electrical and biological parameters on gene transfer by electroporation: a systematic review and meta-analysis, *Pharmaceutics* 14 (2022) 2700, <https://doi.org/10.3390/pharmaceutics14122700>.
- [31] D. Miklavčič, A. Fajgelj, G. Sersa, Tumour treatment by direct electric current: electrode material deposition, *Bioelectrochem. Bioenerget.* 35 (1994) 93–97, [https://doi.org/10.1016/0302-4598\(94\)87017-9](https://doi.org/10.1016/0302-4598(94)87017-9).
- [32] E. Nilsson, J. Berendson, E. Fontes, Development of a dosage method for electrochemical treatment of tumours: a simplified mathematical model, *Bioelectrochem. Bioenerget.* 47 (1998) 11–18, [https://doi.org/10.1016/S0302-4598\(98\)00157-3](https://doi.org/10.1016/S0302-4598(98)00157-3).
- [33] E. Nilsson, J. Berendson, E. Fontes, Electrochemical treatment of tumours: a simplified mathematical model, *J. Electroanal. Chem.* 460 (1999) 88–99, [https://doi.org/10.1016/S0022-0728\(98\)00352-0](https://doi.org/10.1016/S0022-0728(98)00352-0).
- [34] E. Nilsson, H. Von Euler, J. Berendson, A. Thörne, P. Wersäll, I. Näslund, A.-S. Lagerstedt, K. Narfström, J.M. Olsson, Electrochemical treatment of tumours, *Bioelectrochemistry* 51 (2000) 1–11, [https://doi.org/10.1016/S0302-4598\(99\)00073-2](https://doi.org/10.1016/S0302-4598(99)00073-2).
- [35] H. Von Euler, A. Söderstedt, A. Thörne, J.M. Olsson, G. Yongqing, Cellular toxicity induced by different pH levels on the R3230AC rat mammary tumour cell line. An in vitro model for investigation of the tumour destructive properties of electrochemical treatment of tumours, *Bioelectrochemistry* 58 (2002) 163–170, [https://doi.org/10.1016/S1567-5394\(02\)00154-8](https://doi.org/10.1016/S1567-5394(02)00154-8).
- [36] H.M.C. Ciria, M.M. González, L.O. Zamora, L.E.B. Cabrales, G.V. Sierra González, L. O. de Oliveira, R. Zanella, A.C. Buzaid, O. Parise, L.M. Brito, C.A.A. Teixeira, M. das N. Gomes, G. Moreno, V. Feo da Veiga, M. Tello, C. Holandino, Antitumor effects of electrochemical treatment, *Chin. J. Cancer Res.* 25 (2013) 223–234, <https://doi.org/10.3978/j.issn.1000-9604.2013.03.03>.
- [37] M. Phillips, L. Rubinsky, A. Meir, N. Raju, B. Rubinsky, Combining electrolysis and electroporation for tissue ablation, *Technol. Cancer Res. Treat.* 14 (2015) 395–410, <https://doi.org/10.1177/1533034614560102>.
- [38] M. Phillips, H. Krishnan, N. Raju, B. Rubinsky, Tissue ablation by a synergistic combination of electroporation and electrolysis delivered by a single pulse, *Ann. Biomed. Eng.* 44 (2016) 3144–3154, <https://doi.org/10.1007/s10439-016-1624-4>.

- [39] L. Rubinsky, E. Guenther, P. Mikus, M. Stehling, B. Rubinsky, Electrolytic effects during tissue ablation by electroporation, *Technol. Cancer Res. Treat.* 15 (2016) NP95–NP103, <https://doi.org/10.1177/1533034615601549>.
- [40] H.B. Kim, J.H. Chung, Incorporation of reversible electroporation into electrolysis accelerates apoptosis for rat liver tissue, *Technol. Cancer Res. Treat.* 19 (2020) 153303382094805, <https://doi.org/10.1177/1533033820948051>.
- [41] N.R. Rajagopalan, T. Munawar, M.C. Sheehan, M. Fujimori, W.-R. Vista, T. Wimmer, N.B. Gutta, S.B. Solomon, G. Srimathveeravalli, Electrolysis products, reactive oxygen species and ATP loss contribute to cell death following irreversible electroporation with microsecond-long pulsed electric fields, *Bioelectrochemistry* 155 (2024) 108579, <https://doi.org/10.1016/j.bioelechem.2023.108579>.
- [42] A. Vizintin, S. Marković, J. Ščančar, D. Miklavčič, Electroporation with nanosecond pulses and bleomycin or cisplatin results in efficient cell kill and low metal release from electrodes, *Bioelectrochemistry* 140 (2021) 107798, <https://doi.org/10.1016/j.bioelechem.2021.107798>.
- [43] E. Radzevičiūtė-Valčiukė, J. Gečaitė, A. Želvys, A. Zinkevičienė, R. Žalneravičius, V. Malysko-Ptasinskė, A. Nemeikaitė-Čenienė, V. Kašėta, N. German, J. Novickij, A. Ramanavičienė, J. Kulbacka, V. Novickij, Improving nonviral gene delivery using MHz bursts of nanosecond pulses and gold nanoparticles for electric field amplification, *Pharmaceutics* 15 (2023) 1178, <https://doi.org/10.3390/pharmaceutics15041178>.
- [44] K. Balantić, P. Kramar, D. Miklavčič, *In Silico* numerical model of aluminum and iron dissolution during electric pulse application for electroporation, *Bioelectricity* (2024), <https://doi.org/10.1089/bioe.2023.0026> bioe.2023.0026.
- [45] A. Meir, M. Hjouj, L. Rubinsky, B. Rubinsky, Magnetic resonance imaging of electrolysis, *Sci. Rep.* 5 (2015) 8095, <https://doi.org/10.1038/srep08095>.
- [46] A. Meir, B. Rubinsky, Electrical impedance tomography of electrolysis, *PLoS ONE* 10 (2015) e0126332, <https://doi.org/10.1371/journal.pone.0126332>.
- [47] J. Morren, B. Roodenburg, S.W.H. De Haan, Electrochemical reactions and electrode corrosion in pulsed electric field (PEF) treatment chambers, *Innov. Food Sci. Emerg. Technolog.* 4 (2003) 285–295, [https://doi.org/10.1016/S1466-8564\(03\)00041-9](https://doi.org/10.1016/S1466-8564(03)00041-9).
- [48] N. Meneses, H. Jaeger, D. Knorr, pH-changes during pulsed electric field treatments — numerical simulation and in situ impact on polyphenoloxidase inactivation, *Innov. Food Sci. Emerg. Technolog.* 12 (2011) 499–504, <https://doi.org/10.1016/j.ifset.2011.07.001>.
- [49] G. Pataro, G.M.J. Barca, G. Donsi, G. Ferrari, On the modelling of the electrochemical phenomena at the electrode-solution interface of a PEF treatment chamber: effect of electrical parameters and chemical composition of model liquid food, *J. Food Eng.* 165 (2015) 45–51, <https://doi.org/10.1016/j.jfoodeng.2015.05.010>.
- [50] D. Miklavčič, G. Sersa, M. Kryžanowski, S. Novaković, F. Bobanović, R. Golouh, L. Vodovnik, Tumor treatment by direct electric current-tumor temperature and pH, electrode material and configuration, *Bioelectrochem. Bioenerget.* 30 (1993) 209–220, [https://doi.org/10.1016/0302-4598\(93\)80080-E](https://doi.org/10.1016/0302-4598(93)80080-E).
- [51] P. Turjanski, N. Olaiz, P. Abou-Adal, C. Suárez, M. Risk, G. Marshall, pH front tracking in the electrochemical treatment (EChT) of tumors: experiments and simulations, *Electrochim. Acta* 54 (2009) 6199–6206, <https://doi.org/10.1016/j.electacta.2009.05.062>.
- [52] N. Olaiz, C. Suárez, M. Risk, F. Molina, G. Marshall, Tracking protein electrodenaturation fronts in the electrochemical treatment of tumors, *Electrochem. Commun.* 12 (2010) 94–97, <https://doi.org/10.1016/j.elecom.2009.10.044>.
- [53] N. Olaiz, F. Maglietti, C. Suárez, F.V. Molina, D. Miklavcic, L. Mir, G. Marshall, Electrochemical treatment of tumors using a one-probe two-electrode device, *Electrochim. Acta* 55 (2010) 6010–6014, <https://doi.org/10.1016/j.electacta.2010.05.057>.
- [54] E. Luján, H. Schinca, N. Olaiz, S. Urquiza, F.V. Molina, P. Turjanski, G. Marshall, Optimal dose-response relationship in electrolytic ablation of tumors with a one-probe-two-electrode device, *Electrochim. Acta* 186 (2015) 494–503, <https://doi.org/10.1016/j.electacta.2015.10.147>.
- [55] E.M. Calzado, H. Schinca, L.E.B. Cabrales, F.M. García, P. Turjanski, N. Olaiz, Impact of permeabilization and pH effects in the electrochemical treatment of tumors: experiments and simulations, *Appl. Math. Model.* 74 (2019) 62–72, <https://doi.org/10.1016/j.apm.2019.04.041>.
- [56] A. Mokhtare, M. Shiv Krishna Reddy, V.A. Roodan, E.P. Furlani, A. Abbaspourrad, The role of pH fronts, chlorination and physicochemical reactions in tumor necrosis in the electrochemical treatment of tumors: a numerical study, *Electrochim. Acta* 307 (2019) 129–147, <https://doi.org/10.1016/j.electacta.2019.03.148>.
- [57] F. Maglietti, S. Michinski, N. Olaiz, M. Castro, C. Suárez, G. Marshall, The role of Ph fronts in tissue electroporation based treatments, *PLoS ONE* 8 (2013) e80167, <https://doi.org/10.1371/journal.pone.0080167>.
- [58] Z.S. Salameh, K.N. Aycock, N. Alinezhadbalalami, K.M. Imran, I.H. McKillop, I. C. Allen, R.V. Davalos, Harnessing the electrochemical effects of electroporation-based therapies to enhance anti-tumor immune responses, *Ann. Biomed. Eng.* 52 (2024) 48–56, <https://doi.org/10.1007/s10439-023-03403-x>.
- [59] N. Olaiz, E. Signori, F. Maglietti, A. Soba, C. Suárez, P. Turjanski, S. Michinski, G. Marshall, Tissue damage modeling in gene electrotransfer: the role of pH, *Bioelectrochemistry* 100 (2014) 105–111, <https://doi.org/10.1016/j.bioelechem.2014.05.001>.
- [60] E. Luján, M. Marino, N. Olaiz, G. Marshall, Towards an optimal dose-response relationship in gene electrotransfer protocols, *Electrochim. Acta* 319 (2019) 1002–1011, <https://doi.org/10.1016/j.electacta.2019.07.029>.
- [61] T. Jarm, M. Cemazar, D. Miklavcic, G. Sersa, Antivascular effects of electrochemotherapy: implications in treatment of bleeding metastases, *Expert. Rev. Anticancer Ther.* 10 (2010) 729–746, <https://doi.org/10.1586/era.10.43>.
- [62] J.S. Newman, K.E. Thomas-Alyea, *Electrochemical Systems*, J. Wiley, Hoboken, N. J, 2004, 3rd ed.
- [63] M. Pavlin, K. Flisar, M. Kandušer, The role of electrophoresis in gene electrotransfer, *J. Membran. Biol.* 236 (2010) 75–79, <https://doi.org/10.1007/s00232-010-9276-z>.
- [64] E. Albor-Ramírez, M. Reyes-Alberto, L.M. Vidal-Flores, E. Gutierrez-Herrera, M. A. Padilla-Castaneda, Agarose gel characterization for the fabrication of brain tissue phantoms for infrared multispectral vision systems, *Gels* 9 (2023) 944, <https://doi.org/10.3390/gels9120944>.
- [65] N.R. Perkons, E.J. Stein, C. Nwaezeapu, J.C. Wildenberg, K. Saleh, R. Itkin-Ofer, D. Ackerman, M.C. Soulen, S.J. Hunt, G.J. Nadolski, T.P. Gade, Electrolytic ablation enables cancer cell targeting through pH modulation, *Commun. Biol.* 1 (2018) 48, <https://doi.org/10.1038/s42003-018-0047-1>.

2.5 Paper 5

Title: **On the importance of electroosmosis in pulsed electric field treatment of food matrices**

Authors: **Rok Šmerc** and Samo Mahnič-Kalamiza

Publication: *Results in Engineering*

Impact factor: 7.9 (2024)

Quartile: Q1

Rank: 6/175 (Multidisciplinary engineering)

Status: under review

On the importance of electroosmotic flow in pulsed electric field treatment of food matrices

Rok Šmerc and Samo Mahnič-Kalamiza*

University of Ljubljana, Faculty of Electrical Engineering, Tržaška cesta 25, SI-1000 Ljubljana, Slovenia

Abstract

This study explores key aspects of electroosmotic flow (EOF) in plant and animal tissues under pulsed electric field (PEF) and direct current (DC) treatment conditions. First, we investigate the detectability of EOF in potato tubers using texture analysis and evaluate whether PEF treatment is a prerequisite to electroosmotic dehydration due to its ability to liberate intracellular liquid. Second, we extend our analysis to freshly excised animal muscle to assess the role of electroosmosis in mass transfer, given the renewed interest in PEF as a meat processing pretreatment. Third, we examine agarose phantoms as potential surrogates for plant and animal tissues in EOF studies. Additionally, we confirmed earlier observations that EOF occurs and is detectable using texture analysis during individual PEF pulses, not only under DC conditions. These results have significant implications for food processing (and biomedical applications in electroporation-based therapies), offering new insights into fluid transport mechanisms in biological tissues.

Keywords: Electroosmosis; Food matrices; Pulsed Electric Field (PEF) treatment; Texture analysis; Tissue phantoms.

Highlights:

- EOF detected in potato tubers under PEF treatment and in DC conditions.
- EOF influences mass transfer in freshly excised animal muscle as a meat model.
- Agarose phantoms are suitable surrogates for EOF studies in plant and animal tissues.
- EOF occurs during PEF pulse application, impacting mass transfer during treatment.

1 Introduction

Pulsed electric field (PEF) technology has gained significant attention in various scientific and industrial applications. The fundamental mechanism of PEF involves the application of short-duration, high-voltage electrical pulses to biological tissue, resulting in electroporation – the temporary or permanent permeabilisation of cell membranes due to the formation of transient hydrophilic pores [1]. The extent of electroporation is dependent on multiple factors, including the electric field strength, pulse duration and the electrical properties of the tissue [2–4]. This phenomenon is widely utilised in many fields such as food processing [5], biomedicine [6, 7], environmental science [8], and biotechnology [9]. Within the food industry, PEF has been strategically used as a pretreatment to improve mass transfer processes, in particular by increasing juice extraction yields [10], improving drying through accelerated water removal [11],

*Corresponding author. E-mail address: samo.mahnic-kalamiza@fe.uni-lj.si (S. Mahnič-Kalamiza).

improving bioaccessibility of valuable bioactive compounds [12, 13], and reducing the content of toxicants [14, 15]. In addition, electroporation has been used in cryopreservation techniques to introduce cryoprotectants into the cells to prevent crystal formation during freezing, thereby preserving food texture and flavour [5].

While electroporation has been the focus of extensive research, electroosmosis, another phenomenon associated with PEF, has been relatively overlooked. Electroosmosis or electroendosmosis refers to the directional movement of fluid, usually water, through porous media induced by an external electric field. This fluid motion is caused by interactions at charged solid-liquid interfaces, which form an electric double layer, driving ions and subsequently fluid under the influence of the electric field [16]. The superficial electroosmotic flow velocity (u_{EOS}) in porous media is expressed mathematically as:

$$u_{\text{EOS}} = \frac{\varepsilon_w \zeta \varepsilon}{\eta \lambda^2} \nabla \phi, \quad (1)$$

where ε_w is the permittivity of water (F/m), ζ is the zeta potential (V) at the charged interfaces, ε is the porosity of the medium, η is the dynamic viscosity (Pa · s) of the fluid, λ is the tortuosity, describing the complexity of fluid pathways through the porous medium, and $\nabla \phi$ is the gradient of the electric potential (V/m) [17].

Originally introduced in civil engineering for mitigating waterlogged clayey soils [18], electroosmosis subsequently found wide application in addressing soil dewatering, foundation consolidation, and mould growth prevention in buildings, particularly in fine-grained, low-permeability materials such as clays and silts [19, 20]. Electroosmotic flow (EOF) has a directional nature; if the zeta potential of the charged solid-liquid interface is negative, the solid surface attracts positive counterions from the liquid, forming an electric double layer. This layer exhibits a net positive charge, which migrates towards the negative electrode, i.e., the cathode in an external electric field. Thus, the EOF is from the anode towards the cathode, causing the cathode region to become wet while the anode region dries. Vice-versa is also true; given a positive zeta potential of the solid-liquid interface, a negative double layer of counterions will form and migrate towards the anode in the external electric field, with the fluid flowing from the cathode to the anode, wetting the anode and drying up the cathode [21].

Within the context of food chemistry and applications relevant to food processing, it is noteworthy that most food matrices exhibit a negative zeta potential [22]. For intact raw materials of interest to food processing industry that are targets of PEF treatment such as plant tissues (e.g., plant tubers such as potato, beetroot, etc.), the presence of the cell wall is relevant to the establishing of the EOF within the extracellular porous space. The electrical potential of most cell walls was found to be negative [23], and since it was also shown, at least for plant cell membranes, that zeta potential strongly and linearly correlates with the electrical potential [24], we can expect that most plant tissues will exhibit a negative zeta potential at the cell wall–extracellular liquid interface. This means that any EOF within such structures will likely be from the anode to the cathode, directionality-wise.

Recently, the importance of electroosmosis for food technology has been demonstrated by electroosmotic dewatering, which offers improved energy efficiency and environmental benefits compared to conventional thermal drying techniques [25, 26]. Electroosmosis is also important from a biomedical perspective for various applications. It has been theoretically demonstrated that when an electric field is applied to tumour tissue, the anode becomes strongly acidic and the cathode strongly alkaline due to the redistribution of ions, which leads to the denaturation of proteins and cell death [27–29]. Simultaneously, the EOF drives water from the anode to the cathode, intensifying tissue dehydration and amplifying the destructive effects of these localised pH shifts. Nevertheless, electroosmosis has its limitations in electrochemical tumour ablation, as the positioning of the electrodes critically determines the direction of the flow and large tumour volumes pose a major challenge. These factors probably contribute to the limited research into the technique. Another example is electrokinetic convection-enhanced delivery, which improves

the transport of solutes to deep brain regions by directing the flow with an electric field. It offers more precise control and requires lower pressure than conventional methods, which risk tissue distortion [30,31].

While the influence of electroosmosis is often overshadowed by electroporation in pulsed electric field (PEF) applications, its contribution to mass transport – particularly in porous biological tissues such as vegetable tubers or skeletal muscle – could be significant under certain conditions. Specifically, when a constant current is applied across a tissue sample, the electric field strength ($\nabla\phi$) adjusts dynamically depending on the local conductivity. Since electroosmotic flow velocity (u_{EOS}) is directly proportional to the electric field gradient ($\nabla\phi$) (see Eq. 1), it follows that any spatial or temporal variation in conductivity will impact the magnitude and distribution of EOF. Under constant current operation, the relationship between the applied current I , conductivity σ , and electric field $\nabla\phi$ can be described by:

$$I = \int_A \sigma \nabla\phi \cdot dA, \quad (2)$$

where A is the cross-sectional area of the tissue. If tissue conductivity increases due to electroporation or temperature rise, the electric field ($\nabla\phi$) must decrease accordingly to maintain constant current, which in turn reduces electroosmotic flow velocity.

This dependency highlights an inverse relationship between the EOF and local tissue conductivity under constant current conditions. Therefore, electroosmosis is most pronounced in regions of lower conductivity, where the local electric field is intensified. Conversely, in electroporated or highly conductive zones, the reduced field diminishes the contribution of electroosmosis. This interplay suggests that the spatial profile of EOF is non-uniform, and strongly dependent on the evolving electrical properties of the tissue during PEF treatment. Understanding this relationship is crucial for accurately modelling fluid transport in PEF-treated tissues and for optimising pre-treatment strategies that aim to enhance mass transfer or mechanical softening (i.e., structure and texture modification).

Electrochemical reactions also play a crucial role in electroporation and electroosmotic processes, both in food [32,33] and biomedical applications [34,35]. In food, they can lead to contamination (e.g., metal ions, pH shifts) that compromises nutrients or flavour; in biomedicine, they can introduce harmful substances or pH gradients that damage tissue. As soon as current flows, the electrode-electrolyte solution interface behaves like an electrolytic cell. Beyond a certain voltage threshold, oxidation at the anode and reduction at the cathode can cause electrode fouling, corrosion, and metallic contamination of the treated medium. Hence, careful design of the treatment chamber and optimal operating conditions are essential to preserve safety and quality [32,36]. Nonetheless, these complexities emphasise that electroosmosis is still under-researched in both food and biomedical applications, warranting further investigation into its role and effects.

Our study aims to present three key concepts – some newly introduced, others revisited. First, we investigated whether EOF can be detected and studied in plant tissues of industrial relevance, specifically potato tubers, using texture analysis under both pulsed electric field (PEF) and direct current (DC) treatment conditions. As part of this objective, we also examined whether PEF treatment is a prerequisite for electroosmotic dehydration due to its role in releasing intracellular fluids. Second, we shifted our focus to animal tissue, conducting experiments on freshly excised porcine skeletal muscle (two hours post-mortem) to evaluate the role of electroosmosis in mass transfer in this other, completely different matrix to plant materials, since we have previously observed effects that could be attributed to EOF in one of our earlier studies using poultry meat [37]. This line of inquiry is especially timely given the renewed interest in applying PEF as a pretreatment in meat processing [38–40]. Third and finally, we assessed the suitability of agarose phantoms as surrogate models for plant and animal tissues in the study of EOF. In addition to these initial aims, our experiments yielded several unexpected yet significant findings. Notably, we observed EOF generated by the application of electric pulses during

PEF treatment – not only under continuous DC – highlighting potential implications not just for food processing, but also for biomedical applications involving electroporation.

2 Materials and methods

2.1 Experimental study materials

2.1.1 Plant tissue

Fresh potato tubers (*Solanum tuberosum*, cultivar Amaez) were used as the plant tissue model. The potatoes were obtained from a local supplier and stored until testing. Cylindrical samples with a diameter of 26 mm and a height of 6 mm were cut manually with a cork borer to ensure uniform dimensions. Care was taken to ensure that the samples had no visible defects or irregularities. The samples were tested within a short time frame after cutting to prevent dehydration or structural changes.

2.1.2 Animal tissue

The animal tissue used in the experiments was obtained from the trapezius skeletal muscle of a pig (*Sus scrofa domestica*), which was harvested within 30 minutes post-mortem in a slaughterhouse operating under Slovenian law. Immediately after harvesting, the tissue was transported to the laboratory to ensure minimal change in tissue properties or degradation. Experiments were conducted between 2 and 5 hours post-mortem. To maintain consistency of mechanical properties, muscle samples with uniform fibre orientation were selected. Cylindrical samples (diameter: 26 mm, height: 6 mm) were cut manually with a sharp cork borer. Two sets of samples were prepared: one was cut so that compression in texture analysis experiments was applied along the muscle fibres (parallel orientation), and another where compression was applied across the fibres (perpendicular orientation). This allowed a comparative assessment of how the fibre orientation affects the deformation of the tissue under load.

2.1.3 Agarose phantoms

Agarose phantoms were prepared using a 2.5% (w/v) agarose solution in deionised water, supplemented with 0.45% (w/v) NaCl to mimic the electrical conductivity of biological tissues. The agarose powder was dissolved in the prepared solution, heated to boiling until fully dissolved, and then poured into large Petri dishes to a uniform height of 6 mm. The gels were allowed to solidify at room temperature and cool before being removed from the dishes. Cylindrical samples (diameter: 26 mm) were then manually cut with a cork borer to achieve uniform dimensions and ensure consistency across experimental replicates.

2.2 Experimental setup

2.2.1 Force-response (texture) analysis

The compression tests were performed using a texture analyser (Inspekt Solo 1 kN, Hegenwald & Peschke, Germany), with the samples positioned between two parallel stainless steel plate electrodes that served as both compression plates and electrical contacts. The bottom electrode was perforated to facilitate the escape of liquid from the sample, allowing the fluid to drain out of the treatment chamber during compression. The PEF treatment chamber was designed to subject the cylindrical samples to electroporation pulses and mechanical compression simultaneously. The chamber was placed under the piston of the texture analyser, which exerted a constant force of 10 N at a controlled maximum velocity of 20 mm/min. Prior to testing, each sample was subjected to a 30-second pre-compression phase to expel air pockets and ensure uniform electrode contact. The piston was continuously monitored over a compression period of

330 seconds (following the initial pre-compression). This allowed the evaluation of deformation along the axis of applied pressure, perpendicular to the electrodes and aligned with the electric field vector. The deformation was quantified as $(d - d_0)/h_0$, where d represents the current piston displacement during the treatment, d_0 represents the displacement after preloading, and h_0 represents the original sample height (i.e. 6 mm). Data collected during compression were analysed to assess how different electrical conditions affect tissue deformation.

2.2.2 Electric field application (PEF and DC protocols)

The treatments with pulsed electric field (PEF) and direct current (DC) were applied using dedicated power supplies. The PEF pulses were delivered either via a Cliniporator Vitae pulse generator (HVP VG, IGEA, Carpi, Italy) for high-voltage pulses (1000 V) or a laboratory-built pulse generator (HV-LV, University of Ljubljana, Slovenia) [41] for low-voltage pulses (150 V). The PEF protocol comprised 8 unipolar pulses (100 μ s duration, 1 s⁻¹ repetition rate) delivered via parallel stainless-steel electrodes 6 mm apart immediately following the initial preload phase. In the conditions involving DC treatment, a constant current (25, 50, 100, or 200 mA) was applied from 15 s after the preload phase, using a DC power supply (NGL202, Rohde & Schwarz, Germany). The electrical signals were continuously monitored with an oscilloscope (HDO6104A-MS, LeCroy, Chestnut Ridge, NY, USA) equipped with voltage (HVD3206A, LeCroy, USA) and current (CP031A, LeCroy, USA) probes. The experimental setup for the texture analysis experiments is shown in Figure 1.

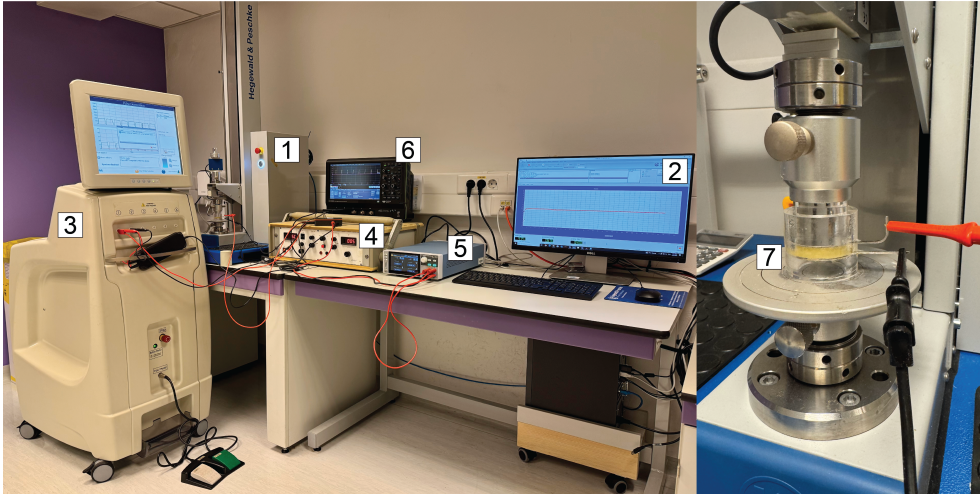


Figure 1: Experimental setup for texture analysis experiments. The setup consists of (1) a texture analyser, which is used to apply a compressive force and measure the sample deformation, (2) a PC to control the texture analyser and record the data, (3) a Cliniporator Vitae pulse generator for delivering PEF pulses with an amplitude of 1000 V, (4) a laboratory prototype pulse generator for delivering PEF pulses with an amplitude of 150 V, (5) a DC power supply for delivering a constant current, (6) an oscilloscope equipped with voltage and current probes to monitor the electrical pulses, and (7) a PEF treatment chamber with two parallel stainless steel plate electrodes, spaced 6 mm apart, designed to hold cylindrical samples while simultaneously applying compression and PEF pulses or constant current. The upper electrode (red connector) serves as the anode, while the bottom electrode (black connector) serves as the cathode.

A note on the employ of a CC (constant-current) rather than a CV (constant-voltage) approach to DC application. In biological tissues, conductivity can vary spatially and temporally (e.g., due to electroporation and/or heating, there can be large variations in initial conductivity

both locally and sample-to-sample, etc.). Under constant-voltage, areas with higher conductivity experience a lower electric field, and low-conductivity regions a higher one, leading to non-uniform EOF (refer to Eq. 1). Conversely, under constant-current, the DC generator dynamically adjusts its output voltage to maintain consistent electrical (and in tissue – ionic) current, which tends to equilibrate the electric field across regions within the sample and reduce hot spots. Therefore, a more stable and homogeneous electric field across the sample should, at least in theory, lead to a more predictable and stable electroosmotic transport. Moreover, since all the tested materials (potato tuber, ex vivo muscle tissue, and agarose) exhibit considerable differences in conductivity and inconsistent heterogeneity/homogeneity of this conductivity, we attempted to “standardise” the measurements by opting for constant-current rather than constant-voltage application and equalising the ionic flow through the different materials used. Another effect to be considered is that in the constant-voltage regime, there is no enforced maintenance of electrical contact between the tissue sample and the electrode. The current will rapidly increase during the initial stage of the experiment, reach peak amplitude, and then crash as the anode loses electrical contact with the liquid phase in tissue once sufficiently desiccated. While not entirely immune to this issue, the constant-current regime helps to mitigate its severity.

2.3 Statistical analysis

All experiments were performed in quintuplicate ($N = 5$). The statistical significance of the differences between the experimental groups was assessed using Student’s t-test, with $p < 0.05$ considered statistically significant. All statistical analyses and data processing were performed using Python.

3 Results and discussion

3.1 Compression response in plant tissue – DC amplitude variation

In the first set of experiments, we investigated how the variation of the amplitude of the applied direct current, either alone or following PEF pulses with an amplitude of 1000 V (chosen to ensure a high degree of electroporation), influences the compression behaviour of the potato tissue. Figure 2 shows the temporal evolution of compression of the potato tissue samples under different conditions, while Table 1 provides a pairwise statistical comparison of the final compression values at 330 s.

A comparison between the load only and PEF only conditions shows that the PEF treatment alone significantly increases tissue compression. This suggests that electroporation-induced membrane permeabilisation causes fluid leakage from the vacuoles and from cells, leading to greater deformation under sustained mechanical load. This observation is consistent with previous findings that electroporation increases water mobility in tissues [42], a phenomenon which is considerably aided by (release of) turgor pressure in turgid plant tissues.

Where DC was applied without prior PEF treatment, a clear trend emerged: higher DC amplitudes led to greater tissue compression. Each DC only condition (25, 50, 100, and 200 mA) was significantly different from the load alone, confirming that electroosmosis contributes to fluid displacement within the tissue. Notably, the compression increases linearly with current amplitude, both under the DC only and PEF + DC conditions (Figure 2c). Provided that the initial sample conductivity is consistent between individual tissue samples, we would expect a roughly linear increase in temperature with higher current amplitude, leading to a corresponding increase in conductivity and a reduction in the applied voltage required to drive this constant current through the tissue, which would ultimately result in a reduction of EOF (according to Eq. 1). This is, however, not the full story. At higher current amplitudes, the anode desiccates sooner and, at the risk of losing the electrode-tissue electrical contact, the generator needs

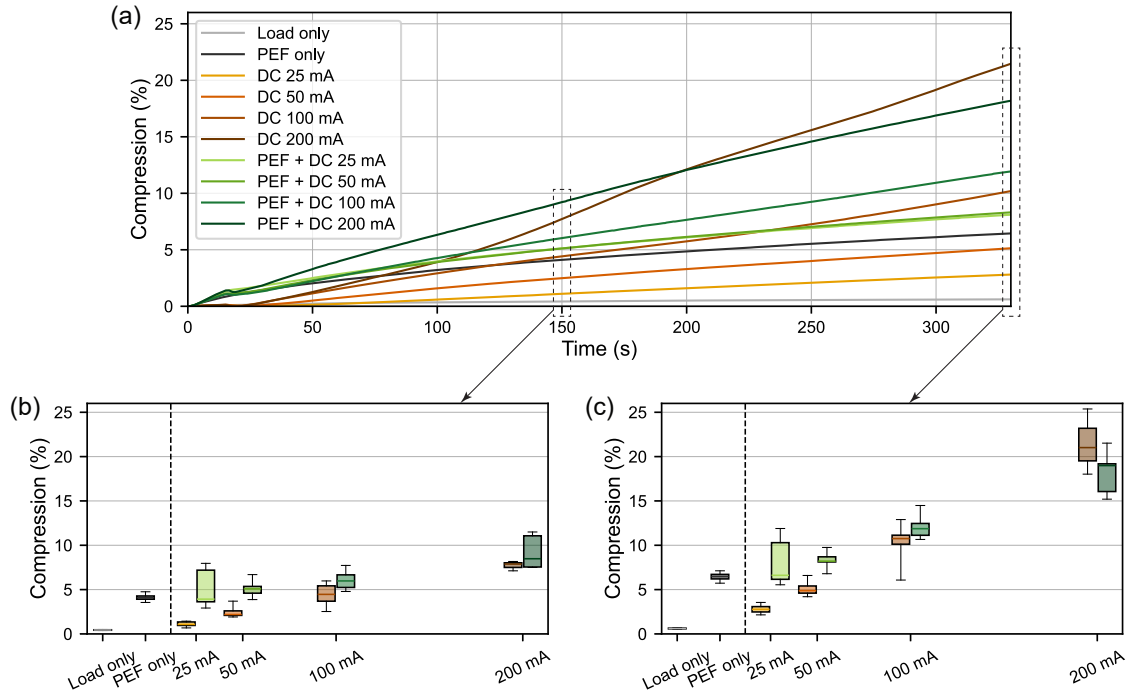


Figure 2: Compression response of potato tissue under different DC amplitudes. (a) Compression curves (expressed as a percentage of the initial sample height) averaged over five replicates ($N = 5$). The curves represent compression after an initial 30 s preload phase, followed by sustained compression, both under a constant force of 10 N. In conditions involving PEF, 8 pulses (1000 V amplitude, 100 μ s duration, 1 s^{-1} repetition rate) were applied at 0 s, while in conditions involving DC, a constant current (25, 50, 100, or 200 mA) was applied from 15 s onwards. Electrical treatments were delivered via parallel stainless-steel electrodes, 6 mm apart. Boxplot representation of the compression at (b) 150 s and (c) the final compression at 330 s (end of the compression test). The centre lines indicate the medians, the boxes represent the interquartile ranges (IQR), and the whiskers extend to the extreme data points.

to maintain a high voltage to prevent the current from dropping below the set point, thus maintaining the rate of EOF. Through this compensatory mechanism, the near-linear increase in tissue sample deformation remains consistent with the theoretical equation for EOF (Eq. 1).

The combination of PEF and DC generally resulted in greater tissue compression than DC alone, particularly at 25 mA and 50 mA, where the differences were statistically significant. At 100 mA, compression remained higher with PEF pretreatment, though not significantly, which is likely due to biological variability. This enhancement can be attributed to PEF's homogenising effect: electroporation and turgor pressure relaxation redistribute intracellular water liberated from the vacuoles into the extracellular space, increasing the fluid available for EOF. As such, PEF pretreatment appears to “prime” tissue for a more efficient DC-driven deformation, especially at lower currents where field strengths are weaker.

Interestingly, at 200 mA, DC-only treatment resulted in slightly greater compression than PEF + DC, suggesting a reversal of this trend. One explanation involves heating: during high-current application, tissues heat up significantly (up to $\sim 50^\circ\text{C}$ above ambient), especially near the anode where desiccation occurs. In PEF-treated tissue, where cell membranes are already compromised, water is more mobile and is lost rapidly through electrode-side desiccation, reducing EOF over time. Indeed, at 150 s, PEF-treated samples showed greater deformation, but were “overtaken” by DC-only samples in the latter half of the test.

Table 1: Pairwise statistical comparisons of final compression (at the end of the compression test at 330 s) in potato tissue under different DC amplitudes. The statistical significance of the differences between two experimental groups was determined using Student’s t-test ($p < 0.05$).

First group	Second group	p-value	Statistically significant?
Load only	PEF only	1.32×10^{-5}	Yes
Load only	DC 25 mA	5.15×10^{-4}	Yes
Load only	DC 50 mA	7.80×10^{-3}	Yes
Load only	DC 100 mA	7.05×10^{-4}	Yes
Load only	DC 200 mA	6.15×10^{-4}	Yes
Load only	PEF + DC 25 mA	4.29×10^{-3}	Yes
Load only	PEF + DC 50 mA	2.00×10^{-5}	Yes
Load only	PEF + DC 100 mA	3.64×10^{-9}	Yes
Load only	PEF + DC 200 mA	2.58×10^{-5}	Yes
PEF only	DC 25 mA	2.54×10^{-5}	Yes
PEF only	DC 50 mA	6.80×10^{-2}	No
PEF only	DC 100 mA	2.39×10^{-2}	Yes
PEF only	DC 200 mA	4.23×10^{-4}	Yes
PEF only	PEF + DC 25 mA	2.92×10^{-1}	No
PEF only	PEF + DC 50 mA	1.70×10^{-2}	Yes
PEF only	PEF + DC 100 mA	1.05×10^{-6}	Yes
PEF only	PEF + DC 200 mA	4.65×10^{-5}	Yes
DC 25 mA	DC 50 mA	3.13×10^{-3}	Yes
DC 50 mA	DC 100 mA	7.36×10^{-3}	Yes
DC 100 mA	DC 200 mA	2.01×10^{-3}	Yes
DC 25 mA	PEF + DC 25 mA	3.30×10^{-3}	Yes
DC 50 mA	PEF + DC 50 mA	2.81×10^{-3}	Yes
DC 100 mA	PEF + DC 100 mA	8.17×10^{-2}	No
DC 200 mA	PEF + DC 200 mA	1.83×10^{-1}	No
PEF + DC 25 mA	PEF + DC 50 mA	8.79×10^{-1}	No
PEF + DC 50 mA	PEF + DC 100 mA	4.97×10^{-5}	Yes
PEF + DC 100 mA	PEF + DC 200 mA	1.51×10^{-5}	Yes

Another factor may be voltage and current instability. PEF-treated tissues showed more frequent inability of the generator to maintain constant current and fluctuations in voltage during operation, potentially slowing down EOF. To the contrary, DC-only samples at 200 mA exhibited a delayed but rapid increase in compression after 100–150 s, likely driven by Joule heating effects that gradually altered tissue structure and released intracellular fluid. In contrast, PEF-treated tissues showed decelerating deformation, suggesting different dynamic responses to sustained EOF under high-current conditions.

Overall, our results confirm that DC-induced EOF plays a dominant role in tissue compression, with a clear dependence on current amplitude. While PEF enhances compression at lower DC amplitudes, its effects become less pronounced at higher currents, where EOF alone appears to be sufficient to drive tissue deformation.

3.2 Compression response in plant tissue – PEF amplitude variation

In the second set of experiments, we investigated how the amplitude of the PEF pulses (150 V vs. 1000 V) affects compression in the potato tissue, both with and without subsequent DC application. Figure 3 shows the compression curves over time, while Table 2 summarises the pairwise statistical comparisons of the final compression values at 330 s.

The PEF only conditions show a strong dependence on the amplitude of the applied pulses. For 150 V pulses, the final compression was significantly higher than for load only, but at the same time also significantly lower than for 1000 V pulses, suggesting that the effects of

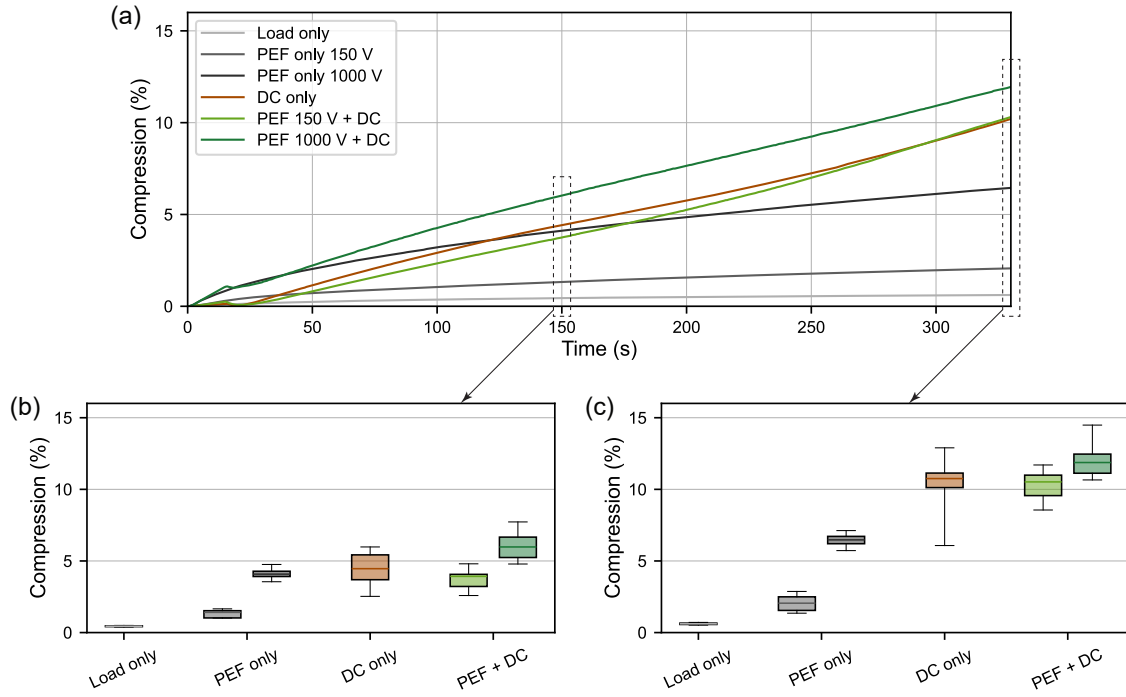


Figure 3: Compression response of potato tissue under different PEF amplitudes. (a) Compression curves (expressed as a percentage of the initial sample height) averaged over five replicates ($N = 5$). The curves represent compression after an initial 30 s preload phase, followed by sustained compression, both under a constant force of 10 N. In conditions involving PEF, 8 pulses (150 V or 1000 V amplitude, 100 μ s duration, 1 s^{-1} repetition rate) were applied at 0 s, while in conditions involving DC, a constant current of 100 mA was applied from 15 s onwards. Electrical treatments were delivered via parallel stainless-steel electrodes, 6 mm apart. Boxplot representation of the compression at (b) 150 s and (c) the final compression at 330 s (end of the compression test). The centre lines indicate the medians, the boxes represent the interquartile ranges (IQR), and the whiskers extend to the extreme data points.

electroporation on tissue deformation under load were more pronounced at the higher amplitude. The 150 V pulses used in this study correspond to the voltage-to-distance ratio (an electric field approximation) of 250 V/cm, which is just above the electroporation threshold in potato tissue, meaning that some membrane permeabilisation occurs, but is not extensive [43]. In contrast, the 1000 V pulses correspond to 1667 V/cm, which completely permeabilises the potato tuber tissue and results in greater water displacement and compressibility under load. The introduction of direct current (100 mA) after PEF further increased compression. Comparing the two PEF amplitudes, PEF 1000 V + DC resulted in significantly greater compression than PEF 150 V + DC, supporting the idea that a higher level of electroporation allows for more efficient fluid displacement under the applied force.

Interestingly, the DC only condition resulted in similar final compression to PEF 150 V + DC, but the compression was slightly lower than in PEF 1000 V + DC, although not significantly different. This is, to some extent, likely due to the variability of the biological tissue samples, which appears to be particularly influential in DC only experiments, which makes sense, since without PEF, these samples are not homogenised. At lower PEF amplitudes (150 V), the contribution of electroporation to overall compression appears negligible compared to DC-driven electroosmosis. However, at 1000 V, where complete permeabilisation of the membrane occurs, electroporation further enhances tissue deformation, probably by enabling increased fluid dis-

Table 2: Pairwise statistical comparisons of final compression (at the end of the compression test at 330 s) in potato tissue under different PEF amplitudes. The statistical significance of the differences between two experimental groups was determined using Student’s t-test ($p < 0.05$).

First group	Second group	p-value	Statistically significant?
Load only	PEF only 150 V	8.87×10^{-3}	Yes
Load only	PEF only 1000 V	1.32×10^{-5}	Yes
Load only	DC only	7.05×10^{-4}	Yes
Load only	PEF 150 V + DC	3.79×10^{-9}	Yes
Load only	PEF 1000 V + DC	3.64×10^{-9}	Yes
PEF only 150 V	PEF only 1000 V	1.37×10^{-5}	Yes
PEF only 150 V	DC only	1.14×10^{-4}	Yes
PEF only 150 V	PEF 150 V + DC	2.94×10^{-10}	Yes
PEF only 150 V	PEF 1000 V + DC	1.58×10^{-10}	Yes
PEF only 1000 V	DC only	2.39×10^{-2}	Yes
PEF only 1000 V	PEF 150 V + DC	9.52×10^{-6}	Yes
PEF only 1000 V	PEF 1000 V + DC	1.05×10^{-6}	Yes
DC only	PEF 150 V + DC	9.03×10^{-1}	No
DC only	PEF 1000 V + DC	8.17×10^{-2}	No
PEF 150 V + DC	PEF 1000 V + DC	2.85×10^{-3}	Yes

placement and structural changes in the tissue in what can be thought of as some sort of tissue homogenisation.

In a previous study using MRI techniques [42], electroporation-induced changes in water distribution were shown to be strongly dependent on the applied electric field, with increasing field strengths leading to greater fluid displacement. Our results are consistent with these findings, as higher PEF amplitudes led to greater compression, both independently and when combined with DC. The significantly greater compression observed with PEF 1000 V + DC further supports the idea that extensive electroporation enhances EOF during application of constant current, leading to increased tissue deformation and reinforcing the role of electroporation in altering fluid transport properties in plant tissue.

3.3 Compression response in animal tissue

We also investigated how the application of direct current affects the compression response of animal tissue, namely porcine skeletal muscle, in two orientations: parallel and perpendicular to the muscle fibres. Figure 4 shows the compression curves for both orientations, while Table 3 provides pairwise statistical comparisons of the final compression values at 330 s. The statistical analysis showed no significant differences between the load only and DC only conditions, neither in the parallel nor in the perpendicular orientations relative to the muscle fibres. Similarly, no significant differences were found between the parallel and perpendicular orientations for either load-only or DC-only groups. However, despite the lack of statistical significance, the trends in the data clearly and strongly hint (see Figure 4d) that electroosmosis may still contribute to tissue compression in animal tissue. Both the mean and median values of compression under DC only conditions are noticeably higher than under load only conditions, indicating a possible effect of EOF. The high variability between the biological animal samples likely contributes to the lack of statistical significance, as does the structural complexity of the muscle tissue, the differences in extracellular fluid content, and the possible variability in the electrical properties of the individual samples.

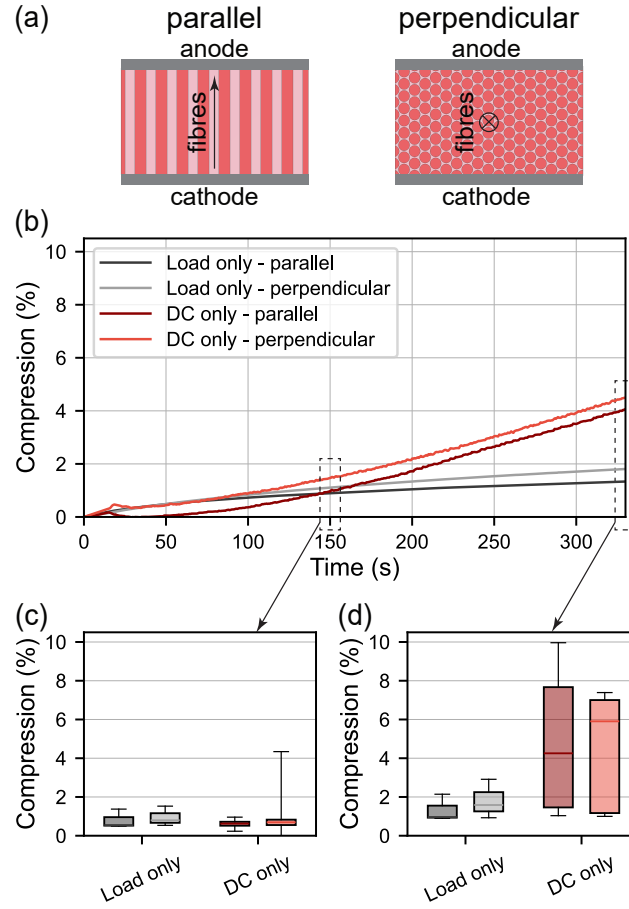


Figure 4: Compression response of porcine muscle tissue under DC application. (a) Schematic representation of the two sample orientations with respect to the muscle fibre direction: in the parallel orientation, the samples were cut so that compression was measured along the fibre direction, whereas in the perpendicular orientation, compression was measured across the fibre direction. (b) Compression curves (expressed as a percentage of the initial sample height) averaged over five replicates ($N = 5$). The curves represent compression after an initial 30 s preload phase, followed by sustained compression, both under a constant force of 10 N. In conditions involving DC, a constant current (100 mA) was applied from 15 s onwards. Electrical treatments were delivered via parallel stainless-steel electrodes, 6 mm apart. Boxplot representation of the compression at (c) 150 s and (d) final compression at 330 s (end of the compression test) for both parallel and perpendicular orientations. The centre lines indicate the medians, the boxes represent the interquartile ranges (IQR), and the whiskers extend to the extreme data points.

Unlike plant cells, muscle fibres have no rigid walls and no internal turgor pressure, so deformation under load depends primarily on the properties of the extracellular matrix rather than on fluid release. It has already been shown that PEF-induced deformation in plant tissue is largely driven by turgor loss, whereas such an effect is inherently limited in animal tissue [37]. This structural difference likely explains the lower absolute compression observed in muscle samples. The large variability of biological animal tissue further obscures the observed differences. Nevertheless, the observed increase in mean and median compression under DC suggests that electroosmosis may still play a role, albeit to a lesser extent than in plant tissue.

To further investigate the role of electroosmosis, we applied 8 PEF pulses (1000 V ampli-

Table 3: Pairwise statistical comparisons of final compression (at the end of the compression test at 330 s) in porcine muscle tissue under different experimental conditions. The statistical significance of the differences between two experimental groups was determined using Student’s t-test ($p < 0.05$).

First group	Second group	p-value	Statistically significant?
Load only – parallel	Load only – perpendicular	5.41×10^{-1}	No
Load only – parallel	DC only – parallel	2.26×10^{-1}	No
Load only – perpendicular	DC only – perpendicular	2.14×10^{-1}	No
DC only – parallel	DC only – perpendicular	8.81×10^{-1}	No

tude¹), 100 μs duration, 1 s^{-1} repetition rate, electrical current in the range of about 30 to 40 A) and observed distinct piston movements in both parallel and perpendicular directions (Figure 5). The stepwise displacement during each pulse application is direct evidence of electrically induced fluid movement, supporting the role of electroosmosis in animal tissue despite its structural complexity.

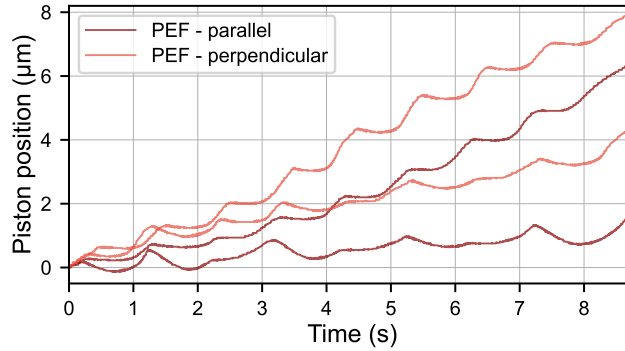


Figure 5: Detailed view of the piston displacement during the delivery of 8 PEF pulses (1000 V amplitude, 100 μs duration, 1 s^{-1} repetition rate) under a constant compressive load of 10 N, highlighting electroosmotic effects. Data show two individual replicates for each orientation, with compression measured in the parallel and perpendicular directions relative to the muscle fibres. Electrical pulses were applied via parallel stainless-steel electrodes spaced 6 mm apart.

These observations are of significant relevance to food processing applications utilising PEF since EOF can be hypothesised to contribute to not only electrical but also thermal homogenisation of tissues through redistribution of liquid. One important factor affecting (plant) tissue homogenisation is thought to be turgor pressure relaxation upon electroporation of cell membranes and vacuoles, liberating intracellular liquid. Another mechanism of such homogenisation is quite possibly the PEF-driven EOF. However, unlike turgor pressure relaxation only present in plant tissues, EOF is, as we have demonstrated, present in animal tissues as well during pulse application, and could significantly contribute to the liquid redistribution in those tissues. Although the extent of EOF during PEF application, especially using short pulses on the order of fewer than 10 μs that are commonly employed in the industry, is not likely to result in significant redistribution of liquid on the macro scale of bulk tissue samples, it could conceivably contribute to liquid redistribution on the scale of at least individual cells, leading to the aforementioned electrical and thermal homogenisation. This is important not only in and of itself, but also in design of improved treatment protocols employing pulses of varying lengths to first achieve electrical homogenisation through EOF and turgor pressure relaxation, and then higher-amplitude,

¹Over a 6 mm thick sample this yields approximately 1667 V/cm voltage-to-distance ratio (an approximation of the electric field strength).

shorter-duration pulses to achieve homogeneous PEF treatment.

3.4 Compression response in agarose phantoms

To further investigate the electroosmotic effects, we examined the compression response of 2.5% agarose phantoms with 0.45% NaCl under DC application of 100 mA amplitude. Figure 6 shows the compression curves. Statistical comparison confirms that the final compression was significantly higher in the DC group than in the load-only group (p-value: 2.14×10^{-2}). However, the absolute difference was smaller than that observed in the plant tissue.

In contrast to plant or animal tissue, agarose phantoms lack discrete cells and turgor pressure, which means that electroporation cannot occur or contribute to deformation due to release of fluid from cells. Instead, compression changes in agarose are primarily driven by EOF through the porous gel network. Although the extent of additional compression due to applied current was smaller than in the plant tissue, the statistically significant difference between the groups with load only and DC only confirms the role of electroosmosis.

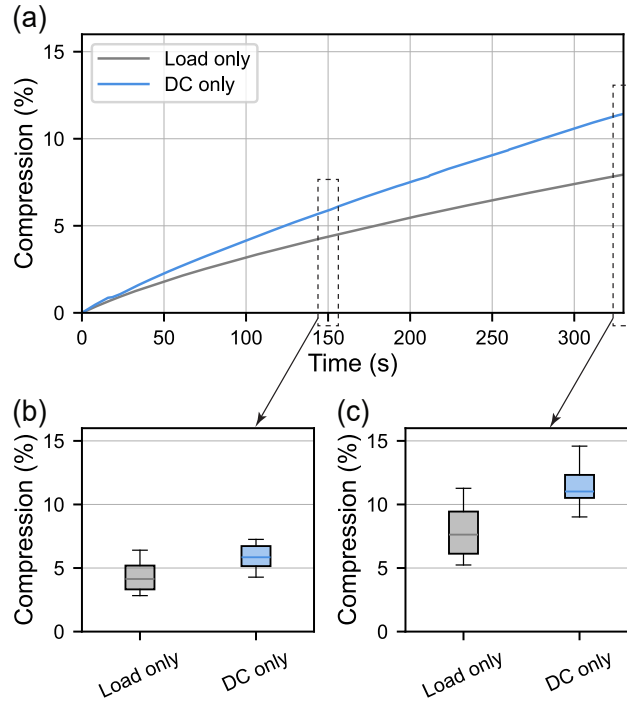


Figure 6: Compression response of agarose phantoms under DC application. (a) Compression curves (expressed as a percentage of the initial sample height) averaged over five replicates ($N = 5$). The curves represent compression after an initial 30 s preload phase, followed by sustained compression, both under a constant force of 10 N. In conditions involving DC, a constant current (100 mA) was applied from 15 s onwards. Electrical treatments were delivered via parallel stainless-steel electrodes, 6 mm apart. Boxplot representation of the compression at (b) 150 s and (c) final compression at 330 s (end of the compression test). The centre lines indicate the medians, the boxes represent the interquartile ranges (IQR), and the whiskers extend to the extreme data points.

4 Conclusions

This study examined the importance of electroosmotic flow (EOF) as a mechanism of electrically induced fluid movement in plant and animal tissues, as well as in agarose-based phantoms, by quantifying its extent and dependence on various treatment parameters.

We have demonstrated that both pulsed electric field (PEF) and direct current (DC) treatments significantly influence compression behaviour in plant tissue, with DC-induced EOF playing a primary role in fluid displacement under mechanical load. The additional application of PEF enhanced compression at lower current levels, likely due to electroporation-facilitated fluid redistribution, though this effect diminished at higher current amplitudes.

In animal muscle tissue, the contribution of electroosmosis was less pronounced, likely due to the absence of turgor pressure and structural differences compared to plant tissue. Nevertheless, direct visual evidence of fluid movement during PEF pulse application suggests that EOF may still occur in animal tissues, albeit to a lesser extent.

Agarose phantoms exhibited statistically significant compression under DC, confirming their suitability as surrogate materials for studying electroosmotic effects in controlled, cell-free systems. Their simplicity makes them valuable tools for isolating and quantifying EOF-driven mass transfer mechanisms.

Our findings highlight the potential of electroosmotic flow (EOF) during pulsed electric field (PEF) treatment to enhance both electrical and thermal homogenisation in tissues by redistributing liquid at the cellular level – an effect observed in both plant and animal tissues, unlike turgor pressure relaxation, which is plant-specific. Understanding and leveraging these mechanisms can inform the future design of optimised PEF protocols, where longer pulses promote initial homogenisation, followed by shorter, high-amplitude pulses for achieving a more uniform treatment.

Overall, the results support the role of electroosmosis as a contributing factor to electrically assisted fluid transport in food-relevant matrices. These conclusions provide a foundation for optimising electro-technologies in food processing, particularly in applications such as tissue softening, dehydration, and diffusion enhancement. The study also highlights the potential of simplified phantom models for mechanistic investigations in cases when accounting for the biological variability is not indispensable.

CRedit authorship contribution statement

Rok Šmerc: Methodology, Software, Validation, Formal analysis, Investigation, Writing – Original Draft, Writing – Review & Editing, Visualization. **Samo Mahnič-Kalamiza:** Conceptualization, Methodology, Investigation, Resources, Writing – Original Draft, Writing – Review & Editing, Supervision.

Declaration of Competing Interest

The authors report no conflict of interest.

Acknowledgements

The authors would like to acknowledge the financial support through research programs and projects granted by the Slovenian Research Agency (ARIS), namely the research programme P2-0249, and University of Ljubljana's internal funding for Start-up Research Programmes. This study was conducted within the Infrastructure Programme: Network of research infrastructure centres at the University of Ljubljana (MRIC UL IP-0510), specifically within infrastructural centre Cellular Electrical Engineering (I0-0022), also funded by the Slovenian Research and Innovation Agency (ARIS).

References

- [1] Kotnik, T., Rems, L., Tarek, M., & Miklavčič, D. (2019). Membrane Electroporation and Electroporomeabilization: Mechanisms and Models. *Annual Review of Biophysics*, 48(1), 63–91. 10.1146/annurev-biophys-052118-115451
- [2] Granot, Y., & Rubinsky, B. (2008). Mass transfer model for drug delivery in tissue cells with reversible electroporation. *International Journal of Heat and Mass Transfer*, 51(23–24), 5610–5616. 10.1016/j.ijheatmasstransfer.2008.04.041
- [3] Kotnik, T., Pucihar, G., & Miklavčič, D. (2011). The Cell in the Electric Field. In S. T. Kee, J. Gehl, & E. W. Lee (Eds.), *Clinical Aspects of Electroporation* (pp. 19–29). Springer New York. 10.1007/978-1-4419-8363-3_3
- [4] Geboers, B., Scheffer, H. J., Graybill, P. M., Ruarus, A. H., Nieuwenhuizen, S., Puijk, R. S., Van Den Tol, P. M., Davalos, R. V., Rubinsky, B., De Gruijl, T. D., Miklavčič, D., & Meijerink, M. R. (2020). High-Voltage Electrical Pulses in Oncology: Irreversible Electroporation, Electrochemotherapy, Gene Electrotransfer, Electrofusion, and Electroimmunotherapy. *Radiology*, 295(2), 254–272. 10.1148/radiol.2020192190
- [5] Dymek, K. *et al.* (2015). Modeling electroporation of the non-treated and vacuum impregnated heterogeneous tissue of spinach leaves. *Innovative Food Science & Emerging Technologies*, 29, 55–64. 10.1016/j.ifset.2014.08.006
- [6] Yarmush, M. L., Golberg, A., Serša, G., Kotnik, T., & Miklavčič, D. (2014). Electroporation-Based Technologies for Medicine: Principles, Applications, and Challenges. *Annual Review of Biomedical Engineering*, 16(1), 295–320. 10.1146/annurev-bioeng-071813-104622
- [7] Chun, K.-R. J. *et al.* (2024). State-of-the-art pulsed field ablation for cardiac arrhythmias: Ongoing evolution and future perspective. *Europace*, 26(6), euae134. 10.1093/europace/euae134
- [8] Huo, Z.-Y., Winter, L. R., Wang, X.-X., Du, Y., Wu, Y.-H., Hübner, U., Hu, H.-Y., & Elimelech, M. (2022). Synergistic Nanowire-Enhanced Electroporation and Electrochlorination for Highly Efficient Water Disinfection. *Environmental Science & Technology*, 56(15), 10925–10934. 10.1021/acs.est.2c01793
- [9] Kotnik, T., Frey, W., Sack, M., Haberl Meglič, S., Peterka, M., & Miklavčič, D. (2015). Electroporation-based applications in biotechnology. *Trends in Biotechnology*, 33(8), 480–488. 10.1016/j.tibtech.2015.06.002
- [10] Mahnič-Kalamiza, S., Vorobiev, E., & Miklavčič, D. (2014). Electroporation in Food Processing and Biorefinery. *The Journal of Membrane Biology*, 247(12), 1279–1304. 10.1007/s00232-014-9737-x
- [11] Sack, M., Eing, C., Berghofe, T., Buth, L., Stangle, R., Frey, W., & Bluhm, H. (2008). Electroporation-Assisted Dewatering as an Alternative Method for Drying Plants. *IEEE Transactions on Plasma Science*, 36(5), 2577–2585. 10.1109/TPS.2008.2002440
- [12] Gagneten, M., Leiva, G., Salvatori, D., Schebor, C., & Olaiz, N. (2019). Optimization of Pulsed Electric Field Treatment for the Extraction of Bioactive Compounds from Blackcurrant. *Food and Bioprocess Technology*, 12(7), 1102–1109. 10.1007/s11947-019-02269-3
- [13] Canelli, G., Kuster, I., Jaquenod, L., Buchmann, L., Murciano Martínez, P., Rohfritsch, Z., Dionisi, F., Bolten, C. J., Nanni, P., & Mathys, A. (2022). Pulsed electric field treatment

- enhances lipid bioaccessibility while preserving oxidative stability in *Chlorella vulgaris*. *Innovative Food Science & Emerging Technologies*, 75, 102897. 10.1016/j.ifset.2021.102897
- [14] Genovese, J., Tappi, S., Luo, W., Tylewicz, U., Marzocchi, S., Marziali, S., Romani, S., Ragni, L., & Rocculi, P. (2019). Important factors to consider for acrylamide mitigation in potato crisps using pulsed electric fields. *Innovative Food Science & Emerging Technologies*, 55, 18–26. 10.1016/j.ifset.2019.05.008
- [15] Schouten, M. A., Genovese, J., Tappi, S., Di Francesco, A., Baraldi, E., Cortese, M., Caprioli, G., Angeloni, S., Vittori, S., Rocculi, P., & Romani, S. (2020). Effect of innovative pre-treatments on the mitigation of acrylamide formation in potato chips. *Innovative Food Science & Emerging Technologies*, 64, 102397. 10.1016/j.ifset.2020.102397
- [16] Alizadeh, A., Hsu, W., Wang, M., & Daiguji, H. (2021). Electroosmotic flow: From microfluidics to nanofluidics. *Electrophoresis*, 42(7–8), 834–868. 10.1002/elps.202000313
- [17] Ou, Y., & Weber, S. G. (2017). Numerical Modeling of Electroosmotic Push–Pull Perfusion and Assessment of Its Application to Quantitative Determination of Enzymatic Activity in the Extracellular Space of Mammalian Tissue. *Analytical Chemistry*, 89(11), 5864–5873. 10.1021/acs.analchem.7b00187
- [18] Casagrande, L. (1949). Electro-osmosis in soils. *Géotechnique*, 1, 159–177.
- [19] Gray, D. H., & Mitchell, J. K. (1967). Fundamental Aspects of Electro-Osmosis in Soils. *Journal of the Soil Mechanics and Foundations Division*, 93(6), 209–236. 10.1061/JSFEAQ.0001053
- [20] Iwata, M., Tanaka, T., & Jami, M. S. (2013). Application of Electroosmosis for Sludge Dewatering—A Review. *Drying Technology*, 31(2), 170–184. 10.1080/07373937.2012.691592
- [21] Iwata, M., Igami, H., Murase, T., & Yoshida, H. (1991). Analysis of electroosmotic dewatering. *Journal of Chemical Engineering of Japan*, 24(1), 45–50. 10.1252/jcej.24.45
- [22] Cano-Sarmiento, C. *et al.* (2018). Zeta Potential of Food Matrices. *Food Engineering Reviews*, 10(3), 113–138. 10.1007/s12393-018-9176-z
- [23] Shomer, I., Novacky, A. J., Pike, S. M., Yermiyahu, U., & Kinraide, T. B. (2003). Electrical Potentials of Plant Cell Walls in Response to the Ionic Environment. *Plant Physiology*, 133(1), 411–422. 10.1104/pp.103.024539
- [24] Kinraide, T. B., Yermiyahu, U., & Rytwo, G. (1998). Computation of surface electrical potentials of plant cell membranes. Correspondence To published zeta potentials from diverse plant sources. *Plant Physiology*, 118(2), 505–512. 10.1104/pp.118.2.505
- [25] Menon, A., Mashyamombe, T. R., Kaygen, E., Mortazavi Nasiri, M. S., & Stojceska, V. (2019). Electro-osmosis dewatering as an energy efficient technique for drying food materials. *Energy Procedia*, 161, 123–132. 10.1016/j.egypro.2019.02.069
- [26] Qiu, L., Zhang, M., Tang, J., Adhikari, B., & Cao, P. (2019). Innovative technologies for producing and preserving intermediate moisture foods: A review. *Food Research International*, 116, 90–102. 10.1016/j.foodres.2018.12.055
- [27] Vijh, A. K. (1999a). Electrochemical field effects in biological materials: Electro-osmotic dewatering of cancerous tissue as the mechanistic proposal for the electrochemical treatment of tumors. *Journal of Materials Science: Materials in Medicine*, 10(7), 419–423. 10.1023/A:1008927114924

- [28] Vijh, A. K. (1999b). Electrochemical treatment of tumors (ECT): Electroosmotic dewatering (EOD) as the primary mechanism. *Drying Technology*, 17(3), 586–596. 10.1080/07373939908917554
- [29] Vijh, A. K. (2004). Electrochemical treatment (ECT) of cancerous tumours: Necrosis involving hydrogen cavitation, chlorine bleaching, pH changes, electroosmosis. *International Journal of Hydrogen Energy*, 29(6), 663–665. 10.1016/S0360-3199(03)00156-3
- [30] Faraji, A. H. *et al.* (2011). Synthesis and Characterization of a Hydrogel with Controllable Electroosmosis: A Potential Brain Tissue Surrogate for Electrokinetic Transport. *Langmuir*, 27(22), 13635–13642. 10.1021/la202198k
- [31] Faraji, A. H. *et al.* (2020). Electrokinetic Convection-Enhanced Delivery of Solutes to the Brain. *ACS Chemical Neuroscience*, 11(14), 2085–2093. 10.1021/acschemneuro.0c00037
- [32] Pataro, G., Falcone, M., Donsì, G., & Ferrari, G. (2014). Metal release from stainless steel electrodes of a PEF treatment chamber: Effects of electrical parameters and food composition. *Innovative Food Science & Emerging Technologies*, 21, 58–65. 10.1016/j.ifset.2013.10.005
- [33] Saulis, G., Rodaitė-Riševičienė, R., Dainauskaitė, V. S., & Saulė, R. (2015). Electrochemical Processes During High-Voltage Electric Pulses and their Importance in Food Processing Technology. In R. Rai V (Ed.), *Advances in Food Biotechnology* (1st ed., pp. 575–592). Wiley. 10.1002/9781118864463.ch35
- [34] Marino, M., Olaiz, N., Signori, E., Maglietti, F., Suárez, C., Michinski, S., & Marshall, G. (2017). pH fronts and tissue natural buffer interaction in gene electrotransfer protocols. *Electrochimica Acta*, 255, 463–471. 10.1016/j.electacta.2017.09.021
- [35] Šmerc, R., Miklavčič, D., & Mahnič-Kalamiza, S. (2025). An experimentally validated numerical model of pH changes in surrogate tissue induced by electroporation pulses. *Electrochimica Acta*, 511, 145363. 10.1016/j.electacta.2024.145363
- [36] Merrill, D. R., Bikson, M., & Jefferys, J. G. R. (2005). Electrical stimulation of excitable tissue: Design of efficacious and safe protocols. *Journal of Neuroscience Methods*, 141(2), 171–198. 10.1016/j.jneumeth.2004.10.020
- [37] Genovese, J., Rocculi, P., Miklavčič, D., & Mahnič-Kalamiza, S. (2024). The forgotten method? Pulsed electric field thresholds from the perspective of texture analysis. *Food Research International*, 176, 113869. 10.1016/j.foodres.2023.113869
- [38] Zhang, Y., Wang, R., Wen, Q.-H., Rahaman, A., & Zeng, X.-A. (2022). Effects of pulsed electric field pretreatment on mass transfer and quality of beef during marination process. *Innovative Food Science & Emerging Technologies*, 80, 103061. 10.1016/j.ifset.2022.103061
- [39] Guo, Y., Han, M., Chen, L., Zeng, X., Wang, P., Xu, X., Feng, X., & Lu, X. (2024). Pulsed electric field: A novel processing technology for meat quality enhancing. *Food Bioscience*, 58, 103645. 10.1016/j.fbio.2024.103645
- [40] Ahmed, M., Ranjan, H., & Roy, S. (2025). Pulsed electric fields for sustainable meat, poultry, and fish processing: Recent advances, prospects, and industry challenges. *Innovative Food Science & Emerging Technologies*, 102, 104008. 10.1016/j.ifset.2025.104008
- [41] Pavlin, M., Flisar, K., & Kandušer, M. (2010). The Role of Electrophoresis in Gene Electrotransfer. *The Journal of Membrane Biology*, 236(1), 75–79. 10.1007/s00232-010-9276-z

- [42] Genovese, J., Stručić, M., Serša, I., Novickij, V., Rocculi, P., Miklavčič, D., Mahnič-Kalamiza, S., & Kranjc, M. (2023). PEF treatment effect on plant tissues of heterogeneous structure no longer an enigma: MRI insights beyond the naked eye. *Food Chemistry*, 405, 134892. 10.1016/j.foodchem.2022.134892
- [43] Genovese, J., Kranjc, M., Serša, I., Petracci, M., Rocculi, P., Miklavčič, D., & Mahnič-Kalamiza, S. (2021). PEF-treated plant and animal tissues: Insights by approaching with different electroporation assessment methods. *Innovative Food Science & Emerging Technologies*, 74, 102872. 10.1016/j.ifset.2021.102872

3 Discussion

3.1 Investigating skeletal muscle anisotropy through multiscale modelling and experimental validation

The directional dependence of electrical conductivity in skeletal muscle has important implications for the distribution of electric fields during electroporation, yet it remains inadequately captured in many existing models. In this context, the first study aimed to quantitatively evaluate the impact of skeletal muscle anisotropy on electroporation-induced tissue damage by combining a multiscale numerical modelling framework with *in vivo* experimental validation. The central question was whether differences in fibre orientation relative to the applied electric field, in particular an electric field applied parallel or perpendicular with respect to the muscle fibres, would result in distinct ablation lesions, and whether these effects could be reliably predicted with a mechanistic numerical model.

To investigate this, a multiscale modelling approach was adopted. First, a single muscle cell model was used to determine the conductivity changes at the cellular level during electroporation, similarly as previously implemented for skin tissue [106], [107], [108]. These results were then generalised and integrated into a larger-scale bulk tissue model, in which the muscle was represented as an anisotropic conductive domain. The modelling was complemented by a series of *in vivo* experiments in porcine skeletal muscle in which electroporation pulses were administered using two needle electrodes (8.0 mm apart) inserted such that the direction of the applied electric field was either parallel or perpendicular to the direction of the muscle fibres. The electroporation protocol consisted of 48 unipolar rectangular pulses with a duration of 100 μ s each, which were

delivered in six trains of eight pulses each. Within each train, the pulses were applied at a repetition rate of 1000 s^{-1} , with a 2-second pause between consecutive trains. The applied voltage ranged from 600 V to 1200 V. After treatment, muscle tissue was excised and stained with the indicator dye 2,3,5-triphenyl-2H-tetrazolium chloride (TTC) to identify regions of irreversibly electroporated, non-viable tissue. The stained tissue was then imaged and processed to allow reconstruction of lesion geometries. We determined the electric field threshold for irreversible electroporation for each experiment by selecting the simulated contour image that achieved the highest Sørensen–Dice similarity coefficient [109] with the corresponding experimentally derived lesion.

We found that the orientation of the applied electric field relative to the muscle fibres significantly influences the morphology of the lesions. When the field was applied parallel to the fibres, lesions appeared more confined and followed the expected shape for a two-needle electrode array, resembling outcomes typically seen in electrically isotropic tissue [110]. In contrast, a perpendicular field orientation resulted in wider lesions that extended far from the line connecting the electrodes, with the most prominent spread occurring along the plane bisecting this line, where the field strength is expected to be the lowest. These differences in the shape of the lesions were consistent with the predictions of the numerical model, supporting the conclusion that the electrical anisotropy of the muscle tissue strongly influences the distribution of the electric field and the extent of electroporation-induced damage.

In addition to evaluating the morphology of the lesions, the study also determined the electric field threshold for irreversible electroporation specific to the muscle tissue and pulse protocol used. The analysis showed that the threshold remained consistent across all applied voltages (600, 800, 1000, and 1200 V), with an overall average of 193.4 V/cm and a standard deviation of 42.1 V/cm. This finding agrees with electroporation theory, which predicts that the threshold should not depend on the amplitude of the applied voltage [4]. Importantly, no statistically significant difference in the threshold was found between parallel and perpendicular orientations of the electric field with respect to the muscle fibres, further supporting the assumption that electroporation sensitivity is not influenced by field direction, but rather by intrinsic cellular properties. The observed variability is attributable to biological and procedural factors inherent to *in vivo*

experiments. The comparatively low threshold compared to previous reports (i.e., 450 V/cm) [111] can be explained by the greater number of pulses used in our study, as well as differences in electrode geometry and pulse delivery parameters. These results emphasise the need to interpret the threshold values within the specific context of the treatment protocol and experimental conditions [112].

Nevertheless, some limitations should be acknowledged. The model was developed and validated for a single tissue type, porcine skeletal muscle, and under a specific pulse protocol. Therefore, the determined threshold and its independence from field orientation must be interpreted in this context. Applying the model to other tissue types or substantially different electroporation parameters would require re-assessment and additional validation.

In summary, this study demonstrates a multiscale modelling approach that combines the dynamics of electroporation in a single cell with the anisotropic field effects at the tissue level in skeletal muscle. The model successfully reproduced the experimentally observed lesion geometry and was subsequently used to determine the irreversible electroporation threshold for the applied pulse protocol. While the model does not yet account for all relevant phenomena, such as the complex mechanisms of cell death, it provides a solid foundation for further development of models that incorporate tissue anisotropy to support electroporation-based treatment planning.

3.2 Anatomically accurate modelling of current pathways in skeletal muscle validated by MRI-based imaging

The second study expanded upon the previous investigation by addressing how the internal structure of skeletal muscle influences current distribution during application of external electric field. While the previous model [61] accounted for anisotropy using directional conductivity functions within a bulk tissue representation, it lacked anatomical detail. The aim of this follow-up study was to investigate how muscle fibrous structure influences current pathways during the application of an electric field, and whether anatomically inspired models improve prediction accuracy. To this end, a numerical model incorporating fibre-

level structure with realistic dimensions was developed and validated using current density imaging (CDI), a magnetic resonance-based technique capable of visualising current flow within tissue.

A three-dimensional model was constructed representing a simplified anatomical arrangement of parallel muscle fibres embedded in an extracellular matrix, with the dimensions and spacing of the fibres chosen to correspond to typical histological features. In this model, the anisotropy resulted from the explicit geometric representation of the individual muscle fibres embedded in the extracellular matrix, rather than from the assigned directional conductivity functions. The conductivity values of the individual tissue constituents were therefore constant values taken from the literature. Two needle electrodes were positioned 10.4 mm apart, and two different orientations with respect to the muscle fibre direction were used: in the parallel orientation, the electrodes were inserted such that the resulting electric field was aligned with the direction of the muscle fibres, while in the perpendicular orientation, the field was applied perpendicular to the fibre alignment. To validate the model, CDI experiments were performed on porcine skeletal muscle approximately 48 hours *post-mortem*, using the same electrode configurations as in the model. In each experiment, a single rectangular pulse of 800 μ s duration and 100 V amplitude was delivered. The simulated current density distributions were then compared with those obtained from CDI measurements.

The comparison between simulation and experiment showed that the current flow patterns were strongly influenced by the orientation of the electric field relative to the muscle fibres. In the parallel orientation, the current was concentrated along the shortest path between the electrodes in both the simulation and the experiments. In contrast, the perpendicular orientation resulted in more dispersed or deflected current patterns aligned with the muscle fibres. Quantitative analysis along the line crossing both electrode centres showed significantly higher current densities in the parallel case, while the perpendicular field application resulted in lower central densities and a redistribution above or below the axis. In addition, the current density profiles along a line perpendicular to the line connecting the electrodes showed a sharp central peak in the parallel orientation and a more uniform distribution in the perpendicular orientation, with a lower central density due to the deflection of the current along the muscle fibres. These results

highlight the influence of skeletal muscle anisotropy on current distribution and support the use of geometrically detailed models for accurate prediction.

Based on these observations, the study confirms the anisotropic behaviour of skeletal muscle, as shown by both simulations and CDI measurements. In particular, the observed current deflection in the perpendicular orientation is likely a consequence of tissue microstructures such as the sarcolemma and connective tissue layers, which impede current flow across the muscle fibres. While the model produced symmetrical patterns due to its idealised geometry, the experimental results displayed asymmetries that may be attributed to structural heterogeneities in the tissue, such as variability in fibre density, the distribution of connective and adipose tissue, and the presence of vessels or nerves. Furthermore, the data suggest that the anisotropic behaviour is still detectable even 48 hours *post-mortem*. These findings emphasise the importance of structural anisotropy in guiding current flow, even in non-viable tissue, and justify the use of geometrically informed models in electroporation research.

Despite these strengths, some limitations should be acknowledged. The muscle model was idealised and did not include detailed representations of the heterogeneous tissue components, which may have contributed to discrepancies between the simulations and the experimental results. In addition, the *post-mortem* interval of 48 hours likely led to at least partial disintegration of the cell membranes, implying that the anisotropy in the experiments was governed primarily by the remaining structural components rather than by the active membrane properties. Although membrane electroporation was not explicitly modelled, it was unlikely that the applied field strength and single pulse protocol would cause significant electroporation except in the immediate vicinity of the electrodes. The inclusion of membrane electroporation, as previously performed [106], [107], [108], would only increase the complexity of the model without significantly altering the results. Therefore, although the model provides valuable insights into the structural determinants of anisotropy, caution is required when interpreting the model's assumptions and input values, such as conductivity or membrane properties, in the context of *in vivo* tissue conditions, where biological mechanisms may differ from those in *ex vivo* tissue.

In summary, this study demonstrated that anisotropic conductivity and fibre

structure play a key role in shaping the current distribution during the application of external electric fields. The agreement between simulated and experimental data supports the utility of anatomically inspired models and emphasises the importance of including structural and directional properties of muscle tissue in future electroporation simulations. These findings provide a foundation for refining treatment planning and improving the predictability of electroporation outcomes in anisotropic tissues.

3.3 *Post-mortem* changes in skeletal muscle anisotropy evaluated by experimental and model-based impedance spectroscopy

The aim of this study was to understand how the anisotropy of skeletal muscle evolves over time after death, and to what extent *post-mortem* tissue retains the electrical characteristics of viable muscle. The combination of impedance spectroscopy and numerical modelling was used to clarify the mechanisms behind the *post-mortem* changes in electrical conductivity and to assess whether the cell plasma membrane is indeed responsible for tissue anisotropy. In particular, the study investigated whether the structural and electrical changes in *ex vivo* muscle tissue can be interpreted in terms of altered membrane permeability, either by natural degradation or by electroporation.

Impedance spectroscopy measurements were performed on porcine trapezius muscle samples at 3, 24, and 72 hours *post-mortem*, with impedance measured in both parallel and perpendicular directions relative to the muscle fibre alignment. At 3 hours *post-mortem*, the measurements showed a pronounced anisotropy of the electrical impedance, with the perpendicular orientation exhibiting more than tenfold higher impedance at low frequencies. This pronounced difference can be attributed to the fibrous structure of the muscle and the preserved integrity of the cell plasma membranes shortly after death. At 24 hours *post-mortem*, the anisotropy was still present but attenuated, indicating a partial degradation of the membrane structures. After 72 hours, the anisotropy was no longer detectable and the impedance was similar in both orientations, indicating a complete degradation of the cellular structures responsible for directional conductivity. These findings

are consistent with the results of other *ex vivo* muscle studies [34], [35], [37], some of which were performed immediately after tissue excision, and support the feasibility of using *post-mortem* muscle as a reliable model to study *in vivo* anisotropy.

To evaluate the effect of electroporation on membrane permeability, the impedance was measured immediately before and after the application of the electrical pulses. This allowed the calculation of an impedance ratio (post-treatment compared to pre-treatment) to quantify the changes in tissue conductivity due to electroporation. Electroporation was performed 3 and 24 hours *post-mortem* using eight 100 μs pulses at either 200 V or 400 V and a pulse repetition rate of 1 s^{-1} . The electrodes were spaced 6 mm apart. After electroporation, a marked decrease in impedance was observed, particularly in the perpendicular orientation, where the membranes are aligned across the direction of the applied electric field. At 3 hours *post-mortem* with a pulse amplitude of 400 V, the impedance was reduced by up to 60% in the perpendicular orientation and by approximately 20% in the parallel orientation. After 24 hours, the effect was diminished, consistent with the progressive loss of membrane integrity over time. Importantly, these results reinforce the idea that the muscle cell membrane acts as the primary barrier contributing to anisotropy. The more pronounced effects in the perpendicular orientation reflect the increased interaction between the electric field and the membranes, which act as a resistive barrier to current flow.

The observed differences between the orientations offer a mechanistic explanation for the orientation-dependent lesion shapes previously reported in both skeletal [61] and cardiac muscle [113]. In the perpendicular orientation, greater impedance reduction indicates more extensive membrane disruption, as the electric field intersects the cell membranes directly. In contrast, in the parallel orientation, the field aligns with the direction of the muscle fibres, allowing current to travel along them with less interaction across membranes, resulting in less disruption. These findings are relevant for electroporation-based therapies and numerical modelling, as they suggest that the increase in conductivity during electroporation depends on the orientation. Existing models often assume the same factor of conductivity increase for both orientations and a constant anisotropy ratio before and after electroporation [111], [113], [114], [115], [116]. The inclusion of direction-specific conductivity changes in such models could improve their

accuracy and predictive ability for electric field distribution and lesion formation.

Numerical modelling was used to validate and interpret the experimental results. A three-dimensional model was developed, with a simplified geometry consisting of cylindrical muscle fibres embedded in a cubic domain. The anisotropy resulted from the spatial arrangement of the fibres and the use of contact impedance boundary conditions to model the plasma membrane. Parametric simulations were performed to assess how varying membrane conductivity affected impedance in both orientations. The best agreement with the experimental results was achieved with a membrane conductivity of 5×10^{-7} S/m at 3 hours and 1×10^{-4} S/m at 24 hours *post-mortem*. In both cases, the modelled impedance was highly sensitive to changes in membrane conductivity in the perpendicular orientation, while the parallel orientation remained largely unaffected. These results confirm the hypothesis that membrane permeability is an important determinant of anisotropy.

While the experimental and numerical results were largely in agreement, some differences were found, particularly at higher frequencies and in parallel orientation. These discrepancies are likely due to uncertainties in the literature-derived conductivity and permittivity values used for the intracellular and extracellular spaces. In addition, the model used a simplified geometry and did not take into account heterogeneities such as fat, blood vessels, or connective tissue, which can also influence impedance. Despite these limitations, the model successfully captured the main features of the experimental data and demonstrated sensitivity to parameters associated with membrane integrity.

In summary, this study demonstrated that skeletal muscle retains its anisotropic impedance properties for at least the first 24 hours *post-mortem*, with the plasma membrane playing a critical role in maintaining this directional behaviour. These results support the use of *post-mortem* muscle tissue as a reliable model for *in vivo* conditions, offering a potential alternative to experiments with living animals and thereby helping to reduce the ethical burden of animal experimentation in medical research. The results have implications for both biomedical and food processing applications.

3.4 Modelling and real-time visualisation of electroporation-induced pH dynamics

In this study, we aimed to characterise and predict local pH changes induced by electroporation, which are caused by electrochemical reactions at the interface between electrode and electrolytic solution. To better understand and predict these effects, we developed a mechanistic multiphysics model derived from first principles of electrochemistry and validated it through carefully designed experiments with agarose gel phantoms. These phantoms served as simplified but controllable tissue surrogates and allowed direct visualisation of pH dynamics via a calibrated camera system with pH-sensitive dyes. By using unbuffered and buffered media, the study also assessed how different tissue-like environments influence the propagation of pH fronts.

Agarose gel experiments were performed in unbuffered saline, bicarbonate buffer, and HEPES buffer to observe the differences in pH changes between media with different buffer strengths. Platinum–iridium needle electrodes with a spacing of 14.3 mm were used to deliver eight monophasic rectangular pulses (10 ms duration, 1 s^{-1} repetition rate) at two amplitudes (200 V and 400 V), reflecting typical parameters used in gene electrotransfer. The experimental setup was reflected in a one-dimensional numerical model that tracked the migration of the pH front over time. The model was based on the Nernst–Planck system of partial differential equations, incorporating ionic transport by migration and diffusion mechanisms as well as chemical reactions at the electrode and within the electrolytic medium.

To convert the colour information from the agarose gel experiments into pH values, the imaging system was calibrated using a set of 27 standard buffer solutions ranging from pH 1.0 to 13.0. Each buffer was mixed with a universal pH indicator and photographed under controlled lighting conditions. The hue component of the RGB (red, green, blue) image data was extracted and correlated with the known pH values of the buffers so that a calibration curve could be generated. This calibration function, composed of three sigmoidal terms reflecting the three indicator components, provided a reliable pH estimation from the image data within a usable range of pH 4 to 10, allowing the determination of

pH values for each recorded pixel throughout the experiments.

The experimental results showed clear differences in the extent and sharpness of the pH front propagation between the media. As expected, the unbuffered medium exhibited the largest and most pronounced pH changes, with an acidic region forming near the anode and an alkaline region forming near the cathode, both extending significantly from the electrodes. The bicarbonate and HEPES buffers showed a more limited spread of altered pH, although subtle differences were noted: the HEPES buffer produced clearer boundaries between altered and unaltered pH regions, whereas the bicarbonate buffer provided slightly better mitigation of acidic changes. These observations were consistent across all replicates, confirming the reproducibility of the experimental setup.

The simulations agreed qualitatively with the experimental data, both in terms of the trends and the relative size of the fronts. However, the model tended to overestimate the spatial extent of the pH changes, probably due to the diffusion coefficients taken from the literature for aqueous solutions, which may not fully reflect the slower diffusion in agarose gels. By adjusting these coefficients to 50% of their original values, the model achieved improved agreement with the experiments. This highlights the sensitivity of the model to parameter selection and the importance of further experimental characterisation to constrain these parameters.

The strength of the presented model lies in its ability to resolve the dynamic behaviour of the pH fronts during and after pulse delivery. In particular, it was able to reproduce phenomena such as the continued diffusion of species after the end of the pulse and, under certain conditions, the retraction of pH fronts in buffered media during the pause between the pulses. Although this retraction was not observed in the present experiments, it has previously been observed in *in vivo* tissue [69] and could become relevant in other pulse protocols. Importantly, the observed pH changes are of significant practical concern. In applications such as gene electrotransfer, even moderate shifts in local pH may compromise DNA integrity or cell viability. In this context, the model provides a valuable tool for the prediction and potential mitigation of such effects by informing pulse design and electrode configuration.

Despite its strengths, the model also has its limitations. It does not yet take into account the electroosmotic effects, which may influence ion transport in real tissue, nor does it take into account the interactions between the pH indicators and the medium. Furthermore, although the current setup has been validated in agarose, extrapolation of the results to actual biological tissue requires caution due to differences in structure, perfusion, and chemical composition. Further experimental and computational work is required to extend the model to more complex geometries and validate it under *in vivo* conditions.

In summary, we presented a mechanistic model capable of capturing electroporation-induced pH changes in a simplified tissue phantom. Supported by reproducible experimental validation, the model provides valuable insights into the spatio-temporal dynamics of pH during electroporation. While refinements are needed to improve its predictive accuracy, particularly with respect to diffusion parameters, this approach lays the foundation for future modelling efforts aimed at optimising electroporation-based protocols where electrochemical side effects play an important role.

It is also worth noting that although this contribution focused on electrochemical pH effects, tissue damage during electroporation is often influenced by thermal effects and irreversible electroporation (IRE). Although these aspects were not modelled explicitly herein, their integration could enhance the predictive accuracy of treatment planning. Incorporating models such as the Pennes' bioheat equation and statistical survival models like the Peleg–Fermi model would enable estimation of temperature-induced damage and probabilistic cell death, respectively. Since integrating IRE and/or effects of heating into the pH model to arrive at a sort of a comprehensive tissue damage model would present too broad of a challenge to be feasible within the scope of this doctoral study, these additions are relegated to future work, aiming to develop a more complete simulation framework for electroporation-based therapies.

3.5 Experimental investigation of electroosmosis in plant and animal tissues under PEF and DC conditions

The fifth study investigated electroosmotic flow (EOF) as an accompanying effect of electroporation and assessed its significance in various biological matrices. Electroosmosis, a phenomenon whereby bulk fluid moves through a porous medium under the influence of an electric field, can significantly affect mass transport in both food processing and biomedical applications. In this work, EOF was experimentally evaluated in three types of media: plant tissue (potato tubers), animal skeletal muscle and agarose phantoms.

To evaluate EOF, we applied four different experimental conditions: load only (control), pulsed electric field (PEF) only, direct current (DC) only, and a combination of PEF followed by DC. The compression tests were performed using a texture analyser, with the samples positioned between two parallel stainless steel electrodes that served as both compression plates and electrical contacts. A constant compressive force of 10 N was applied. Each sample underwent a 30-second pre-compression phase to remove air pockets and ensure good electrode contact. The piston displacement was then recorded continuously for 330 seconds. PEF consisted of eight rectangular monopolar pulses (100 μs duration, 1 s^{-1} repetition rate, amplitude either 150 V or 1000 V), delivered via electrodes 6 mm apart immediately after the preload phase. Under DC conditions, a constant current of 25, 50, 100, or 200 mA was applied starting 15 seconds after pre-compression and maintained until the end of the experiment.

First, we investigated how the amplitude of the direct current, either alone or following high-voltage PEF (1000 V), influences the compression of the potato tissue. Compared to load only, PEF alone led to a significant increase in deformation, probably due to permeabilisation of the membranes, which facilitates the leakage of fluid from vacuoles and cells. These results are consistent with prior findings that electroporation increases water mobility in plant tissues, aided by the release of turgor pressure [117]. In the DC-only conditions, a clear trend emerged: higher current amplitudes led to increasingly greater compression. All DC-only treatments resulted in significantly higher deformation than the load-only control, confirming electroosmosis as a key mechanism. The approximately

linear increase in compression with current amplitude reflects the theoretical dependence of EOF on electric field strength.

The combination of PEF and DC generally resulted in greater compression than DC alone, particularly at 25 and 50 mA, suggesting a synergistic effect. This enhancement likely results from electroporation-induced structural changes that redistribute intracellular fluid into the extracellular space, increasing the volume available for electroosmotic transport. At higher DC amplitudes (100 and 200 mA), this synergistic benefit diminished. At 200 mA, DC-only samples slightly outperformed samples receiving both PEF and DC, indicating a reversal of the trend observed at lower currents. This result may be attributed to increased heating during high current application, particularly near the anode where desiccation occurs. In electroporated tissue, where the membranes are already compromised, this promotes rapid water loss and reduces electroosmotic efficiency over time. In addition, voltage instability was more frequently observed in PEF-treated tissue, potentially affecting the generator's ability to maintain a constant current and slowing down the EOF.

Next, we investigated how the different amplitude of the PEF pulses (150 V vs. 1000 V) affected compression in the potato tissue, with and without subsequent direct current application. The 150 V pulses produced significantly greater compression than load only, but significantly less than 1000 V, indicating a dose-dependent effect of electroporation. At 150 V, membrane permeabilisation was probably only partial and insufficient to strongly enhance deformation, whereas 1000 V pulses produced more extensive electroporation, greater water displacement and increased tissue compressibility [118]. In combination with 100 mA direct current, both PEF amplitudes showed increased compression compared to PEF alone. Final compression was significantly higher at a PEF amplitude of 1000 V than at a PEF amplitude of 150 V, highlighting the role of membrane permeabilisation in facilitating electroosmotic fluid movement.

Interestingly, the DC-only condition yielded a similar final compression to PEF 150 V + DC, but slightly less than PEF 1000 V + DC, although not significantly. This variability is likely related to the heterogeneity of plant tissue samples, particularly in the absence of PEF-induced homogenisation. Our results are in agreement with previous work [117], which showed that water redis-

tribution in potato tissue increases with field strength. Overall, the results show that electroporation can significantly enhance EOF-driven deformation, particularly at higher voltages where more extensive structural changes facilitate fluid transport.

Electroosmosis was also investigated in the porcine skeletal muscle, where direct current was applied both in parallel and perpendicular orientations relative to the muscle fibres. Although no statistically significant differences were observed, compression tended to be higher under direct current than load alone, suggesting a possible contribution of electroosmosis. Compared to plant tissue, the overall contribution of electroosmosis to deformation was lower, likely due to the absence of turgor pressure and the more complex structure of animal tissue [119].

To further investigate the role of electroosmosis, we applied eight PEF pulses and observed a stepwise displacement of the piston in both parallel and perpendicular orientation to the muscle fibres. This direct movement is indicative of electrically induced fluid flow and supports the presence of electroosmosis in animal tissue, despite its structural complexity. These observations are particularly relevant to food processing, where even modest electroosmotic activity could contribute to thermal and electrical homogenisation at the microscale, improving treatment uniformity.

Electroosmotic effects were also explored in agarose phantoms. Despite the absence of cellular structures and turgor pressure, the phantoms under direct current exhibited significantly greater compression than those under load alone. This deformation was driven solely by EOF through the porous gel network, confirming the suitability of agarose as a simplified system for isolating electroosmotic contributions to fluid motion.

Mechanical effects of electroporation were addressed in this work through texture analysis of both plant and animal tissues, providing experimental evidence of electroporation- and electroosmosis-induced deformation. This represents an important step toward understanding how electric field-induced mass transport influences tissue structure. In this study, electroporation was shown to enhance deformation under compression, especially in pre-treated tissue, indicating in-

creased water mobility and altered viscoelastic properties of electroporated biological tissue. These findings are in line with the original objective of assessing mechanical changes under electric field treatment. This work invites future studies that could involve more detailed viscoelastic characterisation, although the current results already demonstrate meaningful progress toward that goal.

In summary, our results show that electroosmosis is an important mechanism for fluid transport during electroporation, particularly in plant tissue, where it synergises with the loss of turgor induced by electroporation. While the contribution was less pronounced in animal tissue, the direct detection of EOF during pulse delivery supports its presence. The use of agarose phantoms confirmed the phenomenon in a simplified, cell-free system, emphasising its utility for mechanistic studies of electroosmosis.

4 Conclusions

This dissertation set out to deepen our understanding of the complex bioelectrical and physicochemical mechanisms involved in electroporation-based treatments. The findings presented across the five studies highlight both the potential and the limitations of current modelling and experimental approaches to the study of electroporation phenomena. Together, they highlight the value of integrating experimental and computational methods to better characterise tissue responses and optimise electroporation treatments for improved efficacy and reproducibility.

The studies investigating skeletal muscle demonstrated the importance of anisotropy in shaping the electrical behaviour and influencing electroporation outcomes. A multiscale modelling approach was developed to evaluate the effects of fibre orientation on the electric field distribution and lesion geometry, with results validated by *in vivo* experiments and image-based analyses. Furthermore, an MRI-based study demonstrated that current pathways in skeletal muscle are anisotropic and dependent on the orientation of the applied electric field, thereby emphasising the critical role of muscle architecture in determining electroporation outcomes. In addition, impedance spectroscopy performed on excised muscle tissue showed that the anisotropic electrical properties persist for at least 24 hours *post-mortem*. This underlines the feasibility of using *ex vivo* tissue for characterisation and experimental validation and reduces the reliance on live animal models. Collectively, these findings provide a foundation for modelling anisotropy in electroporation applications involving skeletal muscle.

In parallel, the study of electroporation-induced pH changes highlighted the importance of accounting for electrochemical reactions at the electrode–electrolyte interface. A computational model based on the Nernst–Planck system

of equations accurately predicted the evolution of the pH fronts during electroporation. This model was validated using a custom-built optical imaging system that was calibrated to convert colour hue into pH values. The findings emphasise that even with commonly used pulse protocols, substantial pH changes can occur, potentially compromising treatment efficacy and contributing to tissue damage in the surrounding area.

The final study focussed on electroosmosis, a mechanism that is often overlooked in biomedical applications. Experiments on plant, animal, and agarose samples confirmed that electrically induced fluid movement contributes to tissue deformation under load. In potato tissue, electroosmosis was identified as the dominant mechanism, with PEF-induced membrane permeabilisation further amplifying compression, particularly at lower current amplitudes. In skeletal muscle, although the contribution of electroosmosis to deformation was lower, primarily due to the lack of turgor pressure, the stepwise piston displacements observed during pulse delivery provided direct visual evidence of electroosmotic flow even in structurally complex, *post-mortem* tissue.

As a whole, the results presented in this dissertation demonstrate the importance of incorporating relevant bioelectrical and physicochemical mechanisms, such as anisotropy, electrochemical reactions, and electroosmotic flow, into both experimental protocols and modelling frameworks. While not all mechanisms are relevant for every application, their inclusion is essential when studying structured tissue such as skeletal muscle or when using pulse protocols that are likely to induce electrochemical effects.

The phenomena investigated in this dissertation – namely electrical anisotropy, electrochemical pH dynamics, electroosmotic fluid flow, and associated mechanical effects – were explored through targeted and rigorous experimental and modelling approaches. Each of these mechanisms plays a critical role in shaping the outcomes of electroporation-based treatments. While they were addressed individually, the results strongly indicate the need for an integrated modelling framework that synthesises these effects into a unified simulation platform.

The present work should, therefore, be understood as a solid foundation whose

future extensions could then be further developed to include models of irreversible electroporation thresholds and tissue heating. The development of such a large-scale multiphysics framework would represent a significant step forward in both understanding and leveraging the full potential of electroporation-based technologies.

Such a platform could be used to estimate regions of reversible and irreversible electroporation, identify zones influenced by electrochemical alterations such as pH shifts, and predict areas subject to fluid redistribution or mechanical softening. By incorporating anisotropic tissue architecture, membrane conductivity evolution, electroosmosis, thermal effects, and mass transport dynamics, a comprehensive map of a “therapy outcome” could be developed. This would enable optimised treatment planning for both biomedical and industrial applications.

5 Original scientific contributions

Multiscale numerical modelling and experimental validation of skeletal muscle anisotropy

Skeletal muscle exhibits anisotropic electrical properties that significantly influence the outcome of electroporation-based treatments, yet a detailed and systematic validation of these properties had previously been lacking. In this contribution, comprehensive multiscale numerical models of skeletal muscle anisotropy were developed and rigorously validated using multiple experimental methodologies, including *in vivo* lesion analyses, and MRI-based current density imaging and impedance spectroscopy *ex vivo*. Quantitative analyses revealed the crucial influence of muscle fibre alignment on the electric field distribution, lesion geometry, and current pathways during electroporation. It was shown that the threshold for irreversible electroporation is independent of fibre orientation. Our combined experimental and modelling findings strongly support the conclusion that the anisotropic electrical behaviour in skeletal muscle primarily results from the insulating properties of the plasma membrane, which significantly impede current flow perpendicular to the muscle fibres. These validated models establish an essential foundation for improving the accuracy and efficacy of electroporation protocols tailored to anisotropic biological tissue.

Experimentally validated numerical model of pH changes induced by electroporation pulses

Electroporation generates electrochemical reactions at the electrode interfaces that lead to significant local changes in pH. A comprehensive mechanistic computational model was developed to accurately predict and characterise these pH changes during and after the delivery of electroporation pulses. To validate the

model, an innovative experimental setup was established, utilising agarose gels containing pH-sensitive indicators to allow real-time monitoring of the evolving pH fronts. This study provided novel quantitative insights into the dynamics of pH changes induced by electroporation and, in particular, highlighted their potential impact on therapeutic applications sensitive to pH variations, such as gene electrotransfer. The validated model provides a valuable framework to guide electrode design and pulse protocol optimisation, with the aim of mitigating unwanted electrochemical effects and improving overall treatment outcomes.

Experimental characterisation of electroosmotic flow in tissues under PEF and DC conditions

The electroosmotic flow (EOF), an electrically induced fluid transport mechanism, remains insufficiently investigated in electroporation research. We systematically characterised the EOF in plant, animal, and surrogate tissues. The experimental analysis allowed direct visualisation and quantitative evidence of the electroosmotic flow and underlined its substantial influence on tissue deformation and fluid redistribution. Furthermore, the study showed a synergistic interaction between electroporation-induced membrane permeabilisation and subsequent electroosmotic fluid flow. These findings emphasise the importance of considering electroosmosis in the development of electroporation protocols and provide new insights to improve applications in biomedicine and food processing.

References

- [1] E. Neumann and K. Rosenheck, “Permeability changes induced by electric impulses in vesicular membranes”, *J. Membrane Biol.*, vol. 10, no. 1, pp. 279–290, Dec. 1972. DOI: 10.1007/BF01867861.
- [2] T. Kotnik, G. Pucihar, and D. Miklavčič, “The Cell in the Electric Field”, in *Clinical Aspects of Electroporation*, S. T. Kee, J. Gehl, and E. W. Lee, Eds., New York, NY: Springer New York, 2011, pp. 19–29, ISBN: 978-1-4419-8362-6 978-1-4419-8363-3. DOI: 10.1007/978-1-4419-8363-3_3.
- [3] L. Rems and D. Miklavčič, “Tutorial: Electroporation of cells in complex materials and tissue”, *Journal of Applied Physics*, vol. 119, no. 20, p. 201101, May 2016. DOI: 10.1063/1.4949264.
- [4] T. Kotnik, L. Rems, M. Tarek, and D. Miklavčič, “Membrane Electroporation and Electropermeabilization: Mechanisms and Models”, *Annu. Rev. Biophys.*, vol. 48, no. 1, pp. 63–91, May 2019. DOI: 10.1146/annurev-biophys-052118-115451.
- [5] S. Mahnič-Kalamiza, “Modeli dvojne poroznosti in njihova raba pri elektroporaciji bioloških tkiv”, *Elektroteh. Vestn.*, vol. 88, no. 3, pp. 75–84, 2021.
- [6] M. L. Yarmush, A. Golberg, G. Serša, T. Kotnik, and D. Miklavčič, “Electroporation-Based Technologies for Medicine: Principles, Applications, and Challenges”, *Annu. Rev. Biomed. Eng.*, vol. 16, no. 1, pp. 295–320, Jul. 2014. DOI: 10.1146/annurev-bioeng-071813-104622.
- [7] T. Kotnik, W. Frey, M. Sack, S. Haberl Meglič, M. Peterka, and D. Miklavčič, “Electroporation-based applications in biotechnology”, *Trends*

- in Biotechnology*, vol. 33, no. 8, pp. 480–488, Aug. 2015. DOI: 10.1016/j.tibtech.2015.06.002.
- [8] Z.-Y. Huo et al., “Synergistic Nanowire-Enhanced Electroporation and Electrochlorination for Highly Efficient Water Disinfection”, *Environ. Sci. Technol.*, vol. 56, no. 15, pp. 10 925–10 934, Aug. 2022. DOI: 10.1021/acs.est.2c01793.
- [9] S. Mahnič-Kalamiza, E. Vorobiev, and D. Miklavčič, “Electroporation in Food Processing and Biorefinery”, *J Membrane Biol*, vol. 247, no. 12, pp. 1279–1304, Dec. 2014. DOI: 10.1007/s00232-014-9737-x.
- [10] A. Gothelf and J. Gehl, “Gene Electrotransfer to Skin; Review of Existing Literature and Clinical Perspectives”, *CGT*, vol. 10, no. 4, pp. 287–299, Aug. 2010. DOI: 10.2174/156652310791823443.
- [11] C. Rosazza, S. Haberl Meglic, A. Zumbusch, M.-P. Rols, and D. Miklavcic, “Gene Electrotransfer: A Mechanistic Perspective”, *CGT*, vol. 16, no. 2, pp. 98–129, Apr. 2016. DOI: 10.2174/1566523216666160331130040.
- [12] S. Sachdev, T. Potočnik, L. Rems, and D. Miklavčič, “Revisiting the role of pulsed electric fields in overcoming the barriers to in vivo gene electrotransfer”, *Bioelectrochemistry*, vol. 144, p. 107 994, Apr. 2022. DOI: 10.1016/j.bioelechem.2021.107994.
- [13] M. Belehradek, C. Domenge, B. Luboinski, S. Orlowski, J. Belehradek, and L. M. Mir, “Electrochemotherapy, a new antitumor treatment. First clinical phase I-II trial”, *Cancer*, vol. 72, no. 12, pp. 3694–3700, Dec. 1993.
- [14] M. Marty et al., “Electrochemotherapy – An easy, highly effective and safe treatment of cutaneous and subcutaneous metastases: Results of ESOPE (European Standard Operating Procedures of Electrochemotherapy) study”, *European Journal of Cancer Supplements*, vol. 4, no. 11, pp. 3–13, Nov. 2006. DOI: 10.1016/j.ejcsup.2006.08.002.
- [15] G. Sersa, D. Miklavcic, M. Cemazar, Z. Rudolf, G. Pucihar, and M. Snoj, “Electrochemotherapy in treatment of tumours”, *European Journal of Surgical Oncology (EJSO)*, vol. 34, no. 2, pp. 232–240, Feb. 2008. DOI: 10.1016/j.ejso.2007.05.016.

-
- [16] R. V. Davalos, L. M. Mir, and B. Rubinsky, "Tissue Ablation with Irreversible Electroporation", *Ann Biomed Eng*, vol. 33, no. 2, pp. 223–231, Feb. 2005. DOI: 10.1007/s10439-005-8981-8.
- [17] J. Edd, L. Horowitz, R. Davalos, L. Mir, and B. Rubinsky, "In Vivo Results of a New Focal Tissue Ablation Technique: Irreversible Electroporation", *IEEE Trans. Biomed. Eng.*, vol. 53, no. 7, pp. 1409–1415, Jul. 2006. DOI: 10.1109/TBME.2006.873745.
- [18] B. Rubinsky, G. Onik, and P. Mikus, "Irreversible Electroporation: A New Ablation Modality — Clinical Implications", *Technol Cancer Res Treat*, vol. 6, no. 1, pp. 37–48, Feb. 2007. DOI: 10.1177/153303460700600106.
- [19] H. J. Scheffer et al., "Irreversible Electroporation for Nonthermal Tumor Ablation in the Clinical Setting: A Systematic Review of Safety and Efficacy", *Journal of Vascular and Interventional Radiology*, vol. 25, no. 7, pp. 997–1011, Jul. 2014. DOI: 10.1016/j.jvir.2014.01.028.
- [20] C. Jiang, R. V. Davalos, and J. C. Bischof, "A Review of Basic to Clinical Studies of Irreversible Electroporation Therapy", *IEEE Trans. Biomed. Eng.*, vol. 62, no. 1, pp. 4–20, Jan. 2015. DOI: 10.1109/TBME.2014.2367543.
- [21] A. Sugrue et al., "Irreversible electroporation for catheter-based cardiac ablation: A systematic review of the preclinical experience", *J Interv Card Electrophysiol*, vol. 55, no. 3, pp. 251–265, Sep. 2019. DOI: 10.1007/s10840-019-00574-3.
- [22] A. Verma et al., "First-in-Human Experience and Acute Procedural Outcomes Using a Novel Pulsed Field Ablation System: The PULSED AF Pilot Trial", *Circ: Arrhythmia and Electrophysiology*, vol. 15, no. 1, e010168, Jan. 2022. DOI: 10.1161/CIRCEP.121.010168.
- [23] V. Y. Reddy et al., "Pulsed Field or Conventional Thermal Ablation for Paroxysmal Atrial Fibrillation", *N Engl J Med*, vol. 389, no. 18, pp. 1660–1671, Nov. 2023. DOI: 10.1056/NEJMoA2307291.
- [24] A. Verma et al., "Pulsed Field Ablation for the Treatment of Atrial Fibrillation: PULSED AF Pivotal Trial", *Circulation*, vol. 147, no. 19, pp. 1422–1432, May 2023. DOI: 10.1161/CIRCULATIONAHA.123.063988.

-
- [25] K.-R. J. Chun et al., “State-of-the-art pulsed field ablation for cardiac arrhythmias: Ongoing evolution and future perspective”, *Europace*, vol. 26, no. 6, euae134, Jun. 2024. DOI: 10.1093/europace/euae134.
- [26] M. Sack et al., “Electroporation-Assisted Dewatering as an Alternative Method for Drying Plants”, *IEEE Trans. Plasma Sci.*, vol. 36, no. 5, pp. 2577–2585, Oct. 2008. DOI: 10.1109/TPS.2008.2002440.
- [27] M. Gagneten, G. Leiva, D. Salvatori, C. Schebor, and N. Olaiz, “Optimization of Pulsed Electric Field Treatment for the Extraction of Bioactive Compounds from Blackcurrant”, *Food Bioprocess Technol*, vol. 12, no. 7, pp. 1102–1109, Jul. 2019. DOI: 10.1007/s11947-019-02283-1.
- [28] G. Canelli et al., “Pulsed electric field treatment enhances lipid bioaccessibility while preserving oxidative stability in *Chlorella vulgaris*”, *Innovative Food Science & Emerging Technologies*, vol. 75, p. 102897, Jan. 2022. DOI: 10.1016/j.ifset.2021.102897.
- [29] J. Genovese et al., “Important factors to consider for acrylamide mitigation in potato crisps using pulsed electric fields”, *Innovative Food Science & Emerging Technologies*, vol. 55, pp. 18–26, Jul. 2019. DOI: 10.1016/j.ifset.2019.05.008.
- [30] M. A. Schouten et al., “Effect of innovative pre-treatments on the mitigation of acrylamide formation in potato chips”, *Innovative Food Science & Emerging Technologies*, vol. 64, p. 102397, Aug. 2020. DOI: 10.1016/j.ifset.2020.102397.
- [31] K. Dymek, L. Rems, B. Zorec, P. Dejmek, F. G. Galindo, and D. Miklavčič, “Modeling electroporation of the non-treated and vacuum impregnated heterogeneous tissue of spinach leaves”, *Innovative Food Science & Emerging Technologies*, vol. 29, pp. 55–64, May 2015. DOI: 10.1016/j.ifset.2014.08.006.
- [32] S. Grimnes, *Bioimpedance and Bioelectricity Basics*, 3rd ed. London, U.K: Academic Press, 2015.
- [33] K. R. Foster and H. P. Schwan, “Dielectric properties of tissues and biological materials: A critical review”, *Crit Rev Biomed Eng*, vol. 17, no. 1, pp. 25–104, 1989.

-
- [34] C. Gabriel, S. Gabriel, and E. Corthout, “The dielectric properties of biological tissues: I. Literature survey”, *Phys. Med. Biol.*, vol. 41, no. 11, pp. 2231–2249, Nov. 1996. DOI: 10.1088/0031-9155/41/11/001.
- [35] S. Gabriel, R. W. Lau, and C. Gabriel, “The dielectric properties of biological tissues: II. Measurements in the frequency range 10 Hz to 20 GHz”, *Phys. Med. Biol.*, vol. 41, no. 11, pp. 2251–2269, Nov. 1996. DOI: 10.1088/0031-9155/41/11/002.
- [36] S. Gabriel, R. W. Lau, and C. Gabriel, “The dielectric properties of biological tissues: III. Parametric models for the dielectric spectrum of tissues”, *Phys. Med. Biol.*, vol. 41, no. 11, pp. 2271–2293, Nov. 1996. DOI: 10.1088/0031-9155/41/11/003.
- [37] D. Miklavčič, N. Pavšelj, and F. X. Hart, “Electric Properties of Tissues”, in *Wiley Encyclopedia of Biomedical Engineering*, M. Akay, Ed., 1st ed., Wiley, Apr. 2006, ISBN: 978-0-471-24967-2 978-0-471-74036-0. DOI: 10.1002/9780471740360.ebs0403.
- [38] D. Dean, T. Ramanathan, D. Machado, and R. Sundararajan, “Electrical impedance spectroscopy study of biological tissues”, *Journal of Electrostatics*, vol. 66, no. 3-4, pp. 165–177, Mar. 2008. DOI: 10.1016/j.elstat.2007.11.005.
- [39] M. B. Lee, G.-H. Jahng, H. J. Kim, E. J. Woo, and O. I. Kwon, “Extracellular electrical conductivity property imaging by decomposition of high-frequency conductivity at Larmor-frequency using multi-b-value diffusion-weighted imaging”, *PLoS ONE*, vol. 15, no. 4, Q. Jiang, Ed., e0230903, Apr. 2020. DOI: 10.1371/journal.pone.0230903.
- [40] Q. Castellví, B. Mercadal, and A. Ivorra, “Assessment of Electroporation by Electrical Impedance Methods”, in *Handbook of Electroporation*, D. Miklavčič, Ed., Cham: Springer International Publishing, 2017, pp. 671–690, ISBN: 978-3-319-32885-0 978-3-319-32886-7. DOI: 10.1007/978-3-319-32886-7_164.
- [41] H. S. Magar, R. Y. A. Hassan, and A. Mulchandani, “Electrochemical Impedance Spectroscopy (EIS): Principles, Construction, and Biosensing Applications”, *Sensors*, vol. 21, no. 19, p. 6578, Oct. 2021. DOI: 10.3390/s21196578.

-
- [42] A. Ivorra and B. Rubinsky, “In vivo electrical impedance measurements during and after electroporation of rat liver”, *Bioelectrochemistry*, vol. 70, no. 2, pp. 287–295, May 2007. DOI: 10.1016/j.bioelechem.2006.10.005.
- [43] S. Laufer, A. Ivorra, V. E. Reuter, B. Rubinsky, and S. B. Solomon, “Electrical impedance characterization of normal and cancerous human hepatic tissue”, *Physiol. Meas.*, vol. 31, no. 7, pp. 995–1009, Jul. 2010. DOI: 10.1088/0967-3334/31/7/009.
- [44] T. García-Sánchez, A. Azan, I. Leray, J. Rosell-Ferrer, R. Bragós, and L. M. Mir, “Interpulse multifrequency electrical impedance measurements during electroporation of adherent differentiated myotubes”, *Bioelectrochemistry*, vol. 105, pp. 123–135, Oct. 2015. DOI: 10.1016/j.bioelechem.2015.05.018.
- [45] T. A. Whitman, J. C. Forrest, M. T. Morgan, and M. R. Okos, “Electrical measurement for detecting early postmortem changes in porcine muscle.”, *Journal of Animal Science*, vol. 74, no. 1, p. 80, 1996. DOI: 10.2527/1996.74180x.
- [46] M. Pavlin, K. Flisar, and M. Kandušer, “The Role of Electrophoresis in Gene Electrotransfer”, *J Membrane Biol*, vol. 236, no. 1, pp. 75–79, Jul. 2010. DOI: 10.1007/s00232-010-9276-z.
- [47] Y. Lv et al., “Analysis of the Electric Field-Dependent Current During Electroporation Pulses”, *IEEE Access*, vol. 8, pp. 93 850–93 856, 2020. DOI: 10.1109/ACCESS.2020.2995151.
- [48] M. Joy, G. Scott, and M. Henkelman, “In vivo detection of applied electric currents by magnetic resonance imaging”, *Magnetic Resonance Imaging*, vol. 7, no. 1, pp. 89–94, Jan. 1989. DOI: 10.1016/0730-725X(89)90328-7.
- [49] U. Mikac, F. Demšar, K. Beravs, and I. Serša, “Magnetic resonance imaging of alternating electric currents”, *Magnetic Resonance Imaging*, vol. 19, no. 6, pp. 845–856, Jul. 2001. DOI: 10.1016/S0730-725X(01)00393-9.
- [50] K. Beravs, D. White, I. Serša, and F. Demsar, “Electric current density imaging of bone by MRI”, *Magnetic Resonance Imaging*, vol. 15, no. 8, pp. 909–915, Jan. 1997. DOI: 10.1016/S0730-725X(97)00038-6.

-
- [51] I. Serša, K. Beravs, N. J. F. Dodd, S. Zhao, D. Miklavčič, and F. Demsar, “Electric current density imaging of mice tumors”, *Magnetic Resonance in Med*, vol. 37, no. 3, pp. 404–409, Mar. 1997. DOI: 10.1002/mrm.1910370318.
- [52] L. M. Mir et al., “High-efficiency gene transfer into skeletal muscle mediated by electric pulses”, *Proc. Natl. Acad. Sci. U.S.A.*, vol. 96, no. 8, pp. 4262–4267, Apr. 1999. DOI: 10.1073/pnas.96.8.4262.
- [53] G. Tevz et al., “Gene Electrotransfer into Murine Skeletal Muscle: A Systematic Analysis of Parameters for Long-term Gene Expression”, *Technol Cancer Res Treat*, vol. 7, no. 2, pp. 91–101, Apr. 2008. DOI: 10.1177/153303460800700201.
- [54] D. C. Hughes, J. P. Hardee, D. S. Waddell, and C. A. Goodman, “CORP: Gene delivery into murine skeletal muscle using in vivo electroporation”, *Journal of Applied Physiology*, vol. 133, no. 1, pp. 41–59, Jul. 2022. DOI: 10.1152/japplphysiol.00088.2022.
- [55] B. Epstein, R. Settle, and K. Foster, “Anisotropic impedance properties of skeletal muscle”, in *Bioengineering*, Elsevier, 1981, pp. 139–143, ISBN: 978-0-08-027207-8. DOI: 10.1016/B978-0-08-027207-8.50034-5.
- [56] M. S. Spach, W. T. Miller, E. Miller-Jones, R. B. Warren, and R. C. Barr, “Extracellular potentials related to intracellular action potentials during impulse conduction in anisotropic canine cardiac muscle.”, *Circulation Research*, vol. 45, no. 2, pp. 188–204, Aug. 1979. DOI: 10.1161/01.RES.45.2.188.
- [57] D. B. Geselowitz, R. C. Barr, M. S. Spach, and W. T. Miller, “The impact of adjacent isotropic fluids on electrograms from anisotropic cardiac muscle. A modeling study.”, *Circulation Research*, vol. 51, no. 5, pp. 602–613, Nov. 1982. DOI: 10.1161/01.RES.51.5.602.
- [58] V. Tayfur, O. Magden, M. Edizer, and A. Atabey, “Anatomy of Vastus Lateralis Muscle Flap”, *Journal of Craniofacial Surgery*, vol. 21, no. 6, pp. 1951–1953, Nov. 2010. DOI: 10.1097/SCS.0b013e3181f4ee7f.
- [59] A. Rehfeld, M. Nylander, and K. Karnov, *Compendium of Histology: A Theoretical and Practical Guide*. Cham: Springer International Publishing, 2017. DOI: 10.1007/978-3-319-41873-5.

-
- [60] J. Malmivuo and R. Plonsey, *Bioelectromagnetism Principles and Applications of Bioelectric and Biomagnetic Fields*. Oxford University Press, Oct. 1995. DOI: 10.1093/acprof:oso/9780195058239.001.0001.
 - [61] R. Šmerc et al., “A Multiscale Computational Model of Skeletal Muscle Electroporation Validated Using *In Situ* Porcine Experiments”, *IEEE Trans. Biomed. Eng.*, vol. 70, no. 6, pp. 1826–1837, Jun. 2023. DOI: 10.1109/TBME.2022.3229560.
 - [62] P. A. Garcia, R. V. Davalos, and D. Miklavcic, “A Numerical Investigation of the Electric and Thermal Cell Kill Distributions in Electroporation-Based Therapies in Tissue”, *PLoS ONE*, vol. 9, no. 8, B. Rubinsky, Ed., e103083, Aug. 2014. DOI: 10.1371/journal.pone.0103083.
 - [63] I. Lackovic, R. Magjarevic, and D. Miklavcic, “Three-dimensional finite-element analysis of joule heating in electrochemotherapy and in vivo gene electrotransfer”, *IEEE Trans. Dielect. Electr. Insul.*, vol. 16, no. 5, pp. 1338–1347, Oct. 2009. DOI: 10.1109/TDEI.2009.5293947.
 - [64] R. V. Davalos, S. Bhonsle, and R. E. Neal, “Implications and considerations of thermal effects when applying irreversible electroporation tissue ablation therapy”, *The Prostate*, vol. 75, no. 10, pp. 1114–1118, Jul. 2015. DOI: 10.1002/pros.22986.
 - [65] W. Van Den Bos et al., “Thermal Energy during Irreversible Electroporation and the Influence of Different Ablation Parameters”, *Journal of Vascular and Interventional Radiology*, vol. 27, no. 3, pp. 433–443, Mar. 2016. DOI: 10.1016/j.jvir.2015.10.020.
 - [66] K. N. Aycock and R. V. Davalos, “Irreversible Electroporation: Background, Theory, and Review of Recent Developments in Clinical Oncology”, *Bioelectricity*, vol. 1, no. 4, pp. 214–234, Dec. 2019. DOI: 10.1089/bioe.2019.0029.
 - [67] P. Agnass et al., “Mathematical modeling of the thermal effects of irreversible electroporation for *in vitro*, *in vivo*, and clinical use: A systematic review”, *International Journal of Hyperthermia*, vol. 37, no. 1, pp. 486–505, Jan. 2020. DOI: 10.1080/02656736.2020.1753828.

-
- [68] P. Turjanski et al., “The Role of pH Fronts in Reversible Electroporation”, *PLoS ONE*, vol. 6, no. 4, B. Rubinsky, Ed., e17303, Apr. 2011. DOI: 10.1371/journal.pone.0017303.
- [69] M. Marino et al., “pH fronts and tissue natural buffer interaction in gene electrotransfer protocols”, *Electrochimica Acta*, vol. 255, pp. 463–471, Nov. 2017. DOI: 10.1016/j.electacta.2017.09.021.
- [70] M. Iwata, T. Tanaka, and M. S. Jami, “Application of Electroosmosis for Sludge Dewatering—A Review”, *Drying Technology*, vol. 31, no. 2, pp. 170–184, Jan. 2013. DOI: 10.1080/07373937.2012.691592.
- [71] A. Menon, T. R. Mashyamombe, E. Kaygen, M. S. Mortazavi Nasiri, and V. Stojceska, “Electroosmosis dewatering as an energy efficient technique for drying food materials”, *Energy Procedia*, vol. 161, pp. 123–132, Mar. 2019. DOI: 10.1016/j.egypro.2019.02.069.
- [72] A. Alizadeh, W.-L. Hsu, M. Wang, and H. Daiguji, “Electroosmotic flow: From microfluidics to nanofluidics”, *Electrophoresis*, vol. 42, no. 7-8, pp. 834–868, Apr. 2021. DOI: 10.1002/elps.202000313.
- [73] P. Turjanski, N. Olaiz, P. Abou-Adal, C. Suárez, M. Risk, and G. Marshall, “pH front tracking in the electrochemical treatment (EChT) of tumors: Experiments and simulations”, *Electrochimica Acta*, vol. 54, no. 26, pp. 6199–6206, Nov. 2009. DOI: 10.1016/j.electacta.2009.05.062.
- [74] E. Calzado, H. Schinca, L. Cabrales, F. García, P. Turjanski, and N. Olaiz, “Impact of permeabilization and pH effects in the electrochemical treatment of tumors: Experiments and simulations”, *Applied Mathematical Modelling*, vol. 74, pp. 62–72, Oct. 2019. DOI: 10.1016/j.apm.2019.04.041.
- [75] A. Mokhtare, M. Shiv Krishna Reddy, V. A. Roodan, E. P. Furlani, and A. Abbaspourrad, “The role of pH fronts, chlorination and physicochemical reactions in tumor necrosis in the electrochemical treatment of tumors: A numerical study”, *Electrochimica Acta*, vol. 307, pp. 129–147, Jun. 2019. DOI: 10.1016/j.electacta.2019.03.148.

-
- [76] E. Nilsson, J. Berendson, and E. Fontes, “Development of a dosage method for electrochemical treatment of tumours: A simplified mathematical model”, *Bioelectrochemistry and Bioenergetics*, vol. 47, no. 1, pp. 11–18, Nov. 1998. DOI: 10.1016/S0302-4598(98)00157-3.
- [77] E. Nilsson, J. Berendson, and E. Fontes, “Electrochemical treatment of tumours: A simplified mathematical model”, *Journal of Electroanalytical Chemistry*, vol. 460, no. 1-2, pp. 88–99, Jan. 1999. DOI: 10.1016/S0022-0728(98)00352-0.
- [78] E. Nilsson, J. Berendson, and E. Fontes, “Impact of chlorine and acidification in the electrochemical treatment of tumours”, *Journal of Applied Electrochemistry*, vol. 30, no. 12, pp. 1321–1333, 2000. DOI: 10.1023/A:1026560806158.
- [79] E. Nilsson and E. Fontes, “Mathematical modelling of physicochemical reactions and transport processes occurring around a platinum cathode during the electrochemical treatment of tumours”, *Bioelectrochemistry*, vol. 53, no. 2, pp. 213–224, Mar. 2001. DOI: 10.1016/S0302-4598(01)00097-6.
- [80] F. Maglietti, S. Michinski, N. Olaiz, M. Castro, C. Suárez, and G. Marshall, “The Role of Ph Fronts in Tissue Electroporation Based Treatments”, *PLoS ONE*, vol. 8, no. 11, M. R. Scarfi, Ed., e80167, Nov. 2013. DOI: 10.1371/journal.pone.0080167.
- [81] N. Olaiz et al., “Tissue damage modeling in gene electrotransfer: The role of pH”, *Bioelectrochemistry*, vol. 100, pp. 105–111, Dec. 2014. DOI: 10.1016/j.bioelechem.2014.05.001.
- [82] E. Luján, M. Marino, N. Olaiz, and G. Marshall, “Towards an optimal dose-response relationship in gene electrotransfer protocols”, *Electrochimica Acta*, vol. 319, pp. 1002–1011, Oct. 2019. DOI: 10.1016/j.electacta.2019.07.029.
- [83] Z. S. Salameh et al., “Harnessing the Electrochemical Effects of Electroporation-Based Therapies to Enhance Anti-tumor Immune Responses”, *Ann Biomed Eng*, vol. 52, no. 1, pp. 48–56, Jan. 2024. DOI: 10.1007/s10439-023-03403-x.

-
- [84] X. Wang, H. J. Lim, and A. Son, “Characterization of denaturation and renaturation of DNA for DNA hybridization”, *Environ Health Toxicol*, vol. 29, e2014007, Sep. 2014. DOI: 10.5620/eht.2014.29.e2014007.
- [85] T. Potočnik, S. Sachdev, T. Polajžer, A. Maček Lebar, and D. Miklavčič, “Efficient Gene Transfection by Electroporation—In Vitro and In Silico Study of Pulse Parameters”, *Applied Sciences*, vol. 12, no. 16, p. 8237, Aug. 2022. DOI: 10.3390/app12168237.
- [86] T. Potočnik et al., “Effect of Experimental Electrical and Biological Parameters on Gene Transfer by Electroporation: A Systematic Review and Meta-Analysis”, *Pharmaceutics*, vol. 14, no. 12, p. 2700, Dec. 2022. DOI: 10.3390/pharmaceutics14122700.
- [87] D. Miklavčič, A. Fajgelj, and G. Serša, “Tumour treatment by direct electric current: Electrode material deposition”, *Bioelectrochemistry and Bioenergetics*, vol. 35, no. 1-2, pp. 93–97, Nov. 1994. DOI: 10.1016/0302-4598(94)87017-9.
- [88] E. Nilsson et al., “Electrochemical treatment of tumours”, *Bioelectrochemistry*, vol. 51, no. 1, pp. 1–11, Feb. 2000. DOI: 10.1016/S0302-4598(99)00073-2.
- [89] H. Von Euler, A. Söderstedt, A. Thörne, J. M. Olsson, and G. Yongqing, “Cellular toxicity induced by different pH levels on the R3230AC rat mammary tumour cell line. An in vitro model for investigation of the tumour destructive properties of electrochemical treatment of tumours”, *Bioelectrochemistry*, vol. 58, no. 2, pp. 163–170, Dec. 2002. DOI: 10.1016/S1567-5394(02)00154-8.
- [90] M. Phillips, L. Rubinsky, A. Meir, N. Raju, and B. Rubinsky, “Combining Electrolysis and Electroporation for Tissue Ablation”, *Technol Cancer Res Treat*, vol. 14, no. 4, pp. 395–410, Aug. 2015. DOI: 10.1177/1533034614560102.
- [91] M. Phillips, H. Krishnan, N. Raju, and B. Rubinsky, “Tissue Ablation by a Synergistic Combination of Electroporation and Electrolysis Delivered by a Single Pulse”, *Ann Biomed Eng*, vol. 44, no. 10, pp. 3144–3154, Oct. 2016. DOI: 10.1007/s10439-016-1624-4.

-
- [92] L. Rubinsky, E. Guenther, P. Mikus, M. Stehling, and B. Rubinsky, “Electrolytic Effects During Tissue Ablation by Electroporation”, *Technol Cancer Res Treat*, vol. 15, no. 5, NP95–NP103, Oct. 2016. DOI: 10.1177/1533034615601549.
- [93] H. B. Kim and J. H. Chung, “Incorporation of Reversible Electroporation Into Electrolysis Accelerates Apoptosis for Rat Liver Tissue”, *Technol Cancer Res Treat*, vol. 19, p. 1533033820948051, Jan. 2020. DOI: 10.1177/1533033820948051.
- [94] N. R. Rajagopalan et al., “Electrolysis products, reactive oxygen species and ATP loss contribute to cell death following irreversible electroporation with microsecond-long pulsed electric fields”, *Bioelectrochemistry*, vol. 155, p. 108579, Feb. 2024. DOI: 10.1016/j.bioelechem.2023.108579.
- [95] Y. Ou and S. G. Weber, “Numerical Modeling of Electroosmotic Push–Pull Perfusion and Assessment of Its Application to Quantitative Determination of Enzymatic Activity in the Extracellular Space of Mammalian Tissue”, *Anal. Chem.*, vol. 89, no. 11, pp. 5864–5873, Jun. 2017. DOI: 10.1021/acs.analchem.7b00187.
- [96] M. Iwata, H. Igami, T. Murase, and H. Yoshida, “Analysis of electroosmotic dewatering.”, *J. Chem. Eng. Japan / JCEJ*, vol. 24, no. 1, pp. 45–50, 1991. DOI: 10.1252/jcej.24.45.
- [97] C. Cano-Sarmiento et al., “Zeta Potential of Food Matrices”, *Food Eng Rev*, vol. 10, no. 3, pp. 113–138, Sep. 2018. DOI: 10.1007/s12393-018-9176-z.
- [98] I. Shomer, A. J. Novacky, S. M. Pike, U. Yermiyahu, and T. B. Kinraide, “Electrical Potentials of Plant Cell Walls in Response to the Ionic Environment”, *Plant Physiology*, vol. 133, no. 1, pp. 411–422, Sep. 2003. DOI: 10.1104/pp.103.024539.
- [99] T. B. Kinraide, U. Yermiyahu, and G. Rytwo, “Computation of Surface Electrical Potentials of Plant Cell Membranes”, *Plant Physiology*, vol. 118, no. 2, pp. 505–512, Oct. 1998. DOI: 10.1104/pp.118.2.505.

-
- [100] L. Qiu, M. Zhang, J. Tang, B. Adhikari, and P. Cao, “Innovative technologies for producing and preserving intermediate moisture foods: A review”, *Food Research International*, vol. 116, pp. 90–102, Feb. 2019. DOI: 10.1016/j.foodres.2018.12.055.
- [101] A. K. Vijh, “Electrochemical field effects in biological materials: Electroosmotic dewatering of cancerous tissue as the mechanistic proposal for the electrochemical treatment of tumors”, *Journal of Materials Science: Materials in Medicine*, vol. 10, no. 7, pp. 419–423, 1999. DOI: 10.1023/A:1008927114924.
- [102] A. K. Vijh, “Electrochemical treatment of tumors (ECT): Electroosmotic dewatering (EOD) as the primary mechanism”, *Drying Technology*, vol. 17, no. 3, pp. 586–596, Mar. 1999. DOI: 10.1080/07373939908917554.
- [103] A. K. Vijh, “Electrochemical treatment (ECT) of cancerous tumours: Necrosis involving hydrogen cavitation, chlorine bleaching, pH changes, electroosmosis”, *International Journal of Hydrogen Energy*, vol. 29, no. 6, pp. 663–665, May 2004. DOI: 10.1016/S0360-3199(03)00156-3.
- [104] A. H. Faraji et al., “Synthesis and Characterization of a Hydrogel with Controllable Electroosmosis: A Potential Brain Tissue Surrogate for Electrokinetic Transport”, *Langmuir*, vol. 27, no. 22, pp. 13 635–13 642, Nov. 2011. DOI: 10.1021/1a202198k.
- [105] A. H. Faraji, A. S. Jaquins-Gerstl, A. C. Valenta, Y. Ou, and S. G. Weber, “Electrokinetic Convection-Enhanced Delivery of Solutes to the Brain”, *ACS Chem. Neurosci.*, vol. 11, no. 14, pp. 2085–2093, Jul. 2020. DOI: 10.1021/acscchemneuro.0c00037.
- [106] S. Huclova, D. Erni, and J. Fröhlich, “Modelling effective dielectric properties of materials containing diverse types of biological cells”, *J. Phys. D: Appl. Phys.*, vol. 43, no. 36, p. 365 405, Sep. 2010. DOI: 10.1088/0022-3727/43/36/365405.
- [107] S. Huclova, D. Erni, and J. Fröhlich, “Modelling and validation of dielectric properties of human skin in the MHz region focusing on skin layer morphology and material composition”, *J. Phys. D: Appl. Phys.*, vol. 45, no. 2, p. 025 301, Jan. 2012. DOI: 10.1088/0022-3727/45/2/025301.

-
- [108] J. Dermol-Cerne and D. Miklavcic, “From Cell to Tissue Properties—Modeling Skin Electroporation With Pore and Local Transport Region Formation”, *IEEE Trans. Biomed. Eng.*, vol. 65, no. 2, pp. 458–468, Feb. 2018. DOI: 10.1109/TBME.2017.2773126.
- [109] A. Carass et al., “Evaluating White Matter Lesion Segmentations with Refined Sørensen-Dice Analysis”, *Sci Rep*, vol. 10, no. 1, p. 8242, May 2020. DOI: 10.1038/s41598-020-64803-w.
- [110] D. Miklavčič, D. Šemrov, H. Mekid, and L. M. Mir, “A validated model of in vivo electric field distribution in tissues for electrochemotherapy and for DNA electrotransfer for gene therapy”, *Biochimica et Biophysica Acta (BBA) - General Subjects*, vol. 1523, no. 1, pp. 73–83, Sep. 2000. DOI: 10.1016/S0304-4165(00)00101-X.
- [111] S. Čorović, L. M. Mir, and D. Miklavčič, “In Vivo Muscle Electroporation Threshold Determination: Realistic Numerical Models and In Vivo Experiments”, *J Membrane Biol*, vol. 245, no. 9, pp. 509–520, Sep. 2012. DOI: 10.1007/s00232-012-9432-8.
- [112] G. Pucihar, J. Krmelj, M. Reberšek, T. Napotnik, and D. Miklavčič, “Equivalent Pulse Parameters for Electroporation”, *IEEE Trans. Biomed. Eng.*, vol. 58, no. 11, pp. 3279–3288, Nov. 2011. DOI: 10.1109/TBME.2011.2167232.
- [113] B. Kos et al., “Determination of lethal electric field threshold for pulsed field ablation in ex vivo perfused porcine and human hearts”, *Front. Cardiovasc. Med.*, vol. 10, p. 1160231, Jun. 2023. DOI: 10.3389/fcvm.2023.1160231.
- [114] S. Corovic, I. Lackovic, P. Sustaric, T. Sustar, T. Rodic, and D. Miklavcic, “Modeling of electric field distribution in tissues during electroporation”, *BioMed Eng OnLine*, vol. 12, no. 1, p. 16, Dec. 2013. DOI: 10.1186/1475-925X-12-16.
- [115] L. Zang, K. Gu, X. Ji, H. Zhang, S. Yan, and X. Wu, “Effect of Anisotropic Electrical Conductivity Induced by Fiber Orientation on Ablation Characteristics of Pulsed Field Ablation in Atrial Fibrillation Treatment: A Computational Study”, *JCDD*, vol. 9, no. 10, p. 319, Sep. 2022. DOI: 10.3390/jcdd9100319.

-
- [116] D. Miklavčič et al., “Biophysics and electrophysiology of pulsed field ablation in normal and infarcted porcine cardiac ventricular tissue”, *Sci Rep*, vol. 14, no. 1, p. 32 063, Dec. 2024. DOI: 10.1038/s41598-024-83683-y.
 - [117] J. Genovese et al., “PEF treatment effect on plant tissues of heterogeneous structure no longer an enigma: MRI insights beyond the naked eye”, *Food Chemistry*, vol. 405, p. 134 892, Mar. 2023. DOI: 10.1016/j.foodchem.2022.134892.
 - [118] J. Genovese et al., “PEF-treated plant and animal tissues: Insights by approaching with different electroporation assessment methods”, *Innovative Food Science & Emerging Technologies*, vol. 74, p. 102 872, Dec. 2021. DOI: 10.1016/j.ifset.2021.102872.
 - [119] J. Genovese, P. Rocculi, D. Miklavčič, and S. Mahnič-Kalamiza, “The forgotten method? Pulsed electric field thresholds from the perspective of texture analysis”, *Food Research International*, vol. 176, p. 113 869, Jan. 2024. DOI: 10.1016/j.foodres.2023.113869.

Permissions

All the papers published at the time of submission of this dissertation are licensed under either the Creative Commons Attribution 4.0 International License (CC BY 4.0) or the Creative Commons Attribution-NonCommercial 4.0 International License (CC BY-NC 4.0).

The CC BY 4.0 license permits others to share (copy and redistribute the material in any medium or format) and adapt (remix, transform, and build upon the material) for any purpose, including commercial use, provided appropriate credit is given, a link to the license is provided, and any changes made are indicated.

The CC BY-NC 4.0 license allows others to share and adapt the material for non-commercial purposes only, under the same conditions of attribution and indication of changes.